Doctoral Dissertation
Doctoral Program in Civil and Environmental Engineering (36th Cycle)

Multidisciplinary investigation of the natural and anthropogenic ground movements in the Po Plain (Northern Italy) using geological and satellite data

Celine Eid

******

Supervisors:
Prof. Christoforos Benetatos
Dott. Mariarosaria Manzo
Ing. Riccardo Lanari
Prof. Vera Rocca

Doctoral Examination Committee:
Prof. Eugenio Carminati, Referee, Sapienza Università di Roma
Prof. Ehsan Ranaee, Referee, Politecnico di Milano

Politecnico di Torino

2024

I hereby declare that, the contents and organization of this dissertation constitute my own original work and does not compromise in any way the rights of third parties, including those relating to the security of personal data.

Celine Eid

2024

* This dissertation is presented in partial fulfillment of the requirements for **Ph.D. degree** in the Graduate School of Politecnico di Torino (ScuDo).

Acknowledgments

I would like to express my deepest gratitude to my supervisors, Prof. Vera Rocca and Prof. Christoforos Benetatos, for their continuous guidance and support during my PhD. I would also like to sincerely thank my PhD colleague, Alberto Manuel Garcia Navarro, for generously dedicating his time and technical expertise to a portion of my thesis project related to the analysis of InSAR data. I extend my thanks to all my colleagues in the Underground Energy Systems and Energy Transition group of Politecnico di Torino for their kindness.

Special thanks to our colleagues from CNR (Naples): Dott. Mariarosaria Manzo (may her soul rest in peace), Ing. Riccardo Lanari, Dott. Claudio de Luca and Dott. Giovanni Onorato for providing the InSAR data used for this thesis and for their helpful and insightful discussions. Sincere appreciation also goes to Ing. Andrea Chahoud from ARPAE Emilia-Romagna for providing the data related to groundwater production and for his continuous cooperation.

A big thanks to my friends scattered around the world, from Turin to Lebanon. Their encouragement and support have been invaluable, sustaining me through both the highs and lows of this journey.

The biggest thanks of all goes to my family; my unconditional support system. I would not be where I am today if not for them. To my parents, Elie and Amal, who have sacrificed everything for us and provide us with endless love and support. To my brother, Eddy, for being my role model and the best big brother any girl could have. To my little sister, Elise, for being my built-in best friend and the person I can always turn to for anything.

Summary

Land movements, i.e., subsidence and uplift, represent a great concern that threatens the sustainable development of many societies around the world from environmental and socioeconomic viewpoints. The Po Plain, a sedimentary basin in northern Italy, contains numerous regions that have been affected by a widespread land subsidence and uplift of natural and anthropogenic origins since the mid 20th century. Most subsidence in the Po Plain is anthropogenic due to its abundance in onshore gas reservoir formations and shallow aquifer systems. The identified uplift, however, is mostly associated with tectonic activities. In this work, a multidisciplinary approach is proposed for the investigation and quantification of the superposition of natural and anthropogenic effects in the Po Plain. A critical assessment on the available datasets of land movements in the Po Plain is performed along with the creation of a fluid (gas and water) production dataset as a first step in the spatial allocation of the phenomena and assessment of their superposition. Then, a specific area in the Po Plain is selected where ground movements have been affected by both a strong water production and underground fluid storage, together with the presence of natural components. A thorough research is performed in order to collect and analyze wells and other available data for the uppermost part of the Po Plain to characterize the sedimentary bodies involved in water production. The research is initially applied in a 3D numerical modelling approach involving the geological modelling of the aquifer system followed by the characterization of the petrophysical and mechanical properties. The geological model is then used to set up the fluid-flow model where the hydrodynamic parameters are assigned and the production scenarios are set up. Finally, the ground displacement analysis is addressed via a stress-strain finite element model, assuming an uncoupling approach, such that the land movements of the area are jointly analyzed and defined using the results from the modelling and simulation process and the results obtained by available studies of ground movements induced by the Underground Gas Storage (UGS) system. Finally, the analysis of an InSAR time series dataset and that of published maps, describing the contribution of both natural and anthropogenic components, is integrated for the full understanding of the phenomena affecting the area of study. This work proves groundwater production to be the main factor affecting subsidence in the area of study characterized by the UGS and minor-producing water wells compared to other areas in the Po Plain with extensive water production. In addition, an existing post-processing technique of InSAR time series

is proved effective in identifying and quantifying the physical phenomena affecting ground movements. The following outcomes can be considered for the further development of a coupled simulation approach of the aquifer and UGS systems, and applying InSAR time series ground deformation in correlation with other monitoring methods for better characterizing the deformation of the shallow layers associated with groundwater activities, and analysis of horizontal components.

Contents

List of Figures

List of Tables

List of Symbols

σ_{ij}	Stress tensor
ε_{ij}	Strain tensor
Ψ	Stress potential
C_{ijhk}	Stiffness tensor
σ	Normal stress
τ	Shear stress
ε	Normal strain
Γ	Shear strain
E	Young’s modulus
v	Poisson’s ratio
G	Shear modulus
λ	Lame’s constant
K	Bulk modulus
σ'	Effective stress
p	Pressure
α	Biot coefficient
ε_{ij}^{e}	Elastic strain
ε_{ij}^{p}	Plastic strain
Λ	Plastic multiplier
Q	Plastic potential
τ_0	Cohesion of material
Φ	Material angle of internal friction
e	Void ratio
V	Volume
v	Specific volume
n	Porosity

p'	Effective mean stress
N	Specific volume of normal compression line at unit pressure
k	Slope of a swelling line
d	Slope of the virgin consolidation line
OCR	Overconsolidation ratio
c_M	Vertical compressibility
∇^2	Laplace operator
∇	Gradient operator
γ	Water specific weight
K_{ij}	Hydraulic conductivity tensor
μ	Viscosity of water
β	Compressibility of water
S_s	Elastic storage coefficient
e_0	Initial void ratio
c_b	Compressibility for aquifer/aquitard
θ	Subsidence
s	Soil thickness

Chapter 1

Introduction

Reliable identification and quantification of land movements, i.e., subsidence and uplift, is essential for global sustainable development from environmental and socioeconomic viewpoints. Land movements result from anthropogenic activities such as the extraction or injection of fluids (groundwater or hydrocarbons and the underground storage of fluids such as methane, hydrogen and carbon dioxide) and local salt mining (Modoni et al., 2013; Galloway, 2014), integrated with natural processes that, among others, include tectonics and sediment compaction (Allen, 1984; Carminati and Di Donato, 1999). The most severe cases of land movements have been associated with subsidence due to fluid extraction (e.g., San Joaquin Valley (Galloway and Riley, 1999); Tianjin (Hu et al., 2002); Jakarta (Ng. et al., 2012)), such that a significant development has been made in terms of measuring and estimating the extent and magnitude of the ground movements and simulating predicted future events. The risk assessment of subsidence is thus considered a key-point for the effective management of the land and the underground resources.

Over the years, synthetic aperture radar interferometry (InSAR) has evolved into a powerful tool used in remote sensing to monitor and study Earth's surface deformation over time. Its ability to detect even small changes of land movements has revolutionized our understanding of processes such as volcanic activity, glacier movement, tectonic deformation and, most importantly in our case, land subsidence. In that context, the analysis of the physical processes involved in underground formation compaction and expansion that result in land subsidence and uplift has also been investigated using analytical methods and 3D multidisciplinary numerical approaches (Gambolati and Teatini, 2015; Benetatos et al., 2020). By incorporating detailed geological, dynamic and mechanical data, these numerical models can provide a more comprehensive understanding of land movements mechanisms and their amplitude and spatial distribution. Additionally, 3D numerical approaches offer the flexibility to simulate different scenarios and assess the effectiveness of mitigation measures, aiding in informed decision-making for sustainable land management and infrastructure planning.

The Po Plain, located in northern Italy, is a highly industrialized and populated region that has been affected by a widespread land subsidence of natural and anthropogenic origin since the mid 20th century (Eid et al., 2022). Most subsidence in the Po Plain is of anthropogenic origin and has been the topic of numerous studies due to its high degree of urbanization and the abundance of shallow aquifer systems (Teatini et al., 2006; Darini et al., 2008; Ferronato et al., 2007) and onshore and offshore hydrocarbon-bearing reservoir formations (Bau' et al., 1999;2002; Teatini et al., 2011; Benetatos et al., 2020). Several of the latter have been converted to and still operate as underground gas storage (UGS) systems. In several areas of the Po Plain, uplift is also identified mostly due to tectonic processes.

The geological complexity of the Po Plain and the coexistence of anthropogenic activities, both close to the Earth's surface and in depth, offer an excellent candidate in order to study and analyze the superposition of effects related to different spatial and temporal timeframes. Although the investigation of the ground movements related to oil/gas production and storage and to groundwater production has been extensively examined, the geological description of the shallow aquifers is still characterized by uncertainties mostly related to the areal extension of the sedimentary bodies, the definition of stratigraphic boundaries, and their petrophysical and mechanical characterization. Furthermore, detailed information regarding the water production volumes and allocation are rarely available. They are usually associated to broad municipality areas and they present time lags during their acquisition, increasing the uncertainties during modelling processes.

In this work, a multidisciplinary approach is proposed for the investigation and quantification of the superposition of natural and anthropogenic effects. Initially, a holistic and detailed review and critical analysis of the available studies on land movements in the Po Plain is performed, such as the identification of the main factors affecting the land movements. All the available data regarding the water production from the Emilia-Romagna region is collected and analyzed. A thorough research is performed in order to collect and analyze well data for the uppermost part of the Po Plain to characterize the sedimentary bodies involved in water production. Then, a specific area in the Po Plain is selected where ground movements have been affected by both a strong water production and underground fluid storage, together with the presence of natural components. The research is applied using a multidisciplinary approach involving geological modelling, petrophysical and mechanical characterization, fluid flow simulation, geomechanical simulation and InSAR data analysis and interpretation.

The 3D numerical modelling is performed on the shallow subsurface involved in groundwater exploitation processes. The modelling begins with a detailed geological characterization describing all the main stratigraphic, structural, lithological and petrophysical properties. The geological model is then used to set up and perform fluid-flow simulations of groundwater production during a certain period. The ground displacement analysis is addressed by a stress-strain finite element model such that the land movements of the area are jointly analyzed and defined using the results from the modelling and simulation process and the results obtained by available studies of ground movements induced by the UGS. Finally, the analysis of an InSAR time series dataset and that of published maps, describing the contribution of both natural and anthropogenic components, is integrated for the full understanding of phenomena affecting the area of study.

The thesis is organized as follows: Chapter 2 gives an overview on the classification of land movements, focusing on subsidence effects and history. The main ground-based and remotely sensed subsidence monitoring techniques are also briefly introduced. Chapter 3 describes the geology of the Po Plain with an emphasis on the Pliocene-Quaternary evolution. In turn, the superficial aquifers of the Po Plain are defined with a focus on the Emilia-Romagna aquifers and groundwater bodies. Chapter 4 critically assesses the most important datasets on land movements in the Po Plain, specifically in the Emilia-Romagna region, that have been collected throughout the years, highlighting present-day vertical velocities and subsidence maps. Chapter 5 discusses the basic principles of the different constitutive models of deformable bodies and their application in groundwater systems. Chapter 6 presents the complete methodology proposed and adopted in this work. Chapter 7 deals with the application of the 3D numerical modelling workflow on a case study in the Po Plain focused on the uppermost part of the stratigraphic record involved in groundwater production processes. Chapter 8 expands on the area of the case study presenting the use of InSAR data to identify and quantify the seasonal and trend behavior related to aquifer exploitation, UGS activities and natural uplift. Chapter 9 summarizes the main results of the thesis and proposes further research development.

Chapter 2

Land movements

Land movements, i.e., subsidence and uplift, are defined in this chapter, with a focus on subsidence effects and history. Land movements monitoring processes and techniques are then introduced in a systematic review.

2.1. Definition and classification

Land subsidence is defined as the downward, vertical settlement of the Earth's surface due to the subsurface movement of Earth's materials. The land lowering process can be a "sudden sinking or gradual settling" (Bates and Jackson, 1980). The latter indicates the steady lowering of the soil that can measure up from a few millimeters to several centimeters per year and is the one dealt with in this thesis.

Subsidence can be classified in terms of its causes: natural and anthropogenic (Scott, 1979). These two drivers act on different spatial and temporal scales. Natural subsidence can act at regional (tens to hundreds of km) or local (up to tens of km) intervals (Johnson, 1991) and takes place over millions to thousands of years, whereas anthropogenic subsidence acts mainly at a local and smaller time scale over hundreds to tens of years (Carminati and Di Donato, 1999).

Carminati and Di Donato (1999) depicted the general relation for the present-day vertical velocity of a specific area with respect to the mean sea level as follows:

$$V_{total} = V_t + V_{sl} + V_c + V_{pgr} + V_a$$

where V_t corresponds to the velocity component from tectonic activity, V_{sl} and V_c are the components from sedimentation and compaction, respectively, and V_{pgr}

represents the post glacial rebound effect related to the Pleistocene deglaciation. The sum of these components make up the natural component of vertical velocity and V_a accounts for all the anthropogenic components. These include subsurface fluids extraction (e.g. water, crude oil and natural gas), underground mining, subsurface and surface erosion and loading, oxidation of peat, among others (Allen, 1984).

Groundwater extraction is considered the most prominent and triggering component of subsidence and makes up the most severe cases around the world. It is caused by the compaction of unconsolidated aquifer sediments following the increment of effective stress and subsequent loss of pore pressure (Galloway and Burbey, 2011). The well-known case of the San Joaquin Valley southwest of Mendota (California) is shown in Figure 2.1. The progressive settlement of the land is caused by years of groundwater pumping for irrigation purposes. A subsidence of approximately 9 m is recorded from the year 1925 to 1977.

Figure 2.1: The San Joaquin Valley (California) subsidence case. Photo shows location of maximum subsidence of approximately 9 m from 1925 to 1977 caused by groundwater pumping. Photograph by R.L. Ireland featuring Dr. J.F. Poland (1977).

On the other hand, land uplift is defined as the increase in the vertical elevation of the Earth's surface either due to an increasing upward force applied from below or a decreasing downward force from above. During uplift, land as well as the sea floor rise. Land uplift is classified in the same way as subsidence; based on its drivers as natural or anthropogenic and is also depicted in the relation presented above. So, most of the same natural and anthropogenic components that affect subsidence also affect uplift but in an opposing manner. For example, subsurface fluids production is counteracted by the injection of fluids into the subsurface that causes the land to rise over time.

2.1.1. Superposition of components

According to Galloway (2014), most anthropogenic drivers of subsidence can either trigger or accelerate natural subsidence processes. The degree of importance associated to land movements occurring in different regions of the world is primarily dependent on the distribution of the occurrence of geological structures. Within that context, areas affected by anthropogenic land movements are considered superimposing already existing natural inclinations to land movements up to a certain extent. On smaller scales, even anthropogenic components can overlap with each other. An example is the simultaneous subsurface production of water from aquifer systems and gas from hydrocarbon reservoirs over the same area. The interdisciplinary nature of the overlapping phenomena, their temporal and spatial variability, their corresponding data availability and quality and their complexity in modelling prove challenging for the accurate assessment and quantification of the induced land movements and have not been thoroughly investigated in the literature.

2.2. Subsidence effects

Subsidence is commonly viewed as a globally hazardous phenomenon that affects the natural environment as well as human infrastructure (Figure 2.2). According to the most recent International Hydrological Programme VIII (2014-2020) of UNESCO (United Nations Educational, Scientific, and Cultural Organization), land subsidence was highlighted as one of the most urgent threats to sustainable development. Since it is mainly characterized by slow and steady movements, it rarely has a huge impact on human life; however, it still causes major social harms that in turn lead to high economic costs of repair.

Figure 2.2: Examples of subsidence effects: (a) cracks in walls; (b) building damages in Jakarta, Indonesia; (c) road damage; (d) coastal flooding in Venice, Italy.

The impacts of subsidence vary depending on: (i) the mechanisms controlling the subsidence (discussed in section 2.1), (ii) the scale of the affected area and (iii) the location of the affected area; whether it's inland or coastal. The following description of these impacts refers to Galloway (2014). Environmental impacts from inland subsidence arise from hydrologic changes in the landscape and processes such as the modification of the land-surface gradients that subsequently affects the surface-water runoff, water infiltration and groundwater recharge and discharge of the natural system. In turn, this affects the ecosystems by the formation of surface-water floods and ponds in areas of surface depressions and the drainage of wetland areas. Corresponding social impacts include the damages to buildings, infrastructures (roadways, canals) and underground structures (pipes, drainageways, wells). These damages are considered direct damages (Gambolati and Teatini, 2021). On the other hand, the main environmental impact from coastal subsidence arises from the relative marine transgression due to the sea-level rise that allows the sudden seawater intrusion inland. In this case, farmland productivity is affected by the limitation of freshwater availability and indicates an indirect damage of subsidence (Gambolati and Teatini, 2021). The major social harm is the increased risk of coastal flooding. The most prevalent indirect damage of subsidence, coastal or inland, is the relative changes in surface and subsurface water levels.

It is important to note that the environmental impacts of subsidence continue long after subsidence ceases. The process of recovering water levels is not always as straightforward and may cause problems such as the accidental recharge of the phreatic aquifer by improperly plugged boreholes that were meant to re-pressurize deep confined aquifers (Paris et al., 2010).

In terms of the economic effects of land subsidence, it is rather complex to estimate the associated costs. This may be due to the long time frame of most subsidence processes and its superposition with other causes of damage making it hard to single out the costs related to subsidence solely. However, several studies report that these costs amount up to billions of dollars per year globally (e.g. Deltares, 2015; Hallegatte et al., 2013). Gambolati and Teatini (2021) report annual costs of over 3.5 billion euros in The Netherlands and around 1.5 billion dollars in China.

In summary, Bagheri-Gavkosh et al. (2021) display the different geological, environmental, hydrogeological and economic impacts of land subsidence based on literature in Figure 2.3.

Figure 2.3: Land subsidence impacts (from Bagheri-Gavkosh et al., 2021).

2.3. History of subsidence

First cases of land subsidence discoveries date back to the 20th century. In fact, the first discovery related to subsurface fluid withdrawal was made in 1926 by Pratt and Johnson, two American geologists who interpreted the corresponding cause of subsidence above the Goose Creek oil field of S. Jacinto Bay in Texas. Their hypothesis was later confirmed by countless case studies, especially after World

War II when an increase in the occurrence of land subsidence occurred globally due to the rising demands on natural resources, specifically groundwater. Some of these historical cases are listed in Table 2.1 and were the result of research projects adopted by UNESCO's International Hydrological Programme in 1965. In 1975, UNESCO formed the Working Group on Land Subsidence that eventually published the "*Guidebook to Studies of Land Subsidence Due to Ground-water Withdrawal*" (Poland, 1984) that served as the first reference introducing the effect of groundwater withdrawal on subsidence. Ten international symposia have been held to date with ongoing research studies on the phenomenon of land subsidence. Table 2.1 also highlights that major areas are still affected by subsidence at present.

Table 2.1: Historical cases of land subsidence worldwide.

Location	**Max. subsidence (m)**	**Period**	**Reference**
Wilmington, California	9	1926-1968	Allen (1969a)
San Joaquin Valley, California	9	1930-present	Galloway and Riley (1999); Borchers and Carpenter (2014)
Mexico City, Mexico	13	1900-present	Figueroa-Vega (1984); Mazari and Alberro (1990); Cigna and Tapete (2021)
Bangkok, Thailand	2.1	1933-present	Nutalaya et al. (1996); Phien-wej et al. (2006)
Tianjin, China	3.2	1959-present	Hu et al. (2002); Yi et al. (2011); Li et al. (2020)
Tokyo, Japan	4.6	1918-1978	Yamamoto (1995)
Jakarta, Indonesia	4	1974-2010	Ng. et al. (2012)
Venice, Italy	0.12	1952-1973 1973-1993	Gambolati et al. (1974) Teatini et al. (1995)
Ravenna, Italy	1.6	1897-2002	Carbognin et al. (1984); Teatini et al. (2006)
Tehran, Iran	3	1989-2008	Mahmoudpour et al. (2013); Dehghani et al. (2013)

2.4. Land movements monitoring

Monitoring land movements is essential for the continuous understanding of their causes and for the identification of temporal and spatial patterns of regional and local land movements that might help in mitigating the phenomena's impacts. Historically, several ground-based geodetic techniques have been developed and applied; however, due to their scattered spatial limitation, they are unable to provide accurate displacement measurements at regional scales. On the other hand, remotely sensed geodetic surveys are characterized by extensive spatial coverage, exceeding 10000 km^2, and provide accurate estimations of land movements. A brief explanation on the most used ground-based techniques (Global Navigation Satellite Systems (GNSS) positioning, leveling and extensometers) and remotely sensed SAR (Synthetic Aperture Radar) techniques is given below.

2.4.1. Global navigation satellite systems (GNSS)

GNSS consist of a constellation of Earth-orbiting satellites that produce radio signals used to provide positioning, navigation and timing data to GNSS receivers. GNSS were developed in the early 1970s and currently include four country-led global operational systems: GPS (led by the U.S.), GLONASS (led by Russia), GALILEO (led by European countries) and BeiDou (led by China). Other regional systems include Japan’s QZSS and India’s IRNSS. It should be noted that GPS is often wrongly interchanged with GNSS due to its established usage in the market.

The “absolute” position of a GNSS receiver refers to its latitude, longitude and elevation with respect to mean sea level. It can be defined when signals from at least four GNSS are received simultaneously. Once the position is defined, the GNSS receiver adjusts its internal clock with the satellite clocks, producing the corresponding time stamps. This method produces and monitors single points at the receivers and is not considered highly precise for surveying. Instead, the differential GNSS technique is used to enhance the accuracy by determining the position of two points on two respective GNSS receivers from signals coming from the same set of satellites (Gambolati et al., 2005). After some time, these two points are reallocated and the relative delta of the strain or ground movement can be measured. In this method, at least one of the receivers is benchmarked as reference. The level of accuracy is thus dependent on the network of benchmarks set which is why it is essential to have a proper network design and survey planning (US Army Corps of Engineers, 1996). An example showing vertical displacement rates in the European Alps on GNSS stations is provided in Figure 2.4.

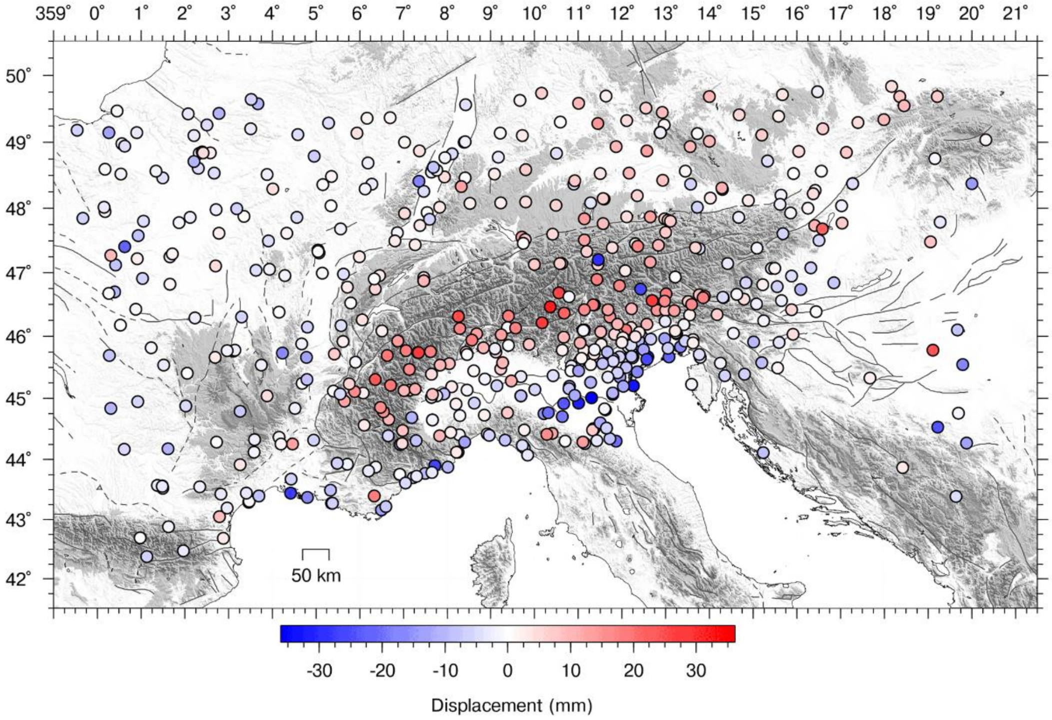

Figure 2.4: Location of GNSS stations in the European Alps with the colors representing vertical displacement rates in mm per year (from Pintori et al., 2022).

2.4.2. Leveling

Geodetic leveling is a simple yet accurate method of determining the difference in ground elevations with respect to mean sea level. It was originally developed in the nineteenth century and is still widely used nowadays. A monitoring network of benchmarks first has to be set up by precise leveling: a precisely leveled telescope and two vertical leveling rods are used to record the elevation difference between two benchmarks. The elevation difference is recorded twice by adding the elevation differences of a number of turning points (Figure 2.5). Repeated surveys at consecutive timings are then used to indicate any movements in the benchmarks, hence ground deformations (Navarro-Hernández et al., 2022).

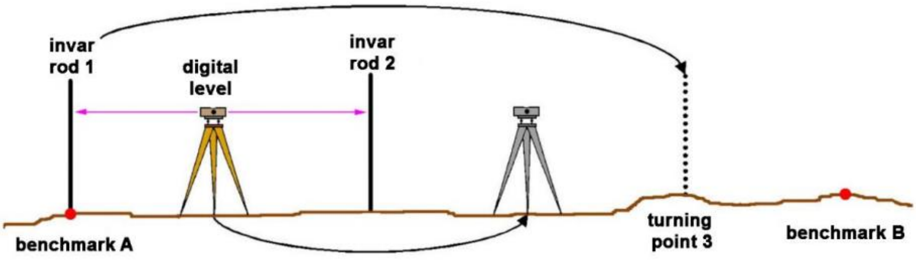

Figure 2.5: Simplified sketch of a leveling survey (from Gambolati and Teatini, 2021).

The rigid location and stability of the benchmarks are essential to ensure long-term time series. The time at which the leveling is done is also important when dealing with heavily pumped basins; it should ideally be performed when subsidence or compaction is minimal (Galloway and Burbey, 2011).

2.4.3. Borehole extensometers

Borehole extensometers are used in order to continuously measure changes in the thickness of sediments or rocks, hence the change in the vertical distance between the ground surface and a subsurface benchmark located at the bottom of a borehole. If that benchmark is positioned below the bottom of the compacting aquifer system, the extensometer can be used as a reliable and stable reference for other local geodetic surveys (Galloway and Burbey, 2011). The generated data related to the deformation analyses of the aquifer complex can be additionally used to determine the stress-strain behavior.

Various types of borehole extensometers exist including horizontal extensometers that were originally developed to measure the horizontal ground movement of earth fissures due to groundwater level changes (Carpenter, 1993). Figure 2.6 shows an example of a magnetic extensometer with a number of markers (magnet rings) at different depths of the formation borehole. The depth of each ring is measured by lowering the magnetic tape probe along the tube. This type of extensometer is usually used in the case of multi-aquifer systems.

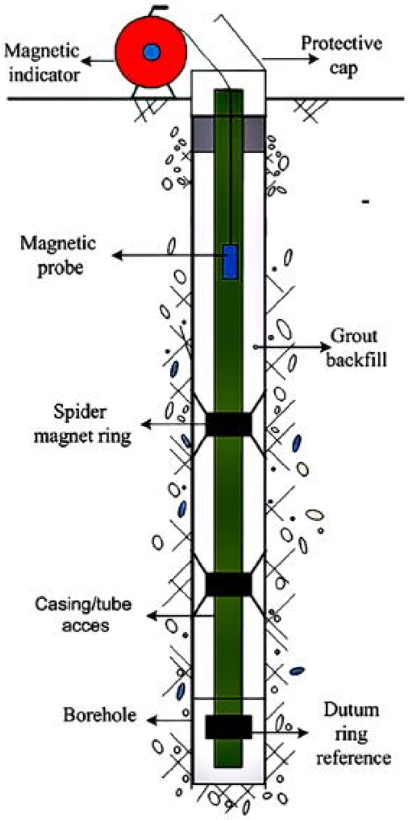

Figure 2.6: Schematic representation of a magnetic borehole extensometer (from Gholinia et al., 2022).

2.4.4. SAR interferometry

Synthetic Aperture Radar (SAR) is a conventional remote sensing technique that uses radar signals to measure the spatial extent and the magnitude of deformation of the Earth's crust. The radar antenna of the remote sensing satellite transmits pulses of electromagnetic microwaves to the Earth's surface that reflect back with a digital image of the surface. The image pixel records the amount of back-scattered energy by carrying the amplitude and phase information of the radar signal within each cell (Gambolati et al., 2005). The high resolution of the image pixel is obtained by focusing the raw radar echoes in the directions of the cross-track and along-track, creating a typical spacing of 20-100 m within an area of 100 km wide. (Bürgmann et al., 2000). Interferometric Synthetic Aperture Radar (InSAR) combines two SAR images to generate a radar interferogram by measuring the phase difference between the corresponding image points. The two images have a spatial baseline; hence acquired from slightly different positions where the radar antennas are separated in the cross-track direction. This allows for the measurement of the surface topography. The Differential InSAR (DInSAR) approach uses two SAR images with a temporal baseline (acquired at different times with the radar antennas separated in the along-track direction) to measure ground surface displacement (CNR-IREA website). The measurements are one dimensional related to projection of the 3D displacement vector along the satellite Line-Of-Sight (LOS). This is due to the fact that the radar viewing angle is tilted to less than 45° from the LOS. Two different acquisition geometries are used by the satellite radar sensor: "ascending mode" when the satellite is moving north and "descending mode" when it moves south. When the SAR images are acquired, the results can then be used to estimate the vertical and the horizontal components of the displacement vector (Figure 2.7). A final, important step is setting the absolute scale, or calibration. Interferometry tends to be a relative measurement. To convert these relative measurements into absolute measurements of displacement, ground control points obtained from GPS measurements or other ground-based techniques are used. By referencing the InSAR measurements to these control points, it becomes possible to determine the absolute magnitude of the surface deformation.

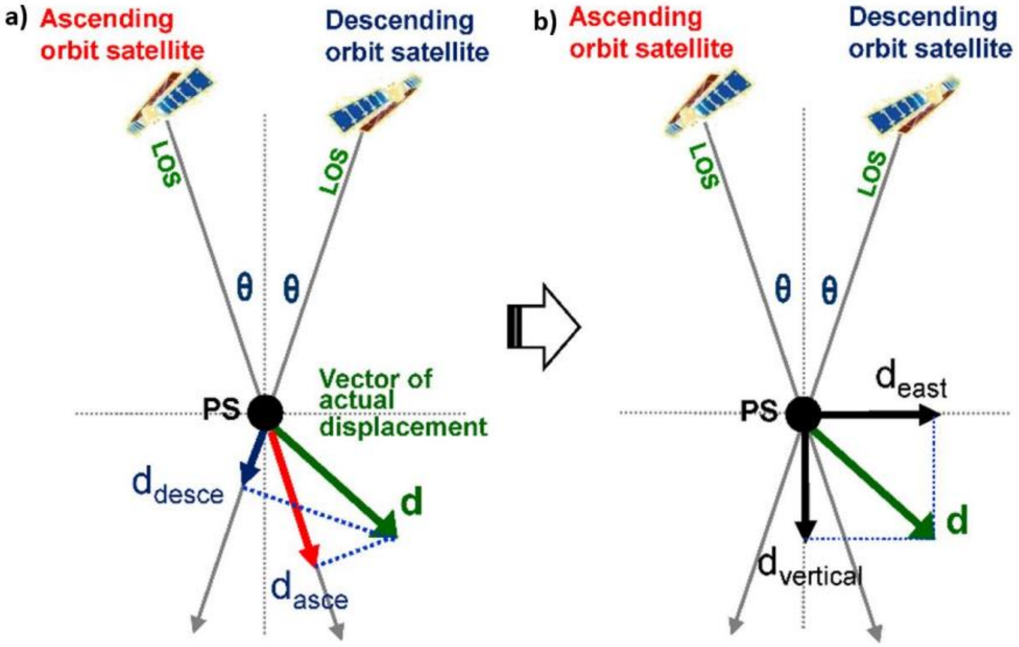

Figure 2.7: (a) Quantification of the vector of actual displacement (d) by combining the ascending (d_{asce}) and descending (d_{desce}) components along the LOS directions; (b) the consequent vertical ($d_{vertical}$) and horizontal (d_{east}) displacement components (from Gambolati and Teatini, 2021).

The increasing use of SAR technologies can be attributed to several features including their spatial resolution discussed above, their spatial variability and their ability to function around the clock. They are also considered less expensive than the ground-based techniques. However, the importance of calibrating SAR results with results from those techniques should be emphasized especially in cases where the SAR signal can loose coherence and can't be used for interpretation (Gambolati and Teatini, 2021).

Table 2.2 provides a summary of the discussed monitoring techniques and their main features.

Table 2.2: Comparison between the most used land movements monitoring techniques.

	GNSS	**Leveling**	**Borehole extensometers**	**SAR interferometry**
Technique type	Ground-based	Ground-based	Ground-based	Remotely sensed
Spatial coverage	Wide coverage, global positioning	Limited to specific points/line	Limited to specific borehole locations	Large area coverage, satellite based
Temporal resolution	Real-time or post-processing continuous monitoring	Typically periodic surveys	Continuous monitoring	Depends on satellite revisit times, typically days to months
Accuracy	Millimeter to centimeter level	Millimeter to centimeter level	Millimeter to submillimeter level	Millimeter to centimeter level
Terrain dependency	No	Yes	No	No

Chapter 3

Po Plain: Geological background

The Po Plain is a major geographical feature of northern Italy and is the most extensive plain in Western Europe, spanning an area of approximately 46,000 km^2. It is a highly industrialized and populated region with a density of roughly 17 million inhabitants that is almost one third of Italy's population and it has been affected by widespread land movements of natural and anthropogenic origin since the mid 20th century. It is especially characterized by a presence of infrastructures, urban centers and intensive agricultural activities. In this chapter, the geological description of the Po Plain is presented starting from the regional geodynamic and stratigraphic settings to an emphasis on the Pliocene-Quaternary evolution. In turn, the superficial aquifers of the Po Plain are defined with a focus on the Emilia-Romagna aquifers and groundwater bodies.

3.1. Geological setting of the Po Plain

Extensive research has been done on the geological evolution and regional subsurface architecture of the Po Plain in the last four decades using a detailed subsurface dataset aimed initially at hydrocarbon exploration activities by Eni-AGIP (AGIP Mineraria, 1959, AGIP, 1977). Seismic reflection profiles and deep-well log data acquired during exploration and development activities were used for the analysis and interpretation of an accurate geological description (e.g. Pieri and Groppi, 1981; Pieri, 1983; Cassano et al., 1986; Doglioni, 1993; Regione Emilia-Romagna and Eni-AGIP, 1998; Casero, 2004; Regione Lombardia and Eni Divisione, 2002; Amorosi et al., 2008; Ghielmi et al., 2013; Turrini et al., 2016).

3.1.1. Geodynamic setting

The Po Plain forms a sedimentary basin that lies on the northernmost buried sector of the Adria microplate, a promontory of the Africa plate, and is located between the Northern Apennines and the Southern Alps (Figure 3.1a,b). The formation of the Po Plain foreland basin system generated by the evolution of these two facing fold-and-thrust belts likely began in the Early Mesozoic and is still ongoing. This is justified by latest research findings and the latest earthquake activities in the central and eastern part of the basin (e.g. Burrato et al., 2003; Livio et al., 2009; Fantoni and Franciosi, 2010).

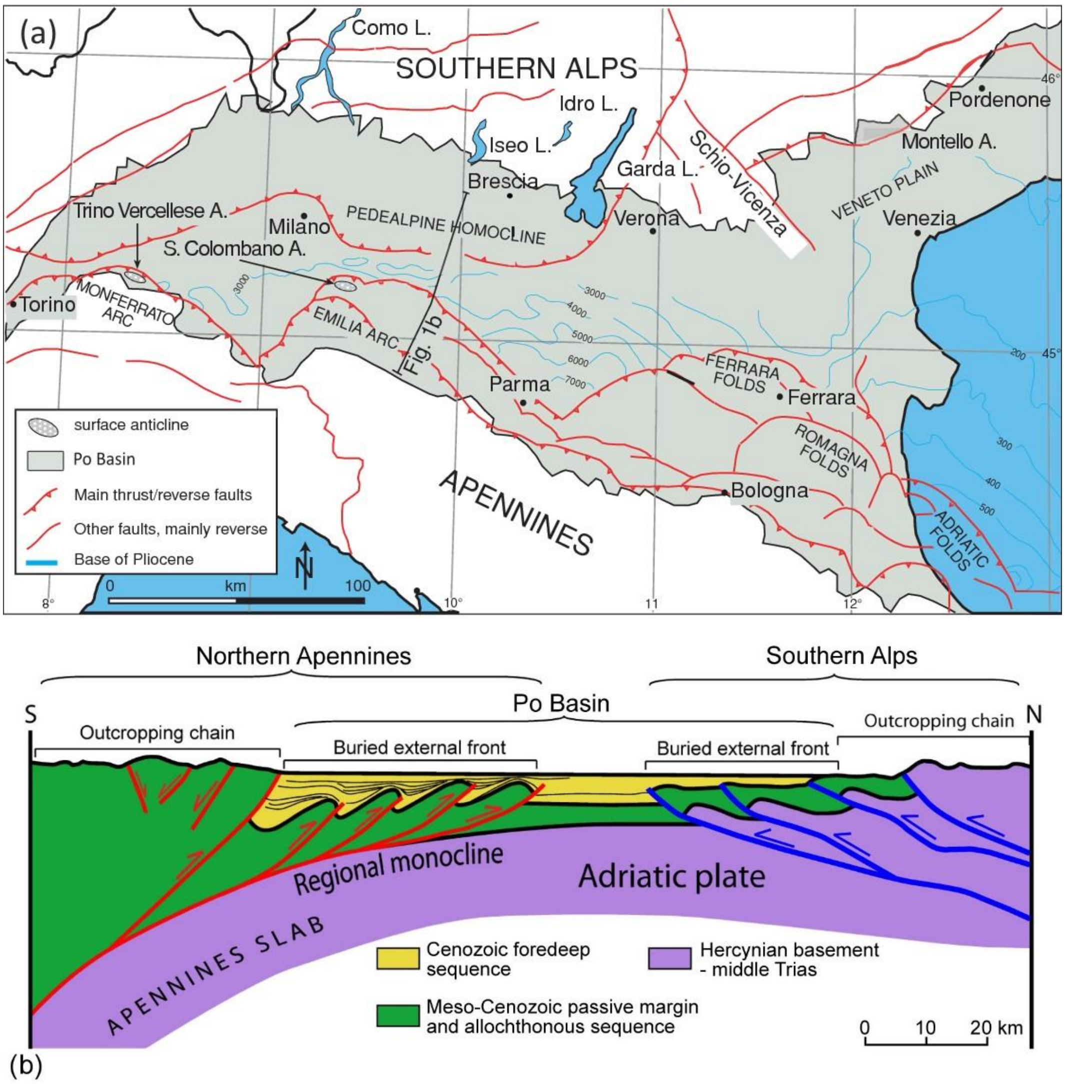

Figure 3.1: (a) Structural map of the Po Plain (modified from Burrato et al., 2003); (b) Structural cross-section of the central Po Plain showing the buried fronts of the Northern

Apennines and the Southern Alps under the Plio-Pleistocene sedimentary sequence (from Livani et al., 2023). Location of the trace is shown in (a).

A Mesozoic extensional tectonic phase was developed by the opening of the Tethyan ocean and the early extension of the Adria microplate and lasted until the Lower Paleogene. It was followed by a Cenozoic compression phase due to the collision between the Adria microplate and Eurasia. This led to the closure of the ocean basin and the development of WNW-ESE thrust zones at the Southern Alps and NW-SE-oriented thrusts of the Northern Apennines (Livani et al., 2023). The continuous thrusting of the two opposite-verging belts gave rise to foredeep basins where a thick syn-orogenic clastic sequence was deposited (Eid et al., 2022). Fast subsidence rates were induced in the whole Po Plain causing the more external fronts of the Apennines and Alpines thrust belts to be buried beneath the plain (Figure 3.1b); with the N–NE verging Northern Apennines system buried beneath the Quaternary cover, whereas the S verging Southern Alps system forms a platform dipping gently into the basin (Eid et al., 2022).

The Po Plain basin represents the external domains of the Southern Alps and the Northern Apennines with the foreland in between that create tectonic arches with subsequent sediment infilling of the foredeep basin (Turrini et al., 2016). The Apennines front shows three blind, north-verging thrusts and folds that are arranged in three asymmetric arcs, from west to east: Monferrato Arc, Emilia Arc, and Ferrara-Romagna Arc (Figure 3.1a). The latter is buried beneath the modern coastal plain and is in turn subdivided into three minor structures: the Ferrara folds (the most external structures of this arc), the Romagna folds and the Adriatic folds (Figure 3.1a). For these structures, the main tectonic event, based on seismic data analysis, dates back to the Late Miocene-Early Pliocene with any later tectonic activity considered negligible (Picotti et al., 2009). On the other hand, the external fronts of the Southern Alps are arranged in a simpler pattern representing the non-metamorphic retrobelt of the Alpine chain with its southern extent almost reaching the northern Apennines front (Livani et al., 2023 and references therein). The Schio-Vicenza Line interrupts the E-W continuity of the Southern Alps' thrust front and thus separates it from the respective thrusts of the Veneto Plain to the east (Figure 3.1a, Burrato et al., 2003).

The active Northern Apennines thrust fronts display a complex architecture that features potential seismogenic sources associated with thrust ramps positioned at various structural levels. The complexity of the thrust geometries arises from the presence of multiple potential detachment levels within the sedimentary sequence deformed by the thrust belt. Among these potential seismogenic sources is a deep thrust ramp situated at depths ranging from approximately 12 to 22 km, studied and depicted as a relatively high angle portion of a regional thrust (Barchi et al. 1998; Vanolli et al., 2014). Without geological evidence of shortening across this deep ramp, seismic activity remains the sole indicator of its activity. Indeed, several earthquakes that have occurred in the area northeast of the Northern Apennines crest (2012 earthquakes near Reggio nell'Emilia and near Parma), at an estimated depth greater than typical (i.e., below 15 km), can potentially be linked to this structure. Contrast to the Northern Apennines mountain front, the foothills of the western Southern Alps do not feature a tectonically controlled mountain front, with the only reported exception being a small area located north of Milan (Michetti et al., 2012).

3.1.2. Stratigraphic architecture

The subsurface stratigraphic succession of the Po Plain overlies the Hercynian metamorphic basement and consists of the following, from bottom (oldest) to top (youngest): (Turrini et al., 2014)

i. Early Permian-Early Triassic evaporitic-siliciclastic sediments formed during the Lower Triassic rifting

ii. Middle Triassic carbonate succession encompassing platform and intra-platform basins

iii. Pelagic succession developed during the Upper Triassic-Jurassic extensional phase

iv. Mesozoic-Eocene sedimentary successions encompassing mainly limestones (mudstone and packstone–grainstone), dolomites with marls and overlying Miocene sandy marls conglomerates representing the deposition of the foreland ramp

v. Late Miocene-Late Pliocene turbidites related to the evolution of the foredeep northern Appenine system

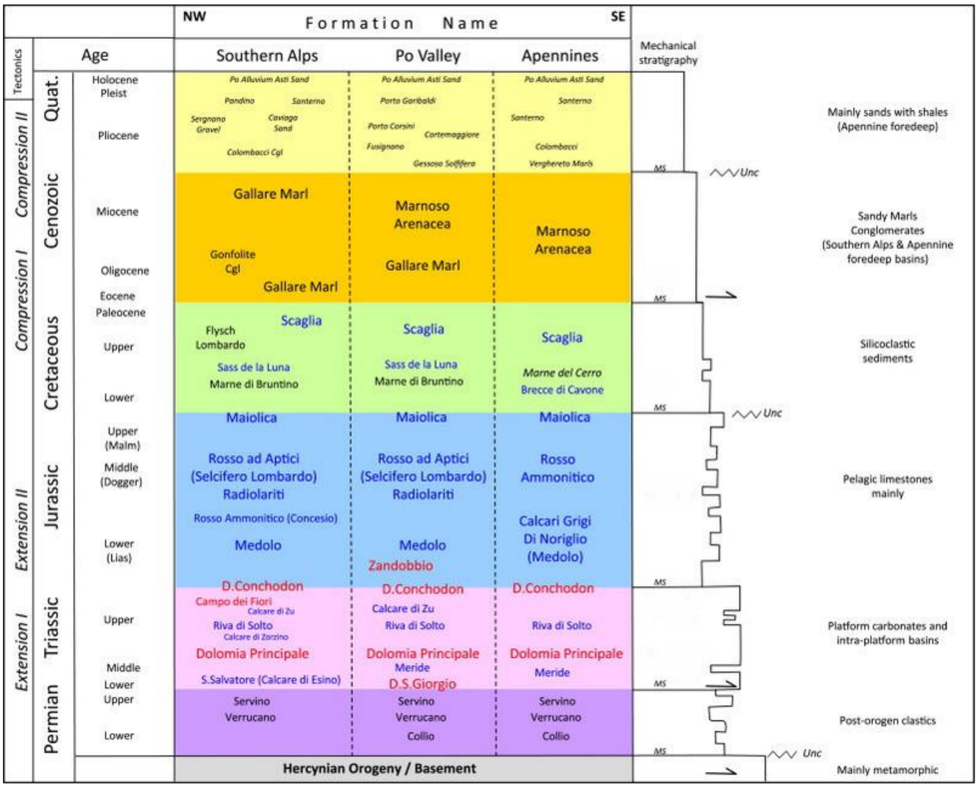

Figure 3.2: Schematic stratigraphic column of the Po Plain (modified from Turrini et al., 2014). MS = major seismic event, Unc = major unconformity.

The stratigraphic representation of the Pliocene-Quaternary is further discussed in the following section.

3.1.3. Pliocene-Quaternary stratigraphic evolution

The overall depositional environment of the clastic succession between the Tertiary and the Quaternary displays an overall regressive evolution from the Pliocene open-marine to Quaternary shallow-marine and alluvial deposits. The sedimentary fill of the Pliocene-Quaternary in the Southern Alps have thicknesses ranging between 2-6 km (Doglioni, 1993; Burrato et al., 2003) whereas it may exceed 7 km of thickness in the deepest depocenters of the Northern Apennines (Pieri and Groppi, 1981). At the top of the buried anticlines, 100 m of thicknesses are recorded (Amadori et al., 2019).

According to Regione Emilia-Romagna and Eni-AGIP (1998), six depositional sequences compose the Plio-Quaternary basin fill (Figure 3.3). In the sense of Mitchum et al (1977), these sequences correspond to third-order depositional sequences. They are represented as unconformity-bounded stratigraphic units (UBSU) and account for phases of significant basin re-organization and evolution. Mutti et al. (1994) interpret these units as allogroups. Corresponding seismic profiles and stratigraphic sections show progressive decrease in the tectonic deformation from bottom to top (Figure 3.3).

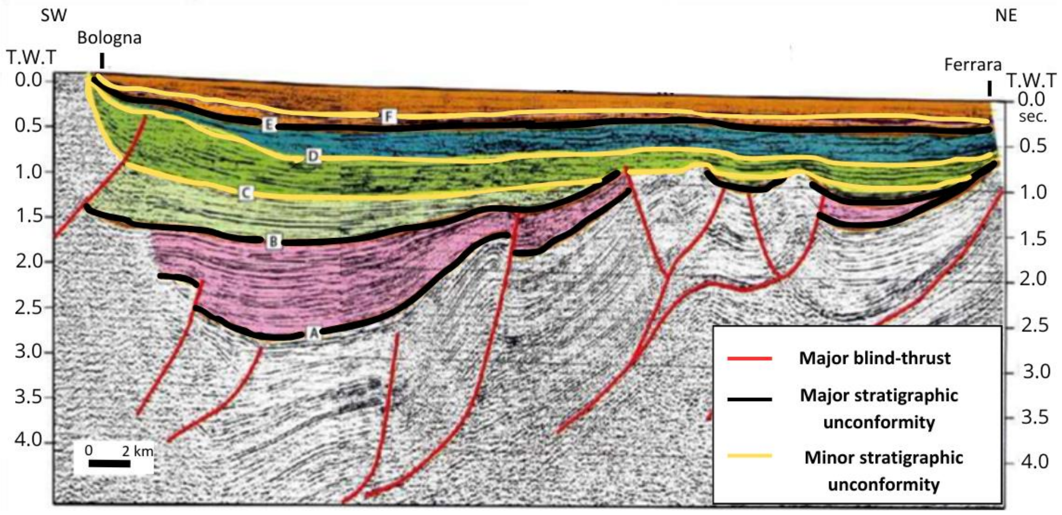

Figure 3.3: Interpreted seismic profile showing the Plio-Quaternary basin fill composed of six depositional sequences (modified from RER and ENI-AGIP, 1998).

Four main Quaternary unconformities were identified in order to subdivide the stratigraphic succession of the Po Plain basin, aging: 1.6 Ma, 1.24 Ma, 0.87 Ma and 0.45 Ma, each represented by C, D, E and F lines in Figure 3.3 respectively. The Po Supersynthem of Amorosi et al. (2008a) makes up the uppermost UBSU and is estimated post-0.87 Ma by Muttoni et al. (2003) whose unconformity is linked to the first Pleistocene alpine glaciation. Its maximum thickness is 800 m beneath the coastal plain; however, it thins towards the Alps and Apennines basin margins. The Po Supersynthem is subdivided into two lower-rank units separated by the 0.45 Ma unconformity: Upper and Lower Po Synthems (Figure 3.4). In turn, each synthem is further split into four subsynthems, making up eight lower-rank (fourth-order) or transgressive-regressive (T-R) cycles.

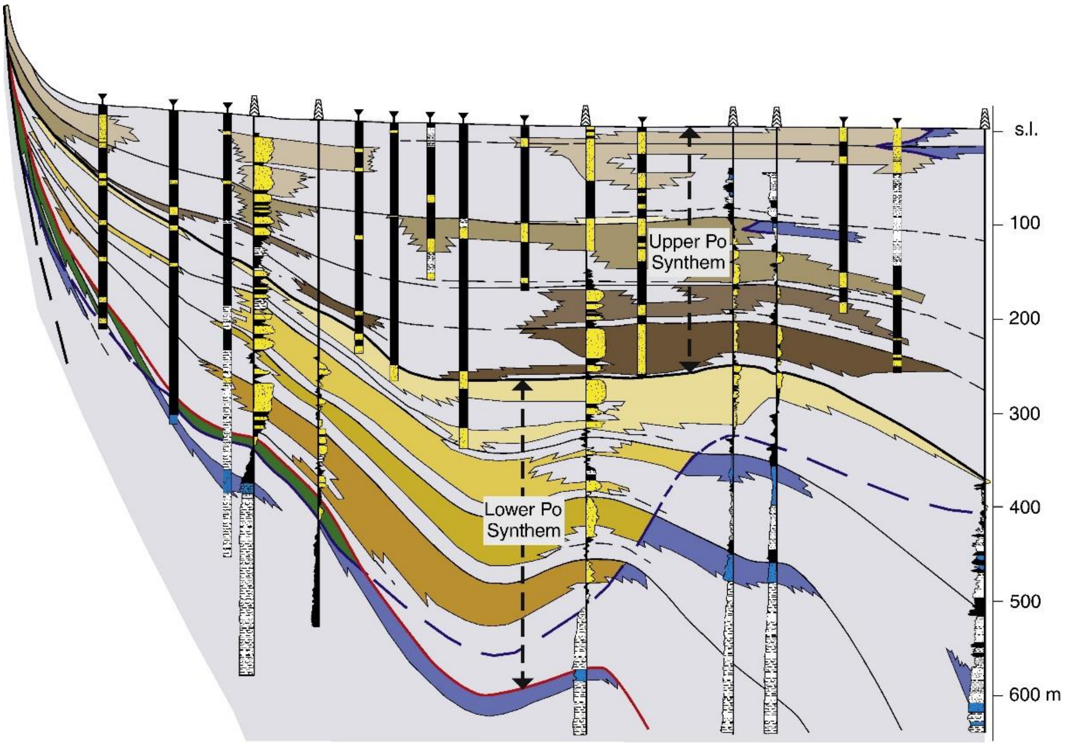

Figure 3.4: Po Supersynthem subdivision into Lower and Upper Po Synthems and their subsequent internal subdivision (from Amorosi et al., 2008a). Red line marks the lower boundary of Po Supersynthem.

Extensive literature recognize the Milankovitch-scale (100 ky) orbital forcing as the major influencing factor for the depositional architecture of the Upper Po Synthem by high-resolution stratigraphic interpretation and pollen analyses (e.g. Amorosi et al. 2001, 2004, 2008a, 2008b). Each depositional cycle is characterized by a repeating alternation of coastal and alluvial deposits in T-R sequences in areas beneath the modern coastal plain, or a dominant stratigraphy of laterally-amalgamated fluvial bodies.

Each T-R cycle represents a single 4th order sea-level fluctuation related to the Milankovitch cyclicity allowing for a classic subdivision in system tracts. The lower unit is characterized by a dominant alluvial succession during an elongated phase of sea-level drop, referred to as: falling-stage systems tract (FST) and lowstand systems tract (LST). It is made up of channel incision and soil development in the interfluves (Figure 3.5). The next unit represents the lower transgressive portion of the T-R sequence and records a rising sea-level phase as transgressive systems tract (TST). It shows a landward shift in facies. The subsequent lowering of the sea-level rise characterizes the upper unit with the increase of fluvial processes as highstand systems tract (HST).

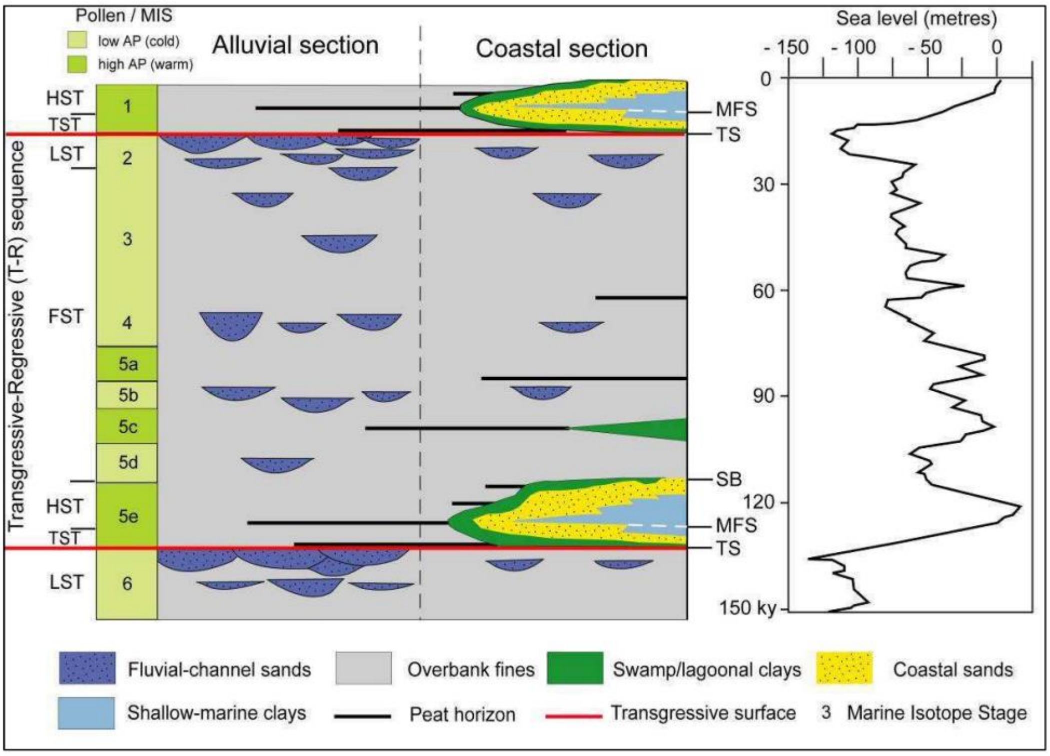

Figure 3.5: Schematic stratigraphic architecture of the post 125 kyrs BP of the Po Basin (from Amorosi and Colalongo, 2005).

T-R cycles are laterally alternated and are bound by transgressive surfaces (TS) that characterize facies alterations and transition from glacial to interglacial periods (Figure 3.6). They are accounted for at basin scale and are easily recognized in the coastal plain whereas at the basin margins, they are dominated by non-marine deposits.

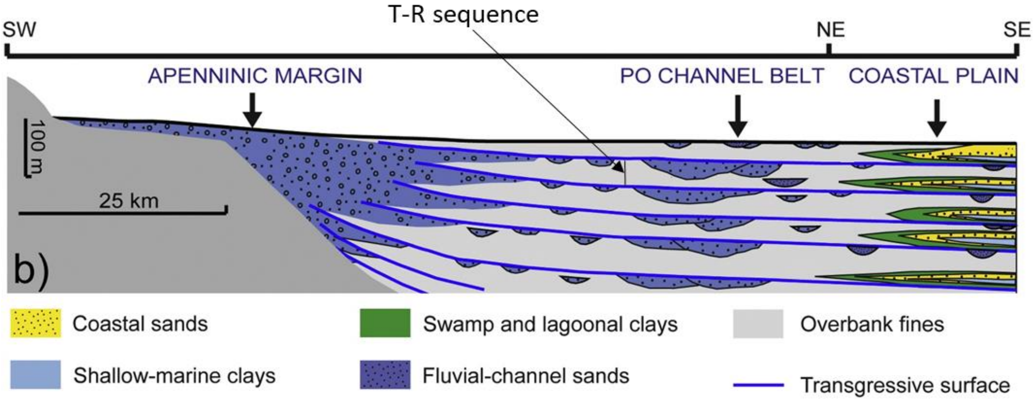

Figure 3.6: Linkage between alluvial and coastal depositional systems of the Po Plain with corresponding T-R cycles and their sequence-stratigraphic subdivision (from Campo et al., 2020).

Depositional systems at a millennial (sub-Milankovitch) scale have been studied and identified by many authors (e.g. Amorosi et al., 2005; Stefani and Vincenzi, 2005). These sub-cycles are bounded by flooding surfaces and display a shallowing-upward trend that suggest a sea-level rise with irregular phases of landward shift in facies followed by a generalized spreading. Figure 3.7 displays a similar parasequence architecture.

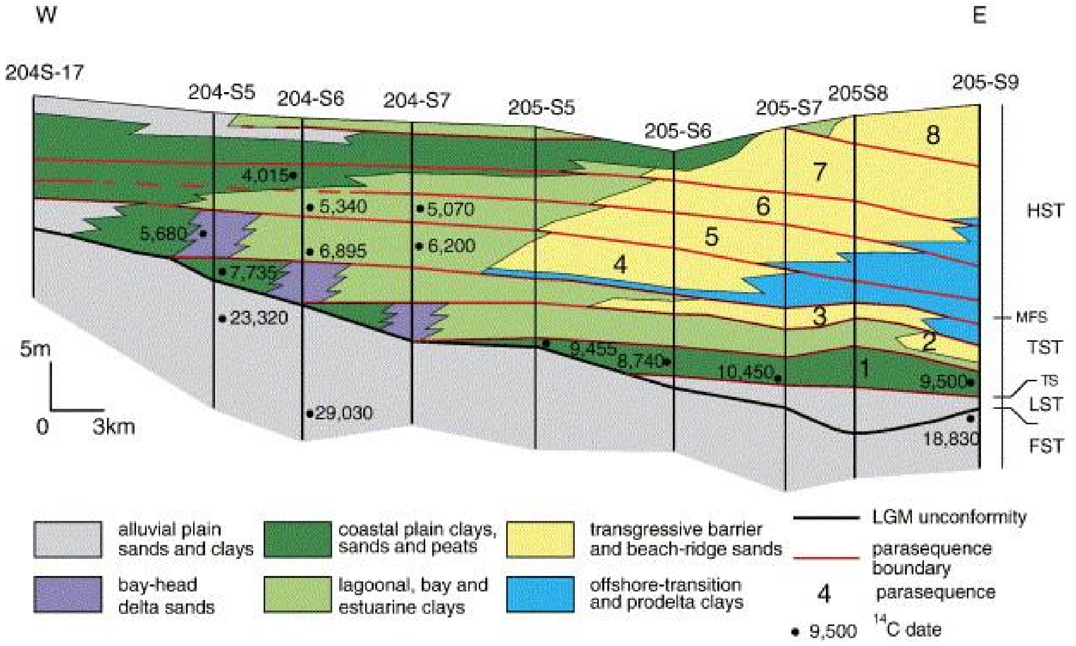

Figure 3.7: Stratigraphic section showing parasequence architecture of the Holocene succession beneath the Emilia-Romagna coastal plain (from Amorosi et al., 2005).

3.2. Superficial aquifers of the Po Plain

An accurate description and understanding of the Quaternary stratigraphic architecture of the Po Plain is essential for the hydrostratigraphic characterization of its aquifers. It is important to note that the representation of the stratigraphic evolution of the Plio-Quaternary of the Po Plain discussed in section 3.1.3 follows the classification adopted by the work of Amorosi et al. (2005; 2008); however, the foundations of the research work done to continuously update the understanding of this stratigraphic architecture and, thus, aquifer distribution differ from one work to another. This is due to the utilization of different types of stratigraphic units (e.g. the use of alloformations versus UBSU) as well as the perpetual changing of the ages of bounding unconformities. Figure 3.8 summarizes and compares the different works with their corresponding classifications of a generalized stratigraphic framework of the Quaternary Po Plain.

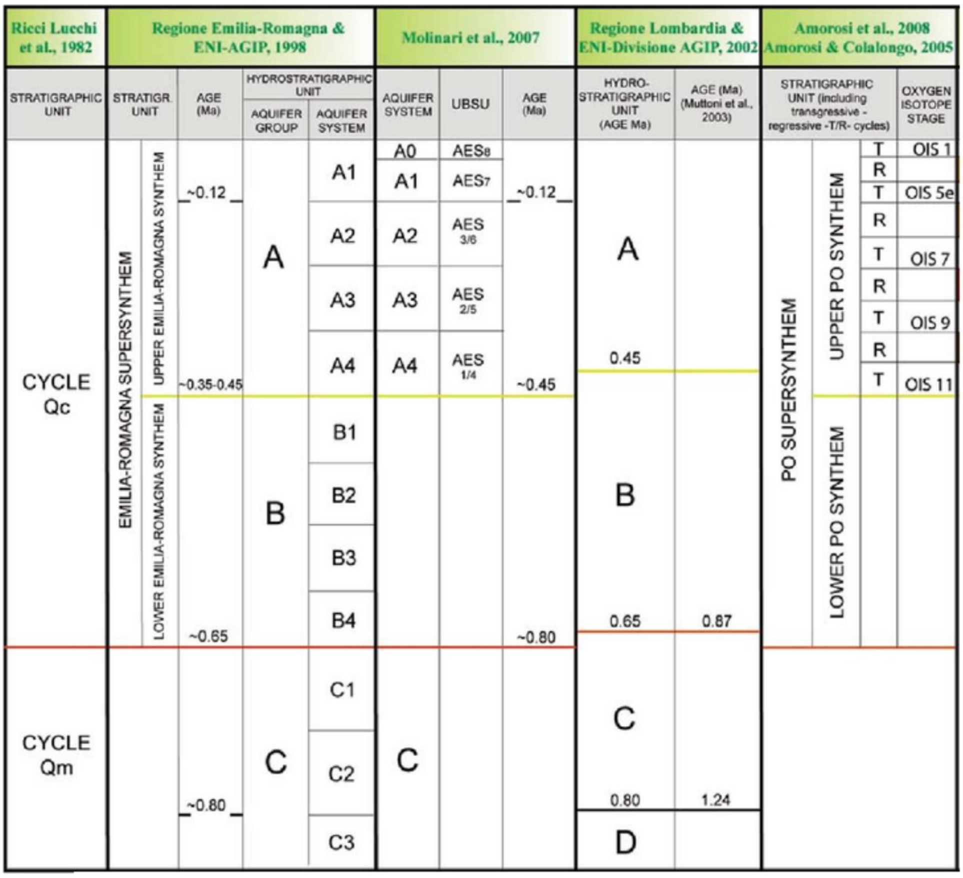

Figure 3.8: Different classifications of the generalized stratigraphic framework of the Quaternary Po Plain (from Amorosi and Pavesi, 2010).

From the Apenninic margin to the coastal plain of the entire Po Plain basin, the major aquifers consist of amalgamated alluvial fans, vertically arranged Po channel belts and nearshore sands, as depicted in Figure 3.7 (Amorosi et al., 2008).

3.2.1. Emilia-Romagna aquifers

Regione Emilia-Romagna and ENI-AGIP (1998) refer to the Lower Emilia-Romagna Synthem as AEI and the Upper Emila-Romagna Synthem as AES (Figure 3.9). Three main depositional sequences are highlighted, each corresponding to respective T-R cycles. The sedimentary infill of the Upper Synthem comprises the seat of the aquifers of the Emilia-Romagna plain and locally exceed 500 m of thickness. In fact, in Figure 3.9, the laterally-extensive bodies represent the three basic aquifer groups nominated A, B and C whereas the muddy deposits from the riverbanks represent the aquitards.

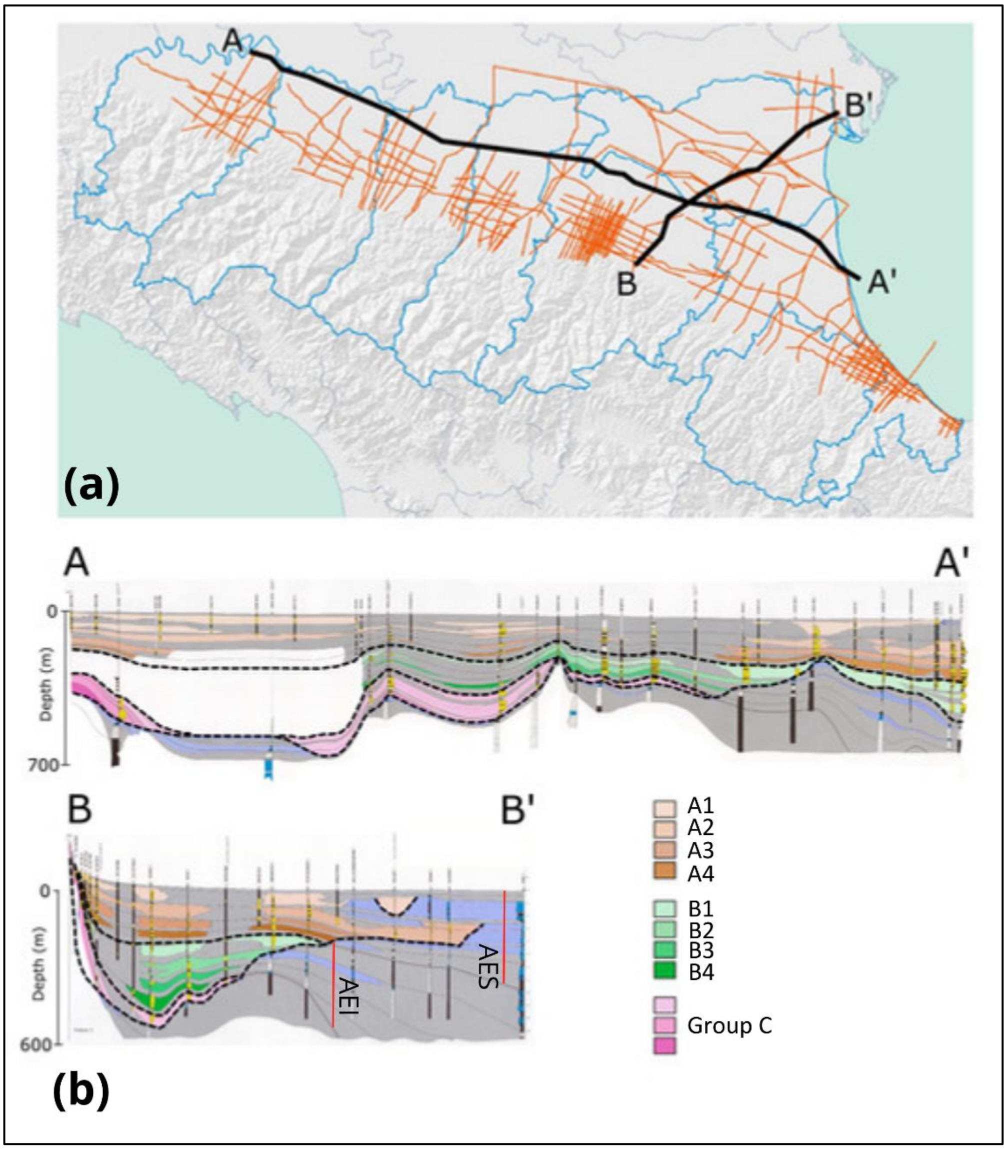

Figure 3.9: (a) Emilia-Romagna map with location of cross-sections AA' and BB'; (b) Cross-sections showing the main aquifer groups and indicating the Upper (AES) and Lower (AEI) Emilia-Romagna Synthems (modified from Eid et al., 2022).

Aquifer group A represents the most recent (Middle Pleistocene-Holocene) hydrostratigraphic unit and extends to the first 150-200 m from ground level. Beneath it, aquifer groups B and C are older (Upper Pliocene-Middle Pleistocene) and reach depths of 300-350 m and deeper, respectively. The first two aquifer groups (A and B) mainly consist of alluvial deposits, including gravels of alluvial conoid origin, fine material of alluvial plain origin and sand deposits of meandric origin (Eid et al., 2022). Aquifer C consists of alternations of sand and finer sediments of coastal and marine-marginal origins.

Aquifer groups A and B are subdivided into minor hydrostratigraphic structures called aquifer complexes, respectively named A1-A4 and B1-B4 from shallow to deep (Figure 3.9). The subdivision is based on the overall volume of aquifers in each unit as well as the areal continuity and thickness of the corresponding aquitards. These aquitards are in turn, referred to as Basal Aquitards and are not related to any depositional sequences or hydrostratigraphic units (RER and ENI-AGIP, 1998).

The location within the plain and the depositional environment of each aquifer group also affect the continuity of sedimentation and, consequently, the hydraulic connection amongst the aquifer groups. The geometry of the deposition and the temporal gap in sedimentation may result in discontinuity surfaces. Sedimentation is more continuous farther away from these active structures, but significant discontinuities are typically seen near faults (Farina et al., 2014). The region's northeast and north also have notable thicknesses, although the thickest portion of the aquifer group corresponds to the river conoids of the Emilia-Romagna region to the south.

3.2.2. Definition of Emilia-Romagna groundwater bodies

The regional aquifers of the Emilia-Romagna plain are vertically subdivided into two groundwater bodies (Regione Emilia-Romagna, 2010a), from top to bottom:

1. Upper groundwater bodies: consist of the confined portions of the more superficial aquifer complexes A1 and A2 and form the upper confined groundwater bodies
2. Lower groundwater bodies: consist of the remaining confined portions of aquifer complexes A3 and A4 and aquifers B and C, forming the lower confined groundwater bodies

Above these two groundwater bodies, a single water body is defined for the entire system that corresponds to the free, unconfined aquifer of the Apennine alluvial fans. The cartographic overlay of these groundwater bodies is shown in Figure 3.10 below.

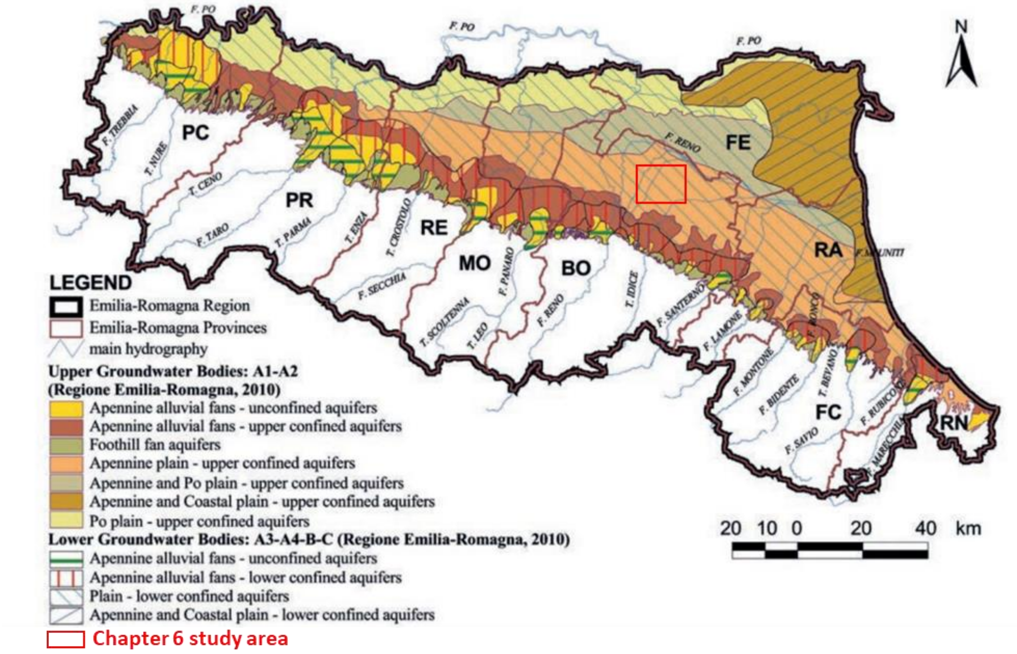

Figure 3.10: Underground water bodies of Emilia-Romagna (from Regione Emilia-Romagna, 2010a). The red boundary refers to the area of the case study in Chapter 7.

The most superficial unconfined aquifer is recharged directly from meteoric infiltration whereas the other confined aquifers (A1 to C) are laterally recharged by meteoric waters of Apennine and Alpine origin (Martinelli et al., 1998). However, confined aquifers in the central part of the Po Plain display low hydraulic gradients and circulation velocities, indicating the absence of significant current recharge processes (Martinelli et al., 2017).

Under the “Water Protection Plan of the Emilia-Romagna Region” by the Agenzia Prevenzione Ambiente Energia Emilia-Romagna ARPAE (2003), the hydrogeological complexes making up aquifer group A were further studied. These complexes are where the concentrations of water withdrawals in the Emilia-Romagna plain come from. They consist of: Apennine alluvial fans and Apennine and Po alluvial plains (see Figure 3.10). These complexes won’t be delineated in this chapter but will be referred to later in the case study.

3.2.3. Petrophysical parameters of Emilia-Romagna aquifers

The petrophysical and hydraulic parametrization of the Emilia-Romagna aquifers was represented by RER and ENI-AGIP (1998) using different methods and techniques: pumping tests, electric logs and optical studies of thin sections. A total of 75 wells were used and parameters studied include porosity (total and effective), hydraulic conductivity, transmissivity and storage coefficient. The characterization of these parameters show a certain regional uniformity and are expressed, in orders of magnitude, in Table 3.1, Table 3.2, Table 3.3 for the three respective aquifer Groups A, B and C.

Table 3.1: Hydrofacies characterization of aquifer group A.

	Aquifer Group A		
	Porosity	**Hydraulic conductivity (m/s)**	**Storage coefficient (m^{-1})**
Alluvial fan and Apennine-fed alluvial plain	15-25%	10^{-3}-10^{-5}	10^{-4}-10^{-6}
Alluvial plain channel-filling axially	--	10^{-3}	10^{-5}
Channel fillings of the paleoPo delta	--	10^{-4}	10^{-5}
PaleoPo deltaic lobes	33-46%	10^{-4}-10^{-5}	10^{-5}

Table 3.2: Hydrofacies characterization of aquifer group B.

	Aquifer Group B		
	Porosity	**Hydraulic conductivity (m/s)**	**Storage coefficient (m^{-1})**
Alluvial fan and Apennine-fed alluvial plain	15-25%	10^{-4}-10^{-5}	10^{-5}
Alluvial plain channel-filling axially	--	10^{-3}	10^{-5}
Channel fillings of the paleoPo delta	--	10^{-4}	10^{-4}-10^{-5}
PaleoPo deltaic lobes	33-42%	10^{-4}-10^{-5}	10^{-5}-10^{-6}

Table 3.3: Hydrofacies characterization of aquifer group C.

	Aquifer Group C		
	Porosity	**Hydraulic conductivity (m/s)**	**Storage coefficient (m^{-1})**
Apennine-fed fan delta	37-39%	10^{-4}-10^{-5}	10^{-5}-10^{-6}
PaleoPo deltaic lobes	34%	10^{-4}-10^{-5}	10^{-6}

Chapter 4

Land movements in the Po Plain

The Po Plain is a rapidly subsiding sedimentary basin that has been the focus of numerous studies since the mid 20th century. Although natural subsidence was already existent in the Po Plain before the 1950s along with some man-induced activities (e.g. extraction of methane-bearing water), it was not until after World War II when the abrupt increase in natural resources exploitation such as groundwater became dominant that the Po Plain started recording its highest rates of subsidence. Despite the subsiding nature of the basin, positive vertical ground movements (i.e. uplifts) of natural and anthropogenic origin have been detected and reported. Understanding the complex interactions between the different components of subsidence in the Po Plain as well as uplift is crucial for managing and mitigating the phenomena on a local scale and for providing insights into the broader challenges associated with land use, water management and environmental sustainability. The main purpose of this chapter is to critically compare the most important datasets on subsidence and uplift in the Po Plain, specifically in the Emilia-Romagna region, that have been collected throughout the years, highlighting present-day vertical velocities and subsidence maps. The chapter is subdivided into sections discussing the latter separately.

4.1. Natural subsidence in the Po Plain

The components of natural subsidence in the Po Plain include tectonic and sedimentological processes, geodynamics and climatic changes (refer to section 2.1). Tectonics and geodynamics make up the long-term component acting on time scales of about 10^6 years whereas glacial cycles control the short-term component on time scales of 10^3-10^4 years.

4.1.1. Long-term natural subsidence

Carminati and Di Donato (1999) resolved the long-term velocity components averaged over the last 1.43Myrs using a backstripping procedure (Sclater and Christie, 1980) on borehole stratigraphic data of 200 onshore and offshore wells. The resulting subsidence rates (Figure 4.1) show a regional pattern of velocity: an increase from the northern border along the Alps with values less than 1 mm/yr to about 2.5 mm/yr eastward in the Po Delta followed by decreasing rates towards the Apennines front and the southern border of the Po Plain.

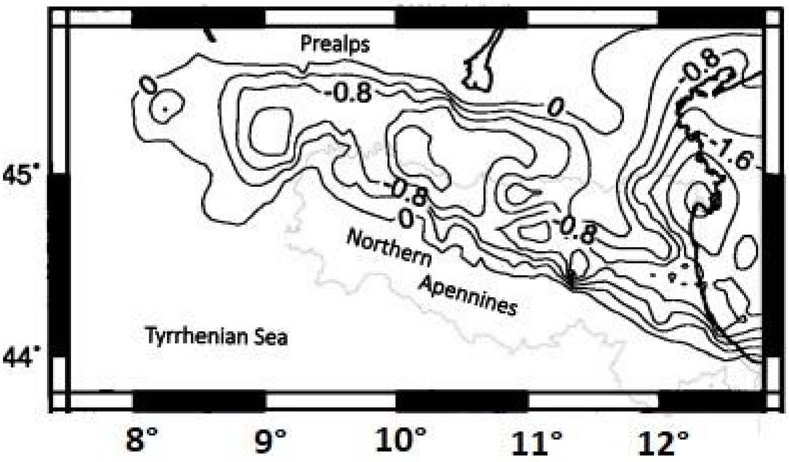

Figure 4.1: Long-term natural subsidence (in mm/yr) in the Po Plain. Emilia-Romagna boundary is shown in light grey (modified from Carminati and Di Donato, 1999).

Carminati and Martinelli (2002) modify and display those rates on a smaller scale (Figure 4.2). Maximum values are recorded in areas with high thickness of Plio-Quaternary sediments.

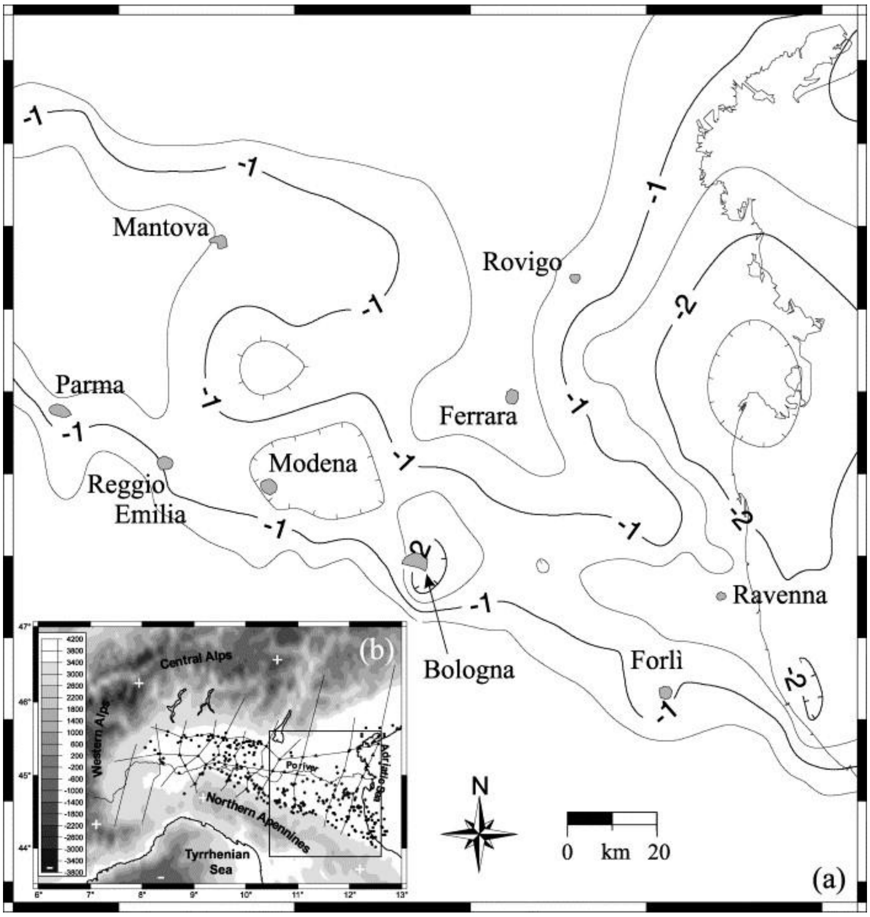

Figure 4.2: Long-term natural subsidence rates (in mm/yr) displayed on a smaller scale (from Carminati and Martinelli, 2002).

Figure 4.3 decomposes the long-term vertical velocities (shown in Figure 4.1) into their corresponding components: sediment compaction, sediment load and tectonic load. Tectonic load is the primary component, accounting for about 50% of the total vertical velocity.

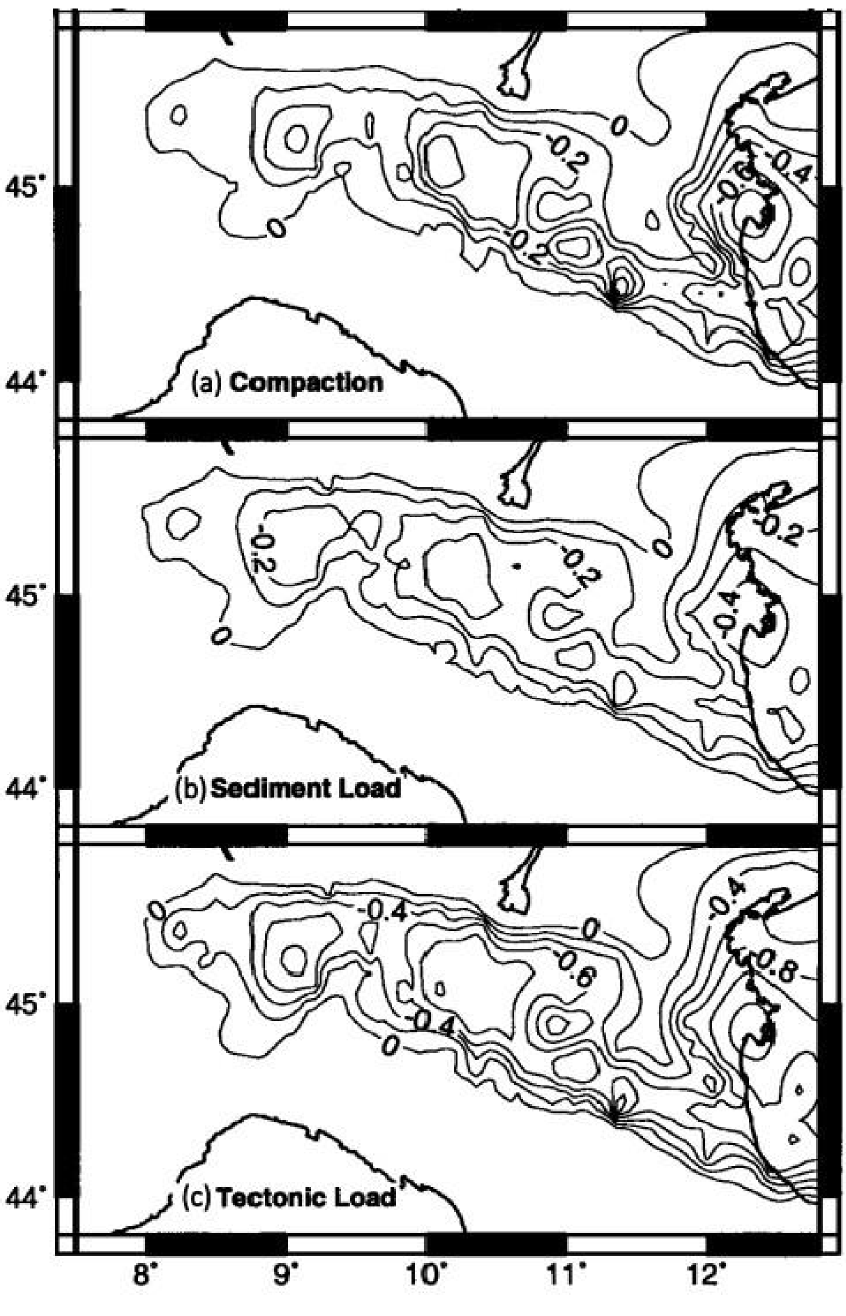

Figure 4.3: Components of long-term subsidence (in mm/yr), due to (a) sediment compaction, (b) sediment loading and (c) tectonic loading (from Carminati and Di Donato, 1999).

Gambolati and Teatini (1998) produced an average natural subsidence map (Figure 4.4) in the coastal areas of the Upper Adriatic Sea by taking into account previous studies (e.g. Groppi and Veggiani, 1984; Bortolami et al., 1984; Carbognin et al., 1981) that use the chronostratigraphic reconstruction to measure the compacted thickness of formations in different geological periods as well as the interpretation of historical remains.

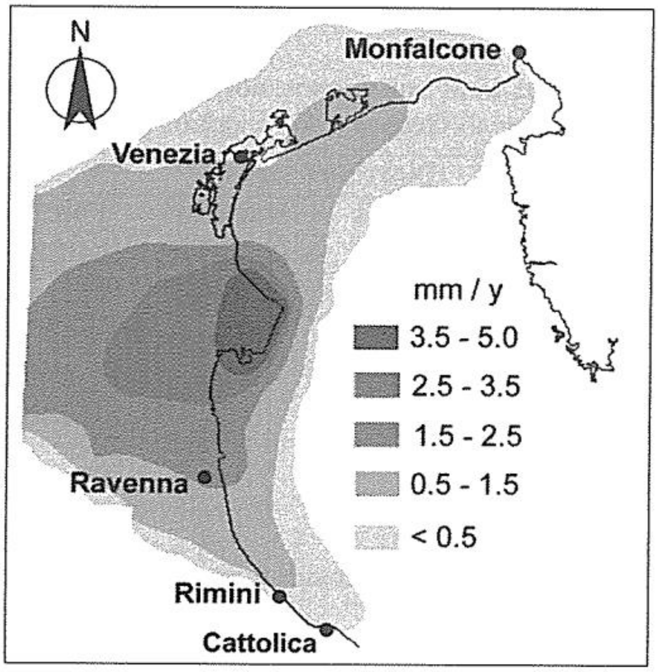

Figure 4.4: Average natural subsidence (in mm/yr) in coastal area of the Po Plain (from Gambolati and Teatini, 1998).

Elmi et al. (2003) reconstructed the mean subsidence map of the Po Plain for the whole Quaternary (Figure 4.5) according to the following formula:

$$V = (S_{tot} - \Delta z)/T \neq 0$$

where V is the velocity, S_{tot} is the total sediment thickness that includes tectonic sinking, sediment compaction and isostatic response, Δz is the algebraic sum of the change in depths due to the filling of the basin or eustatic oscillations and T is the age of the oldest sediments (=1.7My in this case).

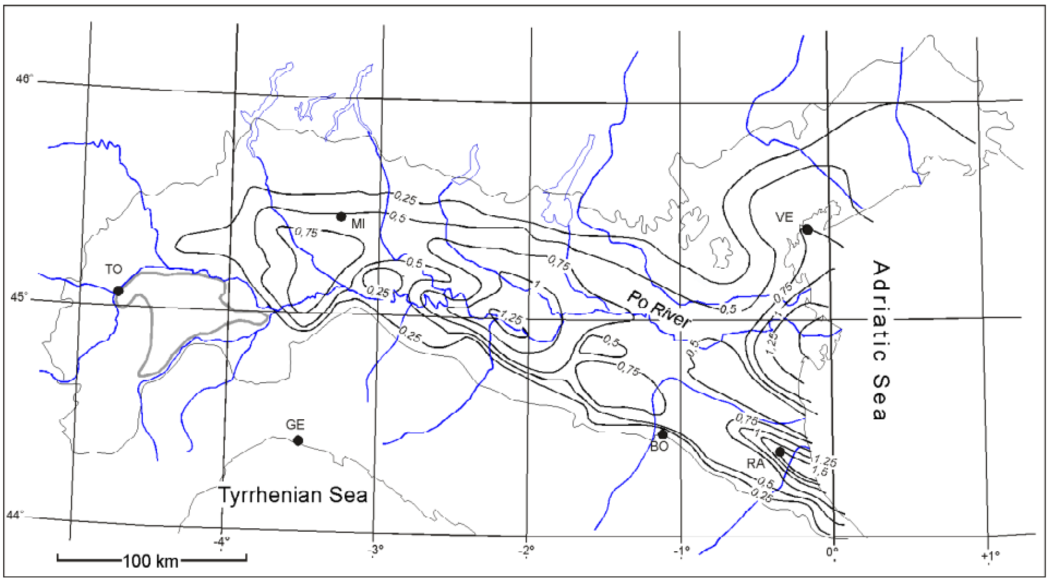

Figure 4.5: Mean subsidence map (in mm/yr) of the Po Plain for the Quaternary, 1.7My (from Elmi et al., 2003).

The long-term natural subsidence maps presented in this section are all in general agreement, such that the maximum subsidence values are recorded in areas with maximum Pleistocene sediment thickness; the Po Delta and the Romagna plain (Ravenna).

4.1.1.1. Long-term subsidence: comparison of different sources and causes

Long-term natural subsidence is due to the downward flexure of the Adriatic plate under the Apennines and active compressional tectonics related to the Apennines (e.g. Carminati et al., 2003b; Carminati et al., 2005; Picotti and Pazzaglia, 2008). Carminati et al. (2003) show that subsidence related to the Apennines subduction decreases from south to north, with it being the sole tectonic component in areas where thrust tectonics from the Alps and the Apennines are absent (e.g. Venice). However, in areas where the Apenninic thrusts are active, subsidence related to the subduction decreases because of the contrasting effect of the overlying formation affected by the compressional tectonics of the anticlines of the Apennines thrusts and folds. Other studies (Mantovani et al., 2009a,b) hypothesize that the evolution of the Apennine belt and Po Plain is driven by the northward movement of the Adriatic plate. Also, the component of sediment loading and compaction contribute to about 1 mm/yr of the total natural subsidence (Giambastiani et al., 2007).

4.1.2. Short-term natural subsidence

Carminati et al. (2003b) evaluated the short-term effects of the last deglaciation (Di Donato et al., 1999) on subsidence using ^{14}C data. Only ^{14}C ages of 13,000 yr and younger were taken into account, considering these years as the slower stages following the sea-level rise due to deglaciation. The anthropogenic effects are filtered out because they take place over much a smaller and recent time span (100 yr) than the studied data. Figure 4.6 shows the subsidence rates obtained using the ^{14}C data in the study and those already available in literature (Fontes and Bortolami, 1973; Bortolami et al., 1977; Brunetti et al., 1998). Subsidence rates range between 0 and 5 mm/yr and maximum rates are observed in the south-east of the Po Plain. Those rates were compared with burial rates of Roman artifacts for validation. This is justified by the fact that the age of the artifacts is about 2000 years, referring to the deglaciation period. The results are validated by coinciding maximum values of burial rates with subsidence rates.

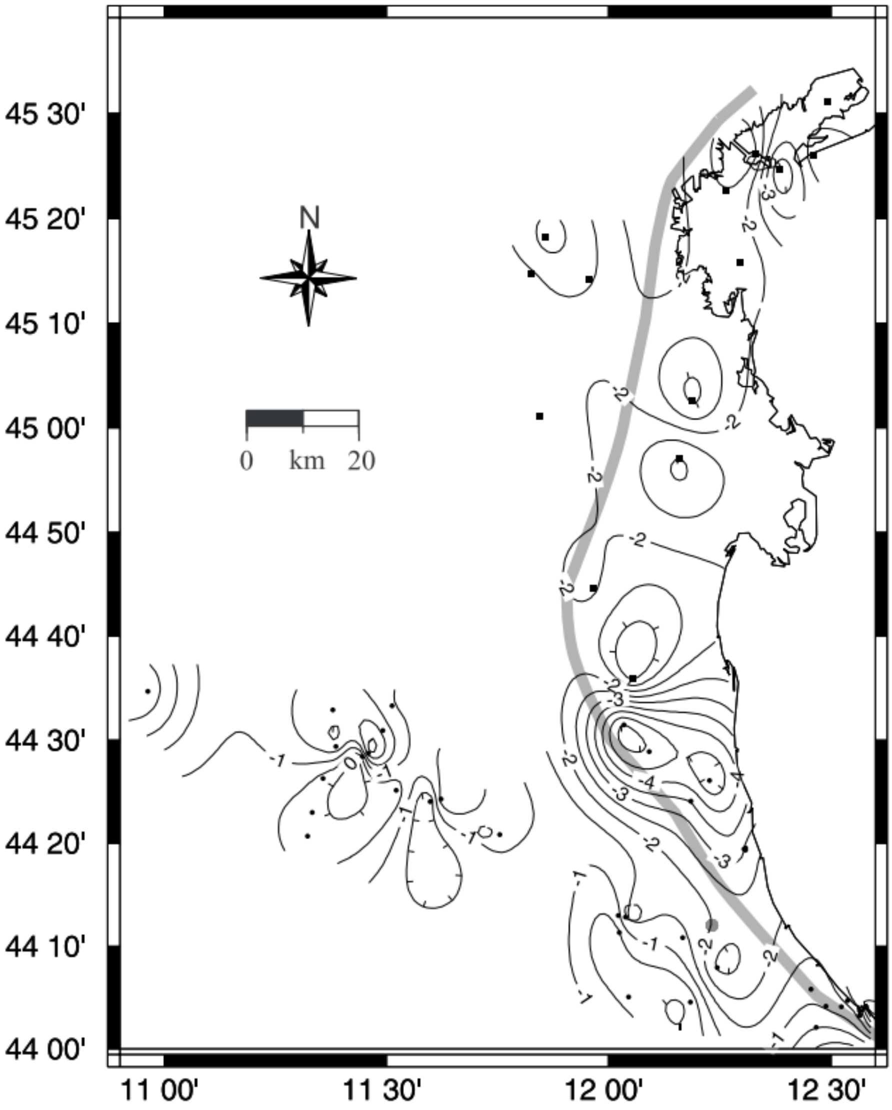

Figure 4.6: Short-term subsidence rates (in mm/yr) related to the last deglaciation (from Carminati et al., 2003b).

The comparison between Figure 4.6 and Figure 4.1 showing the long-term component (Carminati and Di Donati, 1999) highlights that the natural subsidence is divided in half between the long-term and short-term processes such that both components show their maximum effects in the eastern Po Delta.

Bruno et al. (2020) measured subsidence rates in the Po coastal plain for the last 5.6 and 120kyr by using two lagoon horizons as reference marker beds. Subsidence rates range between 0.4-0.8 mm/yr in the last 120 kyr and double to 0.8-2 mm/yr in the last 5.6 kyr. They predicted that the last 5.6 kyr are influenced by the compaction of the Late Pleistocene and Holocene sediments (due to soft peaty clays) whereas throughout the last 120 kyr subsidence was controlled by the location of the Apennines buried thrust-folds.

4.2. Natural uplift in the Po Plain

Severi (2021) analyzed different areas in the Emilia-Romagna plain experiencing uplift over the time period 1992-2016 and attributed the phenomenon to the activity of buried tectonic structures: the Emilia folds, the Pede-Apennine thrust front at Reggio Emilia, Modena and Bologna plain, and in some sectors of the Ferrara folds (Figure 4.7). No uplifts were recorded above tectonic structures in the Romagna sector (Ravenna, Forlì and Rimini plain).

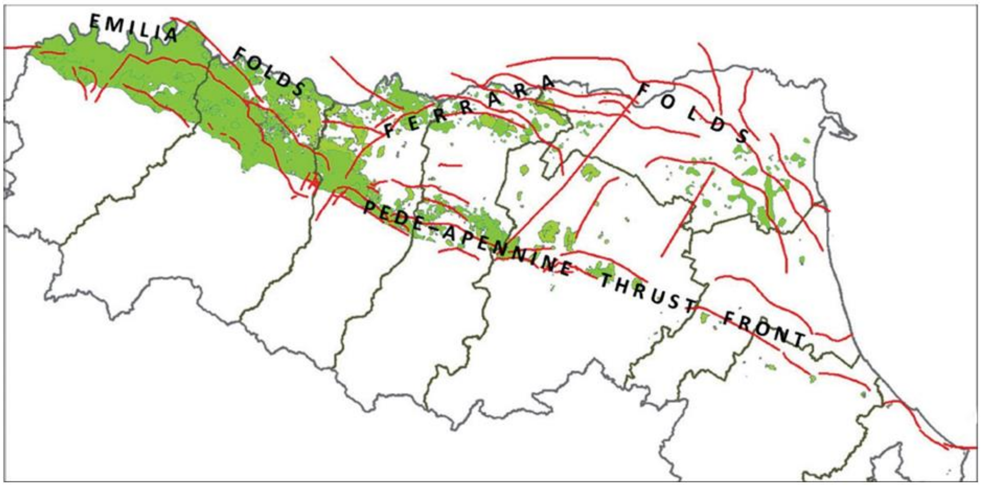

Figure 4.7: Uplifting areas during 1992-2016 in green with the buried tectonic structures (active or potentially active) in the Emilia-Romagna plain (from Severi, 2021).

The two strong earthquakes that occurred in May 2012 (20th and 29th) in Modena caused an uplift of 10-15 cm in areas around the epicenter and were associated with the Ferrara folds (Caputo et al., 2015).

Natural uplift in the Po Plain can sometimes also be due to rainfall precipitation that leads to an increase of the water table and hence, the expansion of the aquifer system leading to the uplift of the soil (Nespoli et al., 2021).

4.3. Present subsidence in the Po Plain

The present subsidence of an area is the sum of the natural and anthropogenic factors acting on that area (refer to section 2.1). It is monitored using the techniques discussed in section 2.4 Present-day vertical velocities are also referred to as modern vertical velocities.

Studies on the vertical movements in the Po Plain began in the 1950s, with the most prominent of works by Salvioni (1957) and Boaga (1957). Following studies were undertaken by several local authorities and institutions including the IGMI (Istituto Geografico Militare Italiano) and the University of Bologna. Within the latter, Caputo et al. (1970) were the first to generate a map of equal movements for the eastern Po Plain for the period 1900-1957 using high-precision leveling. The main result is the drastic movement of the Po Delta of more than 40 cm for the investigated time period with a slope towards the coastline. For the period 1951-1957, maximum rates of 25 cm/yr were recorded in the central Po Delta and 18 cm/yr for the period 1958-1962. After that, subsidence rates started decreasing to values around 3.3 and 3.75 cm/yr till 1974.

Arca and Beretta (1985), within IGMI, produced a subsidence map based on the comparison of leveling data for the years 1897 and 1957. Their results agree with the ones of the authors cited above and the produced map (Figure 4.8) is considered representative of the first half of the 20th century.

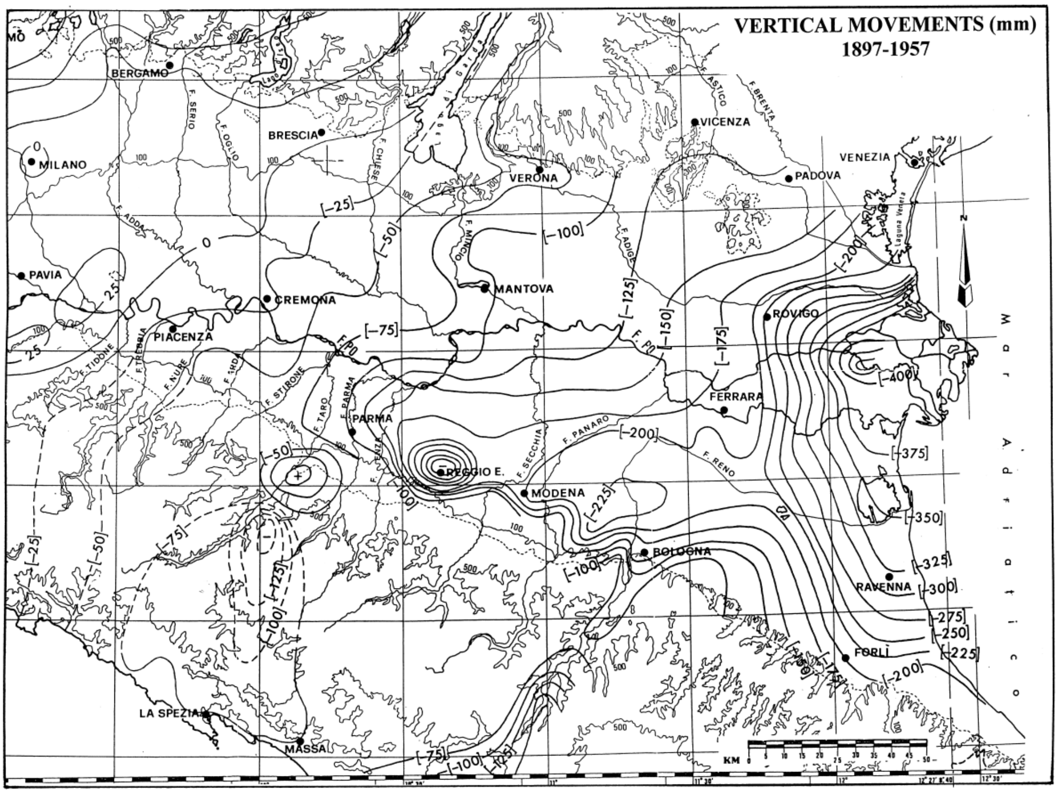

Figure 4.8: Cumulative vertical movements (in mm) for the period [1897-1957] for the northeast part of the Po Plain based on geodetic data (from Arca and Beretta, 1985).

Carminati and Martinelli (2002) measure the modern vertical velocities for the Po Plain (Figure 4.9) based on local and national government data in order to define a regional trend of subsidence for the second half of the 20th century. The data range between the years 1950-1999 and a linear behavior of subsidence is assumed because of the averaging over long periods. Local variations are reported in certain areas (e.g. Ravenna) due to the decrease in groundwater exploitation in the 1970s after a national government law was implemented following the rapid increase in the ‘50s after World War II. Maximum subsidence rates reach up to 70 mm/yr in the areas of the Po Delta and north of Bologna.

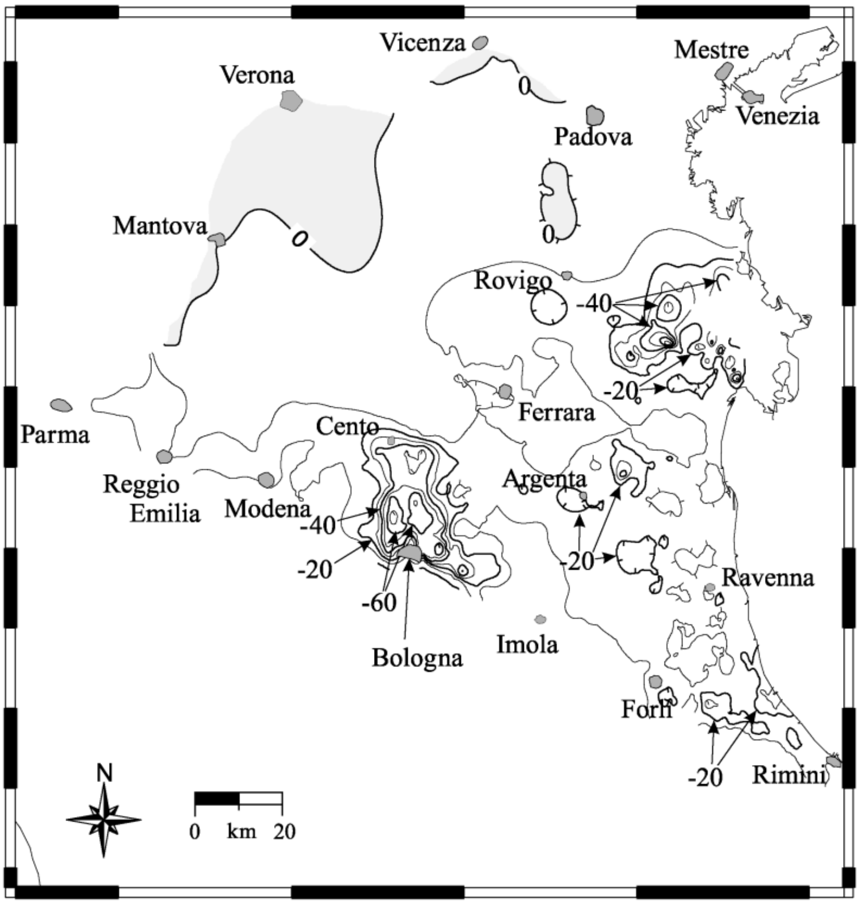

Figure 4.9: Present-day vertical velocities (in mm/yr) of the Po Plain (from Carminati and Martinelli, 2002).

The ARPAE (Agenzia Prevenzione Ambiente Energia Emilia-Romagna), in collaboration with the University of Bologna and TRE ALTAMIRA Milano, carried out four regional campaigns from 1992 till 2016 to produce four subsidence maps (Figure 4.10) of the Emilia-Romagna region using satellite interferometry (InSAR). Table 4.1 lists the techniques used in each campaign, the data sources, the data used for calibration and the number of Permanent Scatterers (PS) and Distributed Scatterers (DS) used.

Table 4.1: Data used to create the four subsidence maps of Emilia-Romagna for the years 1992-2016.

Period	Technique	Data source	Calibration method	PS/DS points

1992-2000	PSInSAR	ERS1 and ERS2 satellites	High-precision geometric leveling based on 1000 benchmarks	160,000 PS
2002-2006	PSInSAR	ENVISAT and RADARSAT-1 satellites	High-precision geometric leveling based on 1000 benchmarks	140,000 PS
2006-2011	SqueeSAR	RADARSAT-1 satellites	Measurements from 17 GNSS permanent stations	315,000 PS and DS
2011-2016	SqueeSAR	RADARSAT-1 and COSMO-SkyMed satellites	Measurements from 22 GNSS permanent stations	1,912,781 PS and DS

For the detailed explanation of the generation of the maps using the data in Table 4.1, refer to (Bitelli et al. 2000, 2014, 2015; ARPAE 2007, 2012, 2018a and references therein).

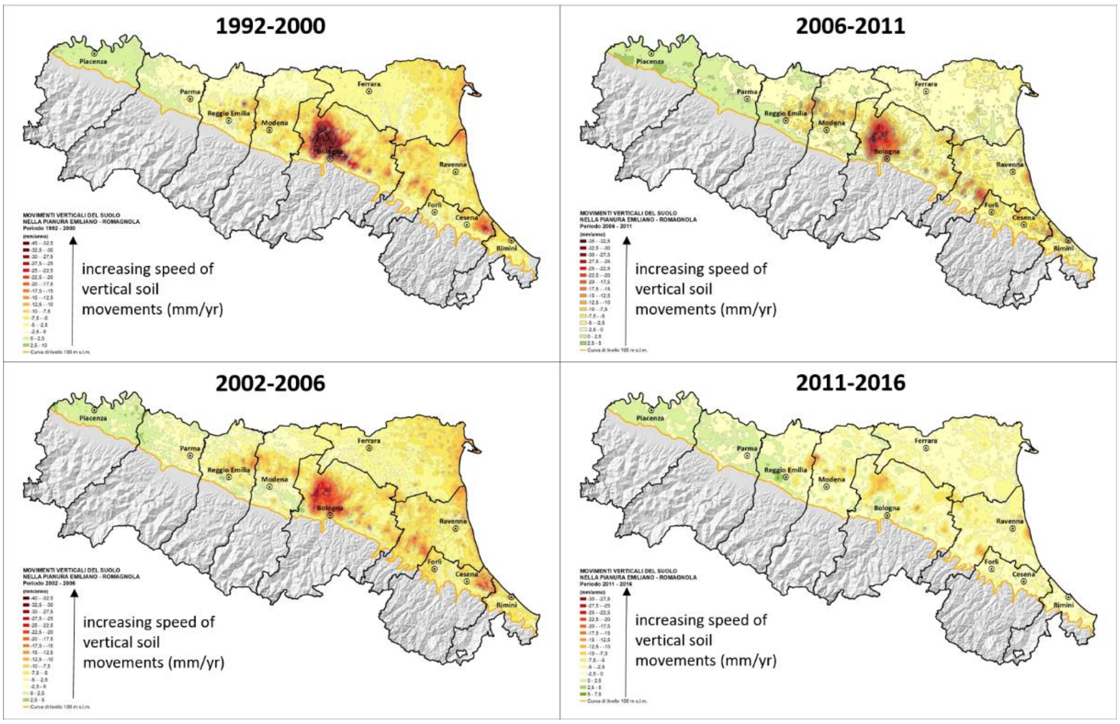

Figure 4.10: Emilia-Romagna subsidence maps for the time periods 1992-2016 (from ARPAE 2007, 2012, 2018a).

The interpretation of the maps above lead to the following conclusions:

- Maximum subsidence rates (in the area of Bologna) significantly decrease from 1999 till 2016
- The extent of the areas affected by subsidence in the first two time periods (1992-2000, 2002-2006) remain approximately the same but then significantly decrease in the following time periods (2006-2016)
- The extent of the areas affected by uplift increases from 1999 till 2016 and spreads eastward, with the maximum surfaces observed in 2006-2011. These areas are located above buried tectonic active structures (Regione Emilia-Romagna, 2017)

The most recent regional campaign for the 2016-2021 period became available on December 22, 2023 by ARPAE. The subsidence map (Figure 4.11) was produced with the following data: SqueeSAR technique, RADARSAT-1, RADARSAT-2 and COSMO-SkyMed satellites, calibration using measurements from 21 GNSS permanent stations and 704,444 PS and DS points.

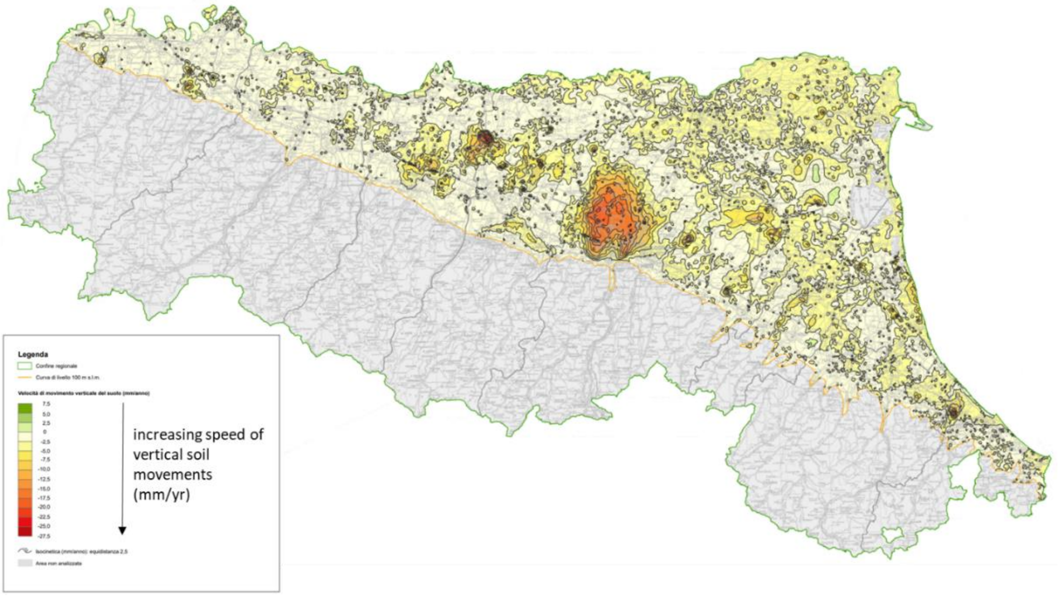

Figure 4.11: Latest Emilia-Romagna subsidence map for 2016-2021 period (from ARPAE, 2023).

The interpretation of this map resulted in the following:

- More than 80% of the areal extent of Emilia-Romagna did not undergo significant trend changes in comparison with the previous time period 2011-2016. Around 10% of the region was affected by an increase in the lowering of the ground surface and around 4% was led by a reduction in the lowering ground movements

- An increase in the subsidence rates in the area of Bologna that had been progressively decreasing up until 2016. The rates, however, are lower than those in the past

4.4. Anthropogenic subsidence in the Po Plain

Anthropogenic land subsidence can be driven by many components (discussed in section 2.1). In the Po Plain, however, the focus has been set on studying anthropogenic subsidence due to fluid extraction, either from deep onshore and offshore oil and gas reservoir formations or from shallow aquifer systems. Most subsidence in the Po Plain is of anthropogenic origin; groundwater extraction being the major controlling factor. The following subsections give an overview of the fluid production history of the Po Plain and some examples of subsidence induced by fluid production.

4.4.1. Fluid production overview

The history of exploration of hydrocarbons in the Po Valley commenced post-World War II, around the mid-1950s. A pivotal development was the discovery of natural gas in the Po Plain and in Italy through the drilling of the Caviaga-1 well in 1944, reaching a depth of 1404 meters below sea level (ssl). Advances in seismic data analyses and technologies, particularly seismic reflection methods, facilitated the exploration of deeper successions in the Po Valley, leading to the exploration of the Mesozoic carbonates (Fantoni et al., 2011). Subsequent explorations led to the identification of significant oil and gas condensate fields within these successions. Gas fields comprised shallow gas accumulations of Miocene, Pliocene, and Pleistocene origins, categorized as thermogenic and biogenic. Predominantly, hydrocarbons discovered in the Po Valley were Pliocene and Pleistocene biogenic/diagenetic gases, with reservoirs located in stratigraphic traps, thrusted anticlines, and drape structures (Eid et al., 2022).

In Italy, from the 1950s to the 1960s onward, several depleted gas reservoirs were converted into underground gas storage (UGS) systems. The Cortemaggiore Field was among the first and was established in 1964 in the Po Plain. UGS activities involve storing natural gas in subsurface geological layers, including depleted hydrocarbon reservoirs, aquifers, and salt caverns. This is achieved through seasonal and cyclical extraction and injection of gas during winter and summer, respectively. The primary motivations for natural gas storage include meeting baseload requirements, addressing peak load demands, and ensuring national strategic reserves (Verga, 2018). Baseload requirements include fulfilling long-term seasonal demand needs with a consistent and stable supply of natural gas, while peak load requirements involve the rapid short-term deliverability of natural gas when needed (Eid et al., 2022).

In the Po Plain, a significant surge in groundwater demand and production occurred in the second half of the 20th century post-World War II. This surge was a direct outcome of population growth, industrial expansion, and technological advancements in agriculture and zoology. The trend persisted until the 1970s when a national government law was enacted, leading to the stabilization of groundwater extraction to the present day. Studies focused on the Po Plain area indicate that periods marked by increased water production align with periods characterized by maximum subsidence rates (Eid et al., 2022).

4.4.2. Anthropogenic subsidence due to gas production and UGS activities

Almost all onshore activities related to gas production and gas storage in Emilia-Romagna and Lombardia are geolocalized in Figure 4.12. Emilia-Romagna currently has 27 concessions permitting the production and storage of gas after the implementation of the Italian law n. 12/2019 that suspended all exploration permits (Ministero dello Sviluppo Economico, 2020b). Table 4.2 provides information relative to the numbered gas fields and UGS systems of Figure 4.12, from their primary production time periods, cumulative gas volumes and conversion into UGS. Figure 4.13 showcases via color-coded symbols the produced cumulative gas volumes. Most of the data were collected from the National Mining Office of MISE (https://unmig.mise.gov.it/index.php/it/dati/ricerca-e-coltivazione-di-idrocarburi) and from the VIDEPI project (http://www.videpi.com/videpi/videpi.asp) promoted by the Ministry for Economic Development (DGRME), the Italian Geological Society and the Italian Petroleum and Mining Industry Association (Assomineraria). Additional data were collected from literature (e.g. Styles et al., 2014; Casero, 2004, and others).

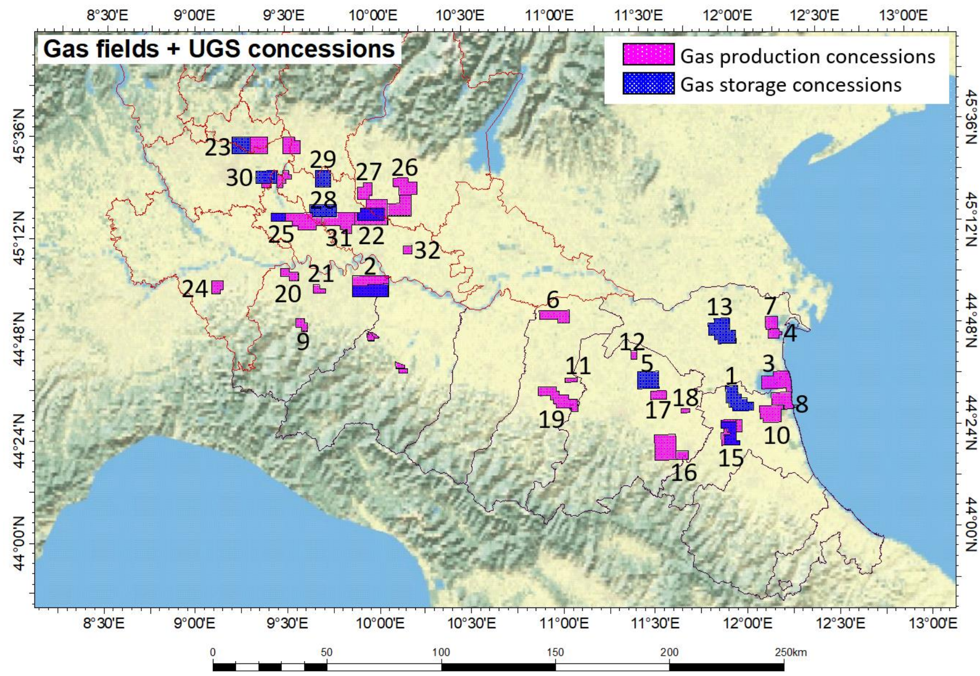

Figure 4.12: Gas production and storage activities in Emilia-Romagna and Lombardia (from Eid et al., 2022).

Table 4.2: Information relative to the numbered gas fields and the UGS systems in Figure 4.12. The (*) symbol indicates the fields converted to gas storage. Four categories

concerning the cumulative gas production are set (in 10^9 m^3_{SC}): A < 5; B: (5–10); C: (10–20); D > 20 (from Eid et al., 2022).

Field # (* indicates fields converted to gas storage)	**Field Name**	**Field Location**		**Primary Production**		**Converted to Storage**
		Region	**Province**	**Time Period**	**Cumulative Gas Production Categories**	
1 *	Alfonsine	Emilia-Romagna	Ravenna	1957–2000	B	1999 (concession
2 *	Cortemaggiore	Emilia-Romagna/Lombardia	Parma, Piacenza/Cremona	1950–1991(pool A) 1950–1964(pool C)	C	1991 1964
3	Dosso degli Angeli	Emilia-Romagna	Ferrara/Ravenna	1970–2015	D	No
4	Manara	Emilia-Romagna	Ferrara	1994–2008	A	No
5 *	Minerbio	Emilia-Romagna	Bologna	1959–1971	C	1975
6	Mirandola	Emilia-Romagna	Modena	1980–2015	A	No
7	Pomposa	Emilia-Romagna	Ferrara	1991–2006	A	No
8	Porto Corsini Terra	Emilia-Romagna	Ravenna	1969–1991	A	No
9	Quadrelli	Emilia-Romagna	Piacenza	2009–2016	A	No
10	Ravenna Terra	Emilia-Romagna	Ravenna	1953–1992	D	No
11	Recovato	Emilia-Romagna	Bologna/Modena	1998–2017	A	No
12	S.Alberto	Emilia-Romagna	Bologna	1959–1995	--	No
13 *	Sabbioncello	Emilia-Romagna	Ferrara	1961–1981	A	1985
14 *	San Pietro in Casale	Emilia-Romagna	Bologna	1960–1976	A	
15 *	San Potito e Cotingola	Emilia-Romagna	Ravenna	1988–1993	A	2009
16	Santerno	Emilia-Romagna	Bologna/Ravenna	1980–2014	A	No
17	Selva	Emilia-Romagna	Bologna	1956–1999	A	No
18	Sillaro	Emilia-Romagna	Bologna	2010-producing	A	No
19	Spilamberto	Emilia-Romagna	Bologna/Modena	1959–2015	C	No
20	Ponetidone	Emilia-Romagna/Lombardia	Piacenza/Pavia	1963–1992	A	No
21	Quarto	Emilia-Romagna	Piacenza	2004–2015	A	No
22 *	Bordolano	Lombardia	Cremona	1952–1974	A	2016
23 *	Brugherio	Lombardia	Milano	1961–1985	A	1966
24	Casteggio	Lombardia	Pavia	1980–2015	A	No
25 *	Cornegliano	Lombardia	Lodi	1952–1995	A	2017
26	Leno	Lombardia	Brescia	1962–2004	A	No
27	Ovanengo	Lombardia	Brescia	1986–2015	A	No
28 *	Ripalta	Lombardia	Cremona	1949–1967	A	1967
29 *	Sergnano	Lombardia	Cremona	1954–1965	A	1965
30 *	Settala	Lombardia	Milano	1981–1986	A	1986
31	Soresina	Lombardia	Cremona	1980–2015	A	No
32	Vescovato	Lombardia	Cremona	1997–2017	A	No

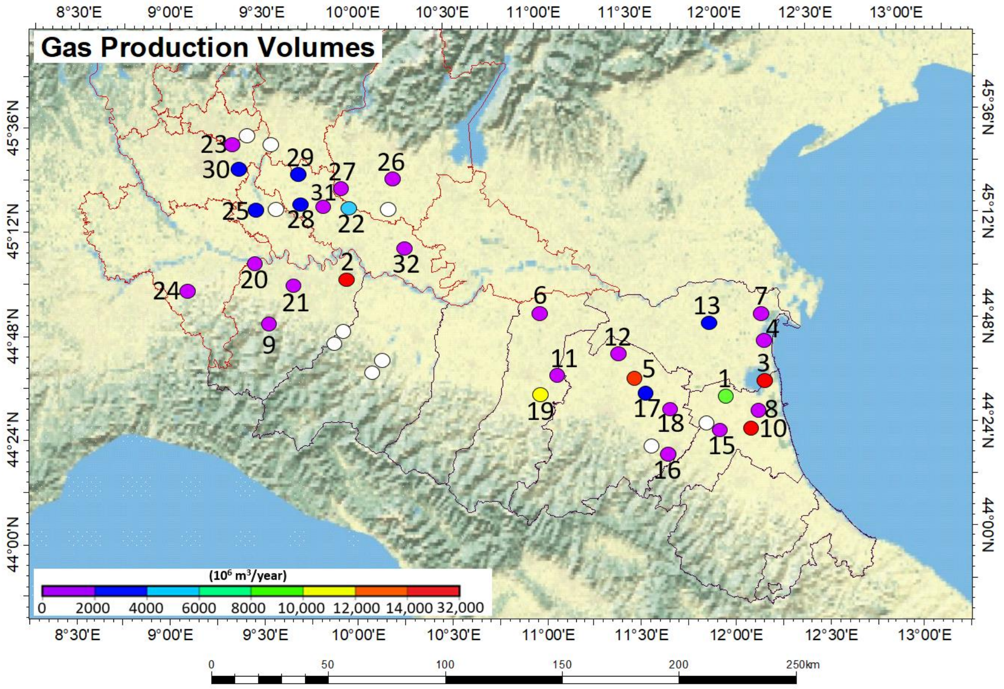

Figure 4.13: Produced cumulative gas volumes of Emilia-Romagna and Lombardia gas fields (from Eid et al., 2022). White circles represent fields with no public information.

Underground gas storage activities usually produce a sinusoidal deformation due to their seasonal/cyclical frequency (injection and withdrawal) and to the fact that the amplitude of the lowering and raising of the ground is generally the same. This type of deformation is easily identifiable in the analysis of InSAR data. An example of the following is given in Figure 4.14 (corresponding to UGS field number 5 in Figure 4.12) showing the seasonal/cyclical trend related to the UGS pore pressure variation.

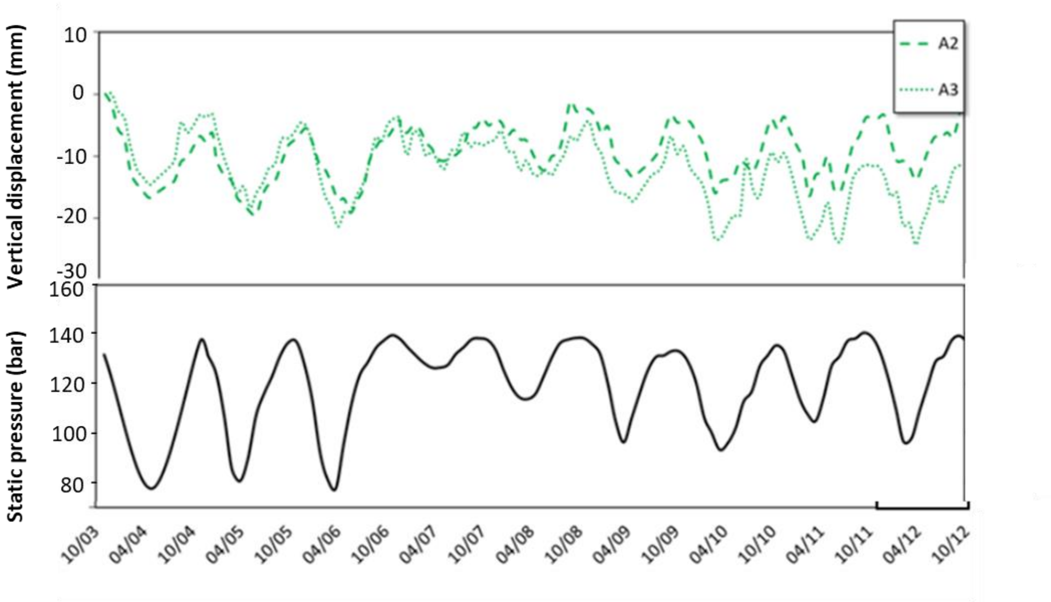

Figure 4.14: Vertical movements of control points for UGS field 5 (Figure 4.12) versus average reservoir pressure (modified from Rocca et al., 2021).

Subsequently, maps of surface vertical displacements (Figure 4.15) were produced for injection and production cycles allowing the visualization of the magnitude and areal extent of the subsidence phenomenon.

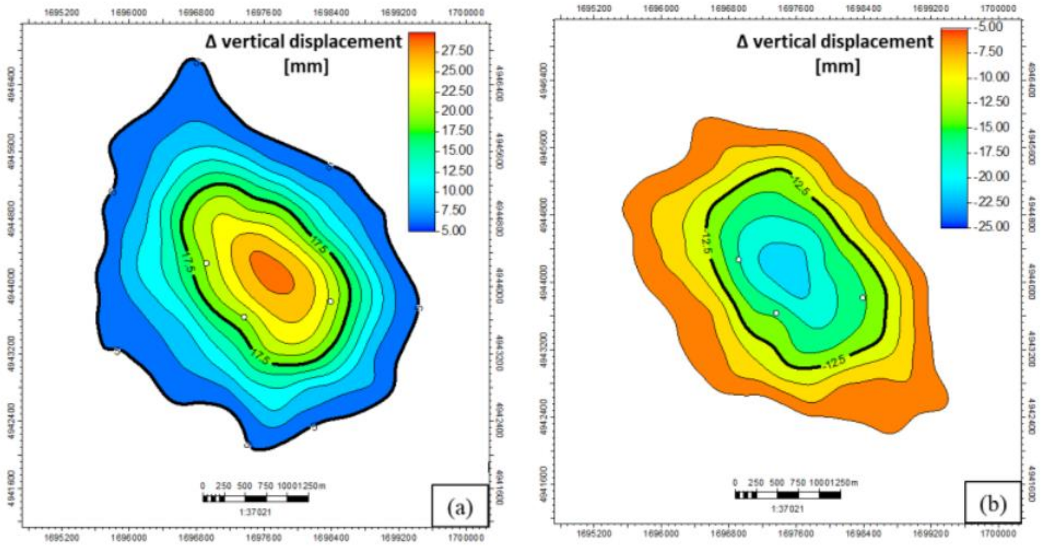

Figure 4.15: Surface vertical movements maps for UGS field 5 (Figure 4.12) for an injection (a) and production (b) cycle (from Rocca et al., 2021).

4.4.3. Anthropogenic subsidence due to water production

Groundwater withdrawal rates in the Emilia-Romagna region are represented in Figure 4.16 for the three time periods: 2003, 2009-2011 and 2015-2018. Data were provided by ARPAE (Agenzia Prevenzione Ambiente Energia Emilia-Romagna) and were acquired partly through accurate measurements and the other half by estimation because of the difference in collection for different production purposes (civil, industrial and zootechnical). It is also important to note that illegal water wells are present and widespread in Emilia-Romagna and their withdrawal rates are not recorded and thus not considered. The definition of a coherent water production dataset is essential for the identification of general and local production trends across space and time. The following can then be used to highlight areas prone to experiencing induced subsidence that should be investigated.

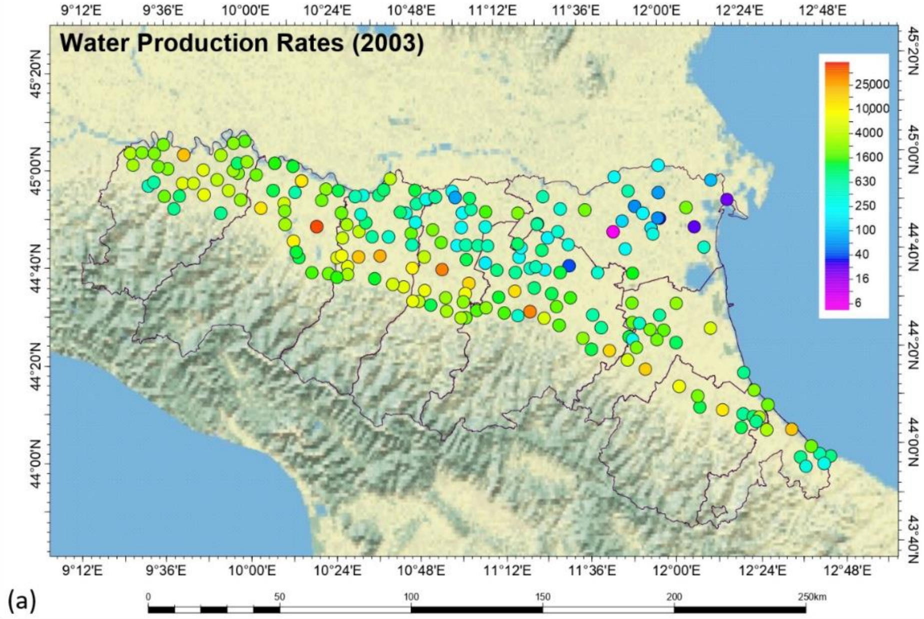
Water Production Rates (2003)
9°12'E
9°36'E
10°00'E
10°24'E
10°48'E
11°12'E
11°36'E
12°00'E
12°24'E
12°48'E
45°20'N
45°00'N
44°40'N
44°20'N
44°00'N
43°40'N
25000
10000
4000
1600
630
250
100
40
16
6
0
50
100
150
200
250km

(a)

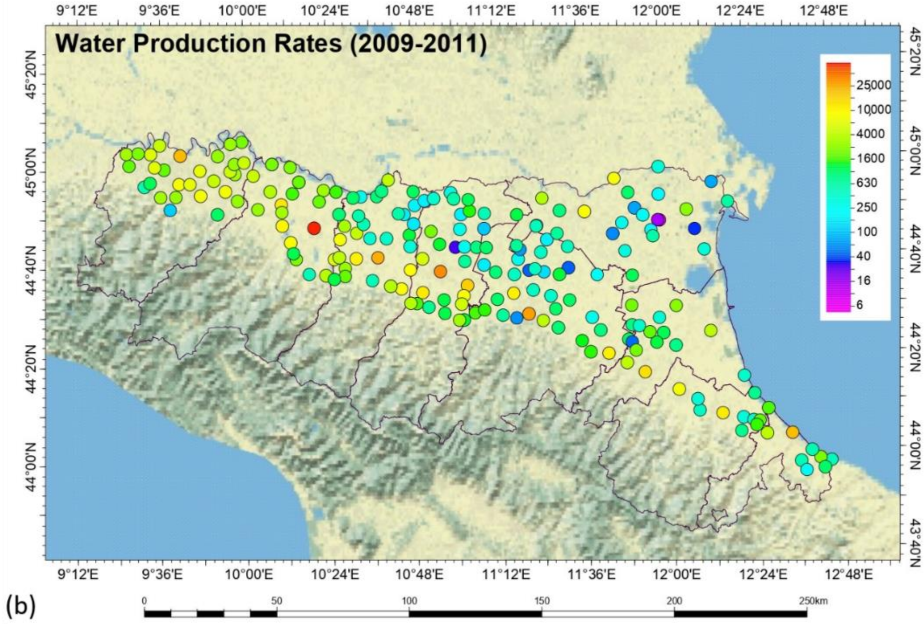
Water Production Rates (2009-2011)
9°12'E
9°36'E
10°00'E
10°24'E
10°48'E
11°12'E
11°36'E
12°00'E
12°24'E
12°48'E
45°20'N
45°00'N
44°40'N
44°20'N
44°00'N
43°40'N
25000
10000
4000
1600
630
250
100
40
16
6
0
50
100
150
200
250km

(b)

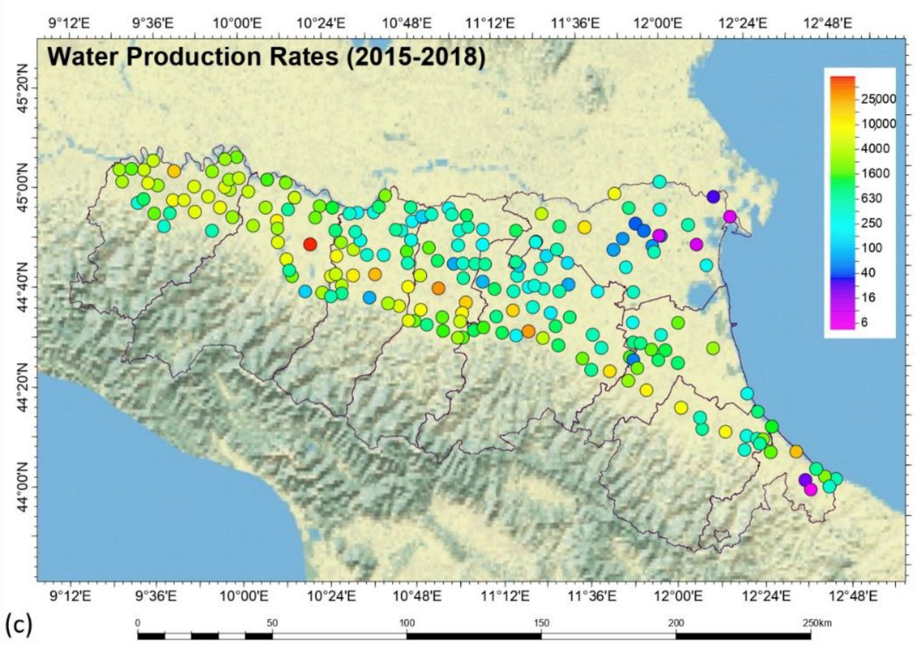

Figure 4.16: Water production rates in 10^6 m^3/year in Emilia-Romagna for the time periods (a) 2003, (b) 2009-2011 and (c) 2015-2018 (from Eid et al., 2022).

The interpretation of the water production dataset can be summarized as follows:

- The general annual trend of water production in Emilia-Romagna shows a slight decrease across the three time periods: from 2009 to 2009-2011 to 2015-2018, with cumulative consumptions of 663×10^6 m^3/year, 659×10^6 m^3/year and 623×10^6 m^3/year respectively.
- Water production exhibits relatively low rates and is distributed widely across each province. However, in certain areas, high production rates are identified locally in the three time periods.

3D numerical models have been used to simulate land subsidence and sediment compaction in Emilia-Romagna caused by groundwater exploitation and to predict future scenarios as well. Figure 4.17 and Figure 4.18 show two examples of the application of mechanical simulations to measure land subsidence due to water production in two areas in Emilia-Romagna.

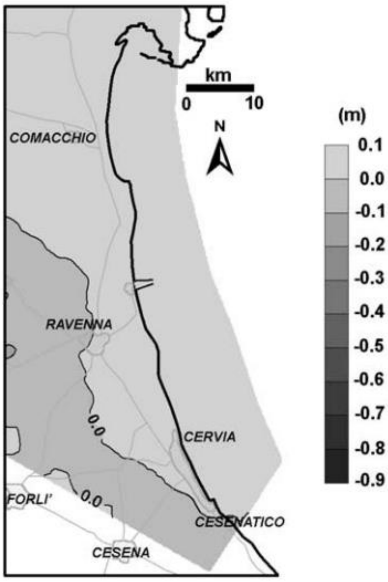

Figure 4.17: Land subsidence (in m) along the Emilia-Romagna coastland caused by water production during the time period 2001-2006 (from Teatini et al., 2006).

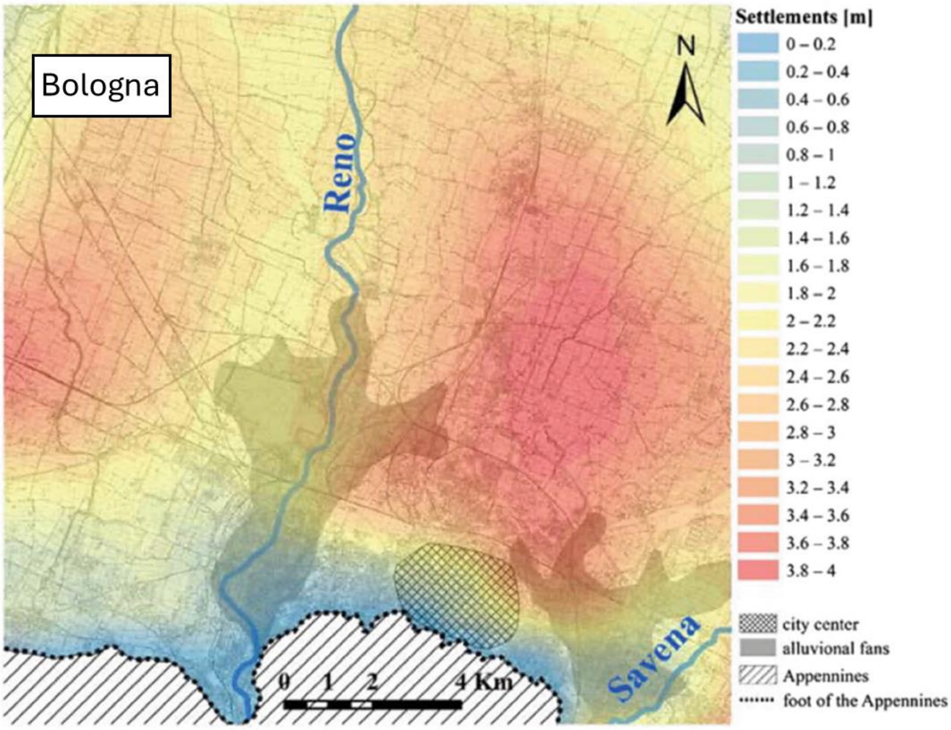

Figure 4.18: Land subsidence (in m) in the city of Bologna caused by water production for the year 2002 (from Spacagna et al., 2020).

Although not a focus area of this thesis, extensive studies utilizing numerical models have also been conducted on the region of Venice simulating significant land subsidence due to groundwater extraction, particularly in the nearby mainland areas like Marghera (Gambolati and Freeze, 1973; Lewis and Schrefler, 1978), as well as predicting its uplift by pumping seawater into deep aquifers (Comerlati et al., 2004) and selecting the appropriate parameters including hydraulic conductivity, rock compressibility and injection pressure (Castelletto et al., 2008; Teatini et al., 2010;2011).

4.4.4. Anthropogenic subsidence: superposition and comparison between the different sources

Although a quantitative comparison between water and gas historically produced is not straightforward, the presented datasets point out that the highest concentrations of gas production and the drastic increases in water production had temporally coincided within the period from the 1950s to the late 1970s. Concerning the Emilia-Romagna region, the strongest superposition between hydrocarbon activities (both primary production and UGS concessions) and water production is located in the following provinces: Piacenza, Ferrara, Bologna, and Ravenna

The following observations can be made in terms of land subsidence in the Po Plain induced by the varying fluids extraction (Eid et al., 2022):

1. Subsidence due to water production is widespread both spatially and temporally, with significant occurrences in areas of high production. However, accurately identifying and quantifying this subsidence is challenging due to insufficient data and precision in production records and spatial distribution. Subsidence due to water production also tends to be greater than that due to gas production.
2. Subsidence resulting from primary gas production is more localized spatially and evolves over time due to the creep phenomenon. Detailed analyses using numerical or analytical methods enable reasonably accurate estimates of its spatial extent and magnitude.

Ground movements induced by UGS exhibit distinctive patterns (“earth breathing”), making them easily identifiable. Similar to primary gas production, the effects of UGS can be estimated with high precision. Experimental evidence suggests that the magnitude of these induced movements is even lower compared to those from primary production.

Chapter 5

Subsidence modelling: Theoretical background

Subsidence modelling has been proven effective not only for the quantification of the phenomenon but also for the management of its impacts. In the scope of this work, subsidence modelling due to groundwater exploitation is to be performed later. This chapter describes the basic principles of the different constitutive models of deformable bodies followed by the laws governing classical groundwater hydrology. A general comparison is finally made between subsidence induced over gas/oil fields versus that over multi-aquifer systems.

5.1. Formation compaction and associated ground movements: general principles and concepts

The processes through which rocks and sediments undergo deformation in response to changes in pore pressure during fluid production have been thoroughly investigated and understood by literature (i.e., Geertsma, 1973a,b; Jaeger et al., 2007; Gambolati and Teatini, 2015). In the case of aquifer systems, the total geostatic load acting on the system and its confining formations is maintained by the pore water pressure along with the effective vertical and horizontal stresses. When the aquifer system is subjected to pumping, the pore water pressure decreases, reducing its ability to support the load from overlying formations. This causes more of the load to be supported by the by the grain-to-grain contacts within the material resulting in an increase in effective stress. This increase in stress causes the entire aquifer system to compact, extending its effects to the ground surface leading to subsidence (Figure 5.1). Conversely, pore water pressure can increase due to the natural or artificial recharge of the aquifer, which may partially reverse or mitigate subsidence in certain circumstances.

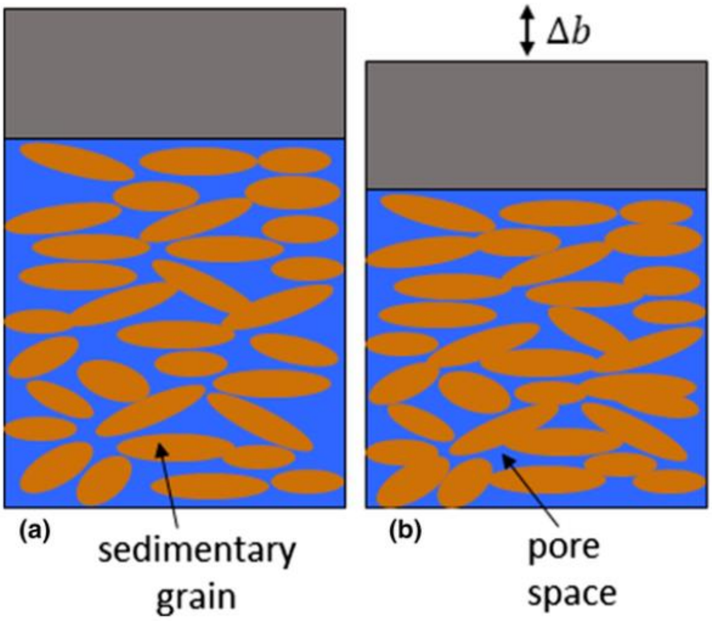

Figure 5.1: (a) Initial condition of aquifer; (b) aquifer after compaction causing land subsidence Δb (modified from Smith & Majumdar, 2020).

Around the pumping well, a cone-shaped depression forms due to the decrease in waterhead level and expands laterally and vertically to a certain extent. The magnitude and timing of the decrease in waterhead level depends on many factors that include the structural and geological characterization of the system as well as the mechanical properties of the system and the fluid itself.

5.2. Constitutive laws

Constitutive laws incorporate a series of equations that describe the response and deformation process of a material body to applied stresses. This section discusses the key principles and parameters related to the theories of elasticity, poro-elasticity, plasticity and visco-elasticity that lay ground for basic constitutive models of deformable bodies. All information are collected from the following sources: Fjaer et al., (2008), Gould (2013), Jaeger et al. (2007), Lancellotta (2008), Zoback (2007).

5.2.1. Elasticity

The behavior of a material body is defined as “elastic” if, when subjected to loading, it has a potential energy which may be released during unloading causing it to fully recover to its original shape. The *elastic constitutive law* takes into account the stress-strain relationship of the elastic body and is represented as follows:

$$\sigma_{ij} = \frac{\partial \psi}{\partial \varepsilon_{ij}} \qquad (5.1)$$

where σ_{ij} represents the infinitesimal stresses, ε_{ij} the infinitesimal strains and ψ the stress potential (strain energy per unit volume). If we were to consider a linear stress-strain relationship (Figure 5.2a) with the initial state of the body being undeformed and in equilibrium, the above function can be written in the form:

$$\sigma_{ij} = C_{ijhk}\varepsilon_{hk} \qquad (5.2)$$

In this case, C, the stiffness tensor, includes the scalar quantities relating the stresses to the consequent strains and are referred to as *elastic constants*.

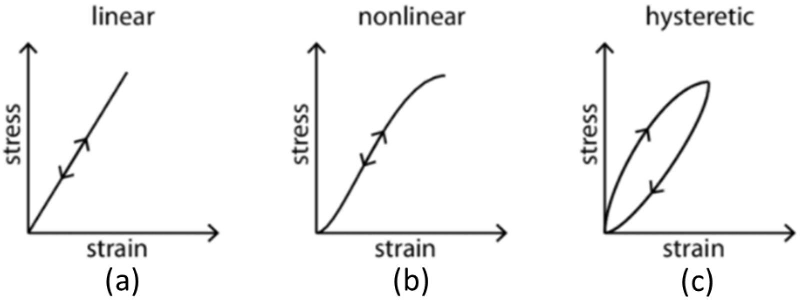

Figure 5.2: Stress-strain relationships for: (a) linear elasticity, (b) nonlinear elasticity and (c) hysteresis (from Jaeger et al., 2007).

The behavior of an elastic material when loaded depends on the magnitude of the applied stress, its elastic properties and the stress history of the material and results in one of the scenarios in Figure 5.2. Although most rocks behave in a nonlinear manner when subjected to large stresses, linear relations can still be applied to describe their behavior if the applied stresses change infinitesimally.

One of the most important constitutive laws is *Hooke's law* (Eq. 5.3). It describes the behavior of a linear elastic material which, when subjected to a state of stress, is independent of the orientation of the applied stress (isotropic).

$$\begin{bmatrix} \sigma_x \\ \sigma_y \\ \sigma_z \\ \tau_{xy} \\ \tau_{yz} \\ \tau_{zx} \end{bmatrix} = \frac{E(1-v)}{(1+v)(1-2v)} \begin{bmatrix} 1 & \frac{v}{1-v} & \frac{v}{1-v} & 0 & 0 & 0 \\ \frac{v}{1-v} & 1 & \frac{v}{1-v} & 0 & 0 & 0 \\ \frac{v}{1-v} & \frac{v}{1-v} & 1 & 0 & 0 & 0 \\ 0 & 0 & 0 & \frac{1-2v}{2(1-v)} & 0 & 0 \\ 0 & 0 & 0 & 0 & \frac{1-2v}{2(1-v)} & 0 \\ 0 & 0 & 0 & 0 & 0 & \frac{1-2v}{2(1-v)} \end{bmatrix} \begin{bmatrix} \varepsilon_x \\ \varepsilon_y \\ \varepsilon_z \\ \Gamma_{xy} \\ \Gamma_{yz} \\ \varepsilon_{zx} \end{bmatrix} \tag{5.3}$$

where σ, τ, ε, Γ correspond to normal stress, shear stress, normal strain and shear strain respectively and the coefficients E, called Young's modulus, and v, Poisson’s ratio, belong to a group of coefficients called *elastic moduli*. These parameters associate the applied stress and the elastic responses of the material and include:

Young's modulus ***E***: is a measure of the material's resistance to withstand uniaxial stress compression, i.e. the material's stiffness. It is equal to the longitudinal stress divided by the strain:

$$E = \frac{\sigma}{\varepsilon} \tag{5.4}$$

Poisson's ratio ***v***: is a measure of the lateral expansion to the longitudinal shortening.

$$v = -\frac{\varepsilon_y}{\varepsilon_x} \tag{5.5}$$

Lame's parameters:

Shear modulus ***G***: is a measure of the material's resistance against shear deformation.

$$G = \frac{E}{2(1+v)} \tag{5.6}$$

Lame's constant **λ**:

$$\lambda = \frac{vE}{(1+v)(1-2v)} \tag{5.7}$$

Bulk modulus ***K***: is a measure of the material's resistance against hydrostatic loading. Its inverse (1/*K*) represents compressibility.

$$K = \lambda + \frac{2}{3}G \tag{5.8}$$

The above elastic parameters depend highly on the depositional history of the material, the stress-strain history and the type of material itself. They can either be classified as dynamic moduli when measured through acoustic velocities or static moduli when obtained using stress/strain measurements.

5.2.2. Poroelasticity

The theory of poro-elasticity considers the material body to be inhomogeneous on a microscopic scale and hence builds constitutive models on the basis of the behavior of a saturated material body subjected to loading while accounting for the role of the non-solid part (void space) in both the fluid flow and the deformation itself.

The theory is originally based on the work of Terzaghi (1923, 1936) who aimed to study the process of soil consolidation while assuming that the solid grains forming the soil are incompressible and hence can be treated as an elastic porous material. His work was performed on a completely saturated soil under oedometric conditions (one-dimensional deformations) and lead to the derivation of the *effective stress principle*. It states that when a saturated porous material is subjected to loading, the stress is partly carried by the solid framework and partly by the fluid within the pores. Hence, the potential energy of the strained poroelastic material is dependent on the interstitial fluid within its pores and can be represented as follows:

$$\sigma' = \sigma - \delta p_f \tag{5.9}$$

where σ' and σ are the effective and total stress respectively, p_f is the pressure of the fluid and δ is the identity tensor such that the total shear stress and effective shear stress are the same.

In 1941, Biot expanded on this theory by considering the problem under three dimensions and removing the assumption of incompressible solid grains. Thus, Eq. 5.9 was reformulated:

$$\sigma' = \sigma - \alpha\delta p_f \tag{5.10}$$

where the parameter α is called the Biot coefficient and equals $1 - \frac{K_{fr}}{K_s}$.

$\boldsymbol{K_{fr}}$ is the bulk modulus of the solid skeleton and can be estimated by performing a drained test (also called "jacketed test"). The test is shown in Figure 5.3a and is carried out such that the fluid situated in the pores is free to escape in order to keep the pore pressure constant during loading. This allows us to characterize the material's stiffness.

$\boldsymbol{K_s}$ is the bulk modulus of the deformable solid grains and can be estimated by performing an undrained test (also called "unjacketed test"). The test is shown in Figure 5.3b and is conducted in a manner such that no fluid flow occurs in or out of the sample while holding the condition $\Delta\sigma = \Delta p_f$. This allows us to characterize the stiffness of the solid grains.

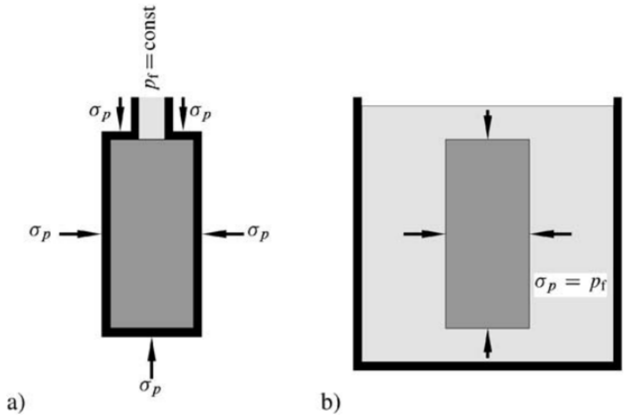

Figure 5.3: (a) “Jacketed” test, (b) “Unjacketed” test (from Fjaer et al., 2007).

5.2.3. Plasticity

The theory of plasticity is a constitutive model that describes the non-elastic behavior of a material. This behavior is *ductile* such that the material undergoes permanent deformations without losing its ability to support the load. Plasticity is based on four major concepts:

1. Plastic strain: The total strain increment is divided into the elastic and the plastic component increments (under the hypothesis of small strain):

$$d\varepsilon_{ij} = d\varepsilon_{ij}^{e} + \varepsilon_{ij}^{p} \tag{5.11}$$

   The elastic component is calculated according to the elastic constitutive relations we have already discussed in section 5.2.1 and disappears when the stress is released whereas the plastic component is permanent and remains when the stress is released.

2. Yield criterion: The yield criterion represents a point beyond which permanent changes occur; it is the onset of plastic deformation. In Figure 5.4, σ_p is the yield stress. In a general state of stress, the yield point becomes a yield surface and the yield stress becomes the yield state of stress.

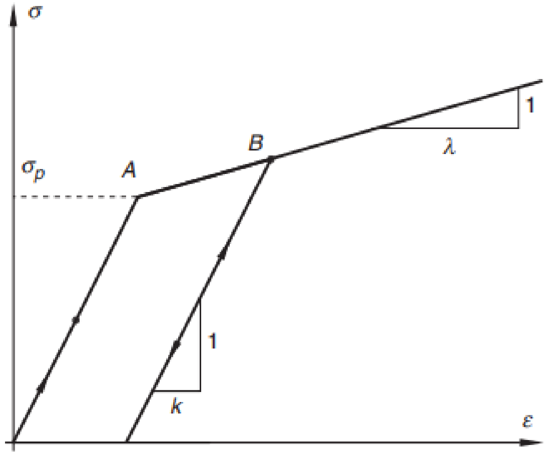

Figure 5.4: Elastic-plastic behavior of a material.

3. Flow rule: describes how the plastic strains evolves for a given loading situation. The material should be *stable* (perturbations produce non-negative work) implying that: the yield surface is convex and plays the role of plastic potential. The plastic strain increment is expressed by:

$$d\varepsilon_{ij}^{p} = \Lambda \frac{\partial Q}{\partial \sigma_{ij}} \quad (5.12)$$

   where Λ is the *plastic multiplier* and function Q is independent of the stress path and is called *plastic potential*. It is a surface orthogonal to all the vectors of plastic straining increment. If G is the same as the yielding surface then the flow rule is "associated".

4. Hardening rule: Hardening is the evolution of the yield stress with the occurrence of plastic deformations. In Figure 5.4, when point B is reached, the new yield stress is represented by point B instead of σ_p and if a loading-unloading cycle is performed, the material is assumed to be elastic if the applied stress is below point B.

There are two modes of hardening: isotropic and kinematic. Isotropic hardening means that the yield surface expands in a uniform manner about the hydrostatic axis whereas kinematic hardening translates the failure surface in stress space without modifications in shape and size.

5.2.3.1. Mohr-Coulomb criterion

The most general and frequently used failure criterion is Mohr-Coulomb (Fjaer et al., 2008). This criterion states that failure is controlled by the maximum shear stress and that this shear failure across a plane is constrained by the cohesion of the material. It is expressed as follows:

$$\tau = \tau_0 + \sigma \tan\phi \qquad (5.13)$$

where τ is the shear stress, σ is the normal stress, τ_0 is the cohesion of the material and ϕ is the material angle of internal friction. The assessment of the Mohr-Coulomb criterion requires conducting numerous triaxial tests on rock samples under varying confining pressures. A set of Mohr's circles can then be plotted (Figure 5.5) such that the locus of the tangent points of the circles represents the failure envelope of the rock. The boundary between stable and unstable stress states is defined accordingly. Once the failure criteria is determined, it becomes possible to predict the failure state (instability) under different conditions.

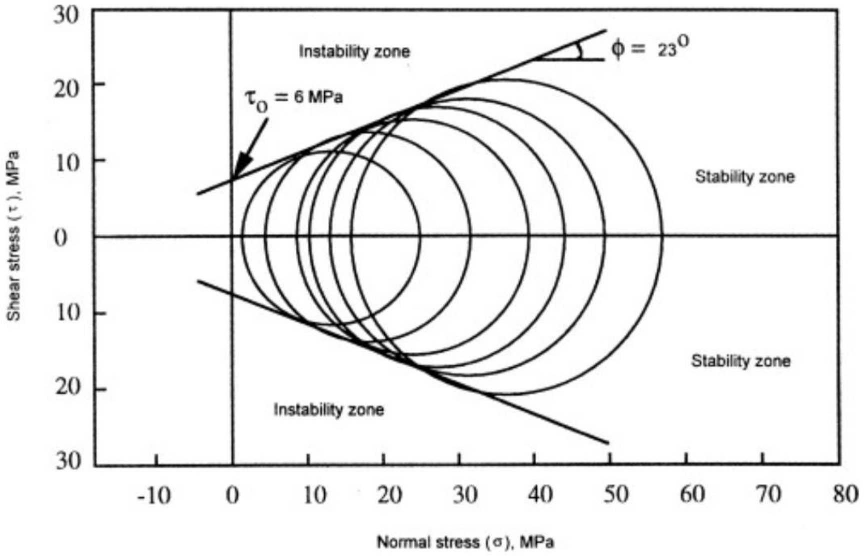

Figure 5.5: Mohr-Coulomb failure criteria for natural intact shale (from Al-Awad, M.N.J, 2002).

5.2.4. Cam-Clay Model

Soil mechanics has been developed for systems with no or little cement between the individual grains. Since clay is a material that fits into this description, its behavior was studied under different test conditions and eventually lead to the formulation of the Cam-Clay (CC) and Modified Cam-Clay (MCC) models.

It is first necessary to define two common concepts used in soil mechanics:

Voids ratio ***e***: the volume of voids V_{void} relative to the volume of the solid grains V_{solid} in the material:

$$e = \frac{V_{void}}{V_{solid}} \qquad (5.14)$$

Specific volume v: the total volume (grains + voids) divided by the volume of the solid grains:

$$\mathrm{v} = \frac{V_{solid} + V_{void}}{V_{solid}} = 1 + e \tag{5.15}$$

Relation with porosity:

$$n = \frac{e}{1 + e} = \frac{\mathrm{v} - 1}{\mathrm{v}} \tag{5.16}$$

The CC and MCC models are cap plasticity models that are able to depict realistic volume changes resulting from soil deformations. They describe three important aspects of soil behavior:

1) Strength
2) Compression or dilatancy (the volume change that occurs with shearing)
3) Critical state at which soil elements can experience unlimited distortion without any changes in stress or volume

Figure 5.6 displays a physical representation of the processes (loading and unloading) that lead to soil deformation. The deposition process (loading), represented by A-B-C in Figure 5.6, exerts an additional overburden weight on the soil sample causing an increase in effective vertical stress σ'_v. This leads to the consolidation of loose sediments inducing a reduction of the void element, i.e. the void ratio *e*. During erosion (unloading), represented by segment DC, the applied effective vertical load is decreased with a respective decrease in void ratio; however, it can be seen on the graph that for the same effective burden, points B and D exhibit different void ratios. This proves that there is evidence of residual strain after unloading.

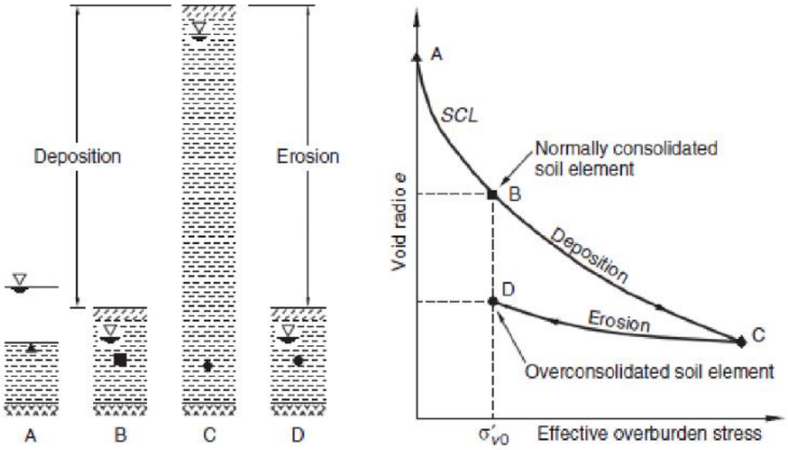

Figure 5.6: Effect of loading and unloading sequences on void ratio of a soil sample.

The soil samples in CC and MCC models are characterized by three parameters that define their state:

1) Effective mean stress ***p'***
2) Deviatoric (shear) stress $\boldsymbol{\tau}$
3) Specific volume v

Under general stress conditions, ***p'*** and ***q*** can be calculated in terms of principal stresses σ_1', σ_2' and σ_3' :

$$p' = \frac{1}{3}(\sigma_1' + \sigma_2' + \sigma_3') \tag{5.17}$$

$$\tau = \frac{1}{\sqrt{2}}\sqrt{(\sigma_1' - \sigma_2')^2 + (\sigma_2' - \sigma_3')^2 + (\sigma_3' - \sigma_1')^2} \tag{5.18}$$

Virgin Consolidation Line and Swelling Lines

The models assume that a soft soil sample is slowly compressed under isotropic stress conditions ($\sigma_1' = \sigma_2' = \sigma_3' = p'$) and under drained conditions. The relationship between specific volume v and ***ln p'*** under these conditions consists of a straight virgin consolidation line (also known as the normal compression line) and a set of straight swelling lines (also called unloading-reloading lines). Figure 5.7 shows an example.

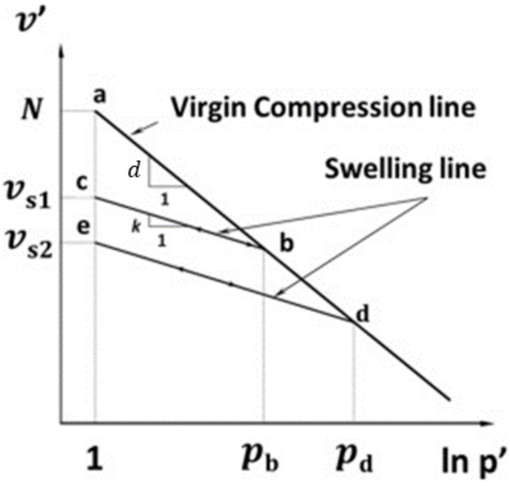

Figure 5.7: Behavior of soil sample under isotropic conditions.

When a soil sample is first loaded to an isotropic stress p_b', it moves down the virgin consolidation line from point *a* to point *b*. If the sample is unloaded at point *b*, the specific volume-mean stress behavior moves up the swelling line *bc* to the point *c*. If the sample is now reloaded to a stress p_d', it will first move down the swelling line for stress values up to p_b'. Once p_b' is exceeded, the sample will again move down the virgin consolidation line to the point *d*. If the sample is unloaded at point *d* to a stress value of p'_a, it will move up the swelling line *de*.

The virgin consolidation line in Figure 5.7 is defined by:

$$\mathrm{v} = N - d\ lnp' \tag{5.19}$$

and the equation for a swelling line:

$$\mathrm{v} = \mathrm{v}_s - k\ lnp' \tag{5.20}$$

where d is the slope of the virgin consolidation line and *k* is the slope of a swelling line. *N* is the specific volume of normal compression line at unit pressure and is dependent on the units of measurement. These parameters are characteristic properties of a particular soil.

If the current state of a soil is on the virgin consolidation (normal compression) line, the soil is described as being **normally consolidated**, i.e. the current stress state is the maximum experienced by the soil and its stress-strain behavior is primarily elasto-plastic. If the soil is unloaded, it becomes **overconsolidated**, i.e. it has experienced a higher vertical stress level during its depositional history and it reaches a lower void ratio than a normally consolidated soil for the same level of applied effective stress.

The stiffness of overconsolidated soils is relatively greater than that of normally consolidated soils (slope of swelling lines is less than that of the virgin consolidation line).

Elastic Material Constants for CC and MCC

Fundamental parameters used in soil modelling: shear modulus *G* and bulk modulus *K* because they allow the effects of volume change and distortion to be decoupled.

$$K = \frac{\mathrm{v}p'}{k} \tag{5.21}$$

where v is the specific volume, *p'* is the mean stress and *k* is the slope of the swelling line.

CC and MCC formulations require specification of either shear modulus *G* or Poisson's ratio v . When *G* is given as a constant, then v is no longer a constant and is calculating as follows:

$$v = \frac{3K - 2G}{2G + 6K} \tag{5.22}$$

When v is given as a constant then *G* is determined using:

$$G = \frac{3(1 - 2v)}{2(1 + v)}K \tag{5.23}$$

The Overconsolidation Ratio

In order to determine the level of consolidation of soil samples, the *Overconsolidation Ratio (OCR)* is used. It is the ratio of the preconsolidation pressure to the current mean effective stress:

$$OCR = \frac{p_o}{p'} \tag{5.24}$$

where the preconsolidation pressure p_o is a measure of the highest stress level the soil has ever experienced (also known as yield stress).

If *OCR* = 1, then the soil is a normal consolidation state; a state in which the maximum stress level previously experienced by a material is not larger than the current stress level. If *OCR* > 1, then the soil is overconsolidated indicating that the maximum stress level experienced by the material is larger than the present stress level.

5.3. Subsidence due to groundwater exploitation

Land subsidence is most effectively studied and analyzed according to Biot's theory of consolidation (Biot, 1941) discussed in section 5.2.2 that states that consolidation represents the response of a compressible porous medium to changes in the flow field operating within it. In order to have a complete analysis of subsidence induced by the exploitation of water from underground aquifer systems, the 3D deformation field relative to the 3D flow field must be determined (Gambolati and Teatini, 2015).

The deformation of the elastic porous body is controlled by the change in the effective stress σ' in Terzaghi's Eq. 5.9. The Cauchy equations represent the incremental effective stress and pore pressure when changes are made to the undisturbed state of equilibrium of the body, and are as follows:

$$\begin{aligned}
&\frac{\partial \sigma_{xx}}{\partial x} + \frac{\partial \tau_{xy}}{\partial y} + \frac{\partial \tau_{xz}}{\partial z} = \frac{\partial p}{\partial \mathrm{x}} \\
&\frac{\partial \tau_{yx}}{\partial x} + \frac{\partial \sigma_{yy}}{\partial y} + \frac{\partial \tau_{yz}}{\partial z} = \frac{\partial p}{\partial \mathrm{y}} \\
&\frac{\partial \tau_{zx}}{\partial x} + \frac{\partial \tau_{zy}}{\partial y} + \frac{\partial \sigma_{zz}}{\partial z} = \frac{\partial p}{\partial \mathrm{z}}
\end{aligned} \tag{5.25}$$

where σ_{xx}, σ_{yy} and σ_{zz} are the normal effective stresses along their respective coordinate directions and $\tau_{xy} = \tau_{yx}$, $\tau_{xz} = \tau_{zx}$ and $\tau_{yz} = \tau_{zy}$ are the shear stresses.

Eq. 5.3 represents the relationship between the incremental stress and strain tensors. It is important to note that in a typical layered aquifer system, the elastic moduli/mechanical parameters (Young's modulus, Poisson's ratio and shear modulus) introduced in Eq. 5.4, 5.5 and 5.6 are different along the vertical direction versus the horizontal direction. They are represented by the following parameters: E_v, E_h, v_v, v_h, G_v. G_h is related to E_h and v_h through the following equation:

$$G_h = \frac{E_h}{2(1+v_h)} \tag{5.26}$$

The vertical compressibility is the main parameter controlling subsidence and is defined through the mechanical parameters for an isotropic soil medium as follows:

$$c_M = \frac{(1+v)(1-2v)}{E(1-v)}, \tag{5.27}$$

$$c_M = \frac{v}{\lambda(1-v)}, \tag{5.28}$$

$$c_M = \frac{(1-2v)}{2G(1-v)} \tag{5.29}$$

If we substitute the aforementioned relationships between the effective stress and strain into the Cauchy equations, we get the equilibrium equations for an isotropic medium conditioned by pore pressure p_p variations within it, represented as:

$$\begin{gathered} G\nabla^2 u + (\lambda + G)\frac{\partial \varepsilon}{\partial x} = \frac{\partial p_p}{\partial \mathrm{x}} \\ G\nabla^2 t + (\lambda + G)\frac{\partial \varepsilon}{\partial y} = \frac{\partial p_p}{\partial \mathrm{y}} \\ G\nabla^2 w + (\lambda + G)\frac{\partial \varepsilon}{\partial z} = \frac{\partial p_p}{\partial \mathrm{z}} \end{gathered} \tag{5.30}$$

where ∇^2 is the Laplace operator, u, t and w are the incremental position vector components along x,y and z coordinate axes and ε is the volume strain or dilatation. These 3 equations have four unknowns: u, t, w and p_p. The fourth equation needed to close the system governs the groundwater flow equation that controls subsurface flow within the aquifer and is derived from the equation originally developed by Biot (1941, 1955). The fourth equation to be added to Eq. 5.30 is:

$$\frac{1}{\gamma}\nabla.\left(K_{ij}\nabla\right) = n\beta\frac{\partial p_p}{\partial t} + \frac{\partial \varepsilon}{\partial t} \tag{5.31}$$

where γ is the water specific weight, ∇ is the gradient operator equal to $\frac{\partial}{\partial \mathrm{x}} + \frac{\partial}{\partial \mathrm{y}} + \frac{\partial}{\partial \mathrm{z}}$, K_{ij} is the hydraulic conductivity tensor equal to $k_{ij}\frac{\gamma}{\mu}$ with k_{ij} the intrinsic permeability and μ the viscosity of water, n is the medium porosity and β is the compressibility of water.

5.3.1. Coupling versus uncoupling consolidation models

Eq. 5.30 together with Eq. 5.31 form the mathematical basis of the **coupled model**, which is a model of flow and stress that uses Biot equations to compute excess pore pressure and deformations in a porous medium throughout the time simultaneously.

The **uncoupled model** has served as the foundation of classical groundwater hydrology starting with Theis (1935) and Jacob (1940). This model is based on the diffusion equation which incorporates the rock structural behavior into a lumped mechanical parameter (elastic storage coefficient) and is solved separately for the pore pressure. Once pore pressure is obtained, it is used as an external source of strength and is integrated in Eq. 5.30. Thus, the uncoupled flow equation is:

$$\nabla\left(K_{ij}\frac{\nabla p_p}{\gamma}\right) = \gamma(n\beta + c_M)\frac{dp_p}{dt} \tag{5.32}$$

When the medium is transversally isotropic relative to the hydraulic conductivity with the axes aligned with the principal directions of anisotropy, Eq. 5.32 becomes:

$$\frac{\partial}{\partial x}\left(K_{xx}\frac{\partial p_p}{\partial \mathrm{x}}\right) + \frac{\partial}{\partial y}\left(K_{yy}\frac{\partial p_p}{\partial \mathrm{y}}\right) + \frac{\partial}{\partial z}\left(K_{zz}\frac{\partial p_p}{\partial \mathrm{z}}\right) = S_s\frac{\partial p_p}{\partial \mathrm{t}} \tag{5.33}$$

with S_s being the elastic storage coefficient referred to previously and is equal to $\gamma(n\beta + \alpha)$.

It is now important to clarify some basic definitions of oedometer vertical compressibility. The definition of c_M given above is derived from the classical theory of elasticity. In geotechnics, compressibility c_b for aquifer/aquitard soil samples are defined and measured as:

$$c_b = \frac{1}{1+e}\frac{de}{dp} \tag{5.34}$$

with e the void ratio equal to $n/(1-n)$ (check Eq. 5.16).

Consider a 1-D soil sample that has a length Δz at the beginning and is deformed vertically by (Δz). The vertical compressibility c_M in the classical elastic theory is defined as:

$$c_M = \frac{\delta(\Delta \mathrm{z})}{\Delta \mathrm{z}}\frac{1}{p} = \frac{\varepsilon}{p} \tag{5.35}$$

where p in the sample compaction $\delta(\Delta z)$ is negative, equivalent to and opposing the incremental effective stress. The void ratio allows us to write:

$$\delta(\Delta \mathrm{z}) = [\Delta \mathrm{z} + \delta(\Delta \mathrm{z})]\frac{e}{1+e} - \Delta \mathrm{z}\frac{e_0}{1+e_o} \tag{5.36}$$

with e_0 being the initial void ratio before compaction.

Figure 5.8 displays that the individual soil grains are incompressible (according to Eq. 5.36) and that sample volume (Δz) is equal to the variation of the porous volume. Dividing and rearranging Eq. 5.36 by Δz allows us to get:

$$\mathcal{E} = \frac{\delta(\Delta \mathrm{z})}{\Delta \mathrm{z}} = \frac{e - e_0}{1 + e_0} \tag{5.37}$$

Also,

$$c_M = \frac{\varepsilon}{p} = \frac{e - e_0}{p(1 + e_0)} \tag{5.38}$$

If c_M is independent of p, then we have:

$$\frac{de}{dp} = c_M(1 + e_0) \tag{5.39}$$

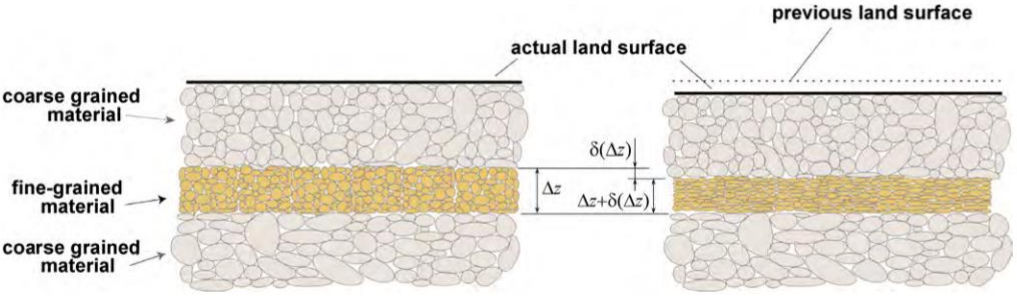

Figure 5.8: Soil compaction with a reduction of porous space and incompressible grains (from Gambolati and Teatini, 2015).

In other words, the void ratio is inversely proportional to the incremental pressure p (for any given initial e_0). Substituting Eq. 5.39 with Eq. 5.34 produces:

$$c_b = c_M \frac{1 + e_0}{1 + e} = c_M \frac{1 + e_0}{1 + e_0 + c_M p(1 + e_0)} = \frac{c_M}{1 + c_M p} \tag{5.40}$$

In general, c_M and c_b are not equal and cannot be considered as constants at the same time. They only coincide when the incremental pressure p nears zero. According to Eq. 5.37, the relationship of c_b versus c_M is:

$$c_b = \frac{1 + e_0}{1 + e} \frac{d\varepsilon}{dp} = \frac{1}{1 + \varepsilon} \frac{d\varepsilon}{dp} \tag{5.41}$$

If c_M is constant, then $\frac{d\mathcal{E}}{dp}$ is constant and:

$$c_b = \frac{c_M}{1 + \varepsilon} = \frac{c_M}{1 + c_M p} \tag{5.42}$$

The general relationship between c_b and c_M by eliminating the assumption of a constant c_M is (Gambolati, 1973b):

$$c_b = \frac{p\frac{dc_M}{dp} + c_M}{1 + c_M p} \tag{5.43}$$

If c_b is constant, Eq. 5.43 is integrated to:

$$c_M = \frac{e^{pc_b - 1}}{p} \tag{5.44}$$

The difference between c_b and c_M does not exceed 2-3% and the two definitions are essentially equivalent if the ultimate relative compaction $c_M p$ does not exceed 5% of the compacting unit (which is quite common in real geologic formations, particularly in shallow formations).

5.3.2. Multi-aquifer system exploitation

Figure 5.9 displays an example of a multi-aquifer system composed of an unconfined and two confined aquifers. Δz_1, Δz_2 and Δz_3 represent the piezometric decline in the three formations aforementioned, respectively. The subsidence θ at the ground surface is represented by:

$$\theta = \theta_1 + \theta_2 + \theta_3 \tag{5.45}$$

where θ_1 denotes the land subsidence relative to the depressurization of the unconfined aquifer and θ_2 and θ_3 represent the compaction of the confined aquifers.

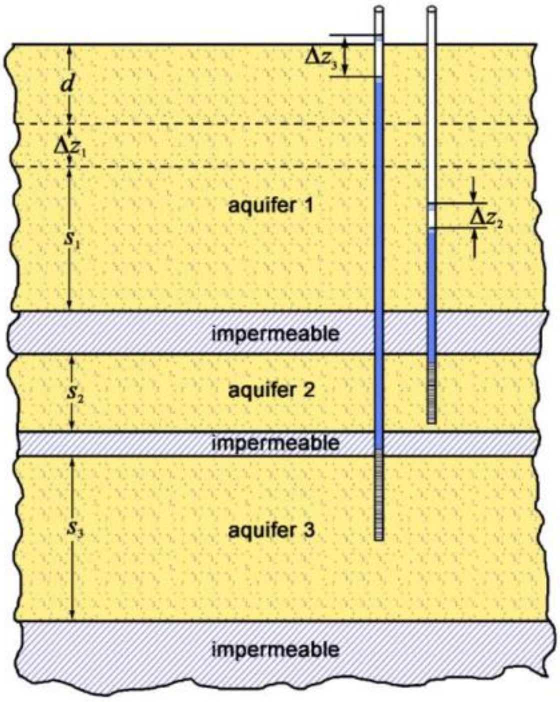

Figure 5.9: Sketch of a multi-aquifer system undergoing groundwater exploitation (from Gambolati and Teatini, 2021).

The compaction of the unconfined/phreatic aquifer is:

$$\theta_1 = \left(s_0 + \frac{\Delta z_1}{2}\right) c_M \Delta\sigma_1 \tag{5.46}$$

where s_0 is the initial thickness of the soil and $\Delta\sigma_z$ the change in the effective intergranular stress.

Regarding the two confined aquifers, the decrease of the total stress equal to $\Delta z_1 \gamma(\mathrm{n}_f - \mathrm{n})$, where γ is the specific weight of water and n_f is the porosity of the unconfined aquifer, should be taken into account. Thus, σ_z for aquifers 2 and 3 in Figure 5.9 increase accordingly:

$$\Delta\sigma_2 = \Delta z_2 \gamma - \Delta z_1 \gamma(\mathrm{n}_f - \mathrm{n}) \tag{5.47}$$

$$\Delta\sigma_3 = \Delta z_3 \gamma - \Delta z_1 \gamma(\mathrm{n}_f - \mathrm{n}) \tag{5.48}$$

The settlements θ_2 and θ_3 of the confined aquifers are then obtained from Eq. 5.37.

5.4. Subsidence over gas/oil fields versus subsidence over multi-aquifer systems

One of the main aspects in which land subsidence induced by gas/oil production differs from that induced by groundwater production is the dimensionality. Due to the thick overburden between the gas/oil reservoir and the ground surface and the stress-strain redistribution within, settlements above reservoirs are typically less but they do extend beyond the field itself (Figure 5.10a). In the case of aquifer systems, since they generally occupy the shallower formations and have a much larger areal extent, compaction directly travels to the ground surface and displacement occurs mainly in the downward vertical direction, even if the fluid flow is in 3D (Figure 5.10b).

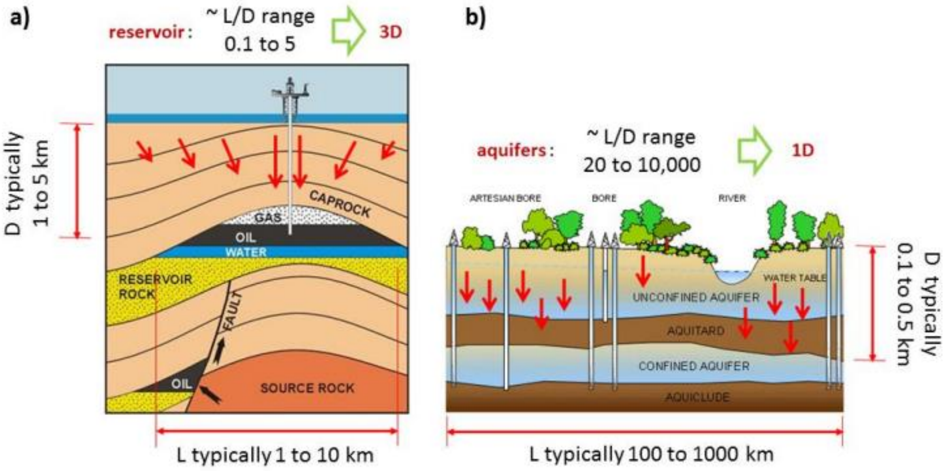

Figure 5.10: Subsidence induced by (a) oil/gas production where the displacement field (red arrows) is in 3D, (b) groundwater pumping where the displacement field is in 1D, downward and vertical (from Gambolati and Teatini, 2021).

In addition, even though both systems are made up of similar lithological compositions; aquifers of sequences of sands and clays and gas/oil reservoirs of sandstones (cemented sands) and shales (buried clays with mineralogical changes), their effect on land subsidence differs. In multi-aquifer systems, the induced subsidence is strongly related to the fraction of clays and silts making up the confining beds, aquitards and interbedded lenses. This is because the geomechanical simplicity found in the shallow layers, related to the depositional alluvial/marine environments, allows the lithological complexity to control compaction and it has been proven that clay is more compressible than sand by up to 2 orders of magnitude (Eid et al., 2021). Also, drainage from the clayey and silty layers can lag behind and cause delayed subsidence even after production is shut. In gas/oil reservoirs however, with the exception of the shallow ones, experimental studies have shown that clastic formations up to 1500 m ssl behave similar to hard rocks when their stress-strain relationship was tested under confining pressures but also act in accordance with soft rocks by an increase in the Young's moduli with density and confining stress yet still displaying high values such that effects of the confining stress become not so relevant in comparison to the behavior of soft rocks (Marzano et al., 2019). However, their degree of consolidation usually guarantees very small to negligible effects in terms of petrophysical variations induced by fluid extraction (Eid et al., 2021).

Chapter 6

Complete methodology

The multidisciplinary approach proposed and adopted in this thesis for the investigation and quantification of the superposition of natural and anthropogenic effects on land movements is described sequentially, highlighting the techniques used along the time framework of activities.

Initially in Chapter 7, the 3D numerical modelling is performed on the shallow subsurface involved in groundwater production activities of a case study also characterized by a UGS. The modelling workflow is delineated in Figure 6.1. It begins with a detailed geological static model characterizing the main stratigraphic, structural, lithological and petrophysical parameters of the alluvium hosting the aquifers. The domain of the geological model is larger than the area of interest and is extended on a regional scale so as to avoid outer boundary conditions effects on geomechanical simulations. Then, a flow model is set up based on the geological model and its hydrodynamic parametrization together with groundwater production well data and piezometric well data for the initialization and calibration of the model. The measured pore pressure change and distribution in the aquifers are produced. Finally, the geomechanical model for the analysis of ground displacement is created via a stress-strain finite element (FEM) model using the extended geological model and mechanical properties derived from literature. The pressure maps produced from the flow model are the forcing function of the geomechanical model simulations. The consequent land movements of the area are jointly analyzed and defined using the results from the modelling and simulation process and the results obtained by available studies of ground movements induced by the UGS.

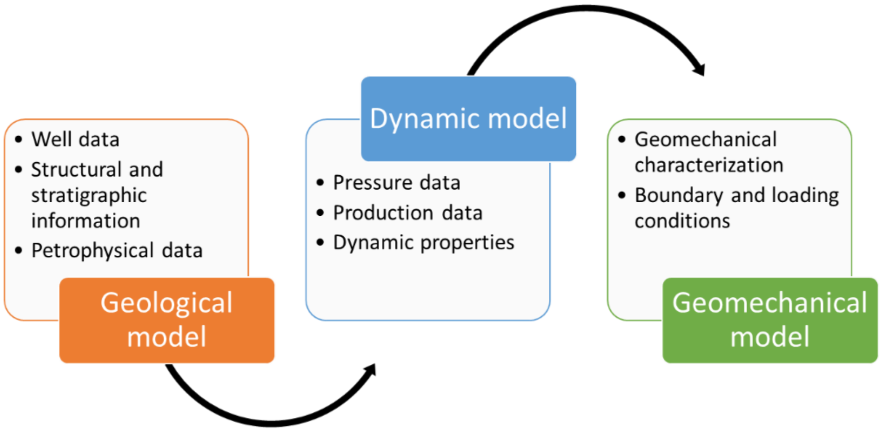

Figure 6.1: Basic schematic representation of the workflow methodology of Chapter 7.

In Chapter 8, an extended area of the case study that is affected by groundwater and gas production and also by natural components is selected in order to be able to spatially identify and quantify the contribution of each of these sources to the ground movements. The workflow of this methodology, presented in Figure 6.2, involves the application of an unsupervised machine learning technique (K-means clustering) on the decomposed time series ground deformation provided by CNR-IREA and processed with an advanced DInSAR approach called the Small BAseline Subset (SBAS) approach.. Only the seasonal or the trend components were used for the clustering in this study. The outcome of the method produces maps in which the spatial distribution of the clusters is represented as well as plots depicting the deformative behavior of the clusters. The methodology had already been tested for the geo-localization and quantification of ground movements induced by UGS activities (Garcia Navarro et al., 2024). In this work, the domain of investigation of the methodology was extended to aquifer exploitation by using the generated seasonal and trend components in comparison with datasets related to groundwater activities and aquifer features (water production, piezometric data, structural geology of the shallow subsurface and existing literature).

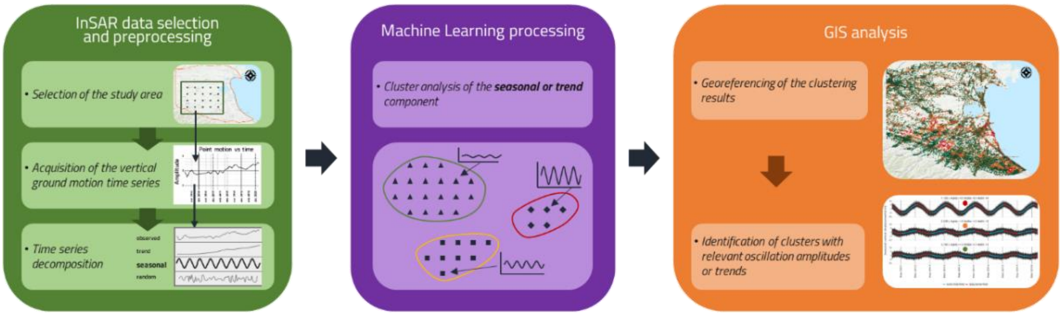

Figure 6.2: Workflow methodology of Chapter 8 (from Garcia Navarro et al., 2024).

6.1. SBAS technique

The SBAS technique relies on an easy combination of the DInSAR interferograms produced by numerous SAR acquisitions. It was developed by Berardino et al. (2002) and can be represented by four main steps: (Manzo et al., 2006; Lanari et al., 2007)

(1) SAR data pairs selection: SAR data pairs used to generate interferograms are selected based on their characterization by a small separation (baseline), temporally and spatially, between the orbits in order to minimize decorrelation phenomena regarded as noise effects (Zebker & Villasenor, 1992). This allows the preservation of the temporal and spatial coherence characteristics of the generated interferograms

(2) Phase unwrapping: the original (unwrapped) phase signals are retrieved based on the minimum cost flow algorithm (Costantini & Rosen, 1999) that is part of a region growing procedure to enhance the performances in areas with low signal to noise ratio

(3) Unwrapped interferograms inversion: the Singular Value Decomposition (SVD) method is used to easily "merge" the acquisition data sets separated by large spatial baselines

(4) Detection and filtering of possible atmospheric artifacts: atmospheric phase signals are highly correlated in space but poorly in time (Goldstein, 1995). This observation was made due to the availability of space-time information and led to the application of the filtering operation: a low-pass filter carried out in the 2D spatial domain that identifies the unfavorable atmospheric artifacts followed by a temporal high-pass filtering. This operation also allows the identification of possible orbital ramps generated by inaccuracies in the sensors orbit information. The identified atmospheric artifacts and orbital ramps are eventually removed

The SBAS algorithm thus generates deformation maps that are spatially dense and deformation time series for each coherent pixel identified in its corresponding image.

The next section summarizes the investigation technique developed by (Garcia Navarro et al., 2024) for InSAR data interpretation that was adopted in our work. The technique is based on time series decomposition and cluster analysis.

6.2. Time series decomposition analysis

The decomposition of time series follows a statistical method used to analyze the behavior of the series by decomposing it into three constituent components: trend, seasonality and a remainder component. The trend refers to the long-term pattern or direction of the data, indicating whether it is increasing or decreasing. The seasonality accounts for the periodic oscillation of the data over the considered time period and the remainder represents all the random fluctuations or noise (Hyndman & Athanasopoulos, 2021). There are two principal types of decomposition analysis: classical and advanced. Only the classical methods are introduced in the next section as they fall inside the scope of this project.

6.2.1. Classical decomposition analysis

The classical additive approach is used when the amplitude of the data oscillation remains relatively constant over time and the variations in the data are roughly constant across different levels of the series (Figure 6.3a). It is represented as follows:

$$Y_t = T_t + S_t + R_t \qquad (6.1)$$

where T_t, S_t and R_t are the trend, seasonality and remainder components, respectively, of the time series Y_t.

The classical multiplicative approach manages data that show a constant increase or decrease in oscillation (Figure 6.3b) and is represented as:

$$Y_t = T_t \text{ x } S_t \text{x } R_t \qquad (6.2)$$

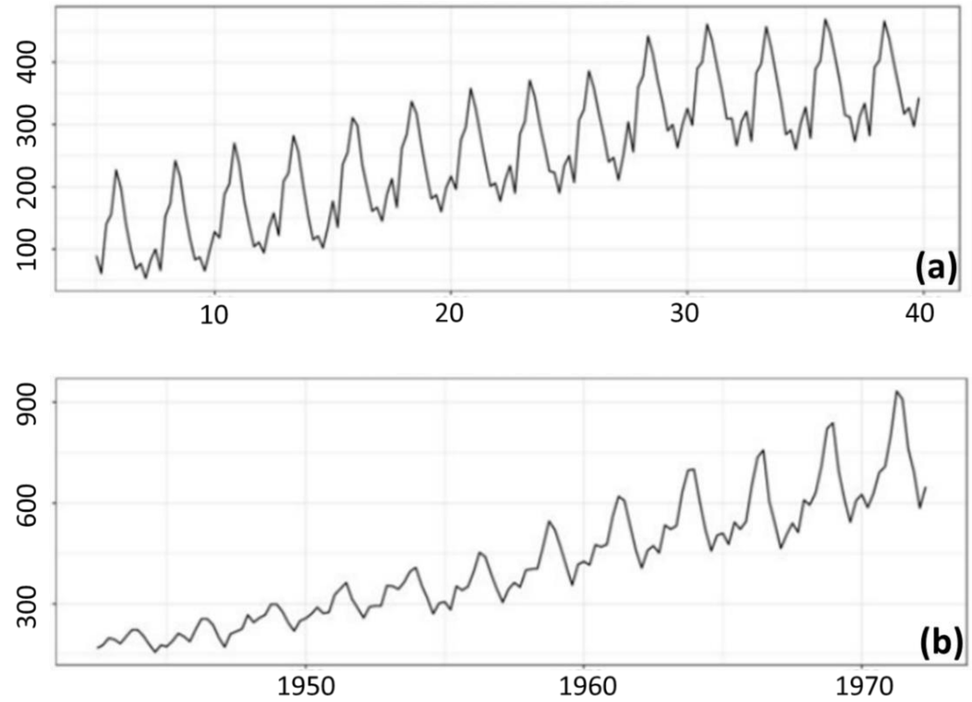

Figure 6.3: Examples of (a) additive time series behavior; (b) multiplicative time series behavior.

For our analysis, we use the additive approach “seasonal-trend decomposition based on Loess” developed by Cleveland et al. (1990) that utilizes locally weighted regression referred to as Loess regression which is a non-parametric method that fits a smooth curve to the data, with greater weight given to nearby data points. It generates smoother decomposed series by reducing the distortions caused by irregular or temporary patterns in the data. Figure 6.4 shows an example of an additive decomposed series.

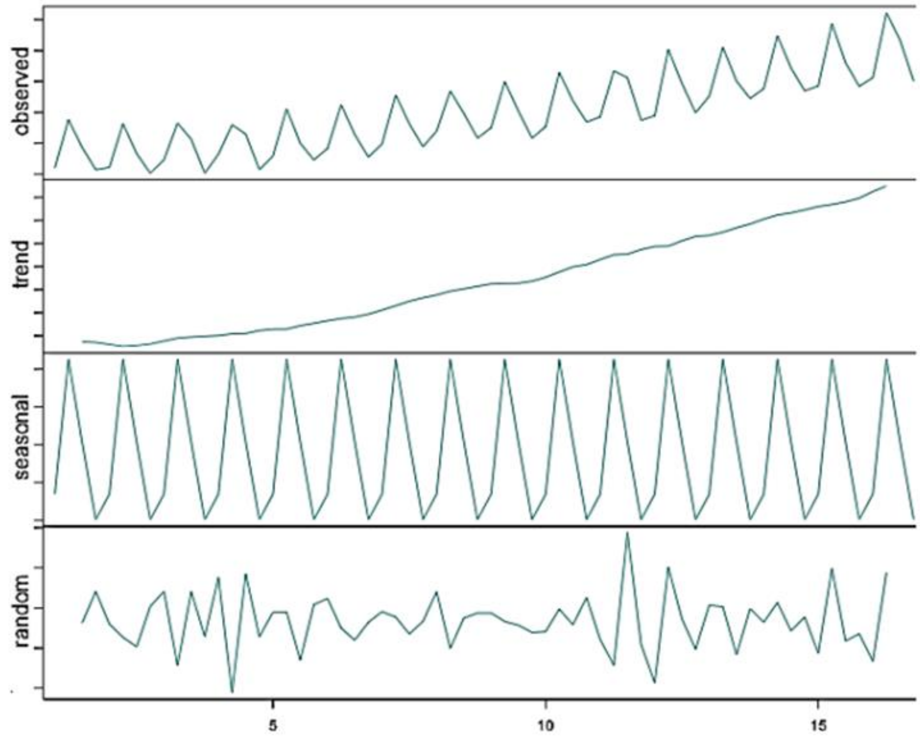

Figure 6.4: Example of decomposition of additive time series (from Garcia Navarro et al., 2024).

6.3. Cluster analysis

Cluster analysis is an unsupervised machine learning technique that groups a set of objects in such a way that the members of each group (i.e., clusters) are more similar to each other than to those in other groups based on some common property or attribute. Among the clustering methods available, the K-means method from partitional clustering is used. Partitional clustering is an unnested method that divides the objects in non-overlapping clusters (Tan et al., 2018).

6.3.1. K-means clustering

The K-means clustering method aims to divide the number of objects in a data set into a user-defined number of clusters such that each data point is assigned to a cluster with the nearest cluster mean (cluster centroid) that serves as the prototype of the cluster. The algorithm works in the following manner:

1. Initialization: user-selection of the number of desired clusters *k* and random or user-defined initialization of *k* points as centroids

2. Assignment: assignment of each data point to the nearest centroid based on a minimization technique, in this case the Euclidean distance metric is adopted, during a first iteration
3. Update: recalculation of the centroids as the mean of all data points assigned to each cluster
4. Iteration: the process is repeated until convergence where the centroids' change between two successive iterations is lower than a threshold value

The implemented algorithm work is that of Morissette & Chartier (2013) that uses Eq. 6.3 (based on Hartigan & Wong (1979)) to optimize the squared error function and enable the selection of the most effective cluster configuration.

$$SSE2 = \frac{N_i \sum_j \| x_{ij} - c_i \|^2}{N_i - 1} < SSE1 = \frac{N_1 \sum_j \| x_{1j} - c_1 \|^2}{N_1 - 1} \qquad (6.3)$$

where SSE is the sum of squared errors, N the number of points assigned to the cluster i, x_{ij} the j point of cluster i and c_i the centroid of the cluster (its mean).

Chapter 7

Case study

The scope of this chapter is the analysis of the superposition of anthropogenic effects in terms of induced ground movements due to groundwater withdrawal and storage activity, both present in the case study selected. To this end, a 3D static, dynamic and mechanical model of the shallow aquifer was set up, characterized and calibrated (workflow in Figure 6.1). The results of the numerical approach were then compared with the analysis of ground movements induced by the UGS activities obtained by a previous study (Benetatos et al., 2020) also developed via 3D numerical simulation approach.

The next chapter 8 is dedicated to the investigation of a broader area around Bologna city in order to also include the ground movements due to natural causes.

7.1. Underground Gas Storage case study: introduction and phenomena description

The case study focuses on a UGS in the Metropolitan City of Bologna in Emilia-Romagna and is situated in the eastern Po Plain in northern Italy. As mentioned previously in Chapter 4, the history of hydrocarbon and groundwater exploration in the Po Plain began and rapidly boomed in the second half of the 20th century after World War II. This is the case for the Metropolitan City of Bologna, which experienced a substantial demographic expansion (Figure 7.1) and a huge industrial development after the 1950s. In particular, a number of gas fields underwent production (fields #5-12-16-17-18-19 in Figure 4.11 and Table 4.2 in Chapter 4) and many of them were converted into a UGS, as the investigated case study. As for groundwater, intensive exploitation was especially concentrated in Bologna city due to its location at the foot of the Apennines between two rivers: Reno and Savena (Figure 7.2). In the investigated area, the UGS activities (started in 1975) have been superimposed with a number of industrial water wells (Figure 7.2)

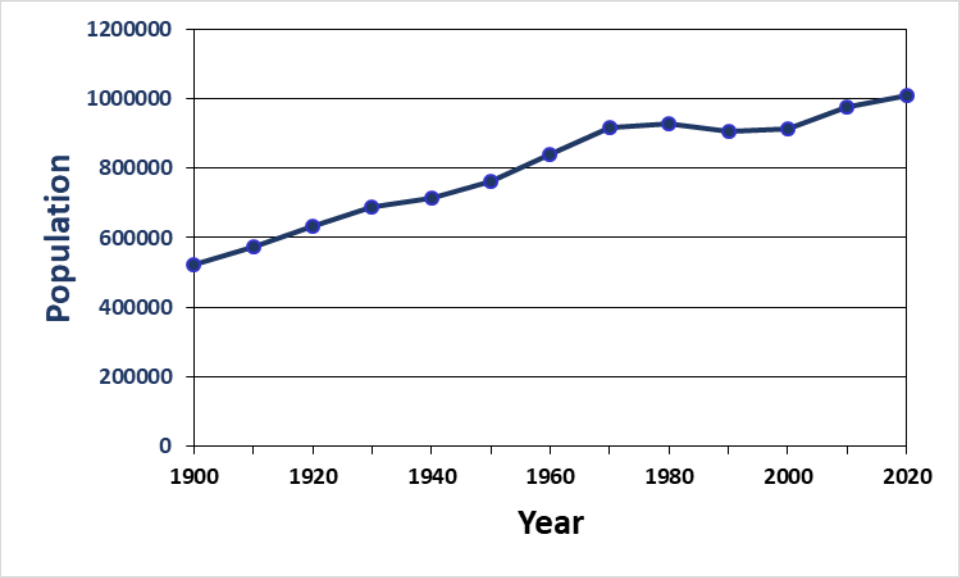

Figure 7.1: Population growth in the Metropolitan City of Bologna (statistical data collected from https://www.tuttitalia.it/emilia-romagna/provincia-di-bologna/statistiche/censimenti-popolazione/).

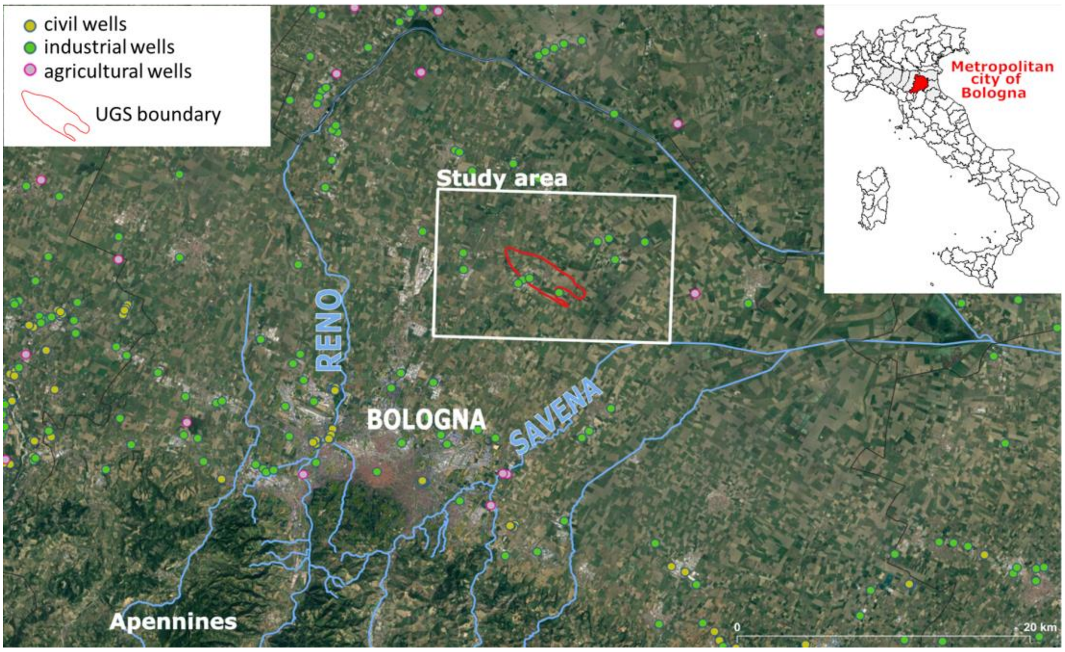

Figure 7.2: Plain view of the study area.

7.1.1. UGS in study area: previous studies

Land movements induced by the UGS field have been subject to analysis by previous studies, among which the following can be sited:

- Multidisciplinary Analysis of Ground Movements: An Underground Gas Storage Case Study (Benetatos et al., 2020).

Those were used as basis for the understanding and description of the field, its activities and the subsidence phenomenon.

7.1.1.1. Gas field description

The gas field is located approximately 20 km NE of Bologna city (Figure 7.2) and started primary production in 1956. It consists of 7 pools, one of which was converted to storage activity in 1975 (Pool C). It lies at an average depth of 1300 m ssl with an initial pressure of the reservoir equal to 150.4 bar at a datum depth of 1334 m ssl. 51 active storage wells are used for storage operations and pressure monitoring.

The field is located within the Romagna fold system of the Apennines Ferrara-Romagna arc in the eastern Po Plain (Figure 7.3A). The geodynamic setting of the regional area was delineated in Chapter 3 section 3.1.1. The reservoir area is characterized by thick successions of Messinian, Pliocene and Pleistocene turbidite deposits (Figure 7.3B; Ghielmi et al., 2013). The eastern Po Plain underwent strong tectonic activity mostly during the Late Pliocene-Pleistocene that led to the deformation, uplift and tilting of the area hosting the reservoir and of the current area of Bologna. This deformation began in the Lower Pliocene with the deposition of syntectonic turbidite sediments in the foredeep, forming the Porto Corsini and Porta Garibaldi formations (Table 7.1). Subsequently, another tectonic event took place during the Upper Pliocene-Lower Pleistocene that led to the complete development of the outer fold and thrust system of Ferrara.

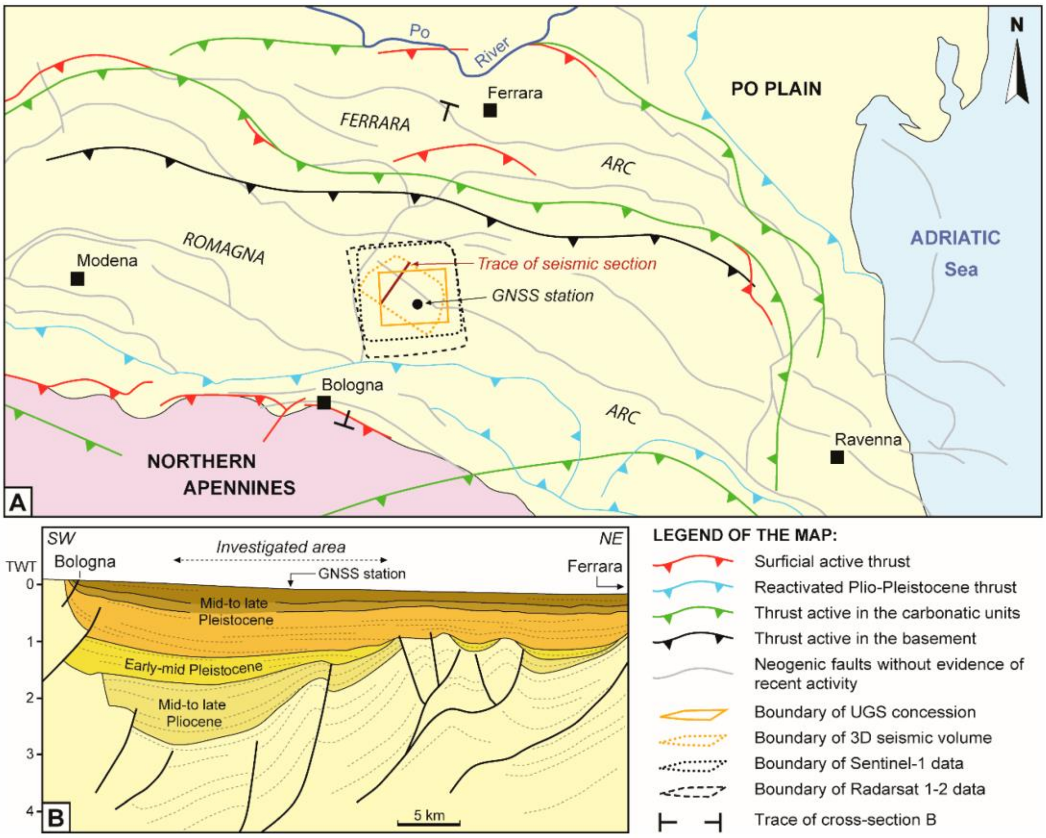

Figure 7.3: (A) Structural map of the eastern Po Plain with the location of the UGS; (B) Schematic seismic section showing the subsurface architecture under the area of study (from Benetatos et al., 2020).

The reservoir consists of a mixed trap (stratigraphic-structural) in which the stratigraphic elements (sandy levels with local pinching-out features) are combined with tectonic structures (asymmetric anticline and NE-verging marginal faults).

Table 7.1 delineates the elements of the system in their hosting formations; the reservoir belonging to the Porto Garibaldi Fm. (Pool C) and made up of alternating sand-clay layers of up to 10 m of average thickness and the caprock belonging to the Upper Santerno Fm. made up of clay and silty-clay and covering the entire area with an average thickness of 130 m guaranteeing the seal of the trap.

Table 7.1: Stratigraphic column of the principal levels of the gas field (from ISTITUTO NAZIONALE DI GEOFISICA E VULCANOLOGIA, 2019).

ETA'	FORMAZIONE	Spessori (m)	LIVELLO e mineralizzazione		POOL
Quaternario	Alluvioni recenti e attuali	200			
Pleistocene	Sabbie d'Asti	800			
Pliocene medio - superiore	Argille del Santerno (sup.)	200		gas	PLQ1,A1,A2,B
	Fm. Porto Garibaldi	300	C1	gas	POOL C
			C2		
			C3		
			C3-1		
			C3-2	acqua	
			C3-3	gas	POOL D, E
			C3-4		
			C3-5		
Pliocene inferiore	Argille del Santerno (inf.)	100		gas	POOL F
	Fm. Porto Corsini	>150		*unconformity*	
Messiniano	Fm. Fusignano				

7.1.1.2. Ground movements induced by the UGS

Benetatos et al. (2020) performed the analysis of ground movements related to the UGS using a multi-physics approach. InSAR and GNSS data and technologies were used to provide quantitative measurements of vertical and horizontal components of the surface movements as well as their areal extension above the field for a period of almost two decades. Subsequently, a geological, fluid-flow and geomechanical numerical modeling approach was developed in order to reproduce the behavior of the formations due to storage activities. Figure 7.4 compares the measured (derived from Radarsat-1/2 data) and simulated (derived from mechanical modeling) vertical displacement values for 3 points located inside the boundary of the UGS field within a withdrawal/injection cycle. It is important to note that the 3 points were used for a focused comparison between the two methods and showcasing how InSAR data can be used for calibrating simulation data. For point P2, a descending trend identified through InSAR analysis, unrelated to UGS operations, was superimposed onto the simulation results. Figure 7.5 shows the comparison between the measured and simulated vertical displacement maps generated for a withdrawal period within UGS boundary.

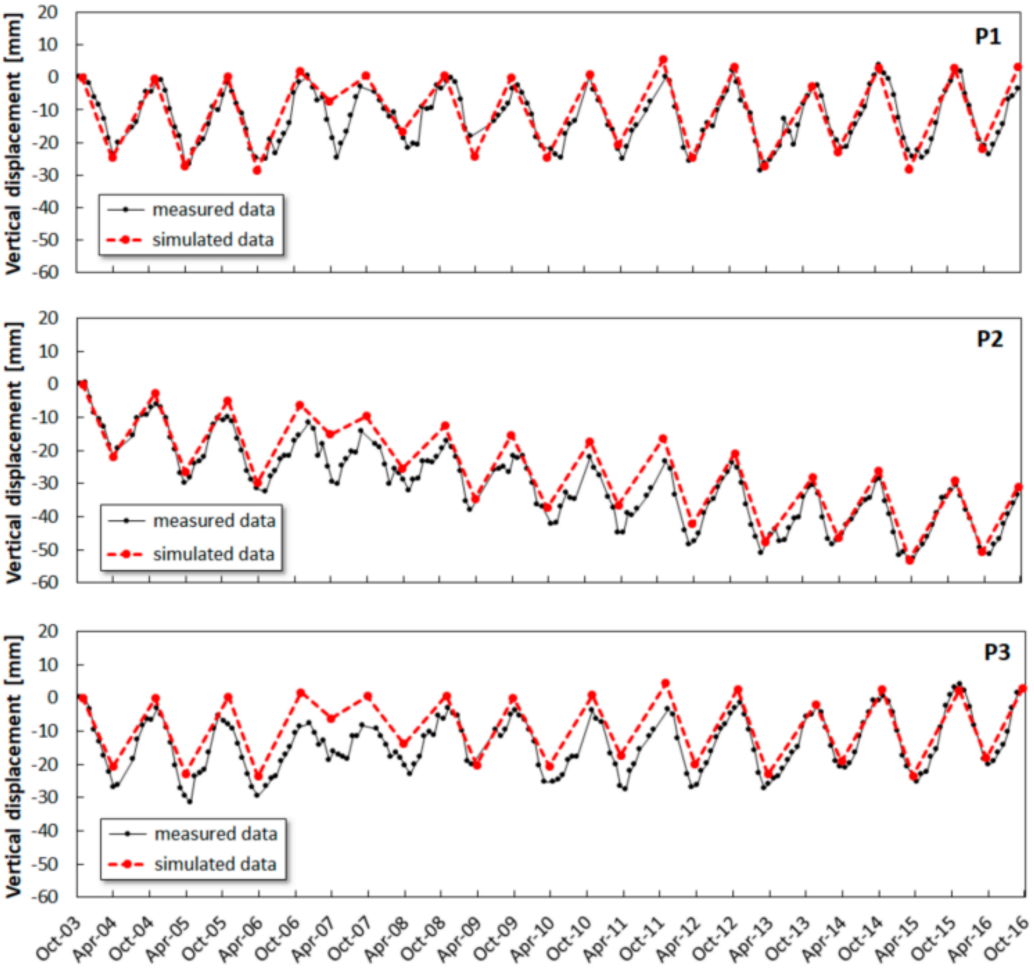

Figure 7.4: Measured versus simulated vertical displacement values for 3 points inside UGS boundary (from Benetatos et al., 2020).

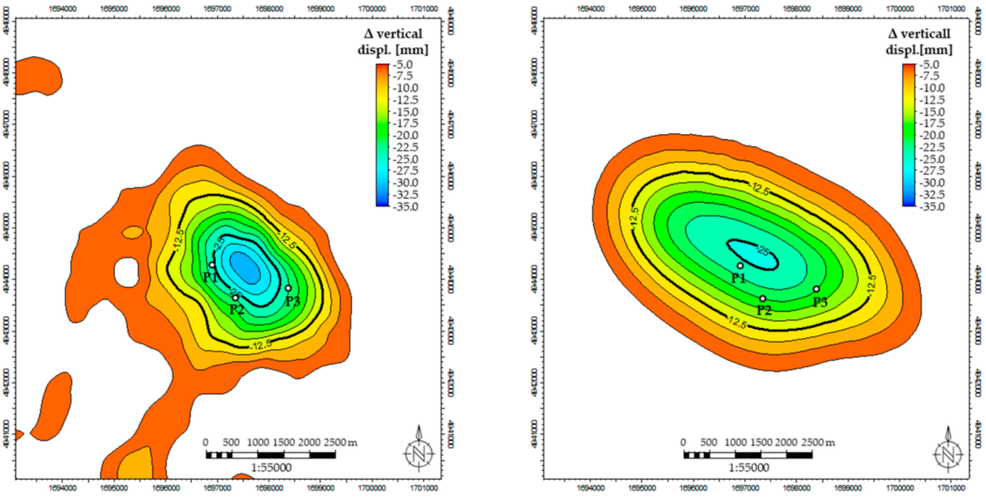

(a) (b)

Figure 7.5: (a) Measured versus (b) simulated subsidence maps for a historical withdrawal period. P1, P2, P3 refer to the same points in Fig. 6.4 inside UGS boundary (from Benetatos et al., 2020).

The main results from Benetatos et al. (2020) were the following:

- InSAR and GNSS results show a general long-term and gentle subsidence trend in the field area not related to storage activities, ranging between -1 and -2 mm/yr (refer to Benetatos et al., 2020 for the vertical velocity map of the monitored area)
- InSAR data suggests no correlation between UGS activities and the mean vertical and horizontal displacement velocities of the area but a strong correlation exists between the curve of the cumulative gas storage volumes and the historical series of ground displacement above the reservoir. GNSS data suggests no correlation between the short-term, seasonal vertical displacements and UGS activities but a strong one with the horizontal displacements
- Both datasets show the decrease of the short-term, cyclical, UGS-related vertical displacement from the center of the field area towards the boundary
- Geomechanical models can be used as an effective tool for forecasting future scenarios of storage activities

7.1.2. Groundwater production

Total groundwater withdrawals of the Metropolitan City of Bologna for the time periods 2003, 2009-2011 and 2015-2018 were provided by ARPAE from three monitoring projects respectively: “Piano di Tutela delle Acque (PTA) del 2005”, “Piano di Gestione (PDG) 2015” and “Progetto di Piano di Gestione (PDG) 2021”. Total production rates decrease from 97.8 x 10^6 m^3/year in 2003 to 73.9 x 10^6 m^3/year in 2009-2011 and then increase to 80.7 x 10^6 m^3/year in 2015-2018. Figure 7.6 displays the frequencies of the water production rates in 10^6 m^3/year for the three time periods for the Metropolitan City of Bologna.

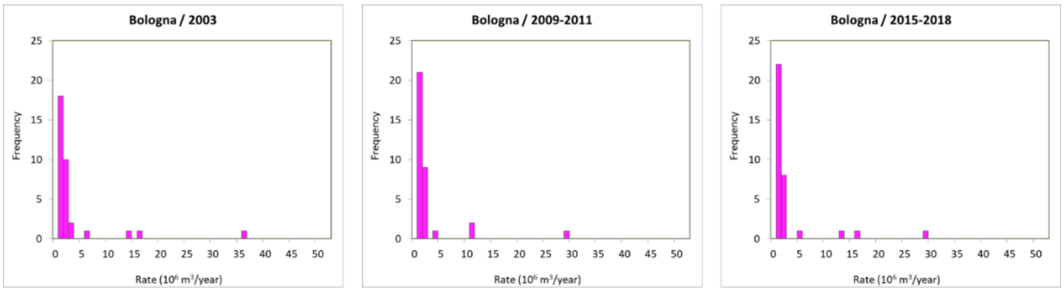

Figure 7.6: Frequency of water production rates for the Metropolitan City of Bologna for the time periods 2003, 2009-2011 and 2015-2018 (from Eid et al., 2022).

The three punctual water production rates greater than 10 x 10^6 m^3/year observed in the three time periods belong to the municipalities (comuni) of Bologna, Calderara di Reno and Imola with Bologna having the largest values of 36.5 x 10^6 m^3/year, 28.3 x 10^6 m^3/year and 29 x 10^6 m^3/year respective of the three investigates periods and aligned with the overall trend of groundwater production in the Metropolitan City of Bologna.

In our case study, 10 water wells are present; all of which are for industrial use (Figure 7.7). Table 7.2 presents the water wells data provided by ARPAE. It is important to note that the average production rates provided per year per well represent accurate measurements but only for the time frame of 2016-2018. The rates discussed earlier on a province level and the maps exhibited in Chapter 4 section 4.3.3 represent total rates acquired from accurate measurements and estimated ones and are only accurate at the scale of the provinces.

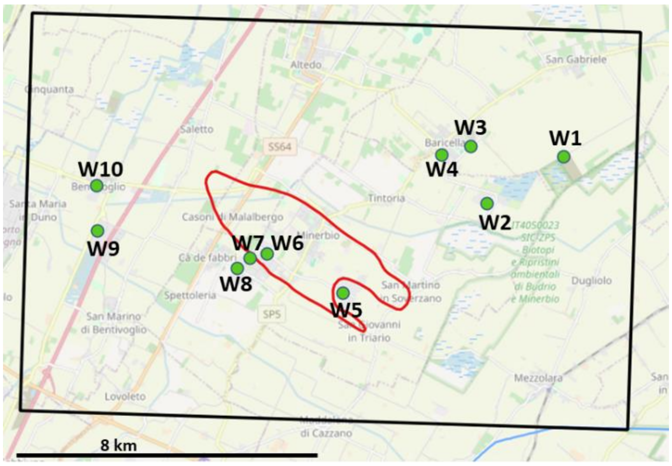

Figure 7.7: Water production wells in the area of study with the outline of the UGS boundary in red.

Table 7.2: Data of water production wells in the area of study (provided by ARPAE).

Well Name	X_ETRS89	Y_ETRS89	Use	Average production rate (Mm3/yr)	Time period
Well 1	704041.8	4946502.1	industriale	0	2016-2018
Well 2	702053.3	4945180.2	industriale	0.3794	2016-2018
Well 3	701580.6	4946691.84	industriale	0.012	2016-2018
Well 4	700812	4946442.22	industriale	0.0156	2016-2018
Well 5	698306.7	4942704.2	industriale	0.0009	2016-2018
Well 6	696253.4	4943673.2	industriale	0.001	2016-2018
Well 7	695794.7	4943545.7	industriale	0.0009	2016-2018
Well 8	695479.7	4943276.3	industriale	0.0446	2016-2018
Well 9	691739.4	4944156.2	industriale	0.003	2016-2018
Well 10	691678.3	4945347.3	industriale	0.03	2016-2018

7.2. Hydrogeological setting

The aquifer system in the study area is made up of two groundwater bodies (refer to Figure 3.10 in Chapter 3): upper confined aquifers (A1-A2) of the Apennine alluvial plain and lower confined aquifers (A3-A4-B-C) of the Apennine and Po alluvial plains.

Regione Emilia-Romagna and Eni-AGIP (1998) compiled two maps for each of the three aquifer groups A, B and C (six maps in total); one for the depth of the bottom of each aquifer and one for the thickness of the porous-permeable sediments. Figure 7.8 and Figure 7.9 show the latter respectively for aquifer group A.

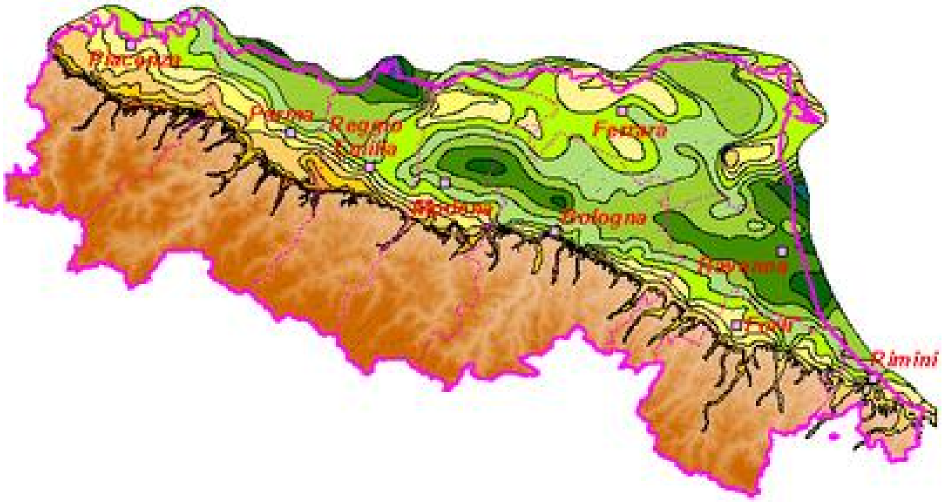

Figure 7.8: Trend of the bottom of aquifer A. Dark green represents areas with greater depths whereas lighter shades of green represent shallow depths (from Regione Emilia-Romagna and Eni-AGIP, 1998).

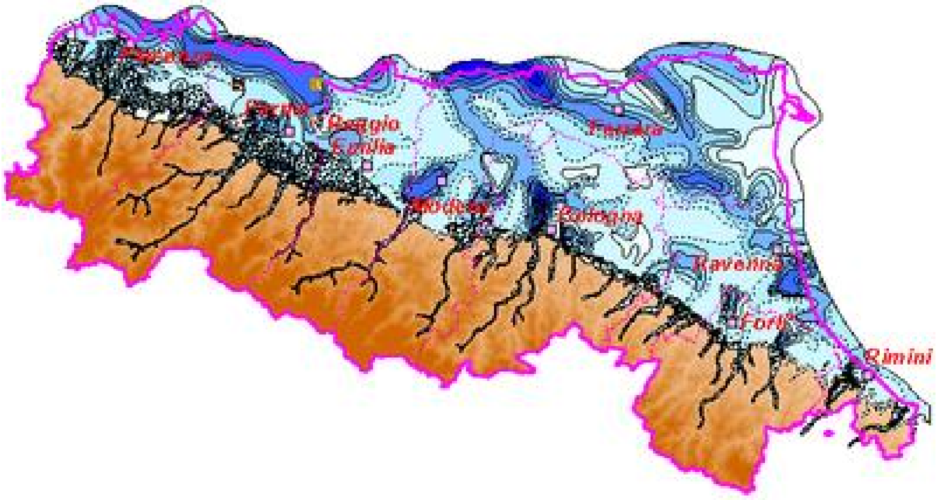

Figure 7.9: Cumulative thickness of the porous-permeable sediments of aquifer A. Dark blue represents areas richer with coarse deposits (from Regione Emilia-Romagna and Eni-AGIP, 1998).

Figure 7.10 shows the trend of the bottom of aquifer A in the Bologna plain. The study area is highlighted in pink and shows depths ranging from 150 to almost 300 m below sea level. The area is characterized by a syncline, whose axis is delineated in red in the figure, and extends from the W-NW to S-SE from Nonantola to the south of Ravenna. The most depressed areas are in the western sector where aquifer group A reaches depths of 300 m below sea level. The area south of the syncline is made up of a monocline that descends from the Apennines and has a greater slope in the area of Bologna, while it immerses more gently in the rest of the Romagna sector. The northern area of the syncline is identified by the structural highs of the Ferrara folds. The first core of these folds, which limits the above-mentioned syncline, is indicated in green in the figure. The trend of the syncline and anticline characterizes the deposition of the most recent sediments (Severi and Bonzi, 2011).

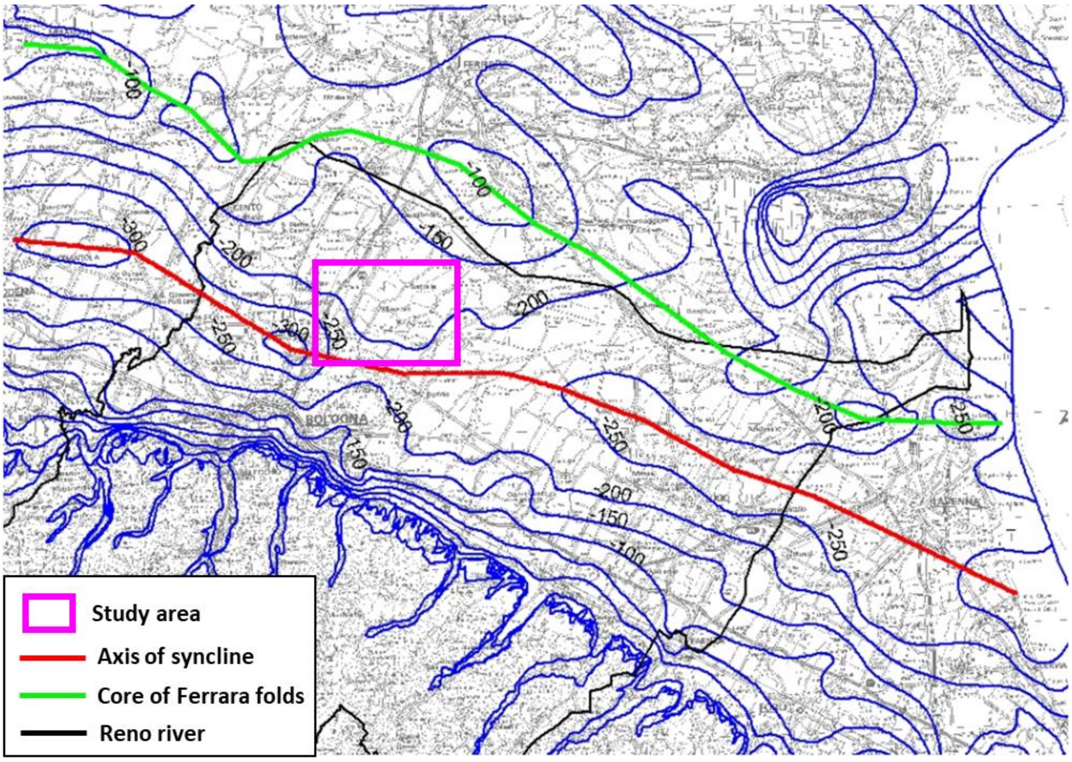

Figure 7.10: Trend of the bottom of aquifer A in the Bologna plain and the area of study (modified from Severi and Bonzi, 2011).

The trend of the bottom of aquifers B and C in the area of study were identified from the physical maps of Regione Emilia-Romagna and Eni-AGIP (1998). Respectively, their depths range from 200 to 400 m and around 300 to 600 m below seal level.

Regione Emilia-Romagna has published over 200 geological cross-sections at a regional and national level from various cartographic projects. Figure 7.11 shows the traces of the cross-sections available around the area of study highlighted in pink.

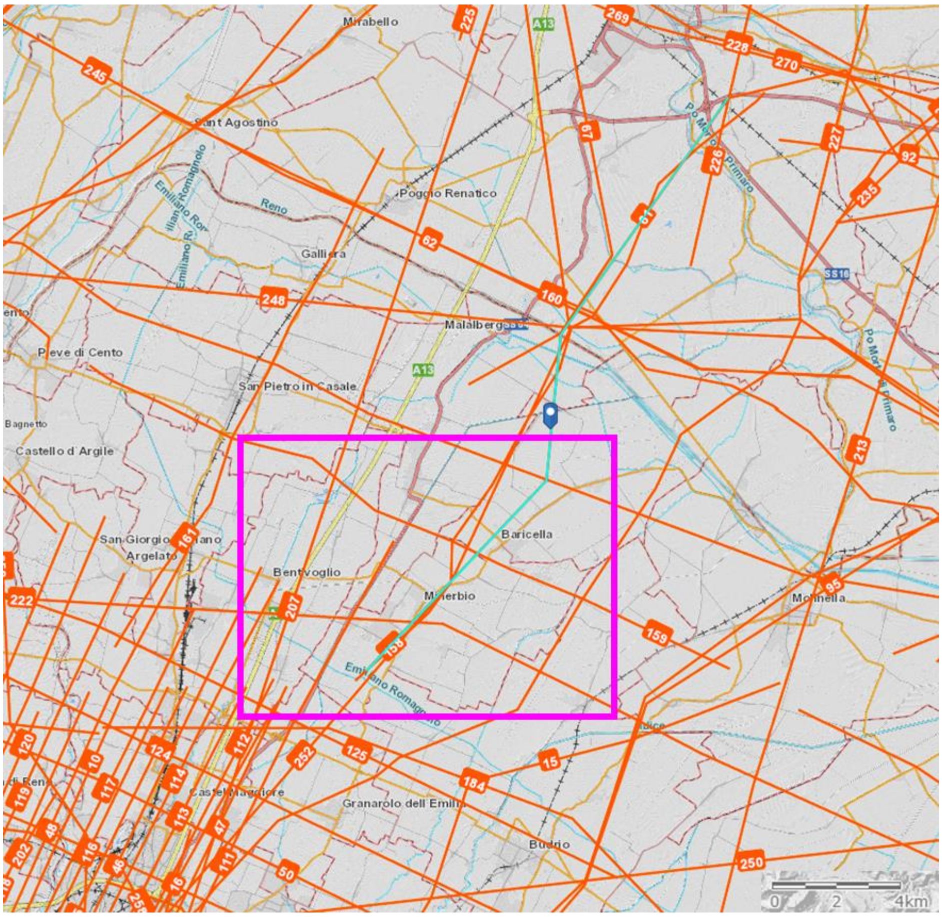

Figure 7.11: Traces of geological cross-sections around the area of study (from https://servizimoka.regione.emilia-romagna.it/mokaApp/apps/pozzi_sez/index.html).

The geological cross-section of the highlighted trace in blue is shown in Figure 7.12. The first half of the cross-section (until after Baricella) represents the area of study. Aquifer A reaches around 280 m below sea level in that area and is characterized by dispersed amalgamated bodies of fluvial sands of Apennines origin.

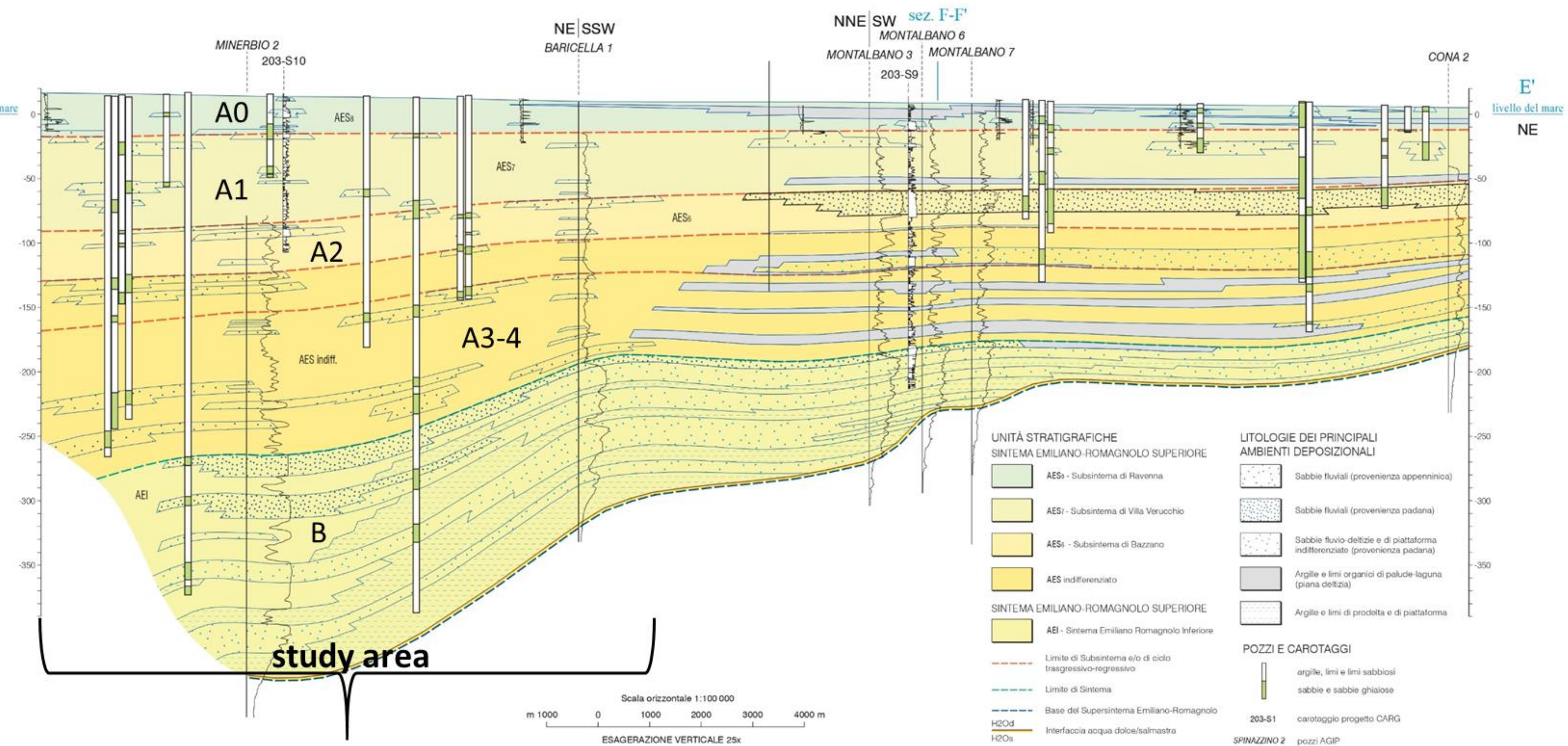

Figure 7.12: Geological cross-section of the trace highlighted in blue in Figure 7.11.

7.2.1. Petrophysical and hydrodynamic parameters

Numerous pumping tests were performed in the Emilia-Romagna region over the period 1978 to 2002 using existing wells as part of a project to create a database for the hydrodynamic parametrization of the aquifers (Figure 7.13; Regione Emilia-Romagna, 2003). These included the parametrization done by RER and ENI-AGIP (1998) summarized in Chapter 3 section 3.2.3. The parameters include transmissivity, permeability/hydraulic conductivity and storage coefficient and were analyzed using the traditional Theis-Jacob method. Table 7.3 displays the corresponding information to the tests performed in the Metropolitan City of Bologna. The number of wells in the Metropolitan City of Bologna is 14 but more than 14 values for transmissivity were recorded as several may have been made on a single measurement point at different times or by different operators.

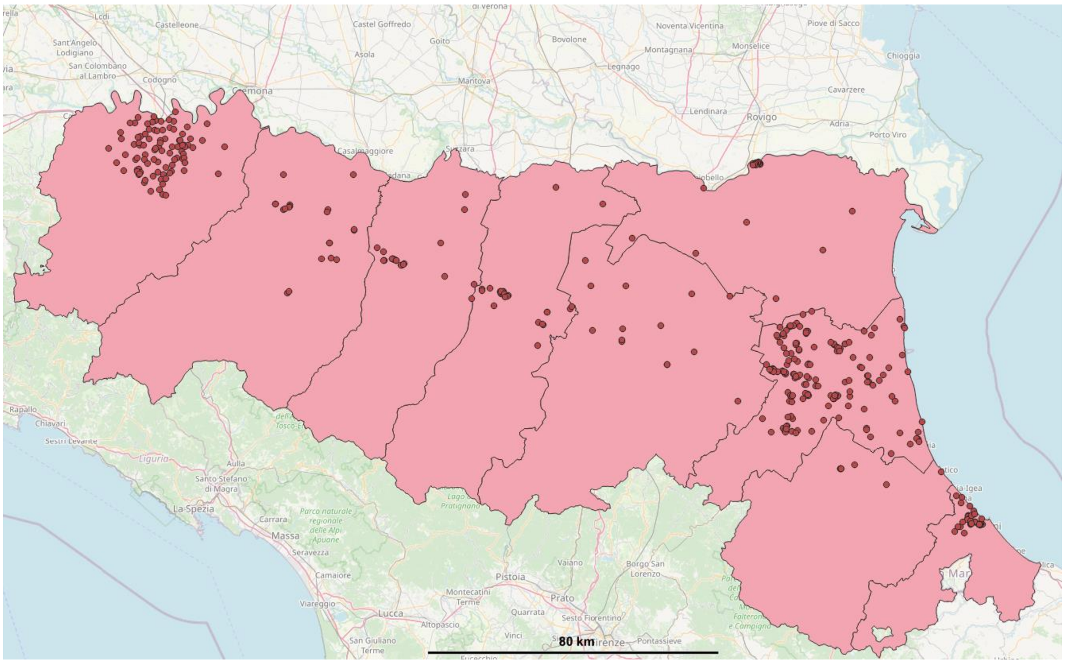

Figure 7.13: Wells used for pumping tests for the hydrodynamic parametrization of Emilia-Romagna aquifers.

Table 7.3: Hydrodynamic parameters tested from wells in Metropolitan City of Bologna (from Regione Emilia-Romagna, 2003).

Well code	Execution date	Transmissivity (T, m2/s)	Permeability (K, m/s)	Storage coefficient (S, ad)
T-BO-01	4-5/4/77	1.13E-02	7.29E-04	2.62E-04
T-BO-02	26-31/3/77	7.72E-03	8.14E-05	7.01E-04
T-BO-03	05/05/1994	4.30E-02	4.30E-04	
T-BO-04	26-28/1/98	2.90E-02		4.57E-03
T-BO-04	26-28/1/98	6.59E-02		2.75E-03

T-BO-04	18-19/10/95		1.36E-04	
T-BO-04	18-19/10/95		4.75E-05	
T-BO-04	27/11/1995		6.00E-04	
T-BO-04	06/02/1996		3.75E-04	
T-BO-04	13/05/1996		2.98E-04	
T-BO-04	30/05/1996		1.35E-04	
T-BO-04	21/06/1996		3.88E-05	
T-BO-05	28-30/5/97	3.20E-02		9.23E-04
T-BO-05	28-30/5/97	3.69E-02		1.27E-03
T-BO-05	23/05/1995		1.58E-03	
T-BO-05	23/05/1995		1.95E-04	
T-BO-05	15/06/1995		8.05E-05	
T-BO-05	15/06/1995		4.55E-04	
T-BO-05	20/10/1995		1.20E-04	
T-BO-05	01/12/1995		2.04E-04	
T-BO-05	01/12/1995		2.16E-03	
T-BO-05	21/03/1996		2.46E-04	
T-BO-06	6-7/4/77	1.35E-02	1.06E-04	1.31E-03
T-BO-07	28-29/3/77	2.18E-04	1.36E-05	3.21E-03
T-BO-08	27-28/1/77	1.54E-02	1.28E-03	1.97E-04
T-BO-09	27-28/3/77	1.80E-03	1.13E-04	2.20E-04
T-BO-10	7-8/7/77	2.49E-03	4.94E-05	2.74E-04
T-BO-11	1-2/4/77	1.90E-03	4.75E-05	4.78E-04
T-BO-12	5-6/4/77	3.19E-03	1.75E-05	1.30E-03
T-BO-13	24-26/3/77	5.71E-03	1.41E-04	4.57E-04
T-BO-14	9-12/5/78	6.50E-03		
T-BO-14	9-12/5/78	7.95E-03		5.08E-04

The permeability/hydraulic conductivity of clayey units is much harder to measure and ranges of values were collected from literature between 10^{-9} and 10^{-11} m/s (Gambolati et al., 1991; Teatini et al., 2006). In aquitards, isotropy is assumed ($k_h = k_v$).

Effective porosity values were collected from literature according to their different lithologies and depositional environments (ARPAE and Regione Emilia-Romagna, 2007). Table 7.4 summarizes the following for the upper aquifer A1.

Table 7.4: Porosity values of aquifer A1 for the different lithologies and depositional environments.

Name	Effective Porosity
Alluvial fan clay	0.095

Apennine clay	0.01
Plain clay	0.01
Alluvial fan gravel	0.305
Apennine gravel	0.265
Alluvial fan medium sand	0.31
Apennine medium sand	0.3
Plain medium sand	0.32
Alluvial fan fine sand	0.2
Apennine fine sand	0.21
Plain fine sand	0.205

Figure 7.14 represents the behavior of medium porosity versus depth and effective stress derived by Gambolati and Teatini (1998) and Baù et al. (1999) for the subsurface system of the Po river plain.

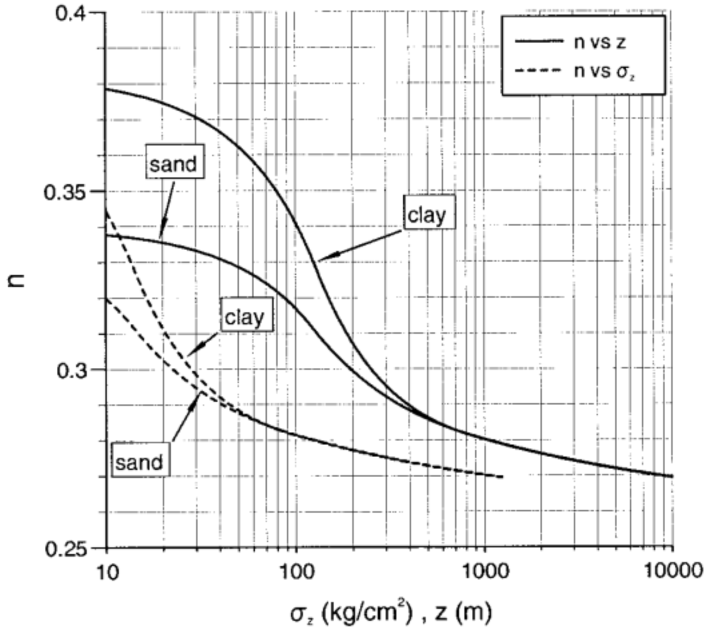

Figure 7.14: Medium porosity $\boldsymbol{n}$ versus depth $\boldsymbol{z}$ and effective stress $\boldsymbol{\sigma_z}$ (from Gambolati et al., 2000).

The uniaxial vertical compressibility is the main parameter controlling formation compaction due to fluid pore variation and subsequent ground movements. It is defined as:

$$c_M = \frac{1}{1+e}\frac{de}{d\sigma_z} \qquad (7.1)$$

where c_M is the compressibility, e the void ratio and σ_z the effective intergranular vertical stress (refer to Chapter 5 section 5.2). Gambolati et al. (1991), Gambolati and Teatini (1998) and Baù et al. (1999) developed representative basin-scale constitutive equations for c_M versus depth z and effective stress σ_z (Figure 7.15) using data obtained from oedometer tests in the area of Ravenna and from other deep wells in the Po Plain.

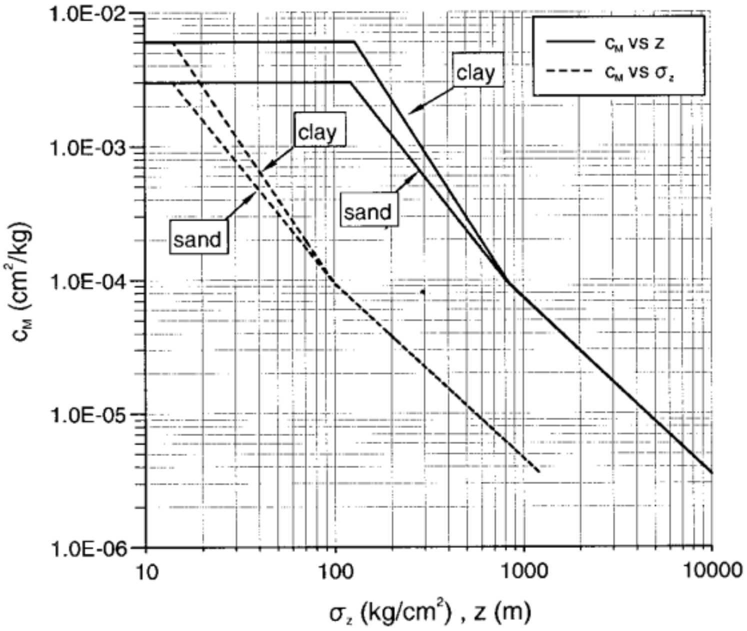

Figure 7.15: Uniaxial vertical compressibility $\boldsymbol{c_M}$ versus depth $\boldsymbol{z}$ and effective stress $\boldsymbol{\sigma_z}$ for clay and sand in the Po Plain (from Gambolati et al., 2000).

Aquitard compressibility is higher than aquifer compressibility for depths less than 1000 m and both decrease with depth. The following constitutive relationships of c_M vs z were derived from Figure 7.15 for depths less than or equal to 1000 m:

For clay: $c_M = 1.53\ z^{-1.175}$ (7.2)

For sand: $c_M = 0.43\ z^{-1.013}$ (7.3)

It should be noted that laboratory tests tend to overestimate the actual c_M due to the tampering of the samples during transportation and handling and can yield values up to 5 to 10 times larger than the actual values.

These relationships hold true for rock compression in inelastic conditions (virgin loading). For shallow formations, a ratio r equal to 10 is assumed between inelastic and elastic (unloading-reloading) conditions (Carbognin et al., 1977; Ferronato et al., 2003).

7.3. Geological modelling

The workflow used to build the 3D geological model in the study area is represented in Figure 7.16. The Petrel E&P (Exploration & Production) software platform by

Schlumberger was used for the modelling, developing fully 3D perspectives from classic 2D views.

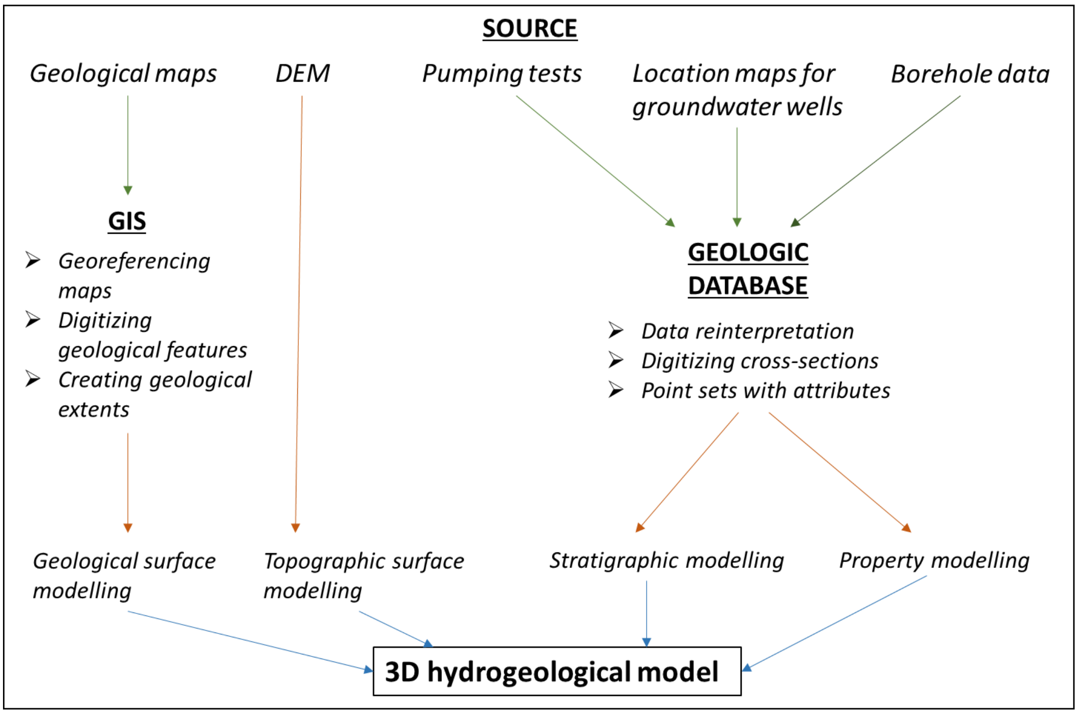

Figure 7.16: Workflow used to build the 3D geological model in the study area.

The source data regarding the geological maps and the digital elevation model (DEM) of the entire area of the Po Plain were provided by Livani et al. (2023) and imported into Petrel. The surface modelling of the study area, specifically the alluvium section, was then reinterpreted on the basis of the imported maps together with collected local data and surface maps. The geologic database used for the stratigraphic and property modelling is introduced in the following section.

7.3.1. Geologic database

The lithological reconstruction of the Pliocene-Quaternary hosting the aquifers of the Po Basin fill was carried through the available data on the Regione Emilia-Romagna (RER) database (Figure 7.17) that includes continuously cored boreholes and water wells log descriptions and the two-dimensional cross sections also carried out by RER discussed above in section 6.2 (Figure 7.11).

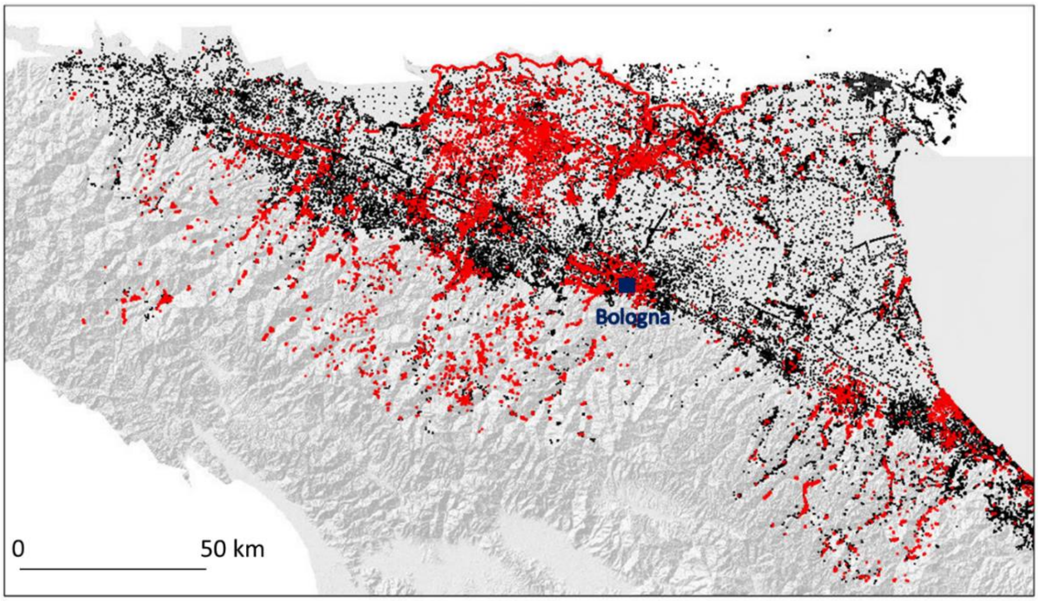

Figure 7.17: RER Geological Survey database. Red points correspond to geotechnical and geophysical analysis (that include continuous core descriptions) and black points correspond to geognostic tests (that include the water wells).

For the last 30 years, the National Geological CARtography project (CARG project) of Regione Emilia-Romagna led to the collection of thousands of geological data through massive drilling campaigns. The database (Figure 7.17) used and analyzed in this study is composed of different types of stratigraphic data with varying vertical resolution, range of depths and quality of description.

- *Continuously cored boreholes:*

  These wells range in depths from 20 to 200 m. They include distinct types of data based on their corresponding surveys: (i) stratigraphic descriptions carried out for the CARG project, which include extensive stratigraphic information from lithology, color, contacts to depositional environment (Figure 7.18a), (ii) stratigraphic descriptions collected from hydrogeological and geotechnical surveys which are less extensive in information (Figure 7.18b).

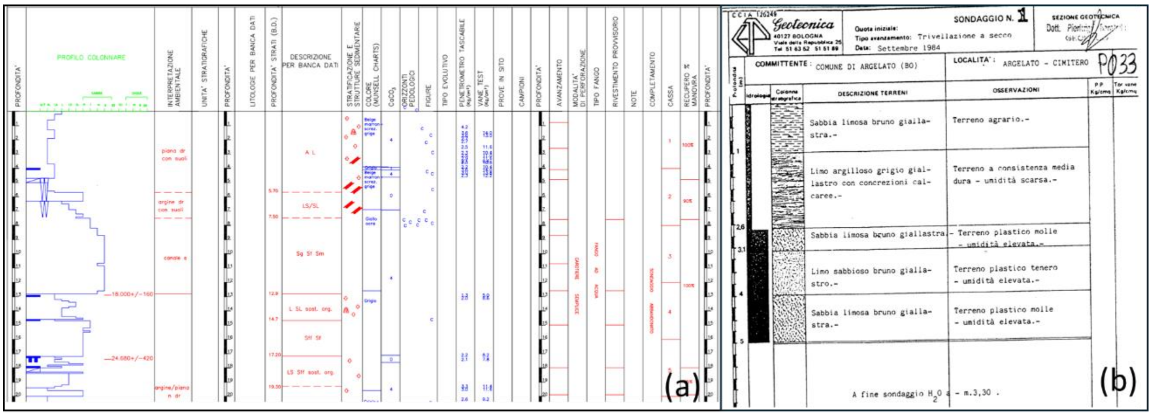

CCIA 126249
Geotecnica
40127 BOLOGNA
Viale della Repubblica 25
Tel 51 63 52 51 61 89

SONDAGGIO N. 1
Quota iniziale:
Tipo avanzamento: Trivellazione a secco
Data: Settembre 1984

SEZIONE GEOTECNICA
Dott.

COMMITTENTE: COMUNE DI ARGELATO (BO)
LOCALITA': ARGELATO - CIMITERO
P033

Profondità (m)	DESCRIZIONE TERRENI	OSSERVAZIONI
	Sabbia limosa bruno giallastra.-	Terreno agrario.-
1	Limo argilloso grigio giallastro con concrezioni calcaree.-	Terreno a consistenza media dura - umidità scarsa.-
2,6	Sabbia limosa bruno giallastra.	- Terreno plastico molle - umidità elevata.-
3,1	Limo sabbioso bruno giallastro.-	Terreno plastico tenero - umidità elevata.-
4	Sabbia limosa bruno giallastra.-	Terreno plastico molle - umidità elevata.-
5		

A fine sondaggio H_2O a - m.3,30 .

Figure 7.18: (a) Example of a stratigraphic core description from the CARG project, (b) Example of a stratigraphic core description from the RER database.

- *Water wells:*

  These wells were drilled for hydrogeological purposes. Their range of depths vary from 15 to 450 m and they have scarce vertical resolution where only thick sedimentary bodies are recorded with basic information on grain size or aquifer system information (Figure 7.19).

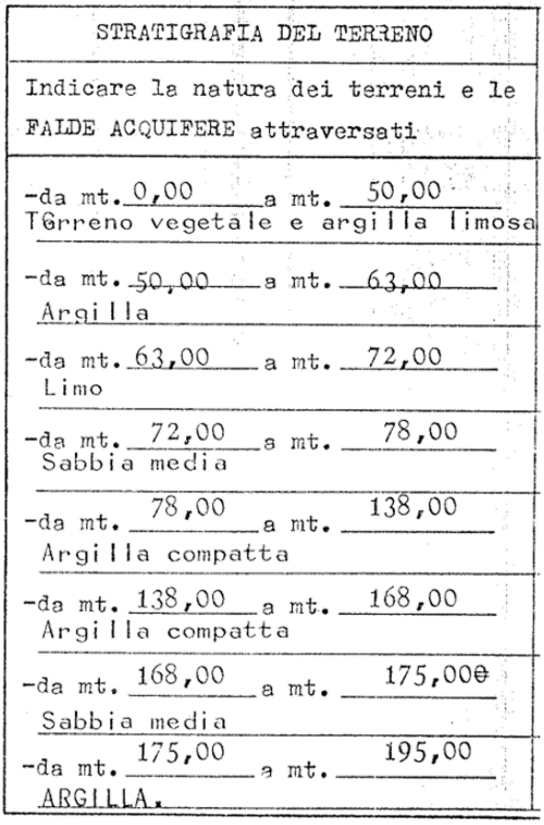

STRATIGRAFIA DEL TERRENO

Indicare la natura dei terreni e le
FALDE ACQUIFERE attraversati

-da mt. 0,00 a mt. 50,00
Terreno vegetale e argilla limosa

-da mt. 50,00 a mt. 63,00
Argilla

-da mt. 63,00 a mt. 72,00
Limo

-da mt. 72,00 a mt. 78,00
Sabbia media

-da mt. 78,00 a mt. 138,00
Argilla compatta

-da mt. 138,00 a mt. 168,00
Argilla compatta

-da mt. 168,00 a mt. 175,000
Sabbia media

-da mt. 175,00 a mt. 195,00
ARGILLA.

Figure 7.19: Example of stratigraphic description from a water well log from RER database.

7.3.2. Petrel data processing

7.3.2.1. Data preparation

The first stage of constructing a geological model involves data preparation. In our case study, the following surface and subsurface data were integrated into the Petrel software for the modelling:

- A total of 618 water wells and continuous-core boreholes were extracted from the RER database and imported into Petrel with the following information: XY location, Kelly Bushing (KB) height, total depth of well, date of execution and type of well. The highest data density is concentrated in the south of our area of study around railway lines and pumping well fields whereas the lower density is in the northern part (Figure 7.20). The stratigraphic description of each of the 618 wells was performed individually. As mentioned in the section above, the wells had differing qualities and investigation depths as well as highly varying time spans (from the early 1900s up until today). This created a complex dataset with different terminologies for the stratigraphic description. We ended up dividing the present lithologies into three classes: gravel, sand and clay/silt.

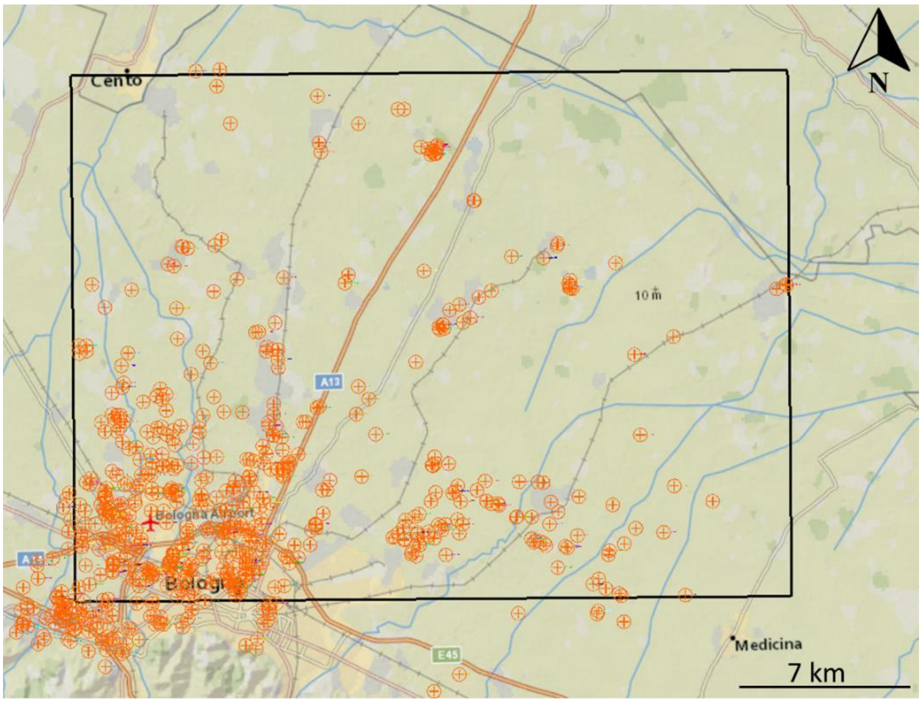

Figure 7.20: Location of water wells and boreholes extracted from RER database.

- Seventeen stratigraphic cross-sections were drawn to identify the main aquifer bodies. Three were in the NE-SW direction whereas 14 in the SSW-NNE direction, all of them covering only the SW portion of our study area

(Figure 7.21). The aquifer A complexes (A0-A4) and aquifer B were correlated based on their stratigraphic position (Figure 7.22); however, due to the lack of information in the remaining portion of our study area, no interpolation method was applied to the well tops for the characterization of the different aquifer bodies.

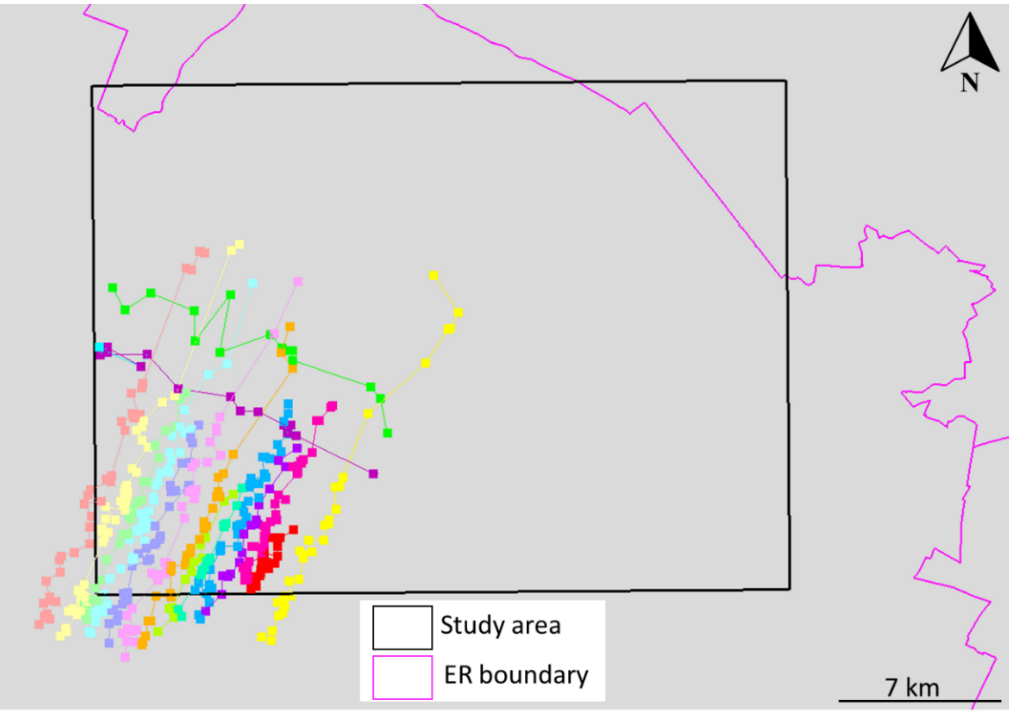

Figure 7.21: Location of stratigraphic cross-sections. Squares represent well and core data.

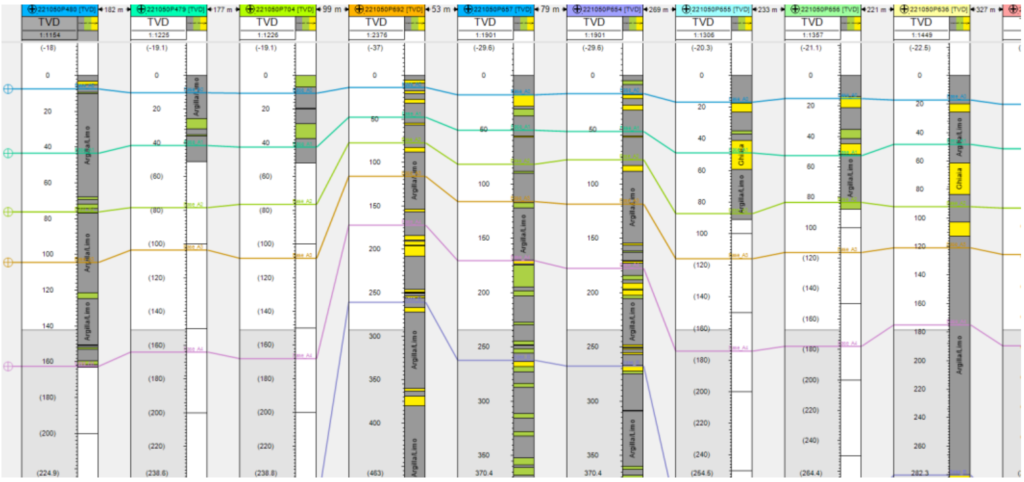

Figure 7.22: Example of well top correlation for aquifers A0-A4 and B from cross-section.

- Five surfaces, provided by Livani et al. (2023), were imported into the software: Topography, Base Alluvium, Base Pleistocene, Base Pliocene and

Top Carbonates. The topographic surface was derived from a public DEM of the entire Italian territory at an original resolution of 10m cell size and the rest of the surfaces from available deep-well composite logs, geological cross-sections and geological maps (refer to Livani et al. (2023) for the detailed description of boundary mapping). In our project, we divided the Base Alluvium surface into two surfaces corresponding to the base of aquifer A and the base of aquifer B by utilizing the contour maps provided by Regione Emilia-Romagna of the bases of these units up to where the units are saturated with freshwater (Figure 7.23).

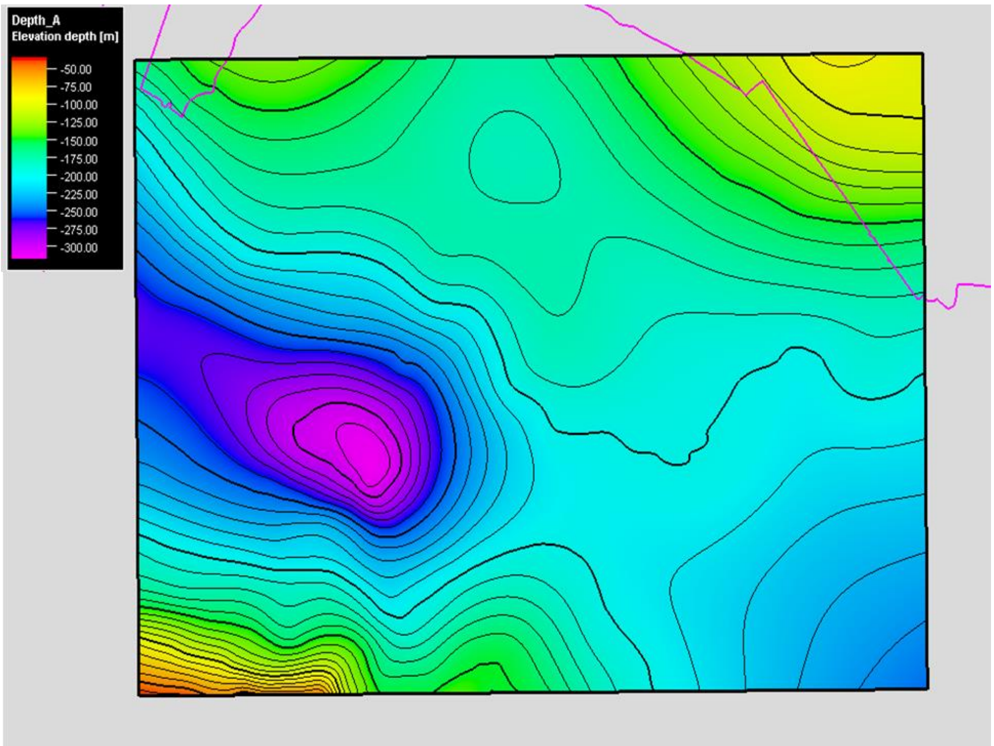

Figure 7.23: Contour map of base aquifer A.

7.3.2.2. Structural modelling

Structural modelling is the second stage of building a geological model and involves the simple gridding and vertical layering of the model. These operations were carried out consecutively in order to create a unified data model.

- 3D Grid Construction:

The 3D grid was created such that the top and base limits are the Topography and Top Carbonates surfaces respectively with the size specified by the selected boundary. A grid of 100x100 X and Y increments was used. This resulted in the generation of the main skeletons (top, mid and base) of the model (Figure 7.24).

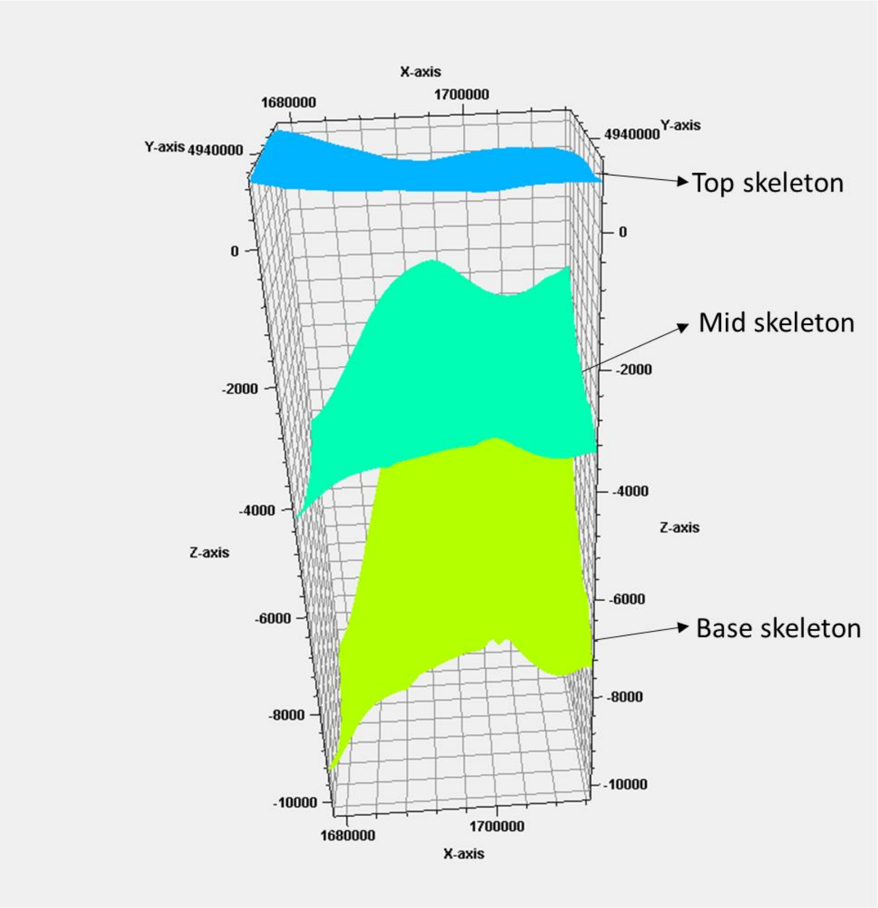

Figure 7.24: Skeletons of the 3D grid model.

- Make Horizons:

The imported and generated 2D surfaces (section 7.3.2.1) were inserted into the pillar grid considering the specified grid increment and their relative relationships to each other. The main horizons of the geological model were then produced (Figure 7.25). It should be noted that an additional surface was added that represents the mean sea level with a constant elevation depth of 0 for the sake of the simulations performed later on in the project.

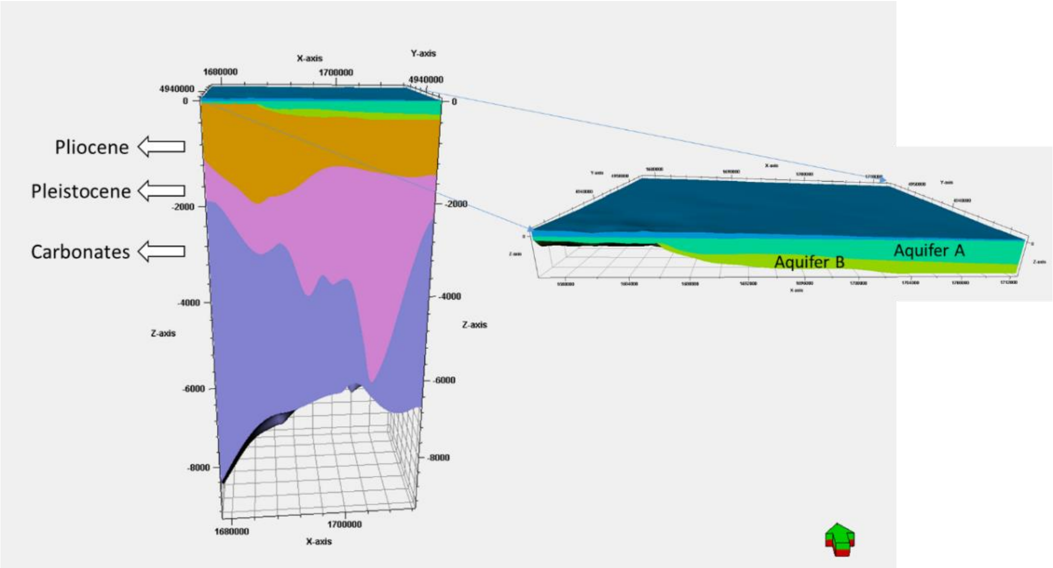

Figure 7.25: Zones of the model.

- Layering:

Only the layering of the zones constituting aquifers A and B was performed, determining the thickness and orientation of the aquifer zones in the 3D grid. Aquifer A was divided into 7 layers whereas aquifer B into 4, considering the thickness of the porous/permeable sediments from isopach maps provided by Regione Emilia-Romagna and accounting for the aquitards in between (Figure 7.26).

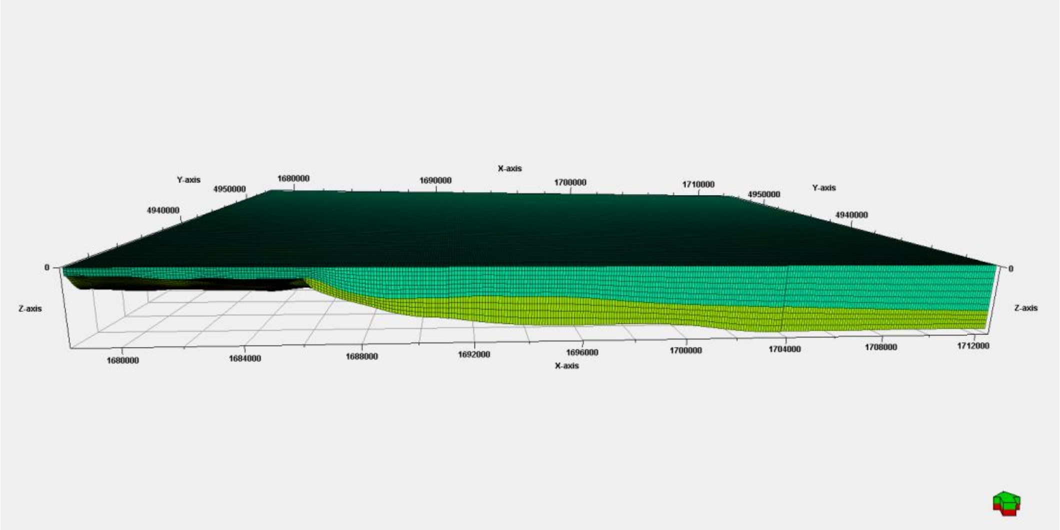

Figure 7.26: Layering of aquifers A and B.

7.3.2.3. Scale up well logs

This process averages values to the cells in the 3D grid that are penetrated by the wells such that each cell is assigned one value per upscaled log. This is because the dimensions of the grid cells are usually greater than the sample density of the well logs so the latter must be scaled up before inserting them into the grid. In this study, the average method "Most of" was used on the logs containing the lithological description of the wells. This method calculates the upscaled value of a cell by taking the average of the values in neighboring cells, excluding the minimum and maximum values. It aims to reduce the influence of extreme values in the neighboring cells, providing a more representative value for upscaling purposes.

After the scale up of the well logs, a quality check was performed by displaying the upscaled logs against the well logs. The correction of errors resulting from upscaling leading to an overestimate of the clay/silt lithologies was carried out by increasing the weight of the sand and gravel lithologies such that less of those lithologies are required for them to be assigned to upscaled cells (Figure 7.27). The weights of the sand, gravel and clay/silt are respectively: 2.50, 1.50 and 1.

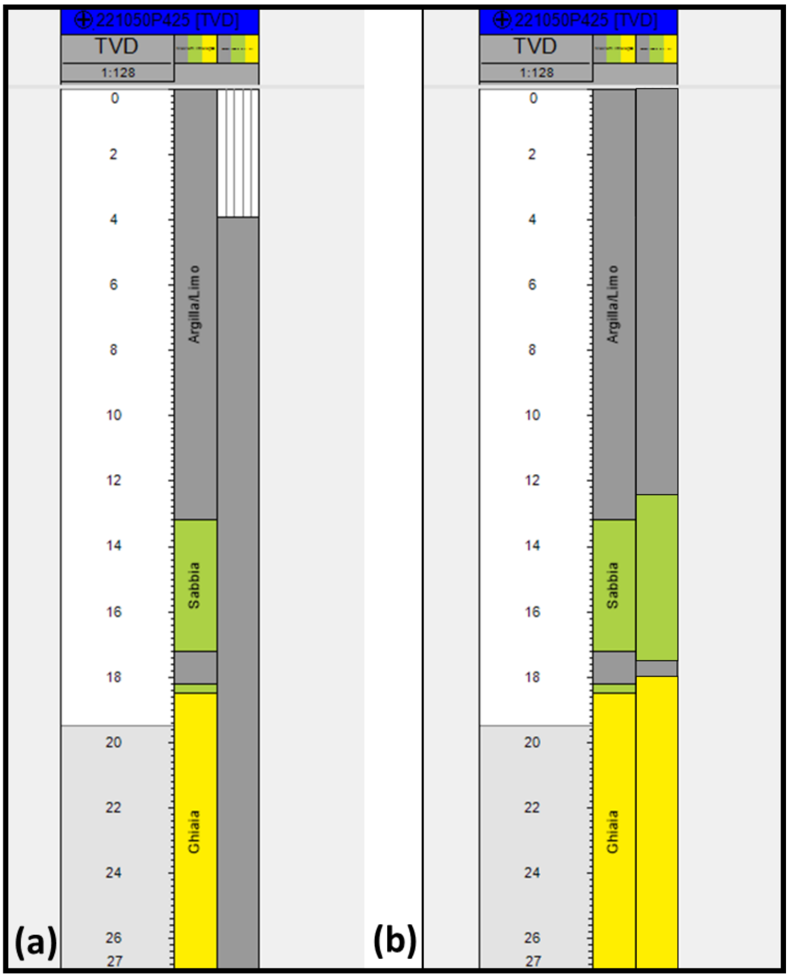

Figure 7.27: Example of (a) scale up of well log before quality check, (b) scale up of well log after quality check and change of weights.

7.3.2.4. Stratigraphic modelling

Data analysis regarding the vertical distribution of the lithologies was performed and variograms for each aquifer zone were calculated. The percentage of the thicknesses of each lithology in aquifers A and B are represented in Figure 7.28 and Figure 7.29 respectively.

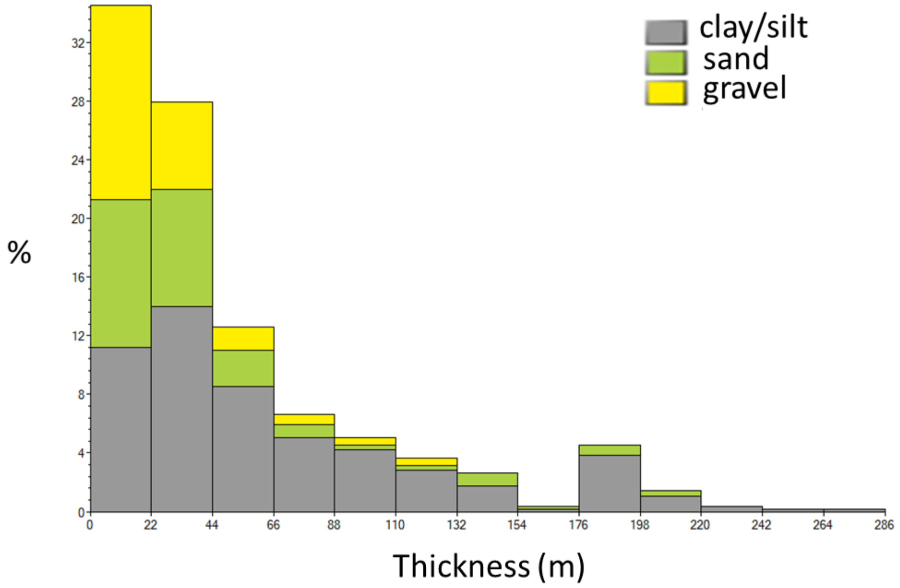

Figure 7.28: Distribution of lithology thicknesses in aquifer A.

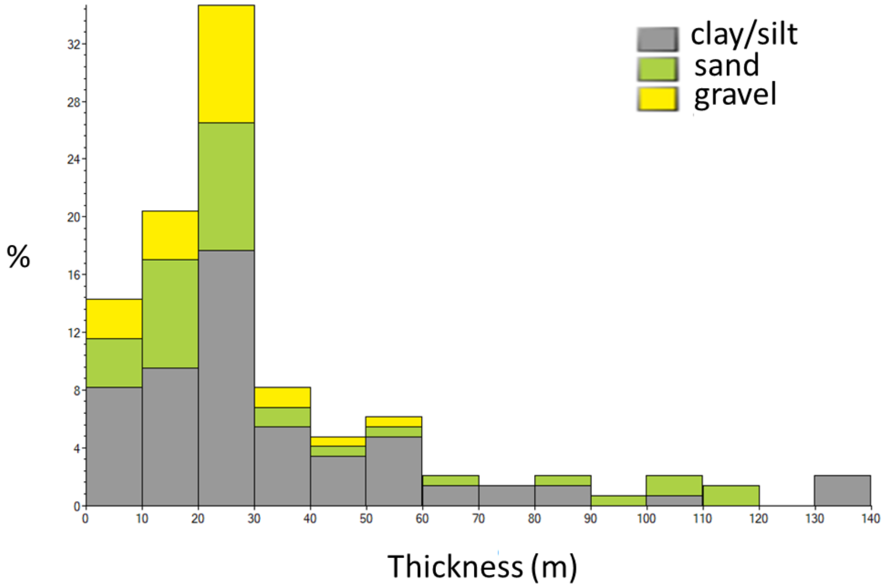

Figure 7.29: Distribution of lithology thicknesses in aquifer B.

The vertical proportion curves were then used in the facies modelling along with two modelling algorithms for their comparison and eventual selection between both for a more accurate representation of our zones. The first applied method was the Sequential indicator simulation that is a cell-based distribution method constrained by directional variograms, divided into major, minor and vertical, that were computed and assigned based on the well data and the analyzed cross-sections (Table 7.5). Considering the lateral geometry and continuity of the modelled bodies (sand/gravel), a very low value of the nugget (0.00001) was used in order to honor this observation and not create additional facies variability that could not be confirmed by other observations. The very low nugget effect guaranteed the continuity of the well lithological values (sand/shale) close to the wells while in larger distances the distribution was controlled by the other variogram parameters (range and direction).The presence or absence of different lithology types at each grid cell is simulated sequentially, incorporating the spatial relationships derived from the variograms. The simulation process considers neighboring cell values to maintain geological consistency and generate any number of stochastic realizations reflecting the uncertainty inherent in the data.

Table 7.5: Parameters of the variograms used for the Sequential indicator simulation and Indicator kriging for aquifer A.

Facies	**Function type**	**Sill**	**Major range (m)**	**Minor range (m)**	**Vertical range (m)**
Clay/silt	Spherical	1	6000	6000	55.7
Sand/Gravel	Spherical	1	3100	2000	47

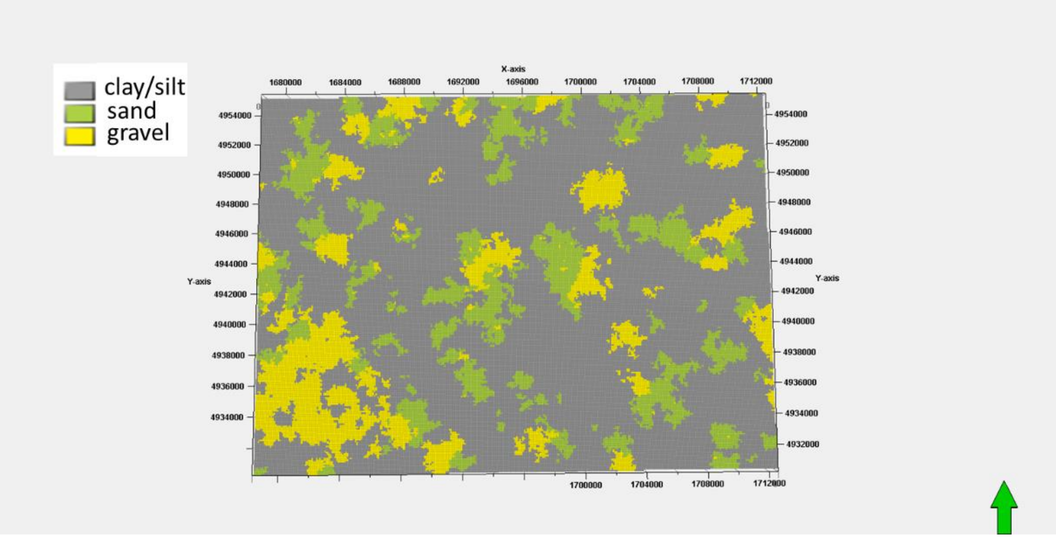

Figure 7.30: Top layer facies model using the Sequential indicator simulation.

The second method that was used for facies modelling was Indicator kriging. This method provides a minimum error-variance estimate at unsampled locations also based on their spatial correlation and covariance between nearby data points. The main difference between these two methods is that the Indicator kriging method creates a deterministic model according to the index with the highest selection expectation whereas the Sequential indicator simulation creates a random probability distribution model according to the number of the random seeds.

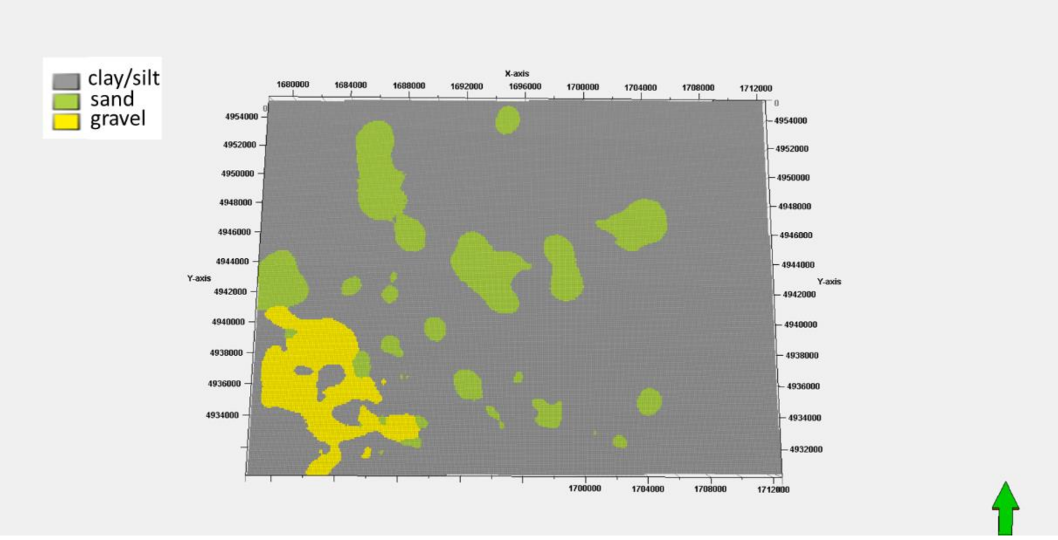

Figure 7.31: Top layer facies model using Indicator kriging.

The results of the two methods show an obvious smoothing effect with the Indicator kriging method that does not depict the heterogeneity of the multi-aquifer system present. The Sequential indicator simulation however eliminates the excessive smoothing effect and shows results consistent with the collected data from the preparation and research. So, the facies model obtained using the Sequential indicator simulation was selected with the percentage of lithofacies of well point statistics of aquifers A and B represented in Figure 7.32.

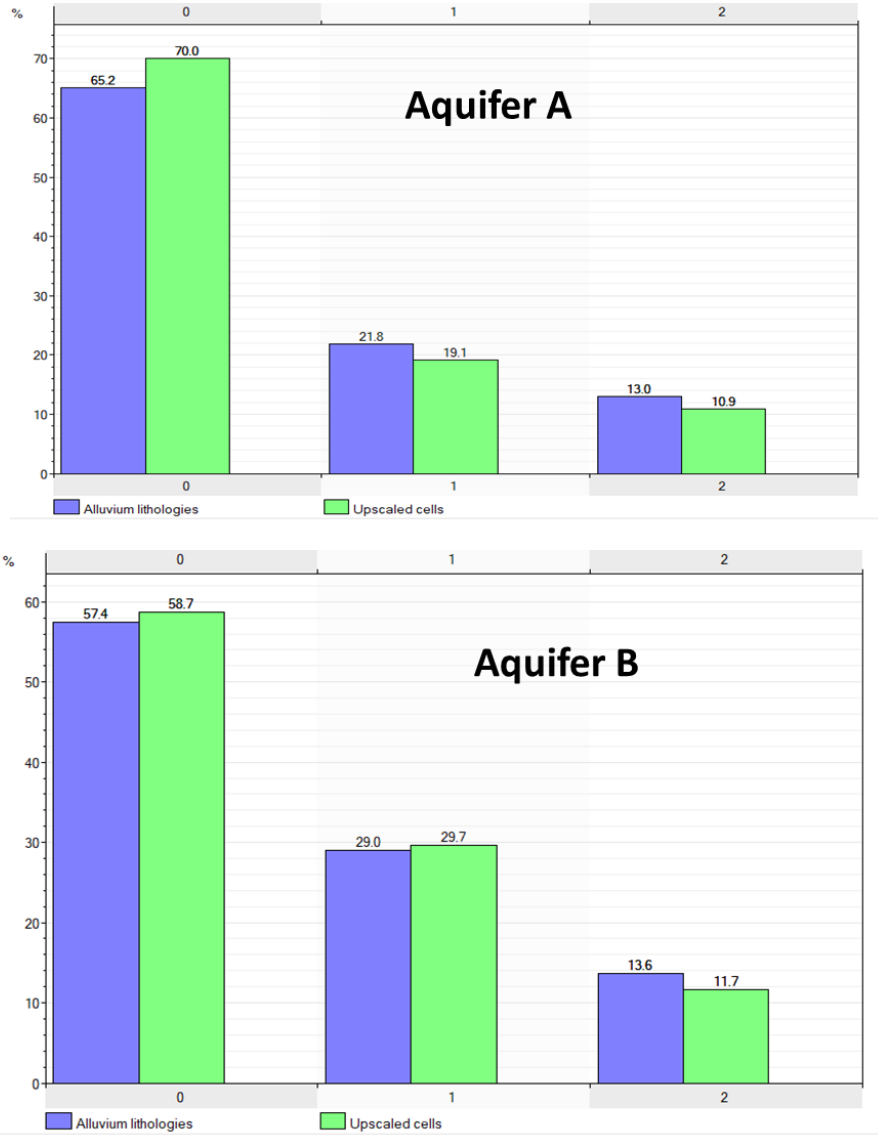

Figure 7.32: Lithologies percentage in aquifers A and B using Sequential indicator simulation. 0: clay/silt, 1: sand, 2: gravel.

7.3.2.5. Property modelling

The petrophysical parameters discussed in section 7.2.1 were modelled. The Gaussian random function simulation is used to model both porosity and permeability. Porosity modelling is through normal distribution by using Table 7.4 and Figure 7.14 to get the minimum, maximum, mean and standard deviation for clay/silt and sand/gravel. A total of 20 uncertainty runs were performed using this method in order to filter out any risks and the most consistent one with the facies model was chosen (Figure 7.33). The same method was used to model horizontal permeability but a log-normal distribution was applied and the corresponding porosity property for collocated co-kriging. The output data range for horizontal permeability for sand/gravel were averaged from Table 7.3 and those of clay/silt from literature (refer to section 7.2.1). In order to differentiate between the permeability values of sand/gravel for the different aquifer groups, a comparison was made between the total depth and the intake depth, and the thickness of these sediments at each well location of Table 7.3 to associate the permeability to the corresponding aquifer. The vertical permeability of sand/gravel was then derived using the anisotropy ratio k_h/k_v=10 where k_v is the vertical permeability. The anisotropy ratio was collected from literature studies concentrated in the eastern Po River basin (Teatini et al., 2000). Table 7.6 summarizes the porosity and permeability values of sand/gravel as generated. The mean and standard deviation of the properties for aquifers A+B were calculated as follows: 0.274 and 0.0263 respectively for porosity, and 6810 mD and 700 mD respectively for horizontal permeability. Figure 7.34 and Figure 7.35 show the porosity and horizontal permeability distributions within a WE-oriented cross section (black line in Figure 7.33) highlighting the heterogeneity of the aquifer system with the ROY (red, orange, yellow) colors of the rainbow scale representing clay/silt and GBIV (green, blue, indigo, violet) colors representing sand/gravel.

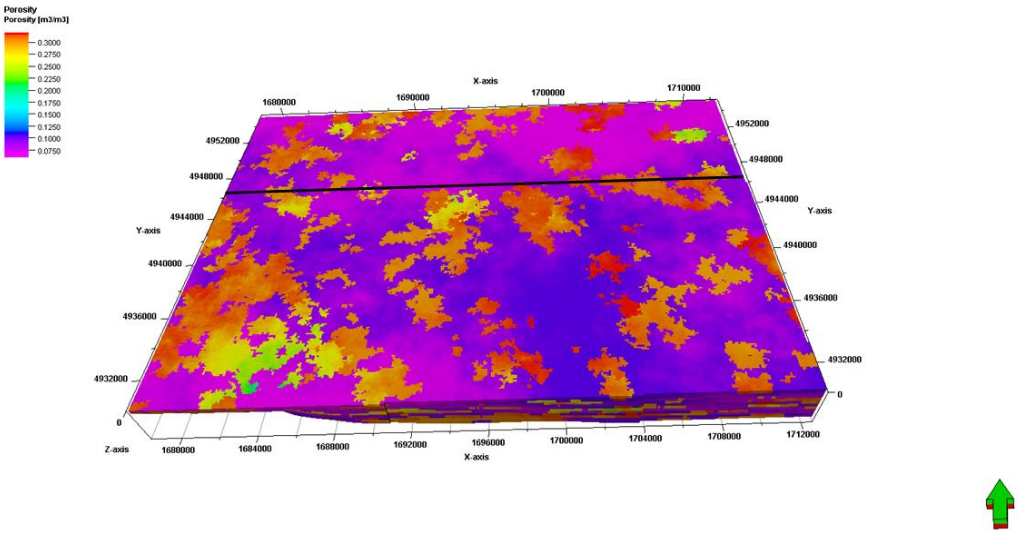

Figure 7.33: Porosity distribution model. Black line represents trace of cross-sections presented in Figure 7.34 and Figure 7.35.

Table 7.6: Porosity and horizontal permeability of sand/gravel as derived from literature and available pumping wells.

Aquifer Group	Porosity		Horizontal Permeability (mD)	
	Minimum	Maximum	Minimum	Maximum
Aquifer A	0.215	0.32	5000	8000

Aquifer B	0.205	0.31	5000	7000

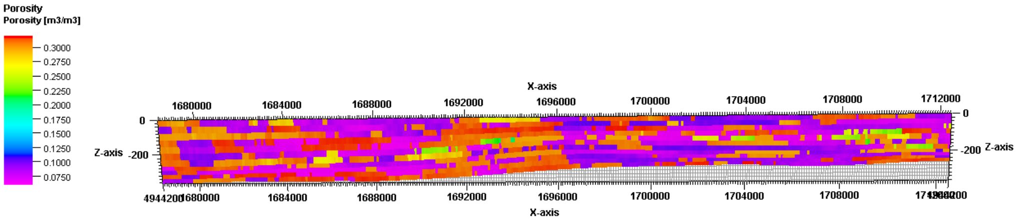

Figure 7.34: Cross-section showing porosity distribution.

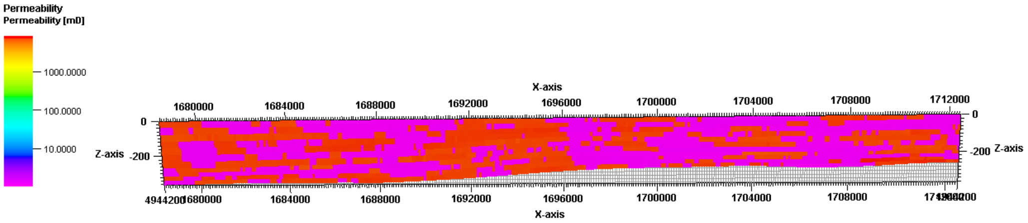

Figure 7.35: Cross-section showing horizontal permeability distribution.

7.4. Dynamic modelling

The Eclipse simulator is used for the fluid flow simulations of the aquifers. Although it was originally developed for oil and gas reservoir simulations, it proved to be effective in simulating aquifers as well. This software was selected for the purpose of performing the coupled simulations of the aquifers with the underlying gas reservoir in the future. The simulation period covers a time-frame of 9 years, from 2009 till 2018, chosen according to the water production data collected and the available groundwater level measurements.

The 3D grid for the flow model was generated based on the reconstructed lithostratigraphy. The global grid was copied filtering the aquifer zones with all the generated properties. Table 7.7 provides the description of the dynamic grid.

Table 7.7: Description of dynamic grid.

Grid cells (nI x nJ x nK)	163 x 106 x 10
Grid nodes (nI x nJ x nK)	164 x 107 x 11
Total number of grid cells	172780
Total number of grid nodes	193028

Number of geological horizons	11
Number of geological layers	10

Ten out of eleven of the created geological layers were used for the dynamic modelling, confining the model by the penultimate layer of the aquifer B bottom and the ground surface with no elevation. Figure 7.36 shows the model with its depth extension.

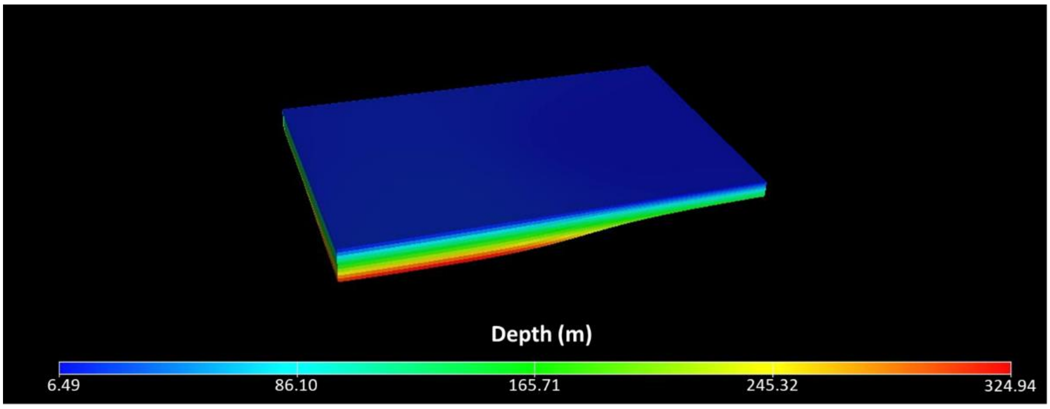

Figure 7.36: Depth of the model.

The flow boundary conditions were defined as follows: the top was assumed to be a no flow surface along with part of the BC outer boundary that intersects the Savena river (Figure 7.2, copied and modified below) and also part of the AB boundary (Figure 7.37). The latter is parallel to the main natural flow direction (Chahoud et al., 2016).

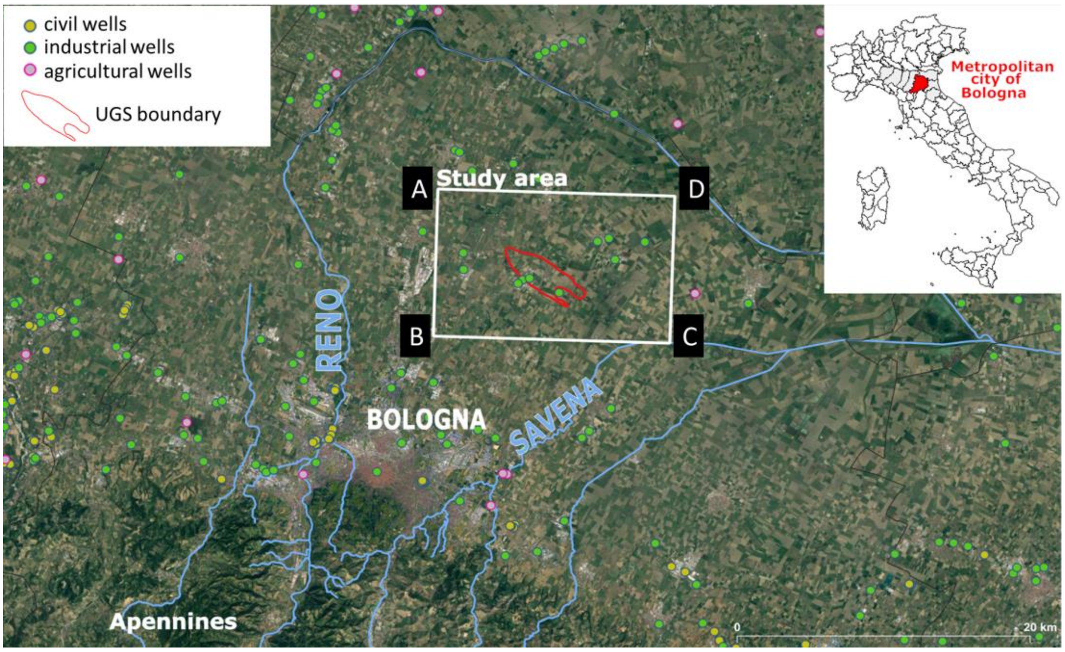

Copy of Figure 6.2: Boundaries of the dynamic model domain and its intersection with Savena river.

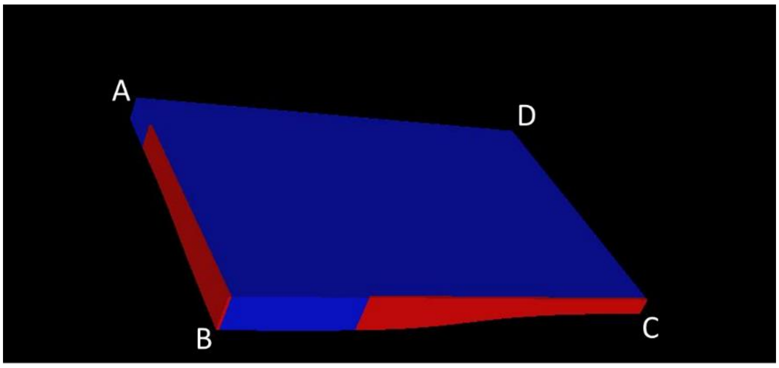

Figure 7.37: Dynamic model with flow boundaries highlighted in red and no flow boundary in blue.

The calibration of the flow model was performed by comparing groundwater levels measured from piezometric wells with the simulated groundwater levels generated. A total of seven piezometric wells were used with the ten production wells (discussed in section 7.1.2) that fall inside the model boundary (Figure 7.38).

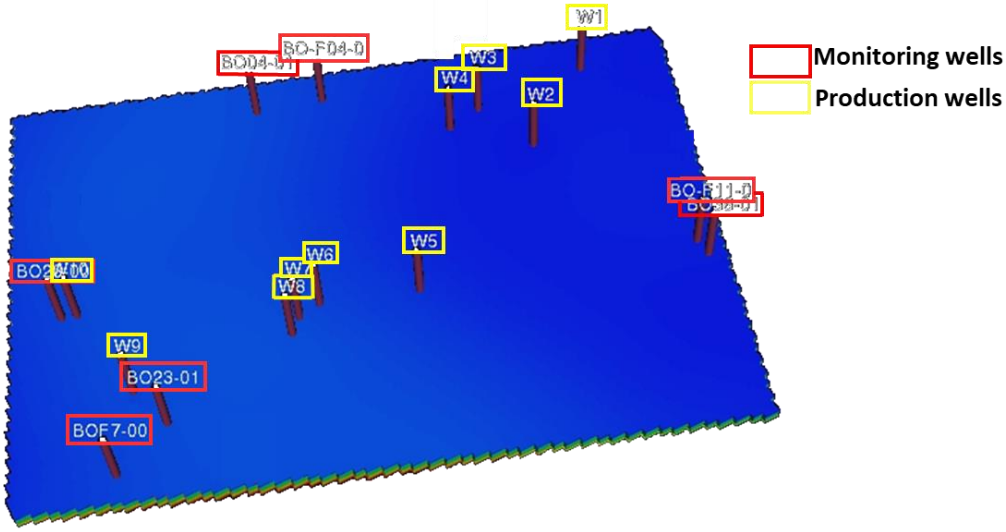

Figure 7.38: Location of monitoring (piezometric) and production wells inside model boundary.

The average water production rates for the 10 wells were provided only for the time period 2016-2018 (Table 7.2). So, the total rates for the time periods 2009-2011, 2015-2018 (Figure 4.15b,c respectively) were used by extracting the rates of the communes (Table 7.8) in which the production wells fall and dividing those rates among the wells. For the time period 2012-2014, a total value was averaged between the total withdrawal values of the periods 2009-2011 and 2015-2018. The average water production rates in Table 7.2 were used to calculate the percentage of division allocated to each well.

Table 7.8: Total groundwater withdrawals (in 10^3 m^3/year) of the three communes bordering the production wells.

Comune	2009-2011	2012-2014	2015-2018
BARICELLA	43	60.5	78
BENTIVOGLIO	142	260	379
MINERBIO	1,266	950	633

The average aquifer productivity index (API) was calculated by using the following formula:

$$API = \frac{S_S \ x \ T}{L} \qquad (7.4)$$

Where S_S and T are the specific storage and transmissivity, respectively, provided in Table 7.3 and L is the thickness of the aquifer provided by the contour maps of RER.

The calibration phase relied on the comparison between simulated and measured pressure and, consequently, the measured groundwater levels were converted into pressure values using the equation:

$$p = \rho_w g(H - h) \qquad (7.5)$$

such that p is the pressure (in Pascal), ρ_w is the density of water (equal to 1000 kg/m^3 since the base of the aquifer system was plotted up to where the units are saturated with freshwater), g is the gravitational force (equal to 9.80665 m/s^2), H is the depth of the aquifer from which the groundwater levels are measured (in m) and h is the recorded groundwater level (in m). H is measured by considering the location of each piezometric well and the groundwater bodies used for water production in wells around the piezometric well. The depth of the corresponding aquifer hosting the groundwater bodies at the location of the piezometric well is then referred to as H. The pressure plots of the six monitoring wells (converted to bar) are presented in Figure 7.39. One of the wells (BO04-01) was not accounted for due to insufficient measurement points.

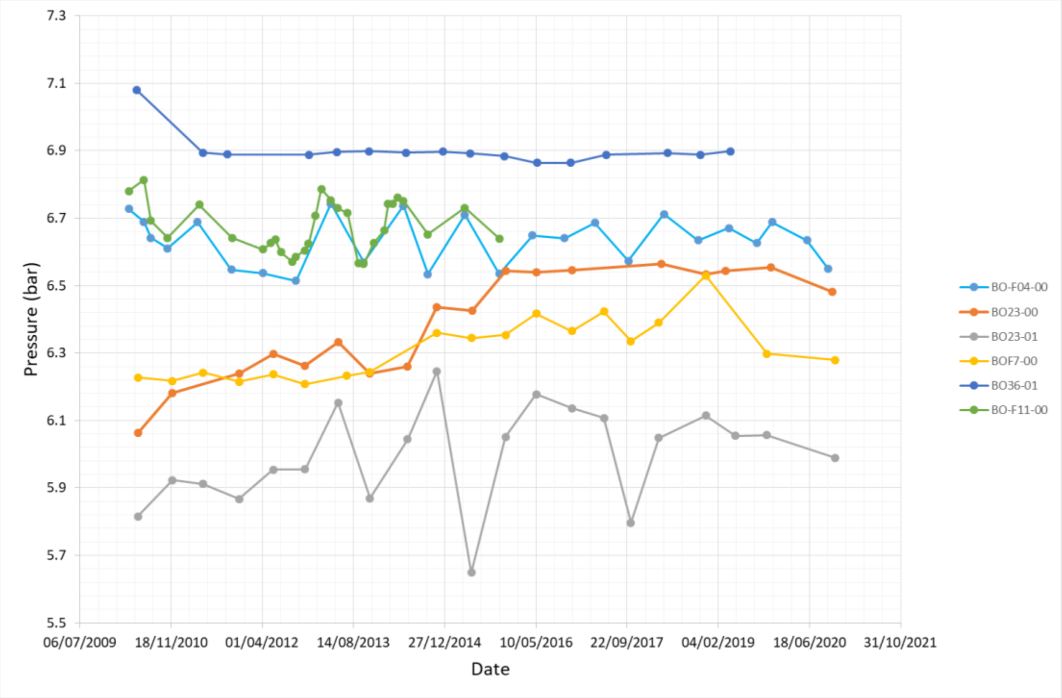

Figure 7.39: Converted pressure plots of the six monitoring wells inside model boundary.

In the case of hydrocarbon production within complex multilayer reservoirs, a continuous model calibration can be performed via history match due to the precise measurements of fluid production and extensive dataset of fluid pore pressure drawdown. However, in the case of shallow multiaquifer systems, it is not as easy due to the system complexity and irregular documentation of exploitation processes (e.g., Agarwal et al., 2000; Teatini et al., 2006). So, in order to calibrate our model, a trial and error process based on the “on the average” calibration procedure was performed with the hydrodynamic parameters discussed in section 7.2.1 as follows: c_M was assigned to clay and sand/gravel according to the constitutive relationships in Eq. 7.2 and Eq. 7.3 and then reducing them by one order of magnitude to get the best match while keeping the horizontal permeability (hydraulic conductivity) as is in Table 7.6. Some of the datum depths (H) of the piezometric wells were also slightly modified to help with the best match. Figure 7.40 compares the simulated pressures versus the observed pressures in the piezometric wells.

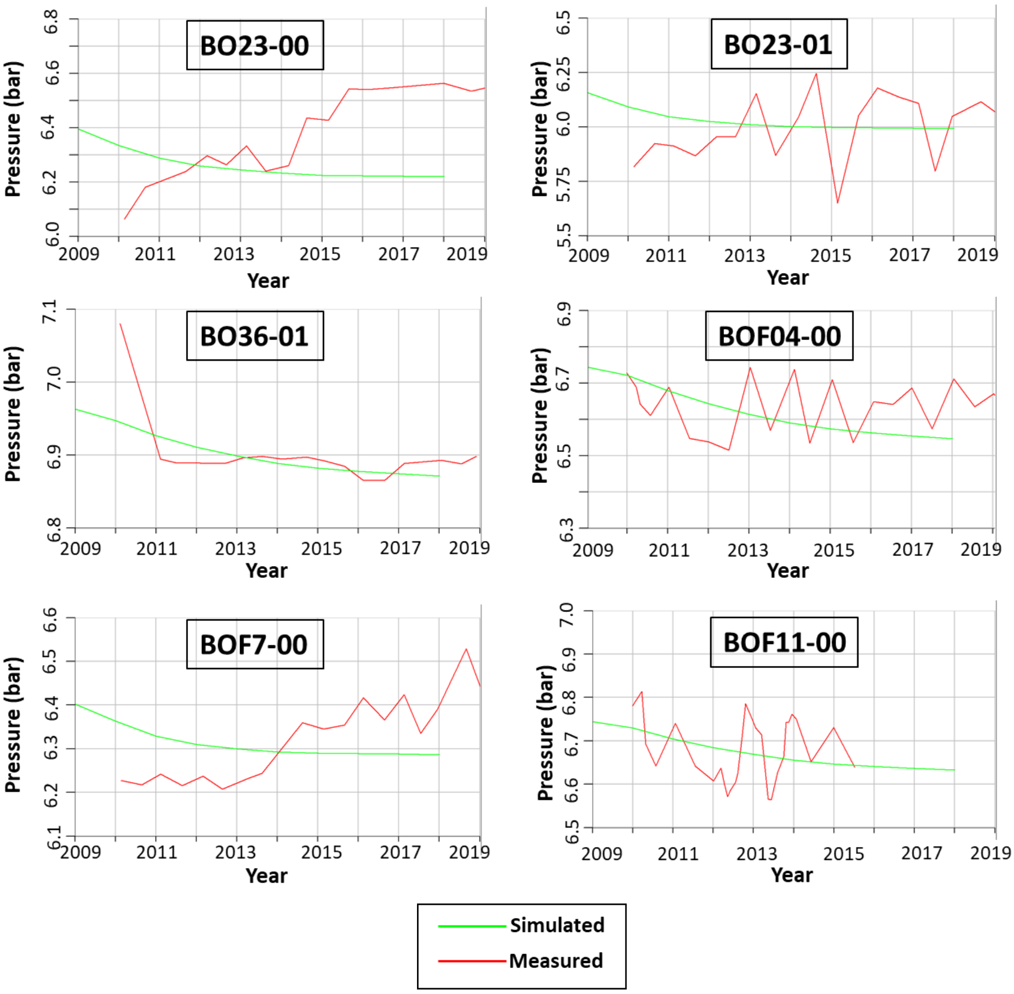

Figure 7.40: Measured and simulated pressures at the monitoring wells. The piezometric location is provided in Figure 7.38.

A general agreement is observed between the simulated and the measured values, considering the studied time-frame, the high complexity of the multi-aquifer model and the procedure that was used to distribute areally and vertically (with depth) the water production.

7.5. Geomechanical modelling

The geomechanical model is prepared in Petrel. Once the case is ready for simulation, it is passed to the VISAGE Finite-Element Geomechanical Simulator which is integrated in the Petrel platform with the name of Petrel Geomechanics. The latter provides the graphical interface needed for resulting data visualization and analysis.

7.5.1. Grid setup

The geomechanical grid was built by extending the dynamic grid and placing the aquifer roughly in the middle of the volume (Figure 7.41) in order to capture the full geomechanical response induced by aquifer production, while also ensuring that the boundary conditions do not impact the calculated outcome. This was done by setting the following:

- ***The overburden:*** represents the rock/soil layers that lie above the study area. In this case study, it is set to none.
- ***The sideburden:*** represents the rock/soil adjacent to the producing zone. In this case study, extended by 15 km on all sides.
- ***The underburden:*** represents the rock/soil that extend from the lower part of the aquifer down to the bottom part of the study. In this case study, extended down to 6 km.

The model only investigates the effect of water withdrawal in the volume described by the dynamic model, and no other superimposed effect was simulated, i.e. the fluid pressure in the side/underburdem remains constant and equal to the hydrostatic one.

Table 7.9 provides the description of the geomechanical grid and Table 7.10 describes the layered formations of the grid. Figure 7.41 visualizes the grid overview.

Table 7.9: Description of geomechanical grid.

Grid cells (nI x nJ x nK)	209 x 186 x 21
Grid nodes (nI x nJ x nK)	210 x 187 x 22
Total number of grid cells	816354
Total number of grid nodes	863940
Number of geological horizons	22
Number of geological layers	21

Table 7.10: Layered formations of the geomechanical grid.

Formation	Depth (m)	Layers
Alluvium	340	1,10
Sabbie di Asti	1000	11,15
Top Argille	1100	16
Top Reservoir	1200	17
Bottom Reservoir	1400	18
Top Carbonates	5000	19,20
Bottom of Model	6000	21

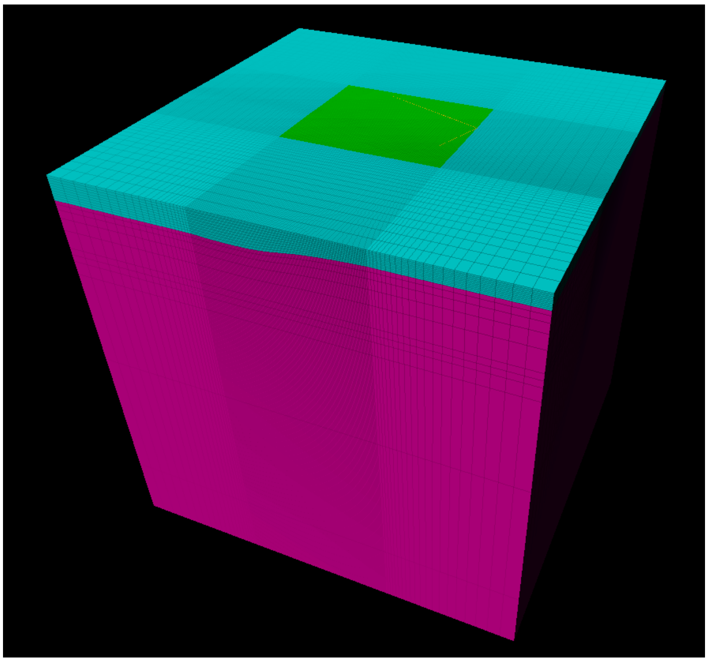

Figure 7.41: Geomechanical grid overview. Green represents extension of dynamic grid, blue the alluvium layers and purple the underburden layers.

7.5.2. Material modelling

The materials corresponding to the layers (Table 7.10) were assigned their relevant mechanical parameters (Table 7.11).

Table 7.11: Mechanical parameters adopted for material characterization.

Formations	Geomechanical class	Numerical layer	Rock bulk density	***Deformation parameters***		
				Young's modulus	**Poisson's ratio**	**Biot's coef**
			(g/cm3)	(GPa)	(-)	(-)
Alluvium	1	form 1 to 10	1.93	***equation***	0.30	1.0
Sabbie di Asti	2	from 11 to 15	2.10	0.5	0.39	
Argille del Santerno	3	16	2.18	5	0.39	
Reservoir (*)	4	from 17 to 18	2.20	4	0.39	
Carbonates	5	from 19 to 21	2.40	35	0.39	

Alluvium properties were collected from technical literature (Teatini et al., 2006 and references therein). Young's modulus was derived using the constitutive relationship in Figure 7.15 as a function of depth (Figure 7.42) by applying: $c_M = \frac{1}{\lambda+2G} = \frac{(1+\upsilon)(1-2\upsilon)}{E(1-\upsilon)}$.

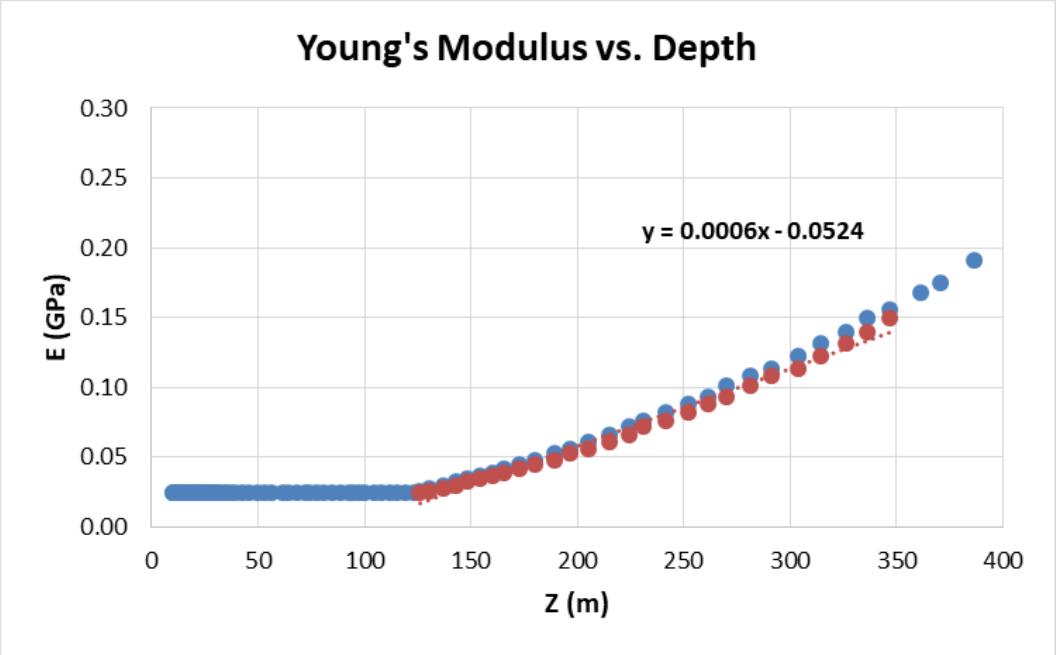

Figure 7.42: Derived Young's modulus function against depth. The red curve highlights where the derived function applies (when Young's modulus varies with depth).

7.5.3. Initial conditions and pressure step analysis

The pressure evolution resulting from the dynamic simulations represent the forcing function for the mechanical simulation by loading the simulation results into Petrel. The results were converted to a property of the geomechanical grid by storing the pressure evolution as independent properties with respect to different time-steps (10 in this case, referring to each year of the time-frame 2009-2018). The pressures were then upscaled from the dynamic model to the geomechanical one by filtering out the producing aquifer in the model. Then, the initial and final pressure profiles were introduced with the defined time-steps in between. Figure 7.43 shows the change in pressure from the beginning till the end of the time period.

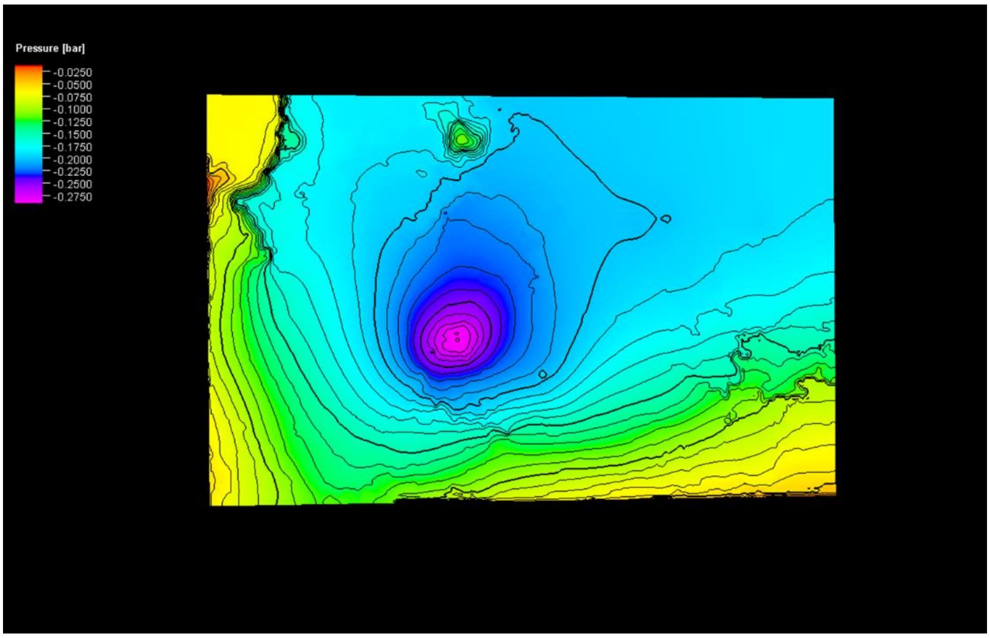

Figure 7.43: Delta pressure from 01/01/2009 till 01/01/2018.

The initialization phase consists of defining for each cell the initial stress and fluid pressure condition. This was done by imposing a hydrostatic pressure regime in each cell external to the dynamic model grid and zero normal stress on the surface. The vertical stress was calculated on the basis of formation densities whereas the horizontal stresses were set equal to 0.6 times the vertical stress. The mechanical method selected for the simulation was the one-way coupling approach, also referred to as uncoupled approach, that has been assumed in the classical groundwater hydrology (refer section 5.3.1) and has been proven effective in the aquifers of the Po River basin (Gambolati et al., 2000; Teatini et al., 2006). This approach solves the stress-strain relationships independently from the fluid-flow dynamics (Figure 7.44) and assumes the petrophysical properties to be constant over formation’s lifetime.

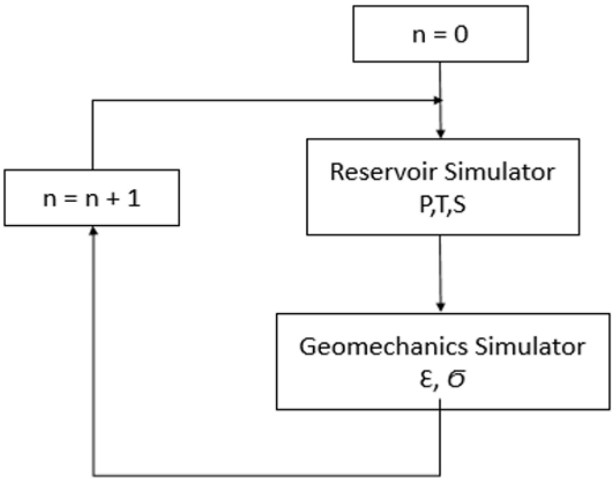

Figure 7.44: One-way coupling approach.

7.5.4. Geomechanical simulation results

Figure 7.45 shows the simulated land subsidence (i.e., cumulative vertical displacement) over the 2009-2018 period due to groundwater production. The maximum settlement bowl reaches a value of 40 mm over the entire period, which coincides with the location of three production wells (W6-W7-W8) with the highest production rates. Figure 7.46 displays the location of those wells as well as the boundary of the UGS with respect to the high settlement bowl.

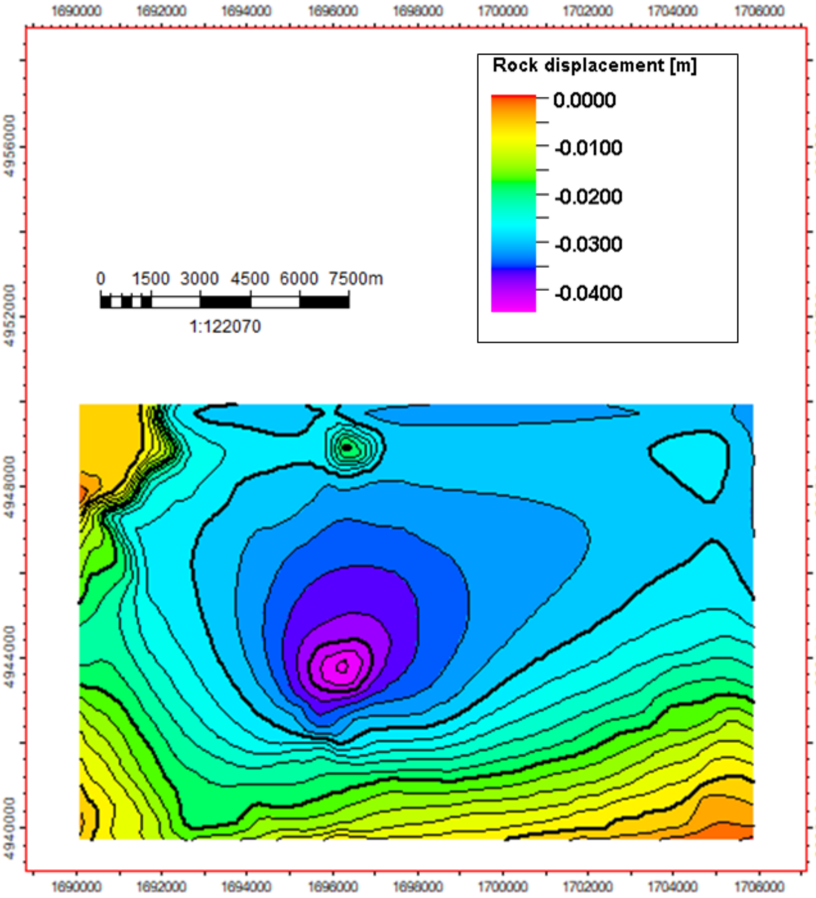

Figure 7.45: Simulated land subsidence over the 2009-2018 period.

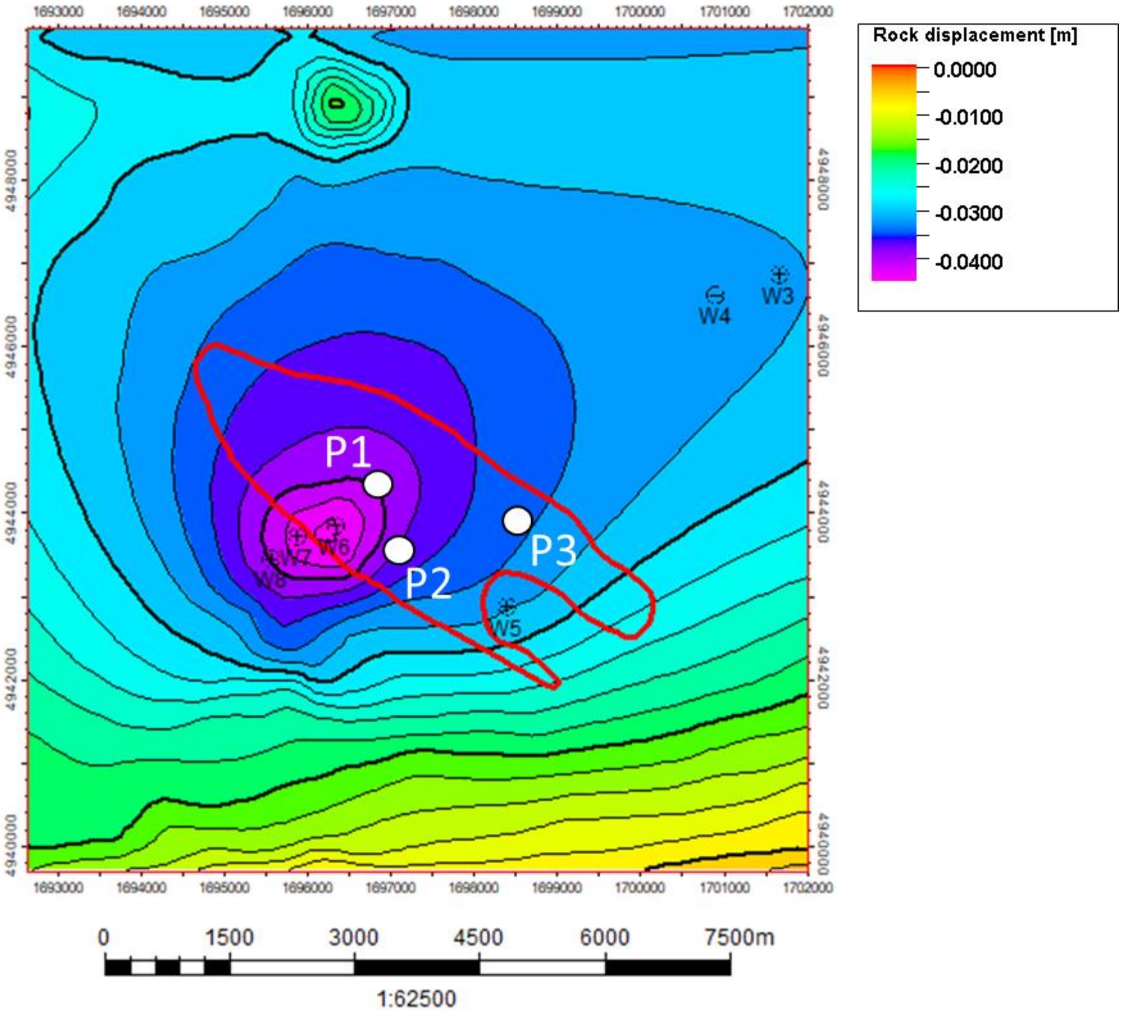

Figure 7.46: Simulated land subsidence over the 2009-2018 period with the UGS highlighted in red and water production wells in black.

In order to quantify the superposition of the groundwater and UGS production effects on the subsidence in the area under investigation, three reference points were selected within the UGS field boundary (P1, P2 and P3 in Figure 7.46) based on the existing study discussed in section 7.1.1 (Benetatos et al., 2020). The simulated vertical displacement (in mm) for the three points, for both the groundwater and UGS production scenarios for the coinciding simulation periods (2010-2016) are presented in Table 7.12.

Table 7.12: Vertical displacement of the reference points during groundwater and UGS activities.

Date	Vertical Displacement (mm)					
	P1		P2		P3	
	Water	UGS	Water	UGS	Water	UGS
2010	-22.2	0.89	-20.9	-2.39	-17.5	-6.24
2011	-30.7	4.9	-28	0.65	-24.5	3.48
2012	-32.4	-2.45	-29.7	-4.57	-26.4	-1.74
2013	-35.4	-5.57	-32.6	-7.17	-29.2	-4.78
2014	-37.9	5.13	-35	1.96	-31.9	4.35
2015	-36.4	0.22	-33.6	-3.26	-30.9	-0.22
2016	-37.2	0.45	-34.3	-0.87	-31.8	0.22

The behavior of the three points due to UGS activities is displayed in Figure 7.47. P1 and P3 display similar patterns with no significant vertical displacement whereas P2 shows a gradual increase in vertical displacement over time.

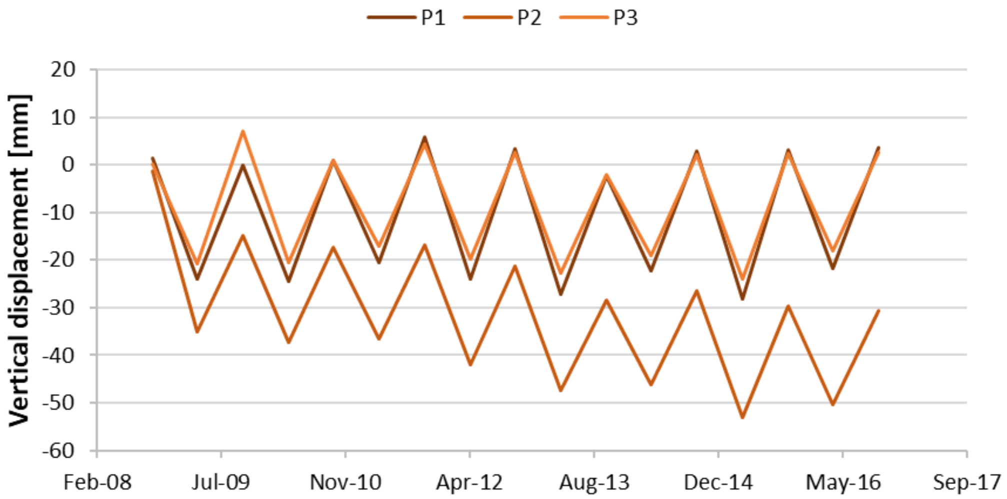

Figure 7.47: Behavior of the three references points due to UGS activities.

The behavior of the three points due to groundwater exploitation is displayed in Figure 7.48. They all behave similarly with a gradual increase in vertical displacement over time.

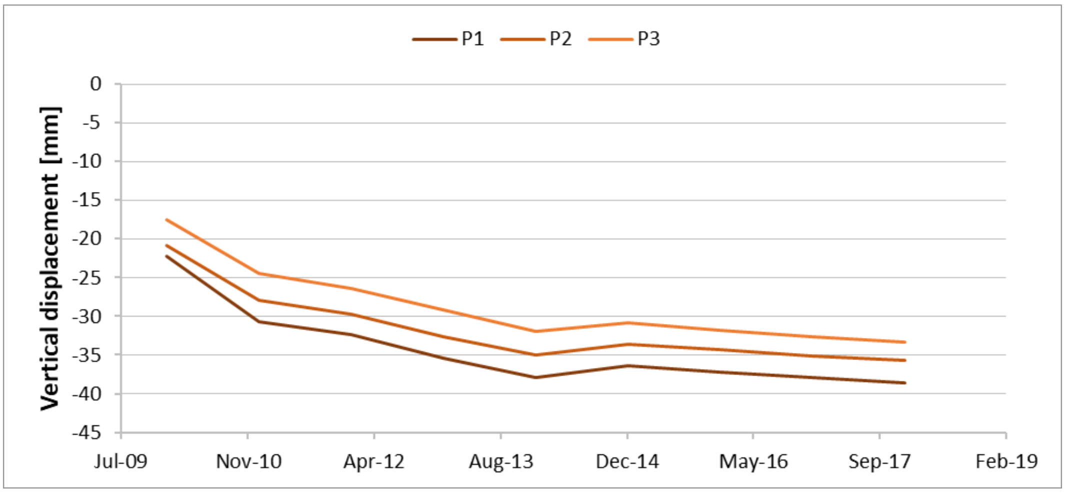

Figure 7.48: Behavior of the three references points due to groundwater exploitation.

The simulated subsidence map of the aquifer was then compared with the present-day subsidence map of Emilia-Romagna over the time period 2011-2016 (Figure 7.49, discussed in Chapter 4 section 4.3). Inside the boundary of the study area, displacements of 2.5-7.5 mm/year are observed by the Emilia-Romagna map. This area with the highest displacement values coincides with the area of maximum displacement simulated by our model (Figure 7.50), which calculated maximum displacement values of about 4.5 mm/year. The highest subsidence peak observed and recorded overlaps with the area encompassing 3 water production wells (W6-W7-W8) in the center of the simulation boundary producing a cumulative of 46.5 x 10^3 m^3/year. The subsequent peak in the NE area of our boundary coincides with wells W3 and W4 producing a cumulative of 27.6 x 10^3 m^3/year. Coherently from both sources of information, groundwater production is assumed to be the main factor affecting the subsidence in this area. In the center of the UGS field boundary, maximum values of up to 2 mm/year are pointed out that dissipate away from the boundary.

The superposition of the groundwater and UGS production effects from the numerical simulations were thus considered satisfactory and representative of the physical phenomenon affecting the land subsidence in the area of investigation.

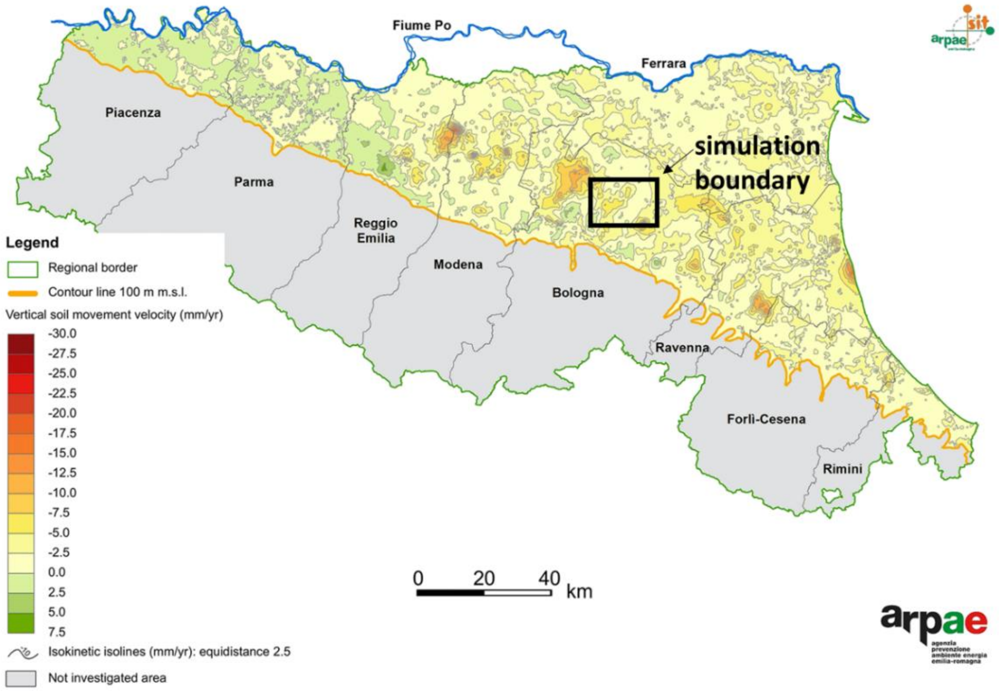

Figure 7.49: Emilia-Romagna subsidence map for the time period 2011-2016 (from ARPAE 2018a).

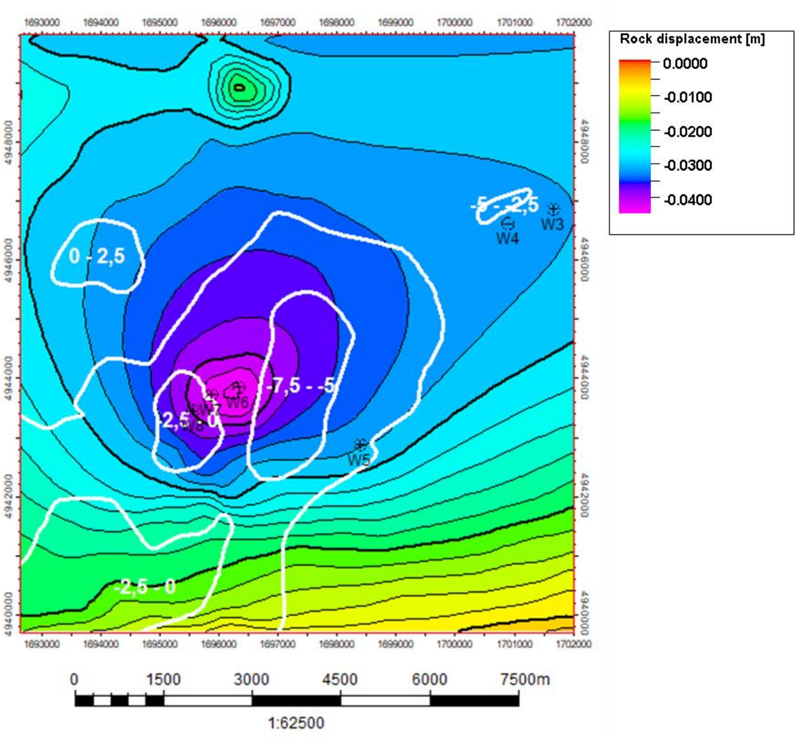

Figure 7.50: Comparison between simulated land subsidence and measured land subsidence represented by contour lines (ranges in mm/year) from ARPAE (2018a).

Chapter 8

Land movement analysis in Bologna area using InSAR data

In this chapter, an extended area of the case study in Chapter 7 that is affected by groundwater and gas production and also by natural components is selected in order to be able to spatially identify and quantify the contribution of each of these sources to the ground movements. The workflow methodology is presented in Figure 6.2 and involves the application of an unsupervised machine learning technique (cluster analysis) on the decomposed time series ground deformation using the SBAS approach along with the detailed geological investigation on a narrower area of what was presented in Chapter 3. Different datasets are used for the analysis from groundwater production data to piezometric data to land use maps.

8.1. Case studies and InSAR dataset

The location of analysis falls in the Metropolitan City of Bologna in Emilia-Romagna in northern Italy (Figure 8.1). The InSAR time series of ground deformation dataset that is used for the processing and clustering was provided by CNR-IREA, with its corresponding description in Table 8.1.

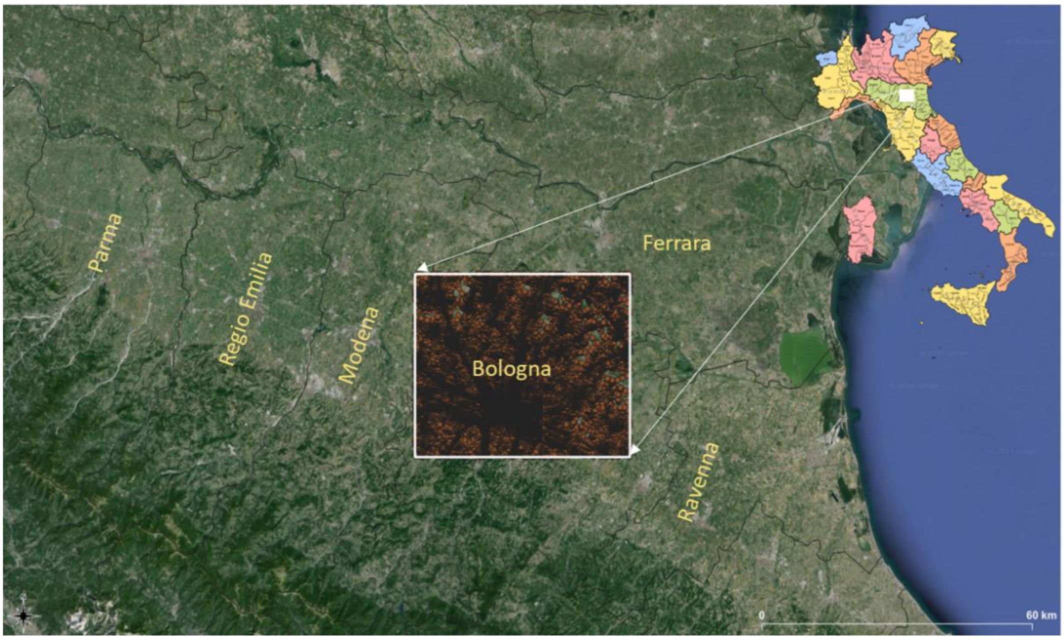

Figure 8.1: Regional location of analysis.

Table 8.1: Information and features of InSAR dataset.

Location	Approx. area [km^2]	Measuring Points (MPs)	MPs density [MP/ km^2]	Grid spatial resolution [m]	Satellite	Processing algorithm	Time-frame
Regional analysis	1850	223311	121	40*30m	Sentinel-1	Parallel SBAS Interferometry Chain	06-2016 10-2021

Inside the boundary of the investigated area, the analysis was performed on two case studies (Figure 8.2); case 1 located to the south of the Metropolitan City of Bologna and in the city of Bologna itself characterized by a high concentration of water production whereas case 2 is to the NE of Bologna with a low concentration of water production. Case 1 has been investigated by numerous studies regarding the overall trend in the city of Bologna that's been affected by intensive subsidence related to groundwater exploitation; whereas case 2 is not characterized by visible strong phenomena and can potentially be assumed as a "stable zone" for comparison. The main focus was thus on the seasonal component, that had not been previously studied into details, and analyzing its behavior in accordance with aquifer geological characteristics and behavior, further investigating the basis in Chapter 3.

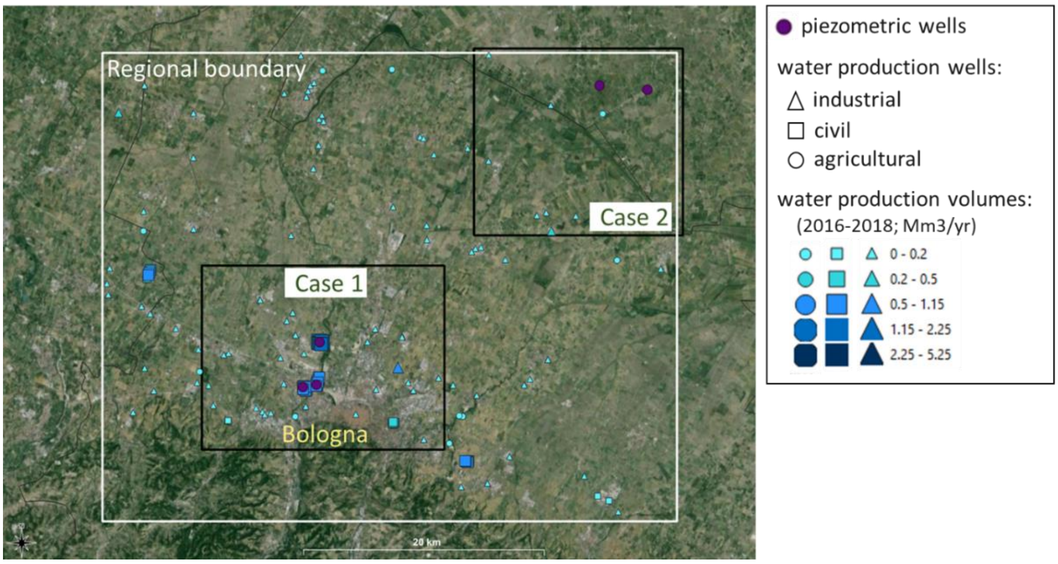

Figure 8.2: Case studies inside regional boundary used for analysis.

8.2. Analysis of seasonal components

8.2.1. Case 1

The distribution of water production wells in case 1 on the basis of the groundwater use, i.e. for agricultural, civil and industrial purposes, with their corresponding production volumes (in Mm3/yr) is presented in Figure 8.3 along with the piezometric wells used for the analysis. Production wells are present abundantly in this area, with a great number of the highest producing wells concentrated in 3 punctual areas.

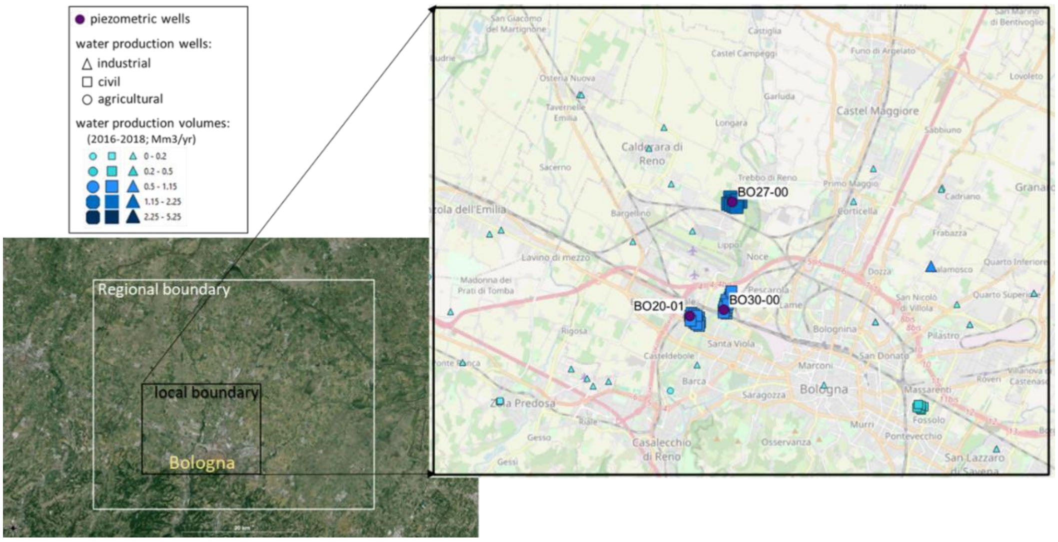

Figure 8.3: Case 1 overview.

The K-means cluster analysis of InSAR time series of the seasonal components on case 1 was performed using 4 clusters. The outcome gave us a map with the spatial distribution of the clusters (Figure 8.4) and a plot showing the seasonal behavior of each cluster with its average amplitude (Figure 8.5). The focus area was concentrated around the water wells with the high water production volumes that fell inside cluster 2 (yellow), which shows uplift in during aquifer recharge autumn-winter period and subsidence in the spring-summer period. The three available piezometric wells coinciding with the production wells in that area were used to try and identify a correlation between the cluster behavior and the phenomenon.

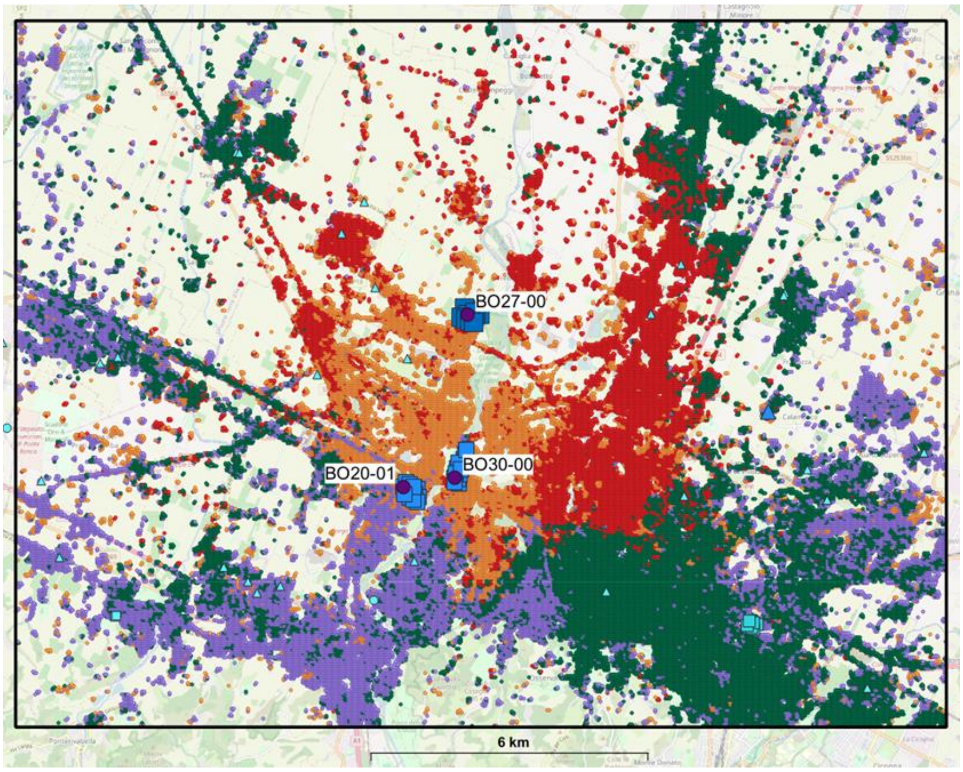

Figure 8.4: Case 1 spatial distribution of the 4 clusters from analysis. Legend same as Figure 8.3.

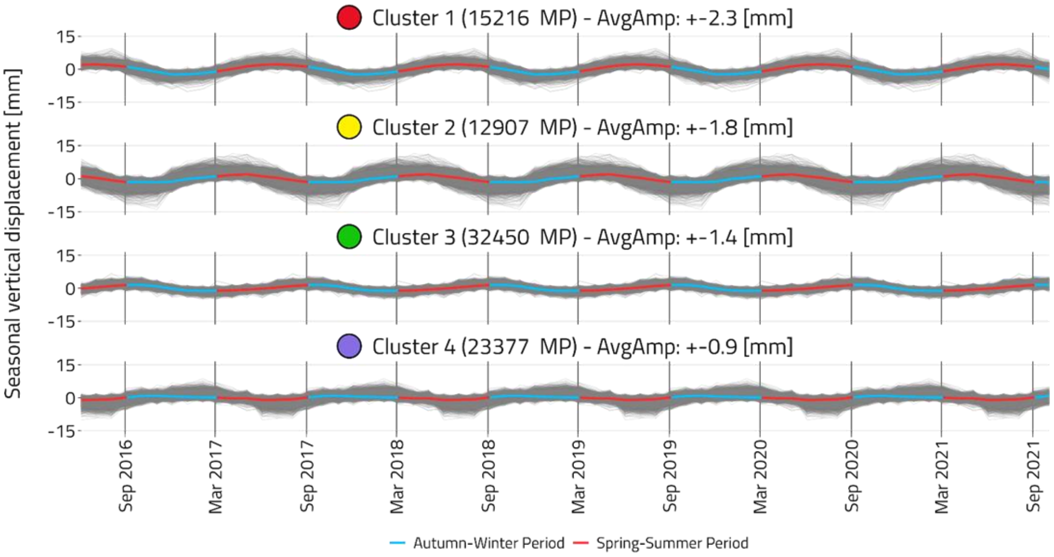

Figure 8.5: Case 1 seasonal behavior of the 4 clusters from the analysis displaying average amplitude.

8.2.1.1. Piezometric level versus InSAR seasonality

Comparing the groundwater piezometric level of the three wells with the seasonality of the InSAR time series was performed using two methods:

(1) Comparison of the groundwater level with the seasonal component of the clusters of the previous InSAR analysis (Figure 8.4 and Figure 8.5) depending on their distribution around the well

(2) Considering a narrow buffer zone around the piezometric well, comparison between the Measured Points (MPs) ground deformation seasonal behavior and the groundwater level

Figure 8.6, Figure 8.7 and Figure 8.8 show the results of wells BO20-01, BO27-00 and BO30-00 respectively using the two methods.

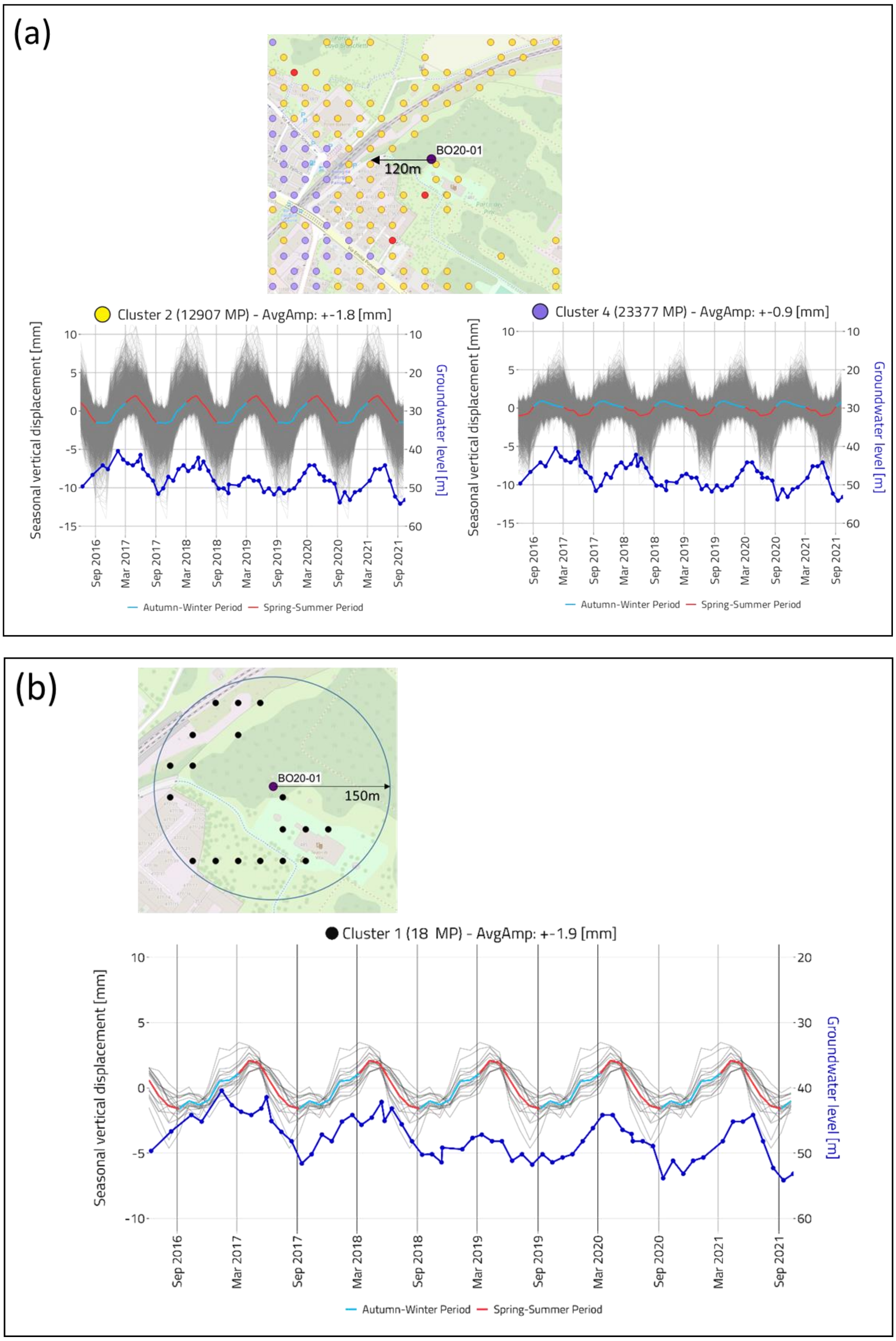

Figure 8.6: Groundwater level versus seasonal vertical displacements for well BO20-01 using (a) seasonal component of clusters 2 and 4, (b) MPs ground deformation seasonal component.

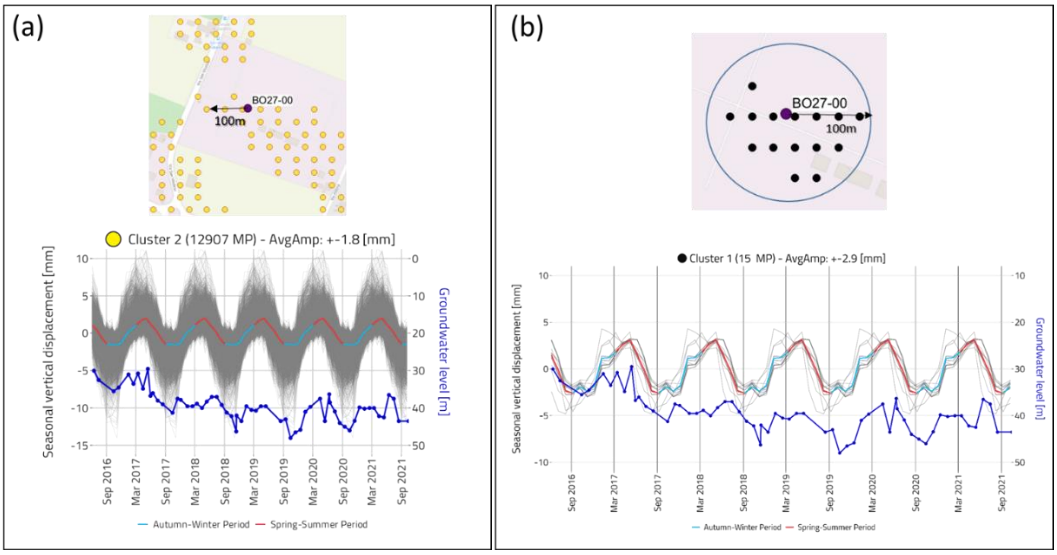

Figure 8.7: Groundwater level versus seasonal vertical displacements for well BO27-00 using (a) seasonal component of cluster 2, (b) MPs ground deformation seasonal component.

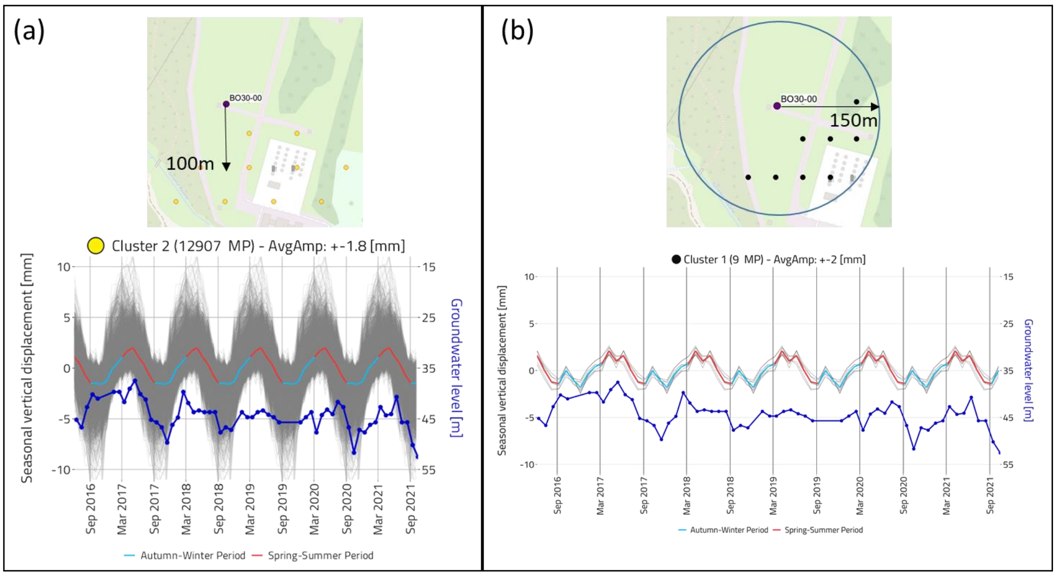

Figure 8.8: Groundwater level versus seasonal vertical displacements for well BO30-00 using (a) seasonal component of cluster 2, (b) MPs ground deformation seasonal component.

For well BO20-01, a direct correlation was observed between the seasonal component of the yellow cluster (that surrounds the well to a distance of around 160m) and the groundwater level with an increase in the autumn-winter period and a decrease in the spring-summer. The correlation with the purple cluster at a greater distance was present to a lesser extent, showing a partial trend with the two different periods and a shifted delay (Figure 8.6a). On the other hand, the comparison with the MPs seasonal behavior in the buffer zone showed an exact correlation with the seasonal behavior of the groundwater level (Figure 8.6b).

For wells BO27-00 and BO30-00, both methods resulted in a direct correlation between InSAR seasonal movements and groundwater level (Figure 8.7, Figure 8.8)

8.2.2. Case 2

The distribution of water production wells in case 2 on the basis of the groundwater use with their corresponding production volumes (in Mm3/yr) is presented in Figure 8.9 along with the piezometric wells used for the analysis. Production wells in this area are scares and sparse, with no wells producing volumes of great significance.

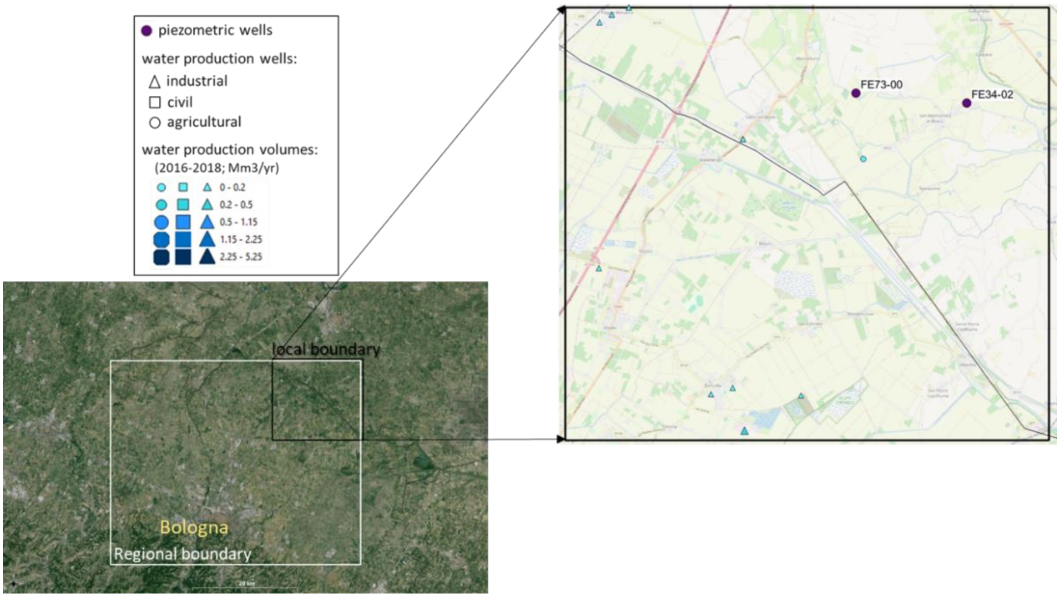

Figure 8.9: Case 2 overview.

The K-means cluster analysis of InSAR time series of the seasonal components on case 2 was performed also using 4 clusters. The outcome gave a map (Figure 8.10) and a plot (Figure 8.11) showing a very stable zone in which the majority of the MPs are in cluster 4 (purple) with an extremely average seasonal amplitude making it almost flat. Very local phenomena are depicted by clusters 2 (yellow) and 3 (green) whereas the highest coherent cluster 1 (red) refers to storage activity, analyzed later on in the chapter.

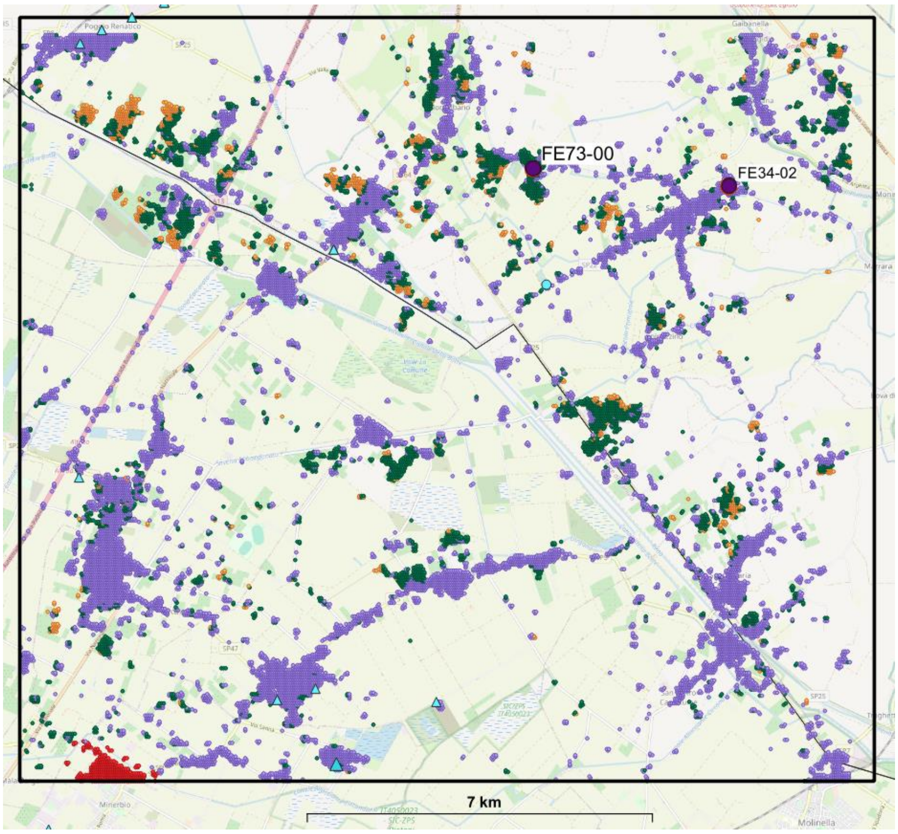

Figure 8.10: Case 2 spatial distribution of the 4 clusters from analysis. Legend same as Figure 8.9.

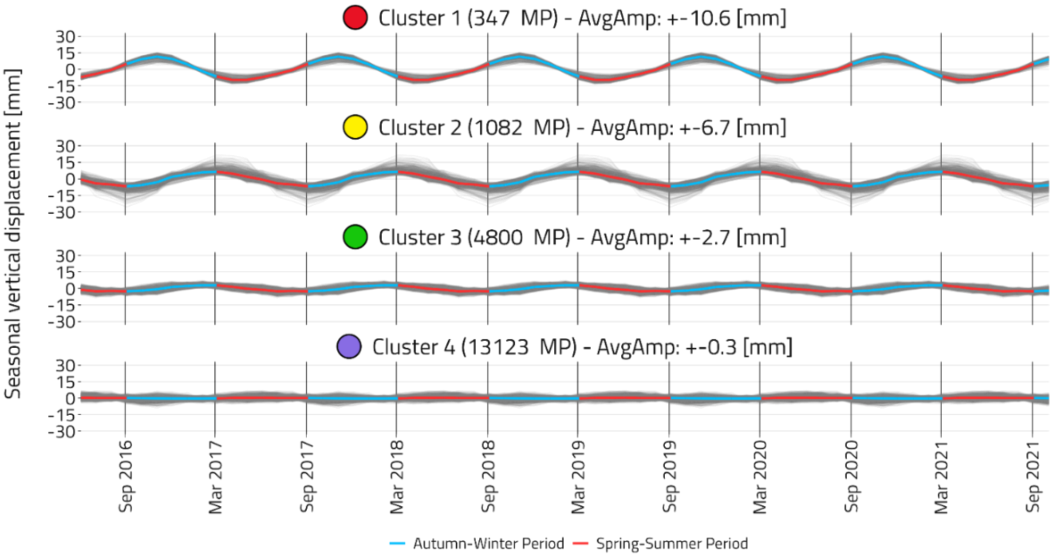

Figure 8.11: Case 2 seasonal behavior of the 4 clusters from the analysis displaying average amplitude

8.2.2.1. Piezometric level versus InSAR seasonality

The groundwater levels of the two wells, FE73-00 and FE34-02 (Figure 8.10), were used for comparison using only the method of the buffer zones. It should be noted that for both wells, the low density of piezometric data within the monitored period decreases the accuracy of the comparison.

Well FE73-00 showed the behavior of points surrounding it in a buffer zone of 100m in two different manners (Figure 8.12); cluster 1 (red) with a direct correlation with the groundwater level whereas cluster 2 (black) showing no correlation whatsoever.

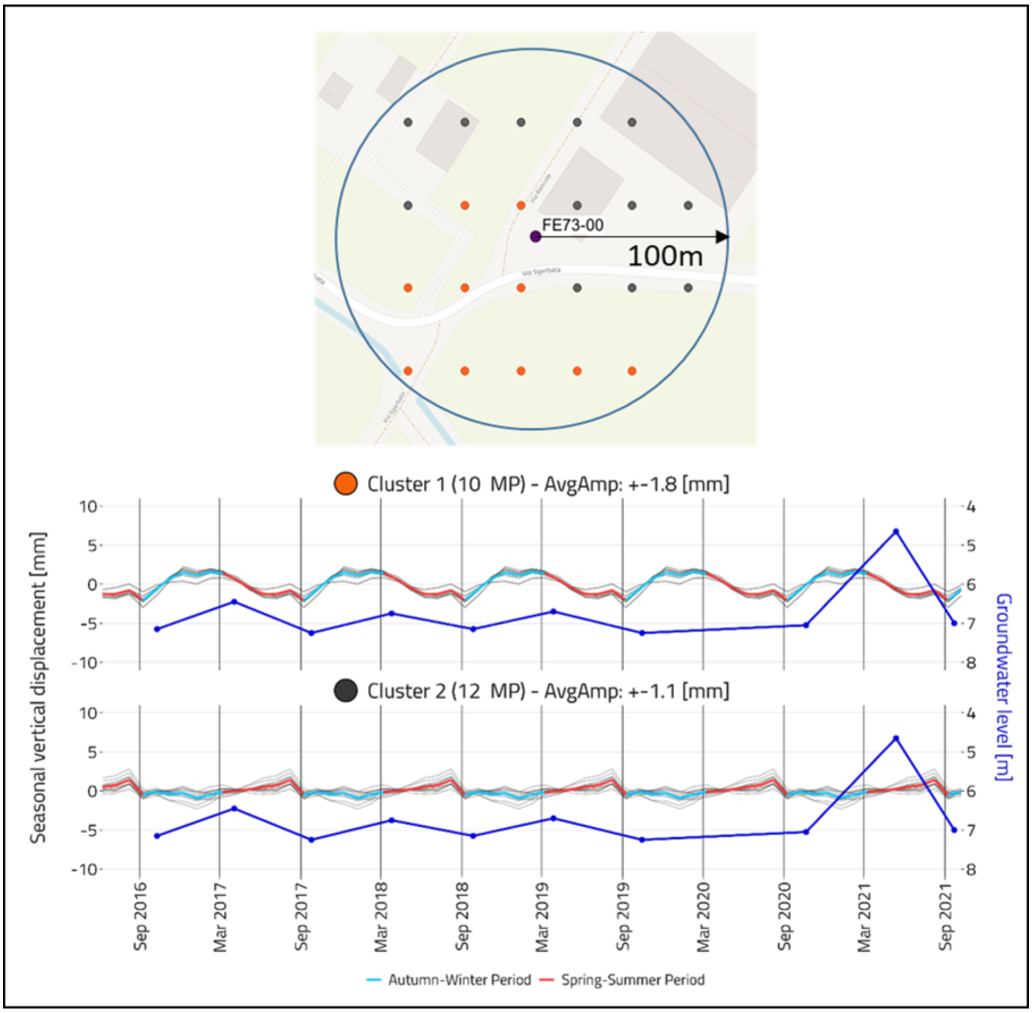

Figure 8.12: Groundwater level versus seasonal vertical displacements for well FE73-00 using MPs ground deformation seasonal component.

Well FE34-02 represented an example in which no correlation of any kind could be made due to the insufficient data from the piezometric well (Figure 8.13). However, it is important to note that the behavior of the MPs around the well were not consistent with the standard groundwater withdrawal/recharge regime.

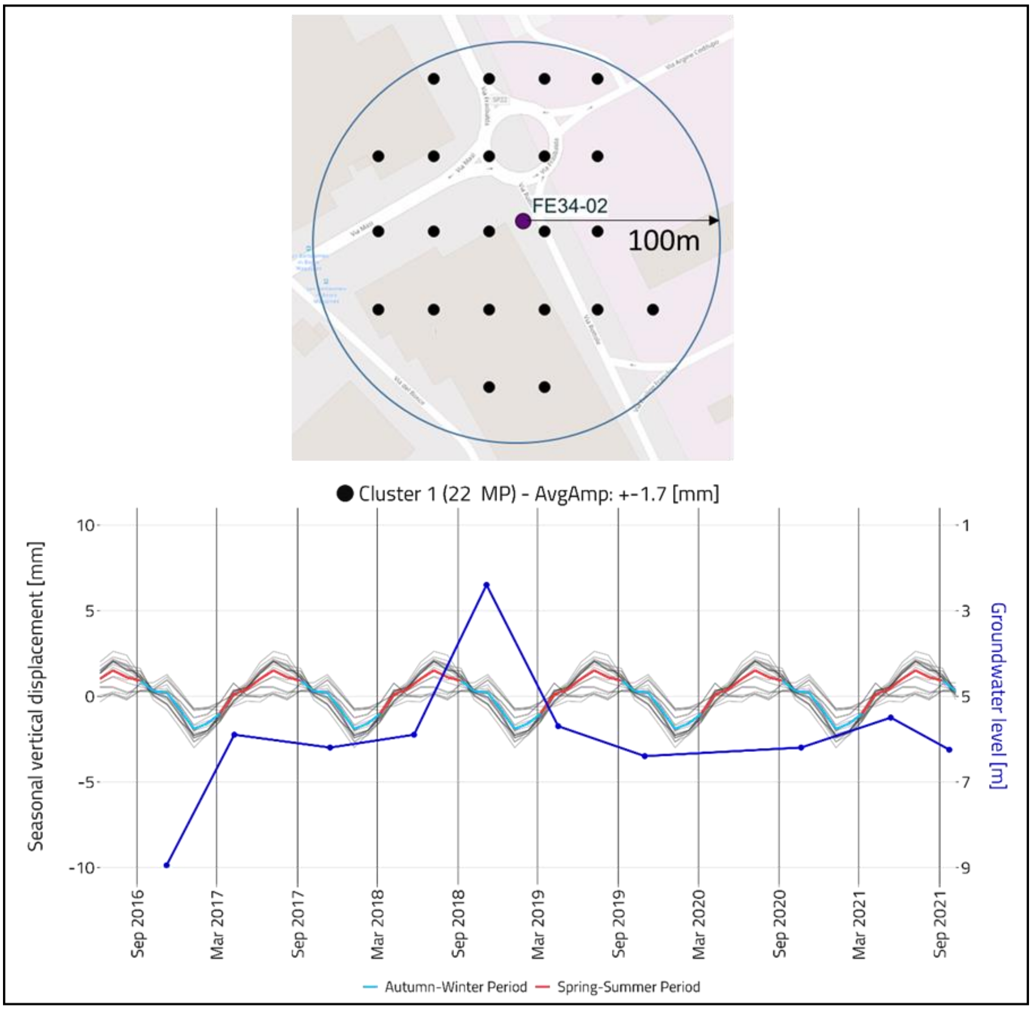

Figure 8.13: Groundwater level versus seasonal vertical displacements for well FE34-02 MPs ground deformation seasonal component.

8.2.3. Discussion

The geology of the area related to groundwater activities was then studied and used for a deeper understanding of the results.

Case 1 in the south, characterized by high concentrations of water production, is located in Reno alluvial fan (Severi, 2021) with a high thickness of sand/gravel deposits and a high areal continuity represented in the geological sections S1 and S2 in Figure 8.15. The groundwater levels of the piezometric wells in this area are consistent with the groundwater recharge/withdrawal regime with high hydraulic heads (30-50m) and are coherent with the InSAR seasonal movements. This can be attributed to the recharge of the aquifers directly from rainfall precipitation with high circulation velocities (Martinelli et al., 2017). Thus, the consistency of the seasonal component of InSAR with the groundwater regime is attributed to the high volumes of water production accompanied by fast recharge. Furthermore, the areal continuity of the sediments allows for pressure areal sink propagation also explaining the seasonal ground movement variation spread throughout all of the investigated area.

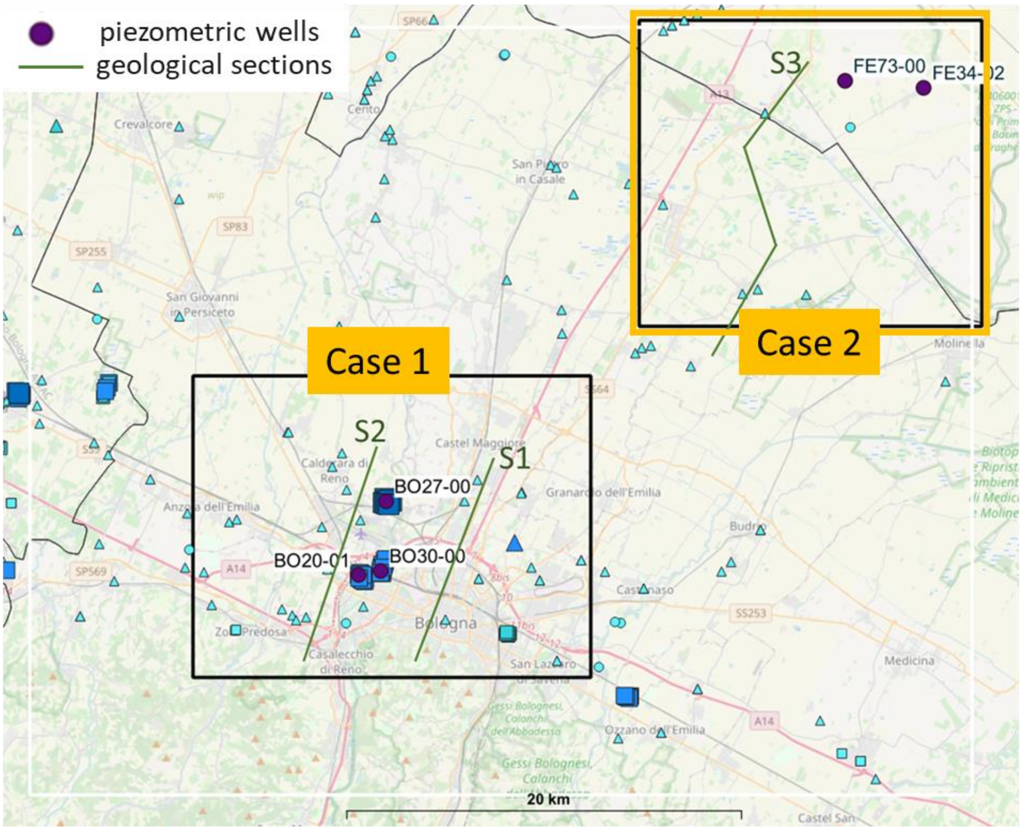

Figure 8.14: Case studies with traces of geological sections in Figure 8.15.

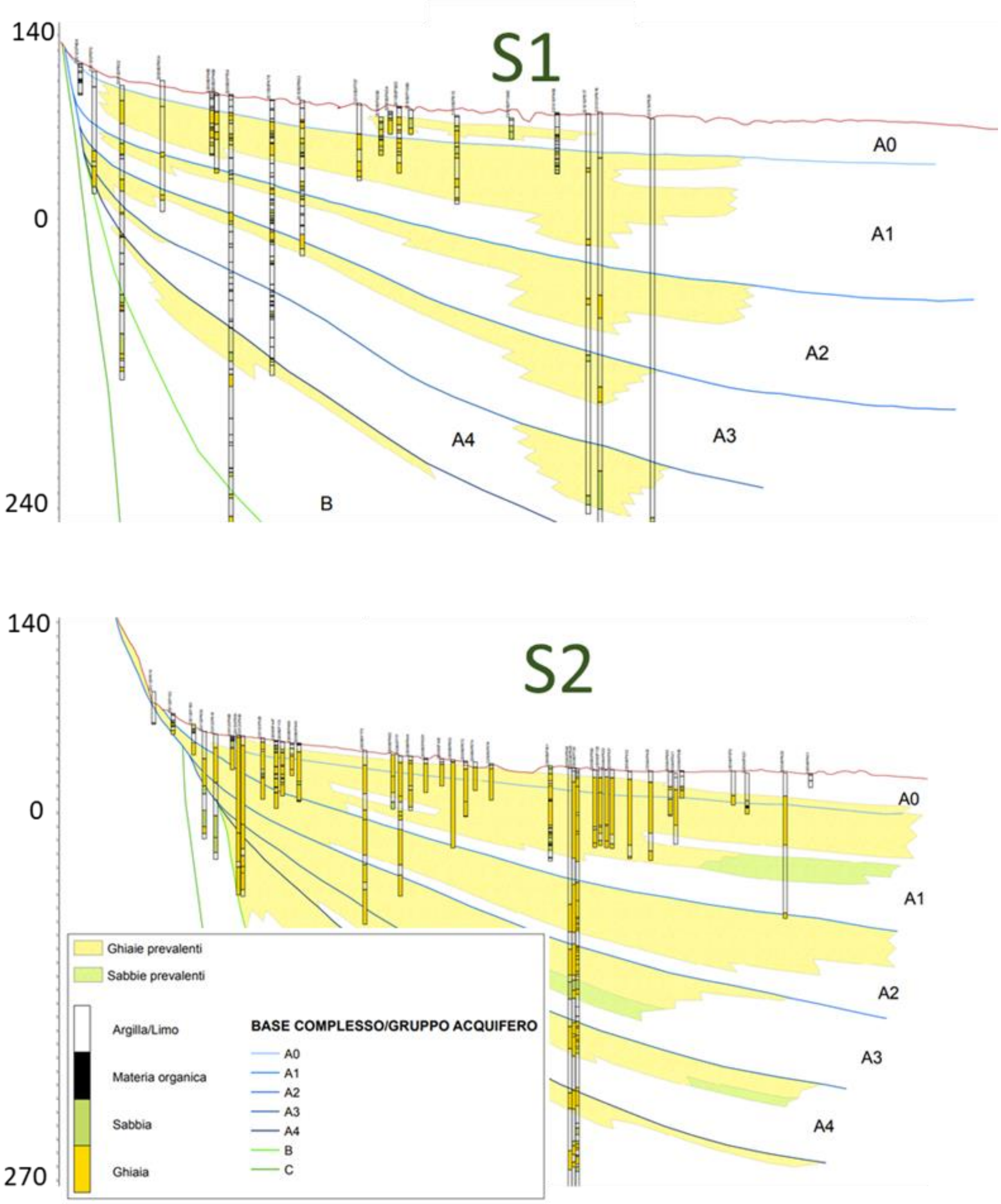

Figure 8.15: Geological sections in case 1 Reno alluvial fan (from RER database: https://servizimoka.regione.emilia-romagna.it/mokaApp/apps/pozzi_sez/index.html).

On the other hand, case 2 in the NE area is located in the Apennine and Po Plain with lower concentrations of sand/gravel deposits and low areal continuity (Figure 8.16). There is not enough data to make a direct correlation between the groundwater levels of the piezometric wells in this area and the InSAR seasonal movements but it is assumed to be a "stable" area in relation to seasonality with low hydraulic heads (2-7 m). The recharge of the aquifers in this area is by meteoric waters from Apennine and Alpine origin (Martinelli et al., 2017) and the inconsistency of the seasonal component of InSAR data with groundwater regime can be attributed to extremely low circulation velocities and lack of present-day recharge phenomena. The seasonal phenomena depicted by the cluster analysis performed on case 2 are very local due to the low areal continuity of the aquifer deposits displaying lenticular shapes.

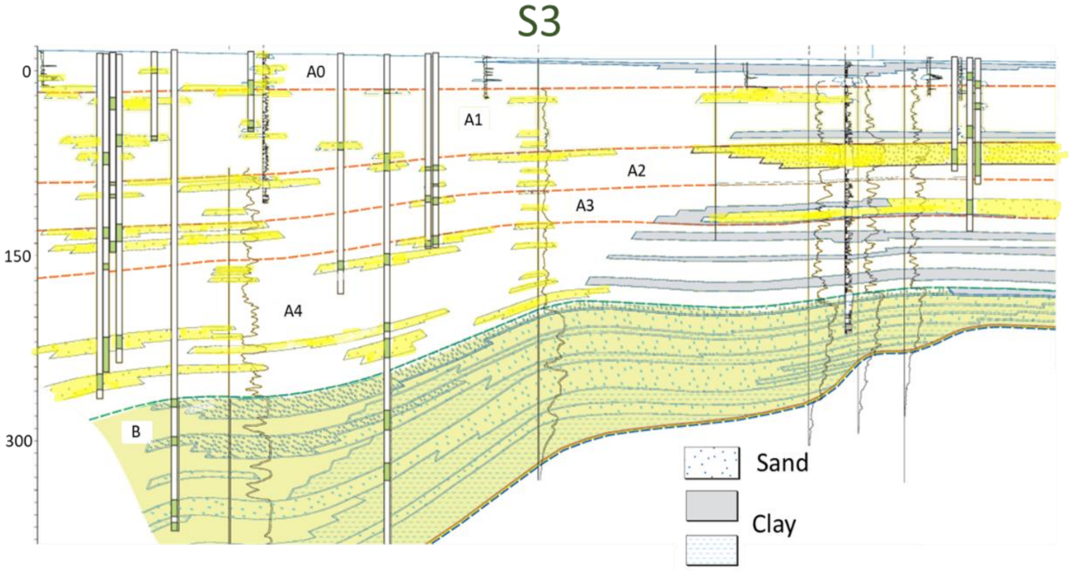

Figure 8.16: Geological section in case 2 (modified from RER database https://servizimoka.regione.emilia-romagna.it/mokaApp/apps/pozzi_sez/index.html).

8.3. Analysis of trend components

The K-means cluster analysis of InSAR time series of the trend components on the entire regional area was performed using 4 clusters. The outcome gave a map with the spatial distribution of the clusters (Figure 8.17) and a plot showing the trend behavior of each cluster with its net average displacement (Figure 8.18). The map depicts a high concentration of net displacement of up to -13.6 mm/yr (cluster 1 – red) over the investigated period [06/2016-10/2021] in the south area with the high water production volumes. The displacement decreases around this area, as shown by cluster 2 (yellow), with a gradual transition towards stable/uplift in the NE area and a more abrupt transition towards the south of Bologna. It is important to note that each cluster net value represents an average value of the centroid for the number of points in that cluster.

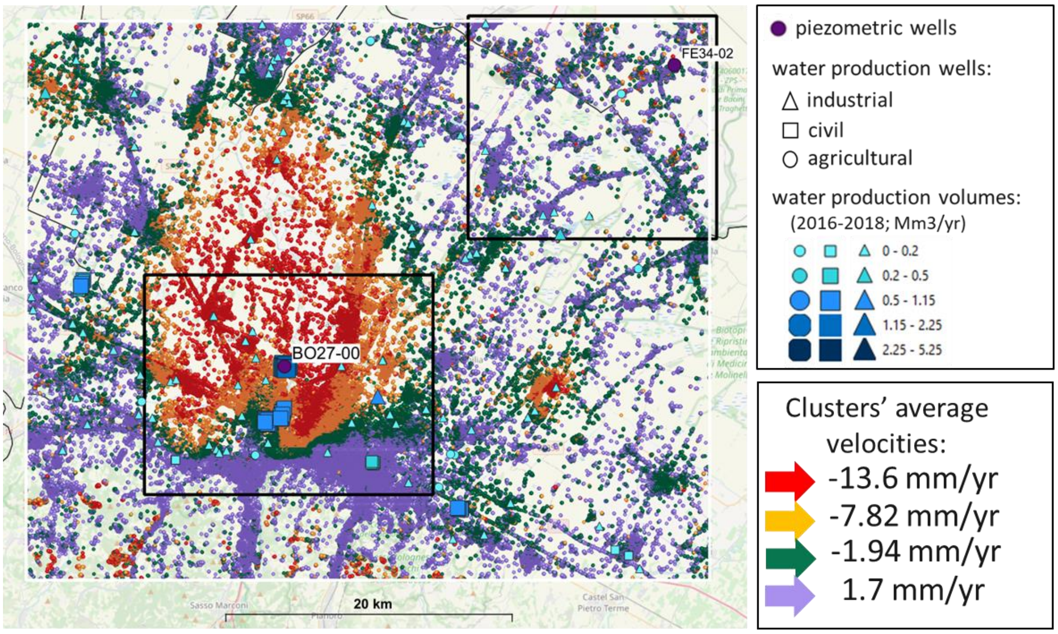

Figure 8.17: Spatial distribution of the 4 clusters from regional trend analysis with clusters' average velocities in mm/yr.

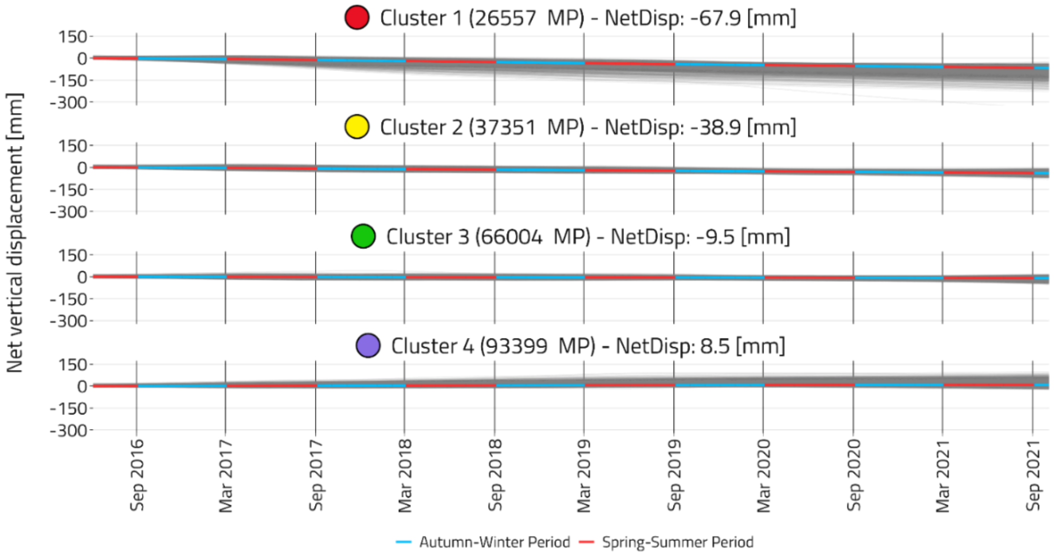

Figure 8.18: Regional trend behavior of the 4 clusters from the analysis showing net displacement over the 5-year time frame.

8.3.1. Pieozometric level versus InSAR trend

The comparison of the trend component against the groundwater level of one well in the south area-case 1 (BO27-00) and another in the NE area-case 2 (FE34-02) was performed using the buffer zone method. Although no direct correlations can be made between the two, the high net displacement associated with a continuous decrease in the trend of the groundwater level on the well to the south (Figure 8.19) is evident, whereas the well in the NE area does not display any drastic changes in the groundwater level and is associated with uplifting points (Figure 8.20), granted that the net displacement of those points are one order of magnitude lower than those subsiding in the south.

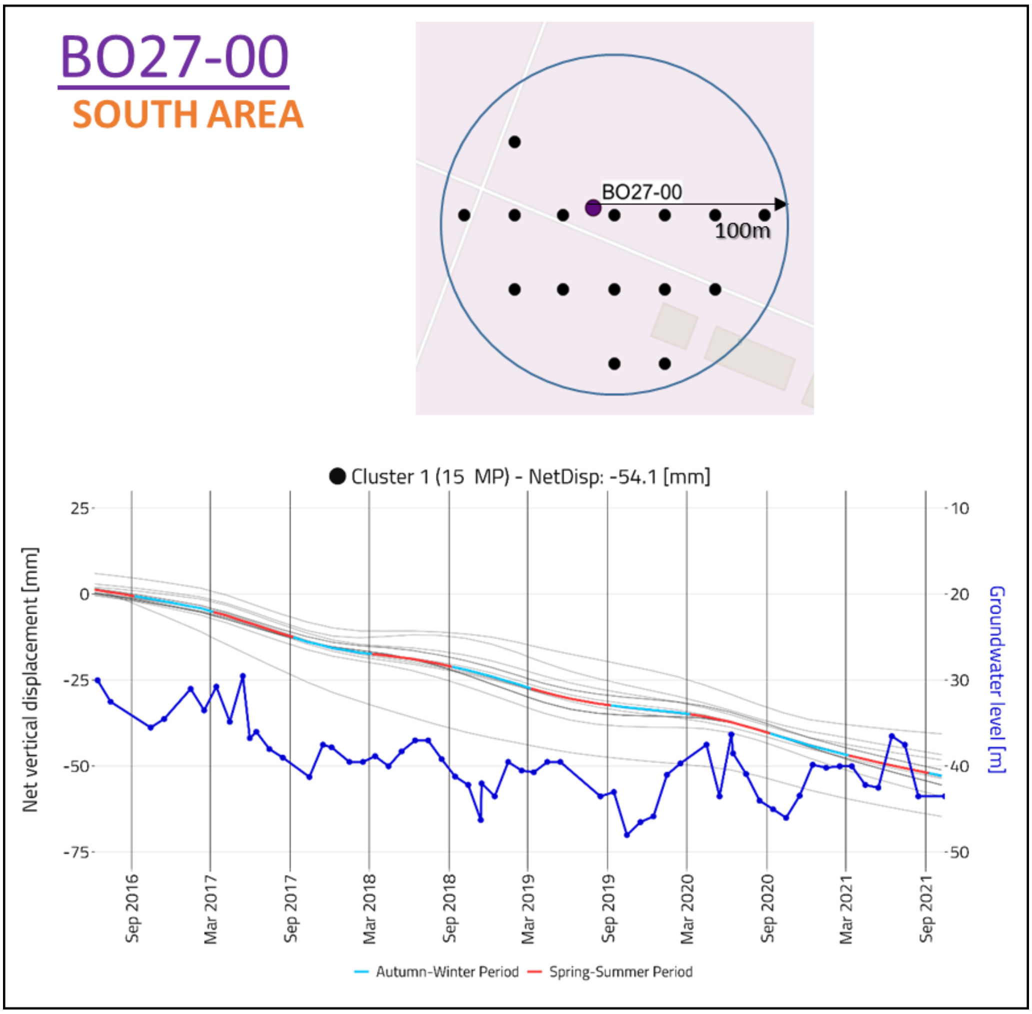

Figure 8.19: Groundwater level versus trend net vertical displacements for well BO27-00 in the south MPs ground deformation trend component.

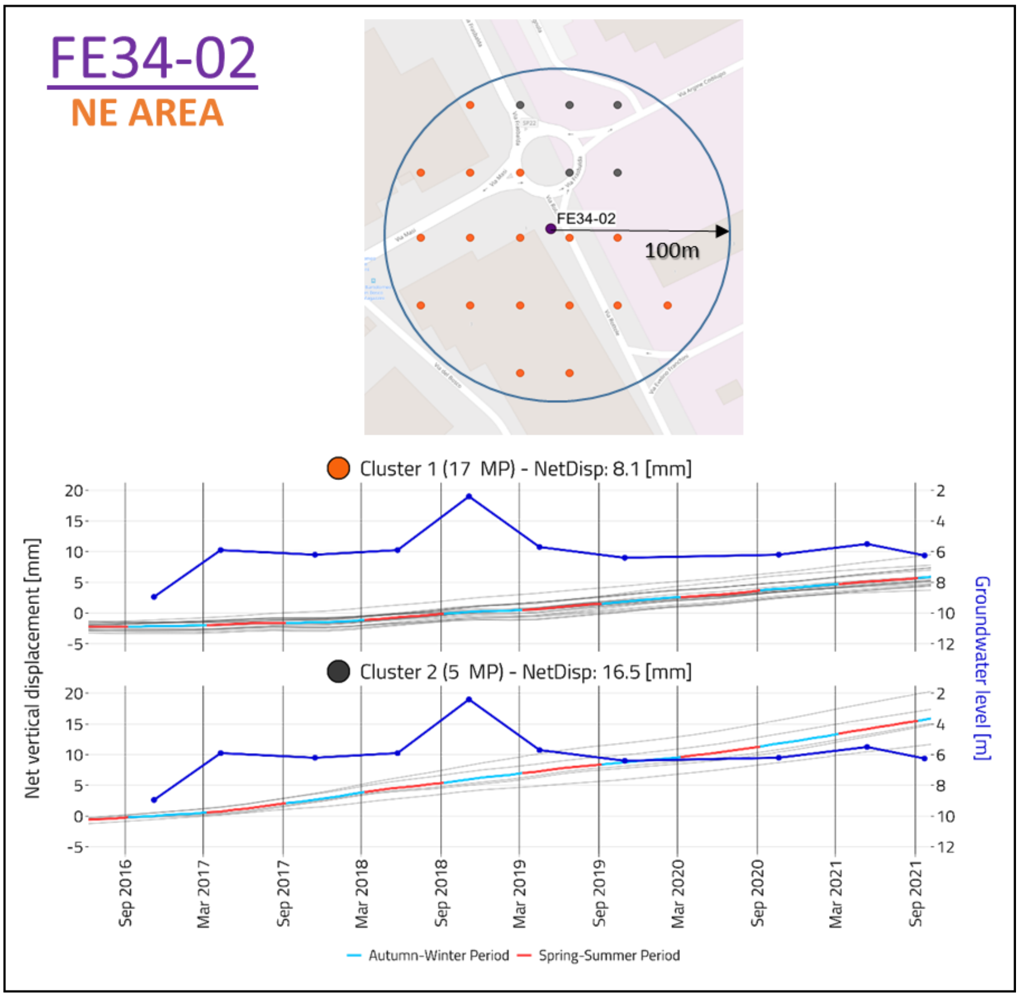

Figure 8.20: Groundwater level versus trend net vertical displacements for well FE34-02 in the NE MPs ground deformation trend component.

8.3.2. Discussion on subsidence

The results confirm the following:

- In the south, the intensive subsidence is associated with high water production and continuous recovery of groundwater levels due to the recharge of the aquifers from rainfall precipitation as discussed in section 8.2.3. Also, the area with the high net displacements coincides with the area where aquifer A’s thickness is higher (Figure 8.21). The highlighted uplift phenomenon south of Bologna was subjected to further investigation , as discussed in the following section.

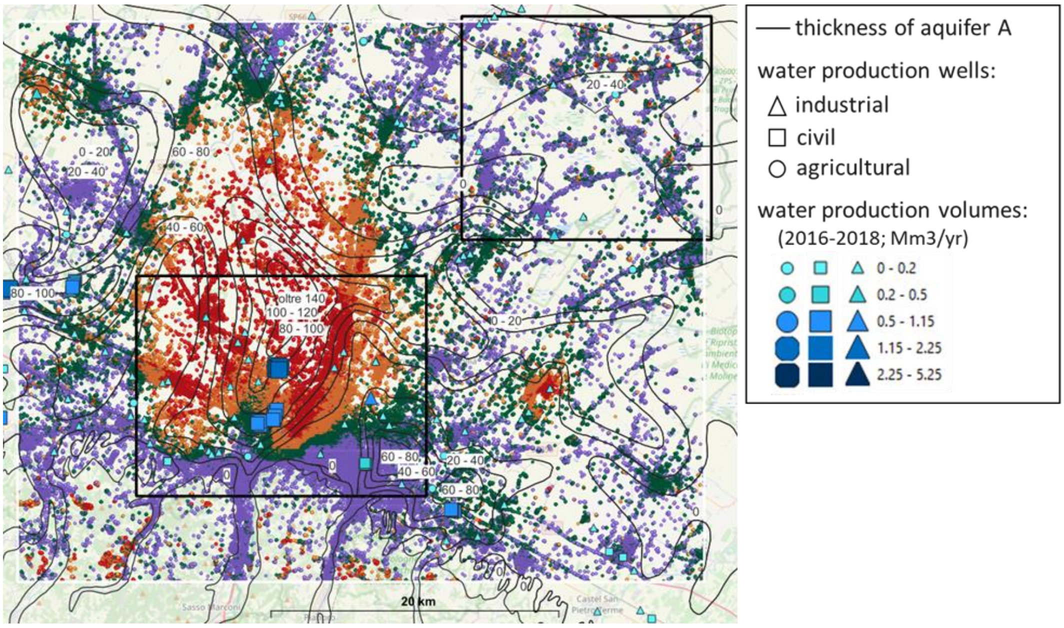

Figure 8.21: Regional trend map with contour lines of aquifer A’s thickness. Black rectangles represent cases 1 and 2.

- In the NE, low water production and no significant subsidence is observed. The groundwater levels do not undergo drastic changes. For further validation, the regional trend cluster distribution (Figure 8.17) was interpolated to produce the map in Figure 8.21. The map is used in comparison with the map published by ARPAE (2023) covering the same time-frame of our analysis (2016-2021) focalized on the Metropolitan City of Bologna (Figure 8.23).

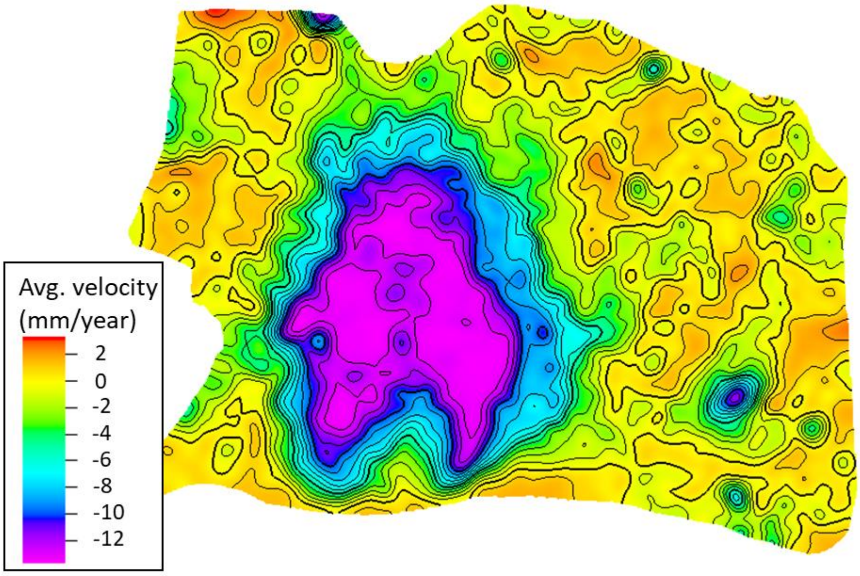

Figure 8.22: Regional trend map interpolated from the average velocities of the 4 clusters.

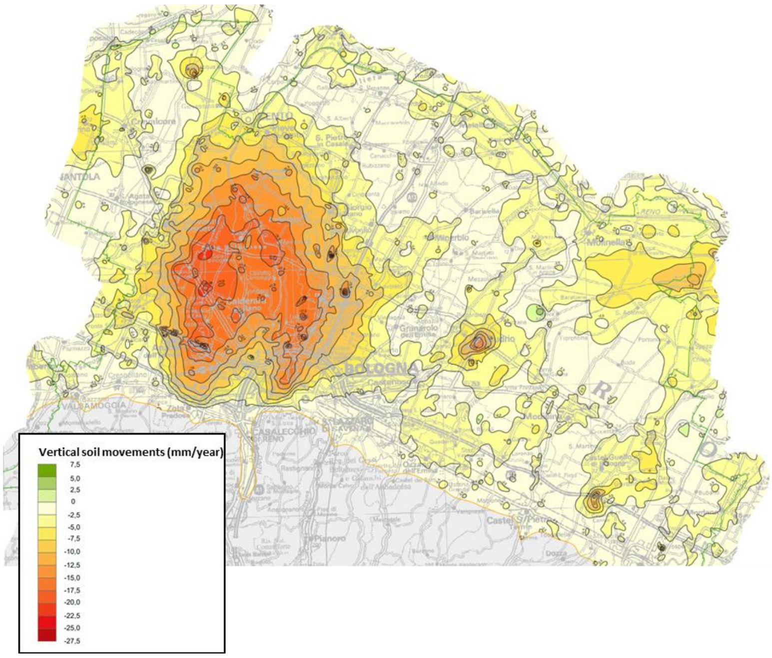

Figure 8.23: Subsidence map of the Metropolitan City of Bologna published by ARPAE (2023).

A satisfactory correlation is observed between the two maps. The subsidence concentrated in the south (city of Bologna) from ARPAE's map displays higher values up to a few millimeters from our regional trend map. This is because the values used to produce our map represent the average velocities of the 4 clusters.

8.3.3. Discussion on uplift

Cluster 4 (purple; Figure 8.17) of the trend analysis pointed out a general uplift surrounding the subsiding Bologna area. The phenomenon was further investigated with a focus on the uplifting areas of cases 1 and 2.

For case 2 (NE area), land use maps overlaying the area for the time periods 2017 and 2021 were used to try and identify any visible focal phenomena affecting the uplift of the points but the areas were mainly covered by "urban fabric" referring to buildings, roads, etc. The raw, undecomposed time series of the uplifting points in that area showed a lower magnitude as an average when compared to the average value of cluster 4 (Figure 8.18); so the uplift can be attributed to the groundwater pressure changes due to the confinement of the aquifers and the tectonic shortening phenomena affecting the geological formations of the Po Valley (Martinelli et al., 2017).

Regarding the high concentration of uplifting points in purple cluster observed and highlighted in Figure 8.24 in the southern area of the city of Bologna (case 1), the clustering analysis was re-performed on a narrow area of investigation in order to better understand and discretize the phenomena underlying that area.

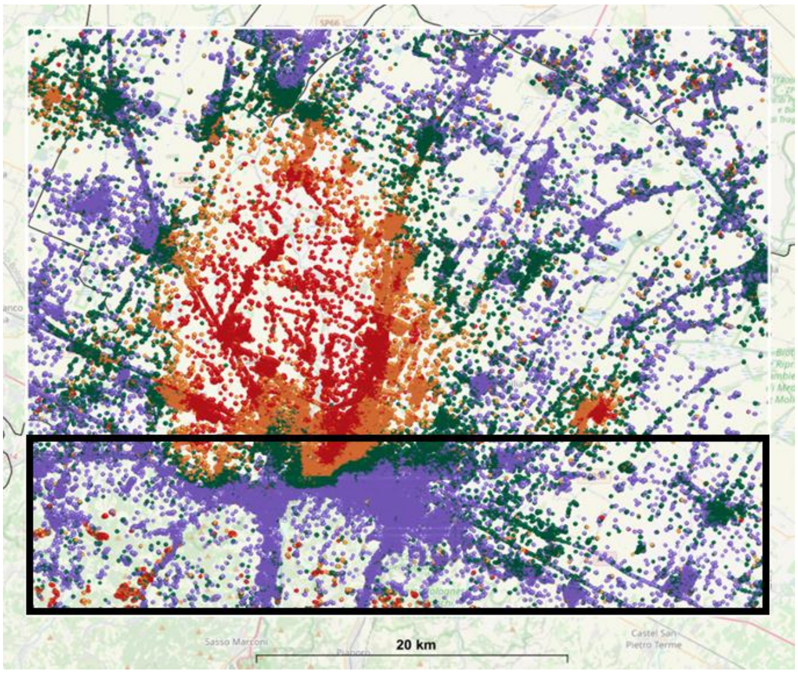

Figure 8.24: Southern area with high concentration of uplifting points highlighted. Legend same as Figure 8.16.

The outcome (Figure 8.25) showed the majority of the MPs still experiencing uplift with up to 0.4 to 3.2 mm/yr. Clusters 1 (red) and 2 (yellow) undergoing subsidence of -12.96 mm/yr and -4.22 mm/yr respectively represent a small number of MPs and are very localized.

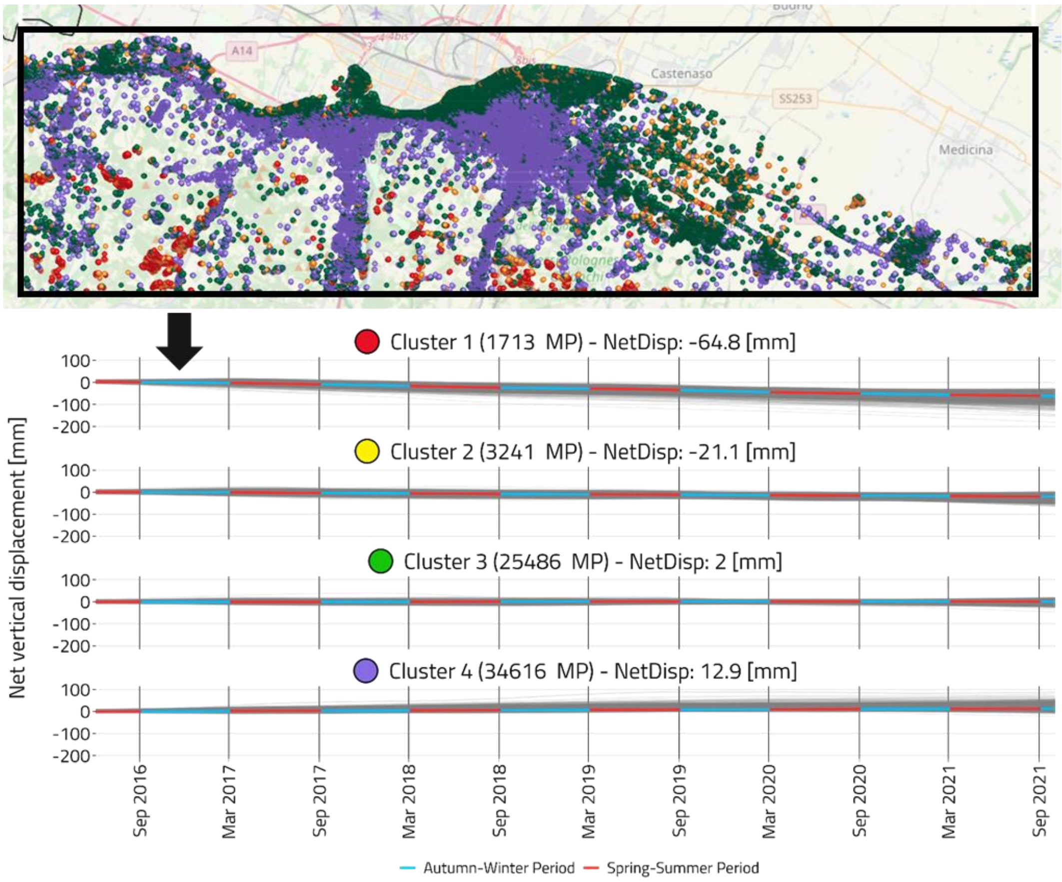

Figure 8.25: Spatial distribution and trend behavior of the 4 clusters on the southern area of the city of Bologna.

Most of the Northern Apennines, that include the area of interest, have undergone a general uplift since the early Pleistocene (Argnani et al., 2003; Giacomelli et al., 2023). Uplift observed in local ranges, such as the area of interest, is caused by the progressive eastward migration of an extensional retro-wedge and compressional pro-wedge system caused by subduction and slab rollback of the Adria plate (Lanari et al., 2023). In fact, the area of interest is affected by the activity of the Bologna anticline associated with an active blind thrust (Figure 8.26; Stramondo et al., 2007; Boccaletti et al., 2010). Even though the investigated time period is not characterized by major seismic activities, the notable uplift, in the range of up to 2 mm/yr and very close to the surface expression of the thrust, is believed to be associated with minor Holocene normal faults perpendicular to the fold axis (Figure 8.26).

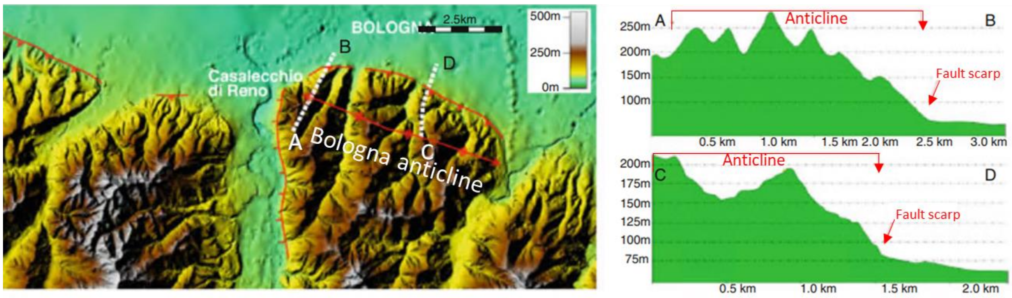

Figure 8.26: Pede-Apenninic Thrust Front and associated growing anticline in the Bologna area (from Boccaletti et al., 2010).

8.4. Case 3

The same workflow of K-means seasonal cluster analysis was applied to a third case roughly situated between cases 1 and 2 using 4 clusters. This case study was chosen based on the presence of an underground gas storage (UGS) system and its superposition with a number of industrial water wells (Figure 8.27). The in-depth description of the area and its overlying phenomena is provided in the next chapter that focuses solely on that area for the 3D numerical modelling.

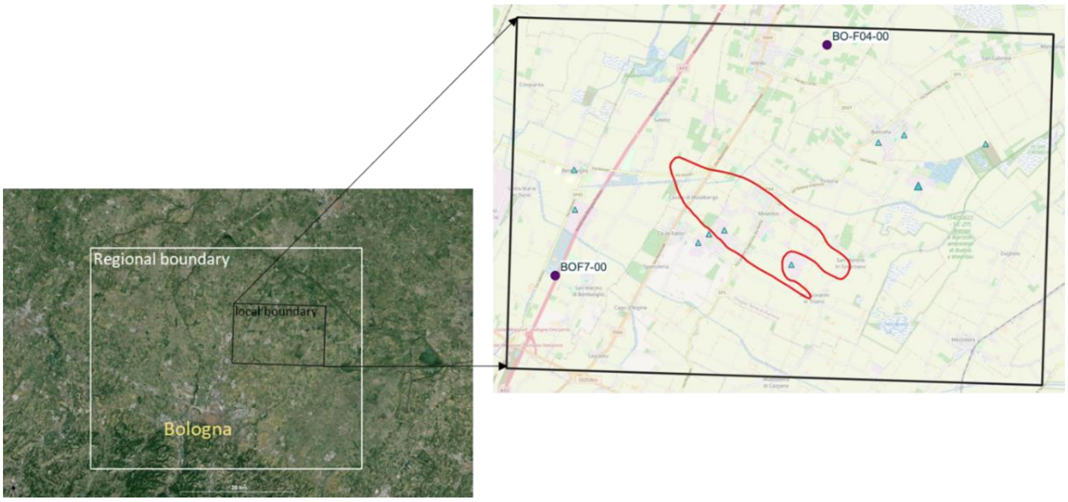

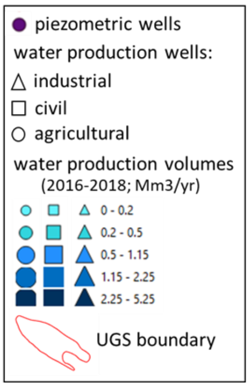

Figure 8.27: Case 3 overview.

The outcome gave a map showing the spatial distribution of the 4 clusters (Figure 8.28) and a plot showing the seasonal behavior of each cluster (Figure 8.29) with its average amplitude such that the highest number of MPs were found in cluster 4 (purple) with the lowest average seasonal amplitude.

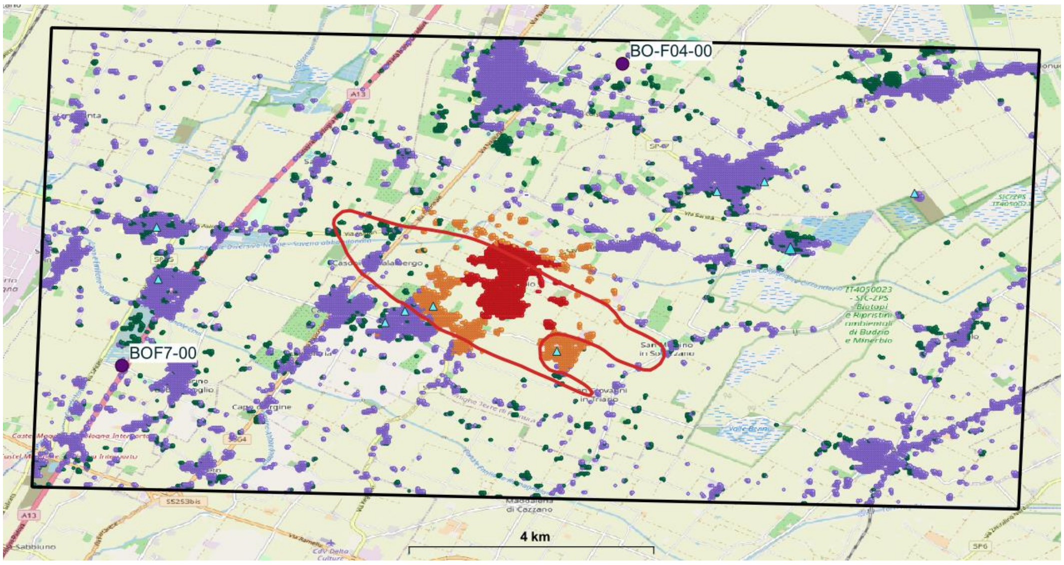

Figure 8.28: Case 3 spatial distribution of the 4 clusters from analysis. Legend same as Figure 8.27.

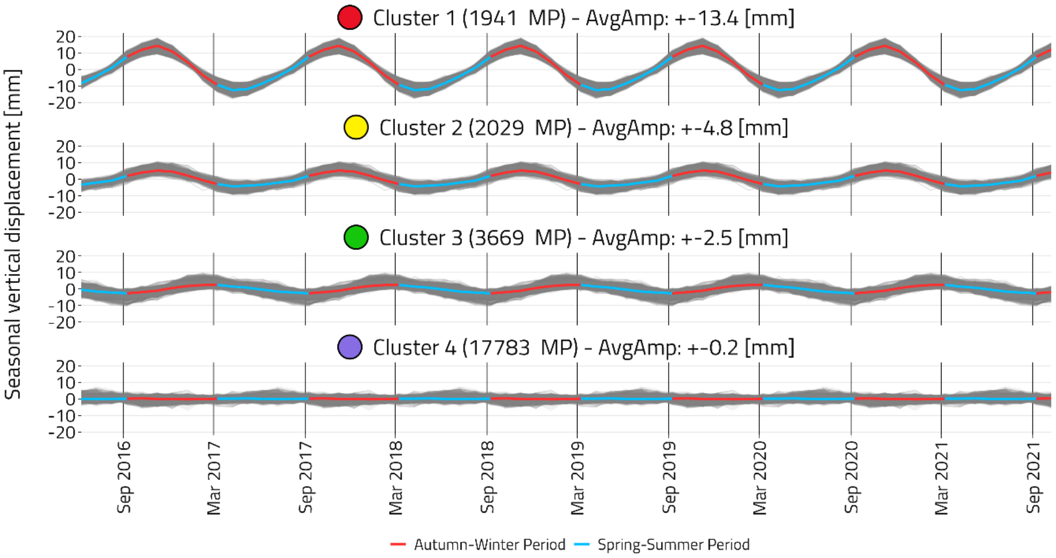

Figure 8.29: Case 3 seasonal behavior of the 4 clusters from the analysis displaying average amplitude.

The distribution of the clusters in this case obviously shows a localized concentration of 2 clusters (red and yellow in Figure 8.28) above the UGS boundary that behaves according to the to seasonal and cyclical storage demand, with an increase in the spring-summer injection period and decrease in the autumn-winter production period. The purple cluster MPs are scattered and considered "stable" due to their extremely low average seasonal amplitude of ±0.2 mm. The green cluster realistically following the behavior of groundwater withdrawal/regime is found locally surrounding some water production wells.

Concerning the trend behavior, no macro effect due to UGS could be identified.

8.4.1. Piezometric level versus seasonality

The groundwater levels of well BOF04-00 (Figure 8.28) were used for comparison using the method of the buffer zones. The comparison with the MPs seasonal behavior in the buffer zone showed an exact correlation with the seasonal behavior of the groundwater level (Figure 8.30). No correlation with UGS is present.

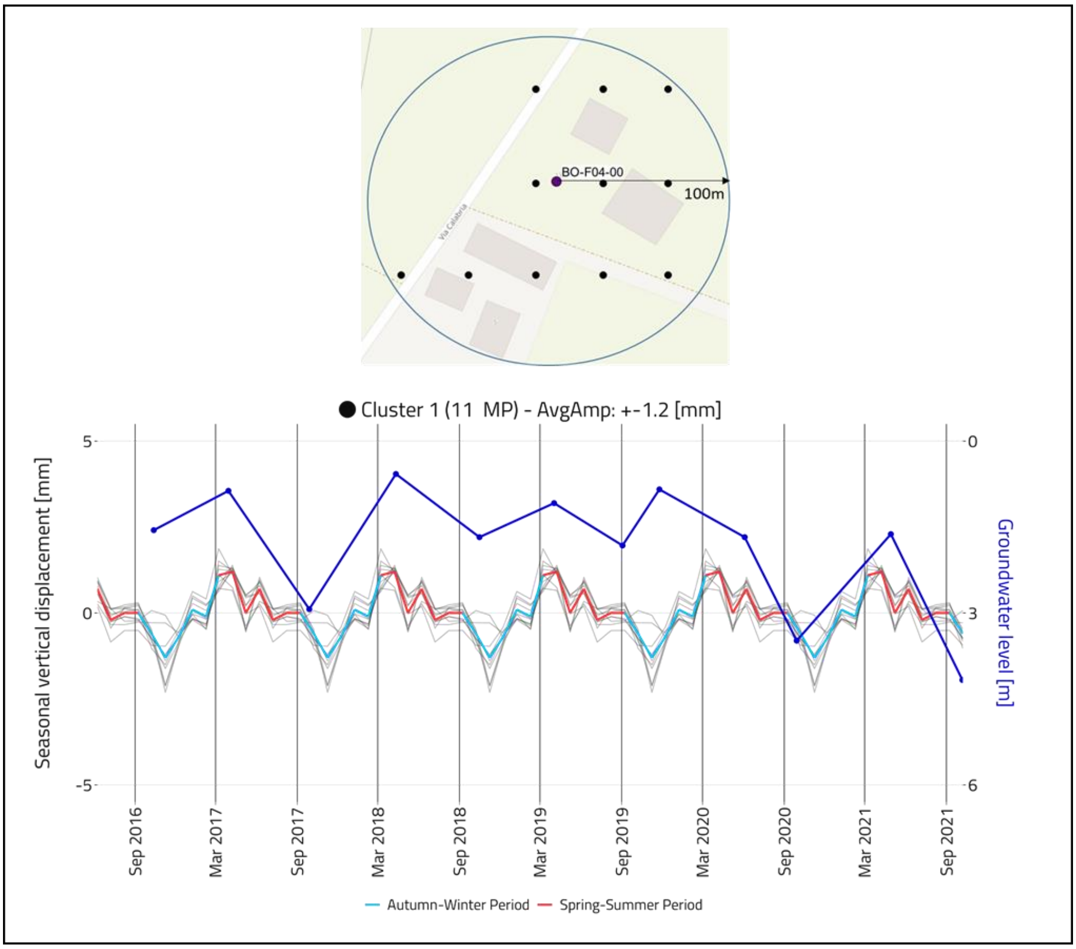

Figure 8.30: Groundwater level versus seasonal vertical displacements for well BO-F04-00 using MPs ground deformation seasonal component.

8.4.2. UGS cumulative volumes versus seasonality

The seasonal components of the time series of 3 points that lie inside the boundary of the UGS belonging to cluster 1 (red cluster; Figure 8.31) were plotted against the periodic behavior of the gas cumulative volume curve (from Benetatos et al., 2020).

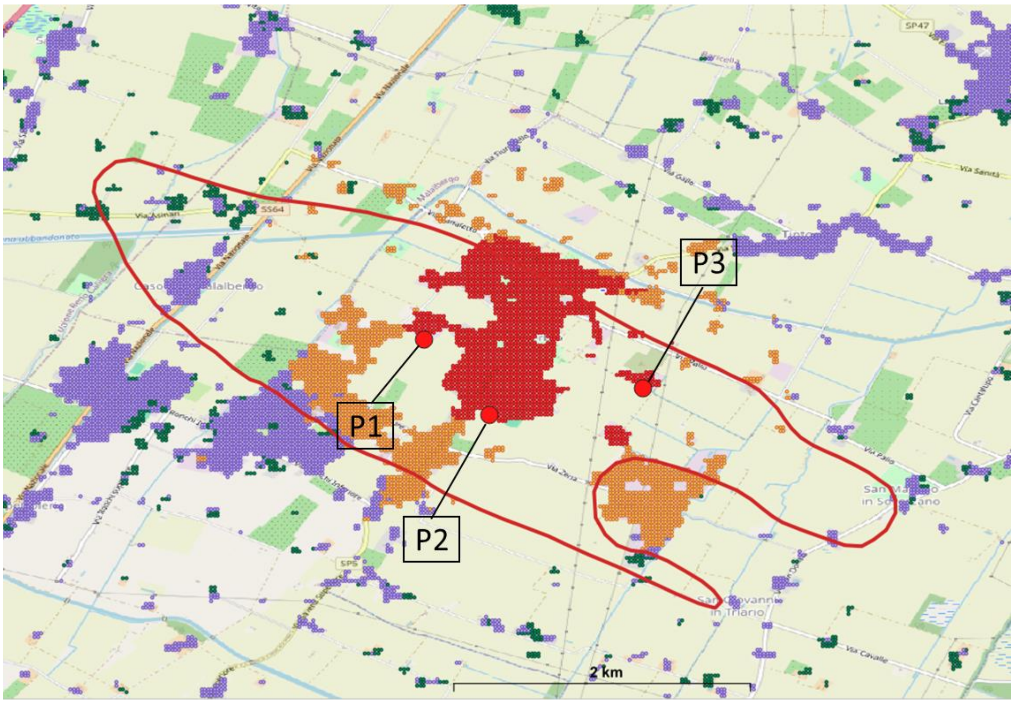

Figure 8.31: Location of points used for comparison.

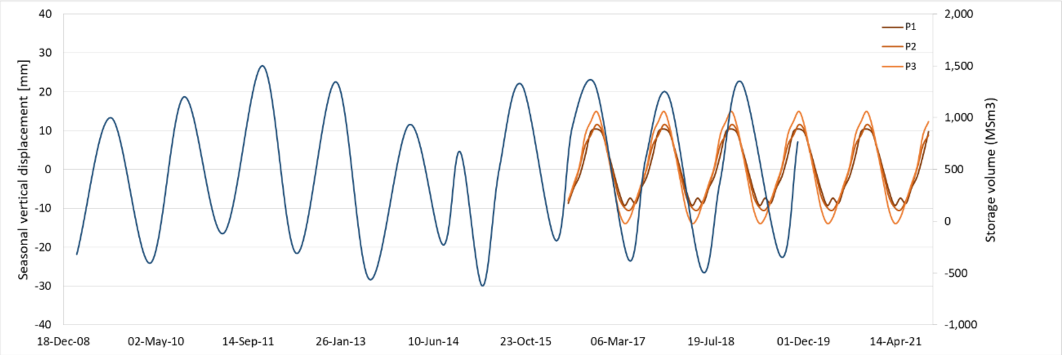

Figure 8.32: Comparison between the seasonal components of the three points inside the UGS boundary and the curve of the field gas cumulative volumes (blue line).

A strong periodic correlation is observed between both for the 3 points for the time period that the two different datasets coincide. The maximum and minimum peaks occur at the end of each injection and withdrawal period, respectively.

8.5. Summary of results

The summary of the results obtained using our multidisciplinary approach for the Metropolitan City of Bolonga are presented separately for the seasonal (Table 8.2) and trend (Table 8.3) components in relation to the average amplitude/magnitude of ground deformation related to the depicted phenomena and their areal effect. These indicate the effectiveness of our methodology in identifying and quantifying the contribution of different phenomena to the ground movements occurring the area.

Table 8.2: Summary of seasonal component analysis results.

Seasonal component				
Phenomenon		**Aquifer lateral continuity**	**Areal effect**	**Average displacement amplitude**
Groundwater activities	Large production	High	Widespread	Up to ± 2.9 mm
	Small production	Low	Very local	Up to ± 1.8 mm
UGS activities		n.a.	Very local	Very high; up to ± 13.4 mm

Table 8.3: Summary of trend component analysis results.

Trend component				
Ground deformation	**Phenomenon**		**Areal effect**	**Average magnitude**
Subsidence	Groundwater activities	Large production from laterally continuous aquifers	Widespread	-13.6 mm/yr
	UGS activities		No effect	No effect
Uplift	Tectonic activities		Zone of active structures	Up to +2 mm/yr
	UGS activities		No effect	No effect

Chapter 9

Conclusions

The Po Plain in northern Italy is a rapidly subsiding sedimentary basin characterized by a dense population and high industrial activities. It encompasses a complex geological history that created an extensive fold and fault system that hosts numerous underground hydrocarbon reservoirs and a highly exploited multilayered aquifer system. The basin has been affected by widespread land movements of natural and anthropogenic origin since the mid 20th century, which have been the focus of numerous studies.

The aim of this thesis was to investigate and quantify the superposition of natural and anthropogenic components on land movements by implementing an integrated multidisciplinary approach to a specific area of the Po Plain where surface and deep anthropogenic activities co-exist and for which a broad dataset of water production measurements, reservoir geological and petrophysical information and satellite interferometric data are available.

The key outcomes of this work can be summarized as follows:

- Coherent analysis of land movements maps available in technical literature of the Po Plain indicating (1) the uniform division of natural subsidence between long-term (such that the maximum subsidence values were recorded in areas with maximum Pleistocene sediment thickness) and short-term components, (2) their maximum effects (rates) in the east Po Delta, (3) natural uplift over buried tectonic structures, (4) the superposition of fluid production activities with areas of subsidence by the creation of a fluid production dataset of UGS and groundwater production activities, with the latter following a generally slightly decreasing trend from 2003 till 2018.

- Geological modelling of the uppermost part of the Po Plain sedimentary deposits linked to groundwater production by performing a detailed analysis on the available data. This was done by the digitization of over 600 wells for lithological classification, the digitization of contour maps for surfaces creation and the application of geostatistical methods for facies modelling for an accurate spatial description of the continuity of the aquifer bodies.
- Definition of a specific area of investigation in the Po Plain NE of Bologna that has been experiencing different but relevant anthropogenic and natural land movement phenomena.
- Dynamic simulations of aquifer behavior in the investigated area over a time-frame of 9 years (2009-2018) reproducing only the average pressure changes due to groundwater production due to the paucity of the data on the production rate distribution. Hydrodynamic parameters from literature were tuned based on a coupled iterative process for matching monitored piezometric levels of surrounding wells.
- Geomechanical simulations via the uncoupling approach based on elastic constitutive laws that solves the stress-strain relationships independently from the fluid-flow dynamics and the consequent calculation of an average behavior of subsidence due to groundwater production in the investigated area. The maximum settlement bowl reached 40 mm over the entire period and coincided with the location of three production wells with the highest production rates.
- Comparison between the simulated subsidence due to groundwater production with land movements caused by the underlying UGS in the area by comparing the simulated vertical displacement of three reference points within the UGS boundary. Groundwater production was assumed to be the main factor affecting the subsidence.
- Analysis of InSAR time series available for the investigated area by the application of an existing clustering algorithm for the identification and quantification of the physical phenomena affecting ground movements. This was done by analyzing the seasonal and trend components in correlation with groundwater production, piezometric, land use, UGS activities and geological data. In details: the areal continuity of the aquifer is significant in the Bologna area, where the majority of water production has been concentrated, and it decreases from SW to NE, where the aquifers are more confined. As a consequence, the pressure sink induced by the groundwater withdrawal and the corresponding land movements exhibit a widespread spatial distribution consistent with the high areal continuity of

the aquifers (Bologna area); whereas they show very local behavior elsewhere. This behavior can be depicted in both the seasonal and the trend components. The seasonal component, even if of low entity, identifies a widespread spatial distribution of movements induced by the water production from aquifers with high lateral continuity near Bologna; whereas it shows very local behavior towards the NE area. The trend component quantifies a strong and widespread subsidence in the Bologna area. Furthermore, it identifies and quantifies an uplift area due to tectonic activities over buried structures. Concerning UGS activities, their effect can be depicted very locally only by the seasonal component analysis, showing no evidence in the trend components.

9.1. Future research development

Based on the results reported in this thesis, the following suggestions can be considered for the development of future work:

1. Application of the coupled approach between fluid flow and the geomechanical analysis of aquifer production to address the mutual effects between petrophysical and deformation parameters. In this work, the uncoupled approach was implemented due to its proven reliability in literature but more importantly due to the lack of lab data for the accurate characterization of the mechanical parameters in the area of investigation.
2. Application of different stress-deformation models, such as Cam-Clay or Modified Cam-Clay, for simulating formation compaction due to groundwater withdrawal.
3. Numerical simulation of the aquifer and UGS systems simultaneously to further optimize the process of quantifying the superposition of effects via numerical modelling.
4. Application of InSAR time series ground deformation in correlation with other monitoring methods, i.e. extensometers, for better characterizing the deformation of the shallow layers associated with groundwater activities, and analysis of horizontal components.

References

AGIP Mineraria (1959). Campi gassiferi padani, in Atti del Convegno su Giacimenti Gassiferi dell'Europa Occidentale (Milano, 30 September–5 October 1957): Accademia Nazionale dei Lincei ed Ente Nazionale Idrocarburi, Milano (ENI), 2, 45–497.

AGIP (1977). Temperature Sotterranee: Inventario dei Dati Raccolti dall'AGIP durante la Ricerca e la Produzione di Idrocarburi in Italia: Milano, Edizioni AGIP, 1930.

Al-Awad, M.N.J. (2002). Simple Correlation to Evaluate Mohr-Coulomb Failure Criterion Using Uniaxial Compressive Strength. *Journal of King Saudi University,* 14, Eng. Sci. (1), 137-145.

Allen, D.R. (1969a). The Mechanics of Compaction and Rebound, Wilmington Oil Field, Long Beach, California, U.S.A. Technical Report, Department of Oil Properties: City of Long Beach.

Allen, S.A. (1984). Types of land subsidence. In Guidebook to Studies of Land Subsidence Due to Groundwater Withdrawal, Poland J.F. (Ed.), UNESCO: Paris, pp. 133–142.

Amadori, C., Toscani, G., Di Giulio, A., Maesano, F.E., D'Ambrogi, C., Ghielmi, M. and Fantoni, R. (2019). From cylindrical to non-cylindrical foreland basin: Pliocene-Pleistocene evolution of the Po Plain-Northern Adriatic basin (Italy). *Basin Research*, 31(5), 991–1015.

Amorosi A., Forlani M.L., Fusco F., Severi P. (2001). Cyclic patterns of facies and pollen associations from Late Quaternary deposits in the subsurface of Bologna. *GeoActa*, 1, 83-94.

Amorosi A., Colalongo M.L., Fiorini F., Fusco F., Pasini G., Vaiani S.C., Sarti G. (2004). Palaeogeographic and palaeoclimatic evolution of the Po Plain from 150-ky core records. *Global and Planetary Change*, 40, 55-78.

Amorosi, A., Centineo, M.C., Colalongo, M.L., Fiorini, F. (2005). Millennial-scale depositional cycles from the Holocene of the Po Plain, Italy. *Marine Geology*, 222-223, 7-18.

Amorosi, A. & Colalongo, M.L. (2005). The linkage between alluvial and coeval nearshore marine succession: evidence from the Late Quaternary record of the Po River Plain, Italy. In: Blum M.D., Marriott S.B., Leclair S.F. (Eds.), Fluvial Sedimentology VII. International Association of Sedimentologists, Special Publication, 35, 257-275.

Amorosi, A., Pavesi, M., Ricci Lucchi, M., Sarti, G., and Piccin, A (2008a). Climatic signature of cyclic fluvial architecture from the Quaternary of the central Po Plain, Italy. *Sedimentary Geology,* 209, 58-68.

Amorosi, A., Dinelli, E., Rossi, V., Vaiani, S.C. & Sacchetto, M. (2008b). Late Quaternary palaeoenvironmental evolution of the Adriatic coastal plain and the onset of the Po River Delta. *Palaeogeography, Palaeoclimatology, Palaeoecology*, 268, 80-90.

Amorosi, A. & Pavesi, M. (2010). Aquifer stratigraphy from the middle-late Pleistocene succession of the Po Basin. *Memorie Descrittive della Carta Geologica d'Italia,* XC, pp. 7-20.

Amorosi, A., Bruno, L., Rossi, V., Severi, P., Hajdas, I. (2014). Paleosol architecture of a late Quaternary basin–margin sequence and its implications for high-resolution, non-marine sequence stratigraphy. *Global and Planetary Change,* 112, 12–25.

Arca, S., Beretta, G.P. (1985). Prima sintesi geodetico-geologica sui movimenti verticali del suolo nell'Italia settentrionale. *Bollettino di Geodesia e Scienze Affini* XLIV, 2.

Argnani, A., Barbacini, G., Bernini, M., Camurri, F., Ghielmi, M., Papani, G., Rizzini, F., Rogledi, S., Torelli, L. (2003). Gravity tectonics driven by Quaternary uplift in the Northern Apennines: insights from the La Spezia-Reggio Emilia geo-transect. *Quaternary International,* 101–102 (2003) 13–26.

ARPAE (Agenzia Prevenzione Ambientale Energia Emilia-Romagna); 2007: Rilievo della subsidenza nella pianura emiliano-romagnola. Analisi interferometrica anno: 2007.

ARPAE (Agenzia Prevenzione Ambientale Energia Emilia-Romagna); 2012. Rilievo della subsidenza nella pianura emiliano-romagnola - seconda fase anno: 2012.

ARPAE (Agenzia Prevenzione Ambientale Energia Emilia-Romagna); 2018a. Rilievo della subsidenza nella pianura emiliano-romagnola - seconda fase, Bologna, 2018.

ARPAE (Agenzia Prevenzione Ambientale Energia Emilia-Romagna); 2023. Monitoraggio dei movimenti verticali del suolo e aggiornamento della cartografia di subsidenza nella pianura dell'Emilia-Romagna, Periodo 2016-2021, Bologna, 2023.

ARPAE & Regione Emilia-Romagna (2007). Elaborazione ed analisi dati raccolti sulle acque superficiali e sottertanee a livello locale per lo sviluppo dei piani di tutela delle acque – Attività B. Bologna, March 2007.

Bagheri-Gavkosh, M., Hosseini, S.M., Ataie-Ashtiani, B., Sohani, Y., Ebrahimian, H., Morovat, F., Ashrafi, S. (2021). Land Subsidence: A Global Challenge. *Science of the Total Environment,* 778, 146193.

Barchi, M.R., Minelli, G., Pialli, G. (1998). The CROP 03 profile: A synthesis of results on deep structures of the northern Apennines. *Memorie descrittive della Carta Geologica d'Italia*, 52, 383-400.

Bates, R.L. & Jackson, J.A. (1980). Glossary of Geology. American Geological Institute, Falls Church, Virginia, 749 pp.

Baù, D., Gambolati, G., Teatini, P. (1999). Residual land subsidence over depleted gas fields in the northern Adriatic basin. *Environmental & Engineering Geoscience*, 5(4), 389–405.

Berardino, P., Fornaro, G., Lanari, R., Sansosti, E. (2002). A new algorithm for surface deformation monitoring based on small baseline differential SAR interferograms. *IEEE Transactions on Geoscience and Remote Sensing*, 40(11), 2375–2383.

Benetatos, C., Codegone, G., Ferraro, C., Mantegazzi, A., Rocca, V., Tango, G., Trillo, F. (2020). Multidisciplinary Analysis of Ground Movements: An Underground Gas Storage Case Study. *Remote Sensing,* 12, 3487.

Biot, M.A. (1941). General Theory of Three-Dimensional Consolidation. *Journal of Applied Physics*, 12, 155–164.

Biot, M. A. (1955). Theory of elasticity and consolidation for a porous anisotropic solid. *Journal of Applied Physics*, 26(2), 182–185.

Bitelli, G., Bonsignore, F., Unguendoli, M. (2000). Levelling and GPS networks for ground subsidence monitoring in the southern Po Valley. *Journal of Geodynamics*., 30, 355-369.

Bitelli, G., Bonsignore, F., Del Conte, S., Novali, F., Pellegrino, I., Vittuari L. (2014). Integrated use of advanced InSAR and GPS data for subsidence monitoring. In: Lollino G., Manconi A., Guzzetti F., Culshaw M., Bobrowsky P.T. and Luino F. (eds), *Engineering Geology for Society and Territory*, Springer, Berlin, Germany, Vol. 5, pp. 147-150.

Bitelli, G., Bonsignore, F., Pellegrino, I., Vittuari L. (2015). Evolution of the techniques for subsidence monitoring at regional scale: the case of Emilia-Romagna Region (Italy). Proceedings of the International Association of Hydrological Sciences, 372, 315-321.

Boaga, G. (1957). Sugli abbassamenti del delta padano. *Metano, Petrolio e Nuove Energie*, 6.

Boccaletti, M., Corti, G., Martelli, L. (2010). Recent and active tectonics of the external zone of the Northern Apennines (Italy). *International Journal of Earth Sciences*.

Borchers, J.W. & M. Carpenter (2014). Land Subsidence from Groundwater Use in California, Full Report of Findings. California Water Foundation, 151 pages.

Bortolami, G. C., Fontes, J. C., Markgraf, V., Saliege, J. F. (1977). Land, sea and climate in the northern Adriatic region during late pleistocene and holocene. *Paleogeography, Paleoclimatology, Paleoecology*, 21, 139–56.

Bortolami, G., Carbognin, L., Gatto, P. (1984). The natural subsidence in the lagoon of Venice, Italy. In Land Subsidence (Proceedings of the III International Symposium on Land Subsidence), Venice, March 1984.

Brunetti, A., Denèfle, M., Fontugne, M., Hatté, C., Pirazzoli, P. A. (1998). Sea-level and subsidence data from a Late Holocene back-barrier lagoon (Valle Standiana, Ravenna, Italy). *Marine Geology*, 150, 29–37.

Bruno, L., Campo, B., Costagli, B., Stouthamer, E., Teatini, P., Zoccarato, C., Amorosi, A. (2020). Factors controlling natural subsidence in the Po Plain. Proceedings of IAHS, 382, 285-290.

Bürgmann, R., Rosen, P.A., Fielding, E.J. (2000). Synthetic Aperture Radar Interferometry to Measure Earth's Surface Topography and its Deformation. *Annual Review of Earth and Planetary Sciences,* 28, 169-209.

Burrato P., Ciucci F., Valensise G. (2003). An inventory of river anomalies in the Po Plain, Northern Italy: evidence for active blind thrust faulting. *Annals of Geophysics*, 46, 865-882.

Campo, B., Bruno, L., Amorosi, A. (2020). Basin-scale stratigraphic correlation of late Pleistocene-Holocene (MIS 5e-MIS 1) strata across the rapidly subsiding Po Basin (northern Italy). *Quaternary Science Reviews,* 237, 106300.

Caputo, M., Pieri, L., Unguendoli, M. (1970). Geometric investigation of the subsidence in the Po Delta. *Bolletino di Geofisica Teorica e Applicata*, 47.

Caputo, R., Pellegrinelli, A., Bignami, C., Bondesan, A., Mantovani, A., Stramondo, S., Russo, P. (2015). High-precision levelling, DInSAR and geomorphological effects in the Emilia 2012 epicentral area. *Geomorphology,* 235, 106-117.

Carbognin, L., Gatto, P., Mozzi, G., Gambolati, G., Ricceri, G. (1977). New trend in the subsidence of Venice, in Land Subsidence. Proceedings of II International Symposium on Land Subsidence, edited by J. C. Rodda, IAHS Publ., 121, 65 – 81.

Carbognin, L., Gatto, P., Mozzi, G. (1981). La riduzione altimetrica del territorio Veneziano e le sue case. In Commissione di Studio dei Provvedimenti per la Conservazione e Difesa della Laguna e della Citt*à* di Venezia – Rapporti e Studi, Istituto Veneto di Scienze, Lettere ed Arti, Venezia, volume VIII, 55-80.

Carbognin, L., Gatto, P., Mozzi, G. (1984). Case history no.9.15: Ravenna, Italy. In Guidebook to Studies of Land Subsidence due to Ground-Water Withdrawal; Poland, J.F., Ed.; UNESCO: Paris, France, 1984; pp. 291–305.

Carminati, E & Di Donato, G. (1999). Separating natural and anthropogenic vertical movements in fast subsiding areas: the Po plain (N. Italy) case. *Geophyiscal Research Letters*, 26(15), 2291-2294.

Carminati, E. & Martinelli, G. (2002). Subsidence rates in the Po Plain, northern Italy: the relative impact of natural and anthropogenic causation. *Engineering Geology*, 66, 241-255.

Carminati, E., Doglioni, C., Scrocca, D. (2003). Apennines subduction-related subsidence of Venice (Italy). *Geophyiscal Research Letters*, 30(13), 1717.

Carminati, E., Martinelli, G., and Severi, P. (2003b). Influence of glacial cycles and tectonics on natural subsidence in the Po Plain (Northern Italy): Insights from ^{14}C ages. *G*^{3}*,* 4(10), 1082.

Carminati, E., Doglioni, C., Scrocca, D. (2005). Magnitude and causes of long-term subsidence of the Po plain and Venetian region. In: Fletcher CA, Spencer T (eds) Flooding and environmental challenges for Venice and its lagoon: state of knowledge. Cambridge University Press, Cambridge, pp 21–28.

Carpenter, M.C. (1993). Earth-fissure movements associated with fluctuations in groundwater levels near the Picacho Mountains, south-central Arizona, 1980-84. United States Geological Survey, Professional Paper, series 497, chapter H, 49 pages.

Casero, P. (2004). Structural setting of petroleum exploration plays in Italy. In: Geology of Italy, edited by: Crescenti, U., d'Offizi, S., Merlino, S., and Sacchi L. Special publication of the Italian geological society for the IGC32nd, Florence, 189–199.

Cassano, E., Anelli, L., Fichera, R., Cappelli, V. (1986). Pianura Padana, interpretazione integrata di dati geofisici e geologici. AGIP, San Donato Milanese, 27 pp.

Castelletto, N., Ferronato, M., Gambolati, G., Putti, M., Teatini, P. (2008), Can Venice be raised by pumping water underground? A pilot project to help decide. *Water Resources Research*, 44, W01408.

Chahoud, A., Gelati, L., Palumbo, A., Patrizi, G., Pellegrino, I., Zaccanti, G. (2016). Groundwater flow model management and case studies in Emilia-Romagna (Italy). *Acque Sotterranee - Italian Journal of Groundwater* (2013) - AS04019: 059 – 073.

Cigna, F. & Tapete, D. (2021). Sentinel-1 InSAR Survey to Constrain Subsidence-Induced Surface Faulting and Quantify its Induced Risk in Major Cities of Central Mexico. EGU General Assembly 2021, 19–30 April 2021, EGU21-15723.

Cleveland, R. B., Cleveland, W. S., McRae, J. E., Terpenning, I. (1990). STL: A Seasonal-Trend Decomposition Procedure Based on Loess (with Discussion). *Journal of Official Statistics*, 6, 3-73.

Comerlati, A., Ferronato, M., Gambolati, G., Putti, M., Teatini, P. (2004). Saving Venice by sea water. *Journal of Geophysical Research,* 109, F03006.

Costantini, M. & Rosen, P.A. (1999). A generalized phase unwrapping approach for sparse data. Proceedings of International Geoscience and Remote Sensing Symposium '99, pp.267−269, Germany:Hamburg.

CNR-IREA website. Differential Synthetic Aperture Radar Interferometry. http://www.irea.cnr.it/en/index.php?option=com_k2&view=item&id=77:differential-synthetic-aperture-radar-interferometry&Itemid=139

Dehghani, M., Zoej, M.J.V., Hooper, A., Hanssen, R.F., Entezam, I., Saatchi, S. (2013). Hybrid conventional and Persistent Scatterer SAR interferometry for land subsidence monitoring in the Tehran Basin, Iran. *ISPRS Journal of Photogrammetry and Remote Sensing*, 79, 157–170.

Deltares (2015). “Sinking cities”. www.deltares.nl

Doglioni, C. (1993). Some remarks on the origin of foredeeps. *Tectonophysics*, 288, 1–20.

Eid, C., Benetatos, C., Rocca, V. (2022). Fluid Production Dataset for the Assessment of the Anthropogenic Subsidence in the Po Plain Area (Northern Italy). *Resources*, 11, 53.

Elmi, C., Forti, P., Nesci, O., Savelli, D. (2003). La risposta dei processi geomorfologici alle variazioni ambientali nella pianura padana e veneto-friulana, nelle pianure minori e sulle coste nord e centro-adriatiche. In: Biancotti, A. & Motta M. (eds.), MIUR - «Risposta dei processi geomorfologici alle variazioni arnbientali». Atti Conv. Bologna 10-11 Feb. 2000, Brigati, Genova, 225-260.

Fantoni, R., Franciosi, R. (2010b). Tectono-sedimentary setting of the Po Plain and Adriatic foreland. *Rendiconti Lincei*, 21 (1), S197–S209.

Fantoni, R., Galimberti, R., Ronchni, P., Scotti, P (2011). Po Plain Petroleum Systems: Insights from Southern Alps outcrops (North Italy). In Proceedings of the AAPG International Conference & Exhibition, Milan, Italy, 23–26 October 2011.

Farina, M., Marcaccio, M., Zavatti, A. (2014). Esperienze e Prospettive nel Monitoraggio Delle Acque Sotterranee. Il Contributo dell'Emilia-Romagna; Pitagora Editrice: Bologna, Italy. ISBN 88-371-1859-7.

Ferronato, M., Gambolati, G., Teatini, P. (2003). Unloading-reloading uniaxial compressibility of deep reservoirs by marker measurements. Proceedings of 11th International Symposium on Deformation Measurements, edited by S. C. Stiros and S. Pytharouli, pp. 341 – 346, Patras Univ. Publ., Patras, Greece.

Fjaer, E., Holt, R.M., Horsrud, P., Raaen, A.M. Risnes, R. (2008). Petroleum Related Rock Mechanics. 2nd edition. Developments in Petroleum Science 53.

Figueroa-Vega, G.E. (1984). Case History No. 9.8, Mexico, D.F., Mexico. In Guidebook to Studies of Land Subsidence due to Groudwater Withdrawal, Poland J.F. (Ed.), UNESCO: Paris, pp. 217 – 232.

Fontes, J. C. & Bortolami, G. (1973). Subsidence of the Venice area during the past 40,000 yr. *Nature*, 244, 339–41.

Galloway, D. L. & Burbey, T. J. (2011). Review: Regional land subsidence accompanying groundwater extraction. *Hydrogeology Journal*, 19(8), pp. 1459–1486.

Galloway, D.L. (2014). The current situations and developing trend of international land subsidence research. Shanghai Land & Resources, 35 (2).

Gambolati, G. & Freeze, R.A. (1973). Mathematical simulation of the subsidence of Venice: 1. Theory. *Water Resources Research*, 9(3), 721–733.

Gambolati, G. (1973b). Equation for one dimensional vertical flow of groundwater: 2. Validity range of the diffusion equation. *Water Resources Research,* 9(5), 1385–1395.

Gambolati, G., Gatto, P., Freeze, R.A. (1974). Mathematical simulation of the subsidence of Venice. 2. Results. *Water Resources Research*, 10, 563 – 577.

Gambolati, G., Ricceri, G., Bertoni, W., Brighenti, G., Vuillermin, E. (1991), Mathematical simulation of the subsidence of Ravenna. *Water Resources Research*, 27(11), 2899 – 2918.

Gambolati, G. & Teatini, P. (1998). Numerical Analysis of Land Subsidence due to Natural Compaction of the Upper Adriatic Sea Basin. In CENAS, 103-131.

Gambolati, G., Teatini, P., Baù, D., Ferronato, M. (2000). Importance of poroelastic coupling in dynamically active aquifers of the Po river basin, Italy. *Water Resources Research,* 36(9), 2443–2459.

Gambolati, G., Teatini, P., Ferronato, M. (2005). Anthropogenic Land Subsidence. *Encyclopedia of Hydrological Sciences*, Edited by M.G. Anderson.

Gambolati, G. & Teatini, P. (2015). Geomechanics of subsurface water withdrawal and injection. *Water Resources Research*, 51, 3922–3955.

Gambolati, G. & Teatini, P. (2021). Land subsidence and its mitigation. The Groundwater Project.

Garcia Navarro, A.M., Rocca, V., Capozzoli, A., Chiosa, R., Verga, F. (2024). Investigation of ground movements induced by underground gas storages via unsupervised ML methodology applied to InSAR data. UNDER REVISION.

Geertsma, J. (1973a). A basic theory of subsidence due to reservoir compaction: the homogeneous case. *Verhandelingen Kon. Ned. Geol. Mijnbouwk. cen.,* 28, 43-62.

Geertsma, J. (1973b). Land Subsidence Above Compacting Oil and Gas Reservoirs. *Journal of Petroleum Technology.*

Ghielmi, M., Minervini, M., Nini, C., Rogledi, S. & Rossi, M. (2013). Late Miocene–Middle Pleistocene sequences in the Po Plain-Northern Adriatic Sea (Italy): The stratigraphic record of modification phases affecting a complex foreland basin. *Marine and Petroleum Geology*, 42, 50-81.

Gholinia, A., Nikkhah, M., Naderi, R. (2022). Validation of borehole extensometers in geotechnical monitoring. *Environmental Earth Sciences,* 81:312.

Giacomelli, S., Zuccarini, A., Amorosi, A., Bruno, L., Di Paola, G., Martini, A., Severi, P., Berti, M. (2023). 3D geological modelling of the Bologna urban area (Italy). *Engineering Geology*, 324, 107242.

Giambastiani, B.M.S., Antonellini, M., Oude Essink, G.H.P., Stuurman, R.J. (2007). Saltwater intrusion in the unconfined coastal aquifer of Ravenna (Italy): a numerical model. *Journal of Hydrology*, 340, 91–104.

Goldstein, R.M. (1995). Atmospheric limitations to repeat-track radar interferometry. *Geophysical Research Letters*, 22, 2517–2520.

Gould, P.L. (2013). Introduction to Linear Elasticity. 3rd edition.

Groppi, G. & Veggiani, A. (1984). Geotectonic structure of the Po plain from Venice to Ravenna, annex 1. In "Guidebook of the Eastern Po Plain (Italy)" by L. Carbognin, P. Gatto and F. Marabini.

Hallegatte, S., Green, C., Nicholls, R.J., Corfee-Morlot, J. (2013). Future flood losses in major coastal cities. *National Climate Change*, 3(9), 802-806.

Hartigan, J. A. & Wong, M. A. (1979). Algorithm AS 136: A K-Means Clustering Algorithm. *Journal of the Royal Statistical Society*, Series C (Applied Statistics), 28(1), 100–108.

Hu, R.L., Wang, S.J., Lee, C.F., Li, M.L. (2002) Characteristics and trends of land subsidence in Tanggu, Tianjin, China. *Bulletin of Engineering Geology and the Environments*, 61, 213 – 225.

Hyndman, R.J. & Athanasopoulos, G. (2021). Forecasting: principles and practice, 3rd edition, OTexts: Melbourne, Australia. OTexts.com/fpp3

Jacob, C. E. (1940). On the flow of water in elastic artesian aquifer. *Trans. AGU*, 21(2), 574–586.

Jaeger, J.C., Cook, N.G.W., Zimmerman, R.W. (2007). Fundamentals of rock mechanics.4th ed.

Johnson, A.I. Ed. (1991). Land Subsidence Proceedings of the 4th International Symposium on Land Subsidence. IAHS Publ. 200, 690 pp.

Lanari, R., Casu, F., Manzo, M., Lundgren, P. (2007). Application of the SBAS-DInSAR technique to fault creep: A case study of the Hayward fault, California. *Remote Sensing of Environment*, 109, 20–28.

Lancellotta, R. (2008). Geotechnical Engineering: Second edition.

Lewis, R. & Schrefler, B. (1978), A fully coupled consolidation model of the subsidence of Venice. *Water Resources Research*, 14(2), 223–230.

Li, D., Hou, X., Song, Y., Zhang, Y., Wang, C. (2020). Ground subsidence analysis in Tianjin (China) based on Sentinel-1A data using MT-InSAR methods. *Applied Sciences*, 10, 5514.

Livani, M., Petracchini, L., Benetatos, C., Marzano, F., Billi, A., Carminati, E., Doglioni, C., Petricca, P., Maffucci, R., Codegone, G., Rocca, V., Verga, F., & Antoncecchi, I. (2023). Subsurface geological and geophysical data from the Po Plain and the northern Adriatic Sea (north Italy). *Earth System Science Data*, 15(9), 4261.

Livio, F.A., Berlusconi, A., Michetti, A.M., Sileo, G., Zerboni, A., Trombino, L., Cremaschi, M., Mueller, K., Vittori, E., Carcano, C., Rogledi, S. (2009). Active fault-related folding in the epicentral area of the December 25, 1222 (Io=IX MCS) Brescia earthquake (Northern Italy): Seismotectonic implications. *Tectonophysics*, 476 (1–2), 320–335.

Mahmoudpour, M., Khamehchiyan, M., Nikudel, M.R., Ghassemi, M.R. (2013). Characterization of regional land subsidence induced by groundwater withdrawals in Tehran, Iran. *Geopersia*, 3(2), pages 49–62.

Mantovani, E., Viti, M., Babbucci, D., Ferrini, M., D'Intinosante, V., Cenni, M. (2009a). Quaternary geodynamics of the Apennine belt. II Quaternario, *Italian Journal of Quaternary Sciences*, 22(1), 97-108.

Mantonavi, E., Babbucci, D., Tamburelli, C., Viti, M. (2009b). A review on the driving mechanism of the Tyrrhenian–Apennines system: Implications for the present seismotectonic setting in the Central-Northern Apennines. *Tectonophysics,* 476(1), 22-40.

Manzo, M., Ricciardi, G.P., Casu, F., Ventura, G., Zeni, G., Borgström, F., Berardino, P., Del Gaudio, C., Lanari, R. (2006). Surface deformation analysis in the Ischia Island (Italy) based on spaceborne radar interferometry. *Journal of Volcanology and Geothermal Research*, 151, 399–416.

Martinelli, G., Minissale, A., Verruchhi, C. (1998). Geochemistry of heavily exploited aquifers in the Emilia-Romagna region (Po valley, northern Italy). *Environmental Geology*, 36, 195-206.

Martinelli, G., Dadomo, A., Italiano, F., Petrini, R., Slejko, F.F. (2017). Geochemical monitoring of the 2012 Po Valley seismic sequence: a review and update. *Chemical Geology*, 469, 147-162.

Marzano, F., Pregliasco, M., Rocca, V. (2019). Experimental characterization of the deformation behavior of a gas-bearing clastic formation: soft or hard rocks? A case study. *Geomechanics and Geophysics for Geo-Energy and Geo-Resources,* 6:10.

Mazari, M. & Alberro, J. (1990). Hundimiento de la Ciudad de México. In Problemas de la Cuenca de México; El Colegio Nacional: Ciudad de México, Mexico, pp. 83–114.

Michetti, A.M., Giardina, F., Livio, F., Mueller, K., Serva, L., Sileo, G., Vittori, E., Devoti, R., Riguzzi, F., Cercano, C., Rogledi, S., Bonadeo, L., Brunamonte, F., Fioraso, G. (2012). Active compressional tectonics, Quaternary capable faults, and the seismic landscape of the Po Plain (northern Italy). *Annals of Geophysics,* 55(5), 969-1001.

Ministero Sviluppo Economico (2020b). *Dati*. Roma, Italy. unmig.mise.gov.it/index.php/it/dati

Mitchum, J.R.M.,Vail, P.R., Thomson III, S. (1977). Seismic stratigraphy and global changes of sealevel, Part 2: The depositional sequence as a basic unit for stratigraphic analysis. In American Association of Petroleum Geologists Memoir 26; Payton, C.E., Ed.; American Association of Petroleum Geologists: Tulsa, OR, USA, 1977; pp. 53–62.

Morissette, L. & Chartier, S. (2013). The k-means clustering technique: General considerations and implementation in Mathematica. *Tutorials in Quantitative Methods for Psychology*, 9, 15-24.

Mutti, E., Davoli, G., Figoni, M., Sgavetti, M. (1994). Part 1: conceptual stratigraphic framework. In: Mutti, E., Davoli, G., Mora, S., Sgavetti, M. (Eds.), The Eastern Sector of the South-Central Folded Pyrenean Foreland: Criteria for Stratigraphic Analysis and Excursion Notes (2nd High-Resolution Sequence Stratigraphy Conference, 20e26 June 1994, Tremp, Spain), pp. 3e16.

Muttoni G., Carcano C., Garzanti E., Ghielmi M., Piccin A., Pini R., Rogledi S., Sciunnach D. (2003). Onset of major Pleistocene glaciations in the Alps. *Geology*, 31, 989-992.

Navarro-Hernández, M.I., Valdes-Abellan, J., Tomás, R., Lopez-Sanchez, J.M., Ezquerro, P., Bru, G., Bonì, R., Meisina, C., Herrara, G. (2022). ValInSAR:

A Systematic Approach for the Validation of Differential SAR Interferometry in Land Subsidence Areas. *IEEE JOURNAL OF SELECTED TOPICS IN APPLIED EARTH OBSERVATIONS AND REMOTE SENSING*, 15, 3650-3671.

Nespoli, M., Cenni, M., Belardinelli, M.E., Marcaccio, M. (2021). The interaction between displacements and water level changes due to natural and anthropogenic effects in the Po Plain (Italy): The different point of view of GNSS and piezometers. *Journal of Hydrology,* 596, 126112.

Ng, A.H.M., Ge, L., Li, X., Abidin, H.Z., Andreas, H., Zhang, K. (2012). Mapping land subsidence in Jakarta, Indonesia using persistent scatterer interferometry (PSI) technique with ALOS PALSAR. *International Journal of Applied Earth Observation and Geoinformation*, 18, pages 232–242.

Nutalaya, P., Yong, R.N., Chumnankit, T., Buapeng, S. (1996). Land subsidence in Bangkok during 1978 – 1988. In Sea-Level Rise and Coastal Subsidence: Causes, Consequences, and Strategies, Milliman J.D. and Haq B.U. (Eds.), Kluwer Academic Publisher: Dordrecht, pp. 105 – 130.

Paris, A., Teatini, P., Venturini, S., Gambolati, G., Bernstein, A.G. (2010). Hydrological effects of bounding the Venice (Italy) industrial harbour by a protection cut-off wall: A modeling study. *Journal of Hydrologic Engineering*, 15 (11), pages 882-891.

Phien-wej, N., Giao, P.H., Nutalaya, P. (2006). Land subsidence in Bangkok, Thailand. *Engineering Geology*, 82, pages 187–201.

Picotti, F. & Pazzaglia, F.J. (2008). A new active tectonic model for the construction of the Northern Apennines mountain front near Bologna (Italy). *Journal of Geophysical Research,* 113, B08412.

Picotti, V., Ponza, A., Pazzaglia, F.J. (2009). Topographic expression of active faults in the foothills of the Northern Apennines. *Tectonophysics,* 474(1-2), 285-294.

Pieri, M. & Groppi, G. (1981). Subsurface geological structure of the Po Plain, Italy. Progetto Finalizzato Geodinamica, 414. CNR Pubblication, p. 23.

Pieri, M. (1983). Three seismic profiles through the Po Plain. Seismic expression of structural styles, 3, 3-4.

Pintori, F., Serpelloni, E., Gualandi, A. (2022). Common-mode signals and vertical velocities in the greater Alpine area from GNSS data. *Solid Earth*, 13, 1541-1568.

Poland, J.F. (ed) (1984). Guidebook to studies of land subsidence due to ground-water withdrawal. UNESCO Studies and Reports in Hydrology 40, UNESCO, Paris.

POLITO-DITAG, Politecnico di Torino-Ingegneria del Territorio dell'Ambiente e delle Geotecnologie (2011). Studio di Impatto Ambientale - Allegato B. Campo di Minerbio - Pool C, modello statico a scala regionale e modello geomeccanico. https://va.minambiente.it/it-IT/Oggetti/MetadatoDocumento/77429

POLITO-DITAG, Politecnico di Torino-Ingegneria del Territorio dell'Ambiente e delle Geotecnologie (2012). Studio di Impatto Ambientale - Allegato A. Campo di Minerbio. Modello statico ed analisi del comportamento dinamico per l'ottimizzazione della gestione operativa del livello di stoccaggio Pool C. https://va.minambiente.it/it-IT/Oggetti/MetadatoDocumento/77425

Pratt, W.E. & Johnson, D.W. (1926). Local subsidence of the goose creek oil field. *Journal of Geology*, 34, 577-590.

Regione Emilia-Romagna & ENI-AGIP (1998). Riserve idriche sotterranee della Regione Emilia-Romagna. A cura di G. Di Dio. Selca, Firenze.

Regione Emilia-Romagna (2003). Creazione di una banca informatizzata per la parametrizzazione idrodinamica degli acquiferi. Quadro Conoscitivo - Attività C.

Regione Emilia-Romagna (2010a). Delibera di Giunta n. 350 del 8/02/2010, Allegato 2 Tipizzazione/caratterizzazione e individuazione dei corpi idrici superficiali e sotterranei, prima individuazione delle reti di monitoraggio "Surface and groundwater bodies definition and characterization, first monitoring network set-up".

Regione Emilia-Romagna (2017). Carta Sismotettonica della Regione Emilia-Romagna e aree limitrofe (2016). Regione Emilia-Romagna, Geologia, Sismica e Suoli, Bologna, Italy, 93 pp.

Regione Lombardia & ENI DIVISIONE AGIP (2002). Geologia degli Acquiferi Padani della Regione Lombardia. Selca, Firenze.

Rocca, V., Benetatos, C., Codegone, G., Mantegazzi, A. (2021). Subsidence Analysis in the Italian Po Plain Area: An Extended Case Study. In: 82nd EAGE Annual Conference & Exhibition, Amsterdam, 18-21 October 2021, pp. 1-5.

Salvioni, G. (1957). I movimenti del suolo nell'Italia Centro-Settentrionale. *Bolletino Di Geodesia e Scienze Affini*, XVI.

Sclater, J.G. & Christie, P.A.F (1980). Continental stretching: An explanation of the Post-Mid-Cretaceous subsidence of the central North Sea basin. *Journal of Geophysical Research*, 85, 3711-3739.

Scott, R.F. (1979). Subsidence – A review. En: Saxena, S.K. (ed.). Evaluation and prediction of subsidence. *Proc. of the Int. Conf.*, Pensacola Beach, Florida, January 1978, Am. Soc. Civil Eng., New York, 1-25.

Severi, P. and Bonzi, L. (2011). Distribuzione degli acquiferi padani nel sottosuolo della pianura bolognese, RELAZIONE GEOLOGICA. *Servizio Geologico, Sismico e dei Suoli e Regione Emilia-Romagna,* Bologna, July 2011.

Severi, P. (2021). Soil uplift in the Emilia-Romagna plain (Italy) by satellite radar interferometry. *Bulletin of Geophysics and Oceanography,* 62(3), 527-542.

Smith, R.G. & Majumdar, S. (2020). Groundwater storage loss associated with land subsidence in Western United States mapped using machine learning. *Water Resources Research*, 56, e2019WR026621.

SPERIMENTAZIONE ILG MINERBIO STOCCAGGIO - Concessione di stoccaggio di gas naturale “Minerbio stoccaggio” (BO) Struttura Preposta al Monitoraggio – Relazione Finale (Luglio, 2019). *ISTITUTO NAZIONALE DI GEOFISICA E VULCANOLOGIA.*

Stefani, M. and Vincenzi, S. (2005). The interplay of eustasy, climate and human activity in the late Quaternary depositional evolution and sedimentary architecture of the Po Delta system. *Marine Geology,* 222-223, 19-48.

Stramondo, S., Saroli, M., Tolomei, C., Moro, M., Doumaz, F., Pesci, A., Loddo, F., Baldi, P., Boschi, E. (2007). Surface movements in Bologna (Po Plain – Italy) detected by multitemporal DInSAR. *Remote Sensing of Environment*, 110, 304-316.

Styles, P., Gasparini, P., Huenges, E., Scandone, P., Lasocki, S., Terlizzese, F (2014). Report on the Hydrocarbon Exploration and Seismicity in Emilia Romagna;

International Commission on Hydrocarbon Exploration and Seismicity in the Emilia Romagna Region: Emilia Romagna, Italy, 2014.

Tan, P., Steinbach, M., Karpatne, A., Kumar V. (2018). Introduction to Data Mining, 2nd edition. Pearson

Teatini, P., Gambolati, G., Tosi, L. (1995). A new 3-D non-linear model of the subsidence of Venice. In Land Subsidence, Proceedings of the 5th International Symposium on Land Subsidence, Hague, The Netherlands, 16–20 October 1995; International Association Hydrogeological Sciences: Wallingford, UK, 1995; pp. 353–361.

Teatini, P., Bau´, D., Gambolati. G. (2000). Water-gas dynamics and coastal land subsidence over Chioggia Mare field, northern Adriatic Sea. *Hydrogeology Journal,* 8(5), 462 – 479.

Teatini, P., Ferronato, M., Gambolati, G., Gonella, M. (2006). Groundwater pumping and land subsidence in the Emilia-Romagna coastland, Italy: Modeling the past occurrence and the future trend. *Water Resources Research*, 42, W01406.

Teatini, P., Ferronato, M., Gambolati, G., Bau´, D., Putti, M. (2010), Anthropogenic Venice uplift by seawater pumping into a heterogeneous aquifer. *Water Resources Research*, 46, W11547.

Teatini, P., Castelletto, N., Ferronato, M., Gambolati, G., Tosi, L. (2011), A new hydrogeological model to predict anthropogenic Venice uplift. *Water Resources Research*, 47, W12507.

Terzaghi, K. (1923). "Die Berechnung der Durchlässigkeitziffer des Tones aus dem Verlauf der hydrodynamischen Spannungserscheinungen". Akademie der Wissens chaften in Wien, Matematisch – Naturwissen – Schaftliche Klasse. Sitzungsberichte. Abteilung II, Wien.

Terzaghi, K. (1936). The shearing resistance of saturated soils and the angle between the planes of shear. First International Conference on Soil Mechanics, Vol1, Harvard University, pp. 54–56.

Theis, C. V. (1935), The relationship between the lowering of the piezometric surface and the rate and duration of discharge of a well using groundwater storage. *Trans. AGU*, 16, 519–524.

Turrini, C., Lacombe, O., Roure, F. (2014). Present-day 3D structural model of the Po Valley basin, Northern Italy. *Marine and Petroleum Geology*, 56, 266-289.

Turrini, C., Toscani, G., Lacombe, O., Roure, F. (2016). Influence of structural inheritance on foreland-foredeep system evolution: An example from the Po valley region (northern Italy). *Marine and Petroleum Geology*, 77, 376-398.

U.S. Army Corps of Engineers (1996). NAVSTAR Global Positioning System Surveying. Engineer Manual 1110-1-1003.

Vanolli, P., Burrato, P., Valensise, G. (2014). The Seismotectonics of the Po Plain (Northern Italy): Tectonic Diversity in a Blind Faulting Domain. *Pure and Applied Geophysics*, 172, 1105-1142.

Verga, F (2018). What’s conventional and what’s special in a reservoir study for underground gas storage. *Energies*, 11, 1245.

Yamamoto, S. (1995) Recent trend of land subsidence in Japan. In Land Subsidence, Barends F.B.J., Brouwer F.J.J. and Schroder F.H. (Eds.), IAHS Publication No. 234: pp. 487 – 492.

Yi, L., Zhang, F., Xu, H., Chen, S., Wang, W., Yu, W. (2011). Land subsidence in Tianjin, China. *Environmental Earth Sciences*, 62, pages 1151–1161.

Zebker, H.A. & Villasenor, J. (1992). Decorrelation in interferometric radar echoes. *IEEE Transactions on Geoscience and Remote Sensing*, 30, 950−959.

Zoback, M.D. (2007). Reservoir Geomechanics.